HARVARD UNIVERSITY
Graduate School of Arts and Sciences

DISSERTATION ACCEPTANCE CERTIFICATE

The undersigned, appointed by the

Committee on Higher Degrees in Systems Biology

have examined a dissertation entitled

A Computational Approach to Analysis and Control of the Mammalian Circadian Oscillator

presented by John H. Abel

candidate for the degree of Doctor of Philosophy and hereby
certify that it is worthy of acceptance.

Signature ______________________________
Typed name: Prof. Johan Paulsson

Signature ______________________________
Typed name: Prof. John Higgins

Signature Charles A. Czeisler
Typed name: Prof. Charles Czeisler

Signature ______________________________
Typed name: Prof.

Date: April 5, 2018

A Computational Approach to Analysis and Control of the Mammalian Circadian Oscillator

A dissertation presented
by
John H. Abel
to
The Department of Systems Biology

in partial fulfillment of the requirements
for the degree of
Doctor of Philosophy
in the subject of
Systems Biology

Harvard University
Cambridge, Massachusetts

April 2018

Dissertation Advisor: Professor Francis J. Doyle III John H. Abel

A Computational Approach to Analysis and Control of the Mammalian Circadian Oscillator

Abstract

Circadian rhythms, endogenous, entrainable, near-24 h oscillations in metabolism, are a nearly ubiquitous feature of life on Earth. Circadian rhythms function as a feedforward biological control system that reorganizes cellular metabolism in anticipation of daily predictable changes in the environment. Because circadian regulation mediates many physiological processes, there is widespread interest in understanding the system generating mammalian circadian rhythms, and developing techniques for reliably manipulating that system through exogenous stimuli such as light or pharmaceuticals. In this dissertation I approach these questions using computational and theoretical tools from dynamical systems and control theory.

The first portion of this dissertation consists of collaborative studies investigating the organization of the mammalian hypothalamic suprachiasmatic nucleus (SCN), the master pacemaker. First, I examined the network structure driving synchrony in the SCN. To observe the network, we desynchronized the SCN using a toxin that prevents neurotransmitter release, then applied an information theoretic metric to correlate circadian gene expression between neurons as they resynchronized spontaneously. We found that the functional network observed during resynchronization is small-world but not scale-free, with hubs primarily located in the central SCN. Next, I present results from a study of the development of circadian rhythms and synchrony in the embryonic SCN. By explanting fetal SCN and recording circadian bioluminescent reporters, we found that circadian rhythms become autonomous within the fetal SCN by embryonic day 14.5 following mating, and synchronize spontaneously around embryonic day 15.5. Intriguingly, spontaneous synchrony preceded the expression of the neuropeptide VIP and its receptor, the primary pathway of neurotransmission associated with synchrony in the mature SCN. Finally, I present a study of the relationship between electrical activity and VIP release in the SCN. Using optical tagging, we found that VIP and non-VIP neurons of the SCN express distinct firing patterns that are consistent across multiple days despite prolonged silences in firing at circadian night. Furthermore, firing at frequencies observed in SCN recordings resulted in phase delays *in vitro* that are abolished by a VIP

antagonist, and phase delays *in vivo*. These three studies highlight the complex nature of neurotransmission in the SCN. Most importantly, these studies indicate that VIP is not the only significant neurotransmitter driving SCN synchrony, as VIP does not exactly explain the network structure, synchrony appears before VIP expression, and VIP evokes primarily phase delays though the SCN can exhibit advances or delays.

The second portion of this dissertation discusses the inverse problem: optimal resetting of circadian phase. First we formulated the optimal phase shifting problem by reducing a multistate mechanistic model of circadian oscillation to a phase-only formulation, with the control input included as a parametric phase sensitivity. We then applied Pontyagin's maximum principle, and show that this is a steering problem, where the optimal path to resetting is applying either maximal advances or delays. Next, we derived bounds on the errors incurred by applying model predictive control (MPC) rather than an optimal control policy, and demonstrate *in silico* results for two real-world scenarios of phase resetting. Finally, I present a study showing that the single-oscillator control approach may be inappropriate when considering that the body is comprised of numerous oscillators. We showed that a simple modification of the MPC optimization is sufficient to maintain oscillator synchrony and still achieve phase control.

In both portions, I conclude by providing several paths of future study that remain unaddressed. The studies within this dissertation indicate that control of circadian oscillation in mammals is within reach.

Contents

Acknowledgement

I owe such an intellectual debt to so many individuals that it feels like the true author list for this dissertation should be half its content. Most prominently I would like to thank my primary advisor Frank Doyle for his unwavering support during this process. It's only in retrospect that I can understand how valuable your contributions were to the development of my thinking. To my coadvisors, Professors Linda Petzold and Beth Klerman, and my additional mentors Professors Erik Herzog and Hyunmin Yi: thank you for committing your time and intellectual energy to my development. Sorry for the late hours at which I replied to your emails. I've also been quite lucky to have a remarkable cast of collaborators, and I would like to thank Vania Carmona-Alcocer, Ankush Chakrabarty, Brian Drawert, Daniel Granados-Fuentes, Cristina Mazuski, Peter St. John, and Steffen Waldherr. I'm humbled to be considered your peer. In particular, Peter St. John's mentorship has had a disproportionate positive effect on my research, and for that I am grateful. I am also grateful for the community that the entire Doyle group has been throughout my time in it. From squash, to ill-advised witch hunts (apologies to Lindsey Brown, no apologies to Kelsey Dean), to Thanksgivings at Eyal's, it's been a remarkable time. Thank you especially to Alejandro Laguna, Kelsey Dean, Faith Barcelo, Eyal Dassau, Sunil Deshpande, Joon Bok Lee, Ravi Gondhalekar, and Gunjan Thakur for moving across the country with me.

I have been extraordinarily privileged to have had the support of numerous educators and institutions, all of which contributed to my completion of this dissertation. Harvard, UC Santa Barbara, and Tufts have been fantastic developmental environments to which I hope to return frequently. To Liz Pomerantz and Sam Reed: I could not have survived here without your help, and the Systems Biology program has felt like an intellectual home ever since I arrived on campus. Finally, I would like to thank the educators who inspired me to embrace challenging questions from early on, especially Matthew McDonough, Thomas Morey, and Sr. Carol Ann Murray.

To my family {Anthony, Frederick, Joseph, Judy, Katrina, Virginia} Abel, {Faith, Kim} Blake, {Alyssa, Mary} Miller: thank you for making me who I am. I hope I have made you proud. I would like to especially acknowledge Faith Blake for her often unnoted intellectual contributions to my work, most prominently in interpreting data recorded from the fetal suprachiasmatic nucleus and in editing and questioning every manuscript I have written. It seemed out of place to acknowledge you on the papers, in that all of my ideas were also fundamentally yours. I hope that I can contribute to your career even half of what you have to mine. I would also like to thank my friends, but in lieu of listing names I'll list locations significant to us: Beacon Hill, Big Sur, Hemenway, Holualoa, Indio, Isla Vista, the Louvre, West End Avenue, Winthrop.

"My name is Ozymandias, king of kings:
Look on my works, ye Mighty, and despair!"
-*Ozymandias*, Percy Bysshe Shelley

Chapter 1

Introduction

Circadian rhythms are endogenous oscillations in gene expression, metabolism, and behavior that allow an organism to adjust its internal state to predictable cyclic changes in the environment. This advantageous feed-forward approach to life in a temporally cyclic environment allows an organism with a circadian rhythm to anticipate environmental variability and adjust its physiology without a time lag. Circadian regulation of biological processes is therefore highly-conserved: these rhythms have been identified in diverse species from mammals, insects, plants, and fungi to prokaryotic cyanobacteria [1–4]. Although circadian clocks share common properties between species, the mechanistic origins and hierarchical complexity of these rhythms can vary significantly. Prokaryotes have been shown to use minimal phosphorylation-based non-transcriptional oscillators, which may be reconstituted *in vitro* [5, 6]. Meanwhile, eukaryotic organisms employ transcriptional-translational feedback loops in addition to post-translational protein modification for timekeeping [7, 8]. In larger organisms such as mammals, circadian rhythms must be coordinated across cells and tissues, resulting in a complex yet robust circadian control system [9, 10].

The inherently complex (i.e. involving nonlinearity and feedback) and stochastic (i.e. fundamentally involving randomness and noise) nature of these processes has necessitated mathematical approaches for understanding biological clocks, as their properties emerge from the often-imprecise interaction of numerous molecules and pathways. Such approaches have in-

---

Portions of this chapter appear as J.H. Abel and F.J. Doyle III, "A systems approach to analysis and control of mammalian circadian dynamics," *Chemical Engineering Research and Design*, vol. 116, 2016. DOI: 10.1016/j.cherd.2016.09.033; and J.H. Abel, A. Chakrabarty, and F.J. Doyle III "Pharmaceutical-based entrainment of circadian phase via nonlinear model predictive control," submitted. The text has been modified to provide a more thorough introduction.

cluded mechanistic and empirical process modeling [11–19], robustness and sensitivity analysis [13, 20–25], and optimal or feedback control [10, 26–29]. This thesis presents recent advances in developing an understanding of, and artificially exerting control over, the mammalian circadian system through mathematical approaches.

On organization

In this chapter, I begin by presenting a brief historical overview of the study of daily patterns of behavior, culminating with the identification of clock genes in multiple organisms in the 1990s. I next define the general characteristics that constitute a circadian rhythm. I then introduce biological generation of mammalian circadian rhythms, and also note how this structure compares to that of other organisms. I present a mathematical framework for modeling and analysis of circadian dynamics based on the limit cycle oscillator, and present derivations for relevant quantities. Finally, I discuss motivation for feedback control of circadian rhythms, and the components of a system to achieve this.

The ensuing dissertation is then divided into two main sections to reflect the two foci of my research. In Section I, I present projects in fundamental biology toward the aim of understanding the structure and function of mammalian circadian rhythm generation and synchronization in the suprachiasmatic nucleus (SCN). In Section II, I present a mathematical framework for taking control of this system, and derive results that aim to guide the development of this capability. Future research aims are included separately for each Section.

My exact contributions are noted for each section so as to avoid claiming credit for the work of my dedicated and highly skilled collaborators. The majority of this work has already been published, and for published chapters I have attempted to edit as little as possible for this volume. This serves two purposes: consistency in the literature record and avoiding the introduction of new errors of my own making.

On notation

Where possible, I have generally attempted to adopt a uniform notation throughout this thesis. This has primarily affected the presentation of this Introduction: the notation has been changed from the original publication to match with Section II. For the confused reader, I would recommend studying the original publications in detail: the notation in these is certainly internally consistent and self-contained.

1.1 An introduction to circadian rhythms

A brief history of circadian biology

It has long been noticed that organisms adjust their physiology in accordance with day-night cycles. Androsthenes of Thasos, an admiral in the navy of Alexander the Great, noted daily rhythms in leaf movements of *Tamarindus indicus*, but did not suspect that these rhythms were more than a response to light [30]. It was not until the 1700s that the first "true" chronobiological experiment was performed, demonstrating that rhythms in leaf movement are endogenous, rather than a response to the light-dark cycle [31]. In the following 200 years, endogenous rhythms in physiology were observed in more plant species, arthropods [32], and eventually, rats [33]. By the mid 20th century, it was well-established that an unidentified endogenous process was driving the near-24 hour rhythms in behavior observed under constant conditions.

Perhaps the most important discovery in identifying the underlying basis of circadian rhythms was the discovery of the *Period* (*Per*) gene in *Drosophila melanogaster* in 1971 [34]. In a classic work, Konopka and Benzer demonstrated that inducing mutations in a single gene on the *Drosophila* X chromosome can induce lengthened, shortened, or abolished circadian eclosion rhythms in constant darkness. Furthermore, these mutations conferred altered circadian period phenotypes in adults, indicating that an underlying genetic oscillator drives circadian rhythms, and that this oscillator persists through metamorphosis. It was this and the ensuing studies that led to the discovery of the autoregulatory function of *Per* [35], the discovery of the gene involved in its nuclear localization (*Timeless*) [36], and the 2017 Nobel Prize in Physiology or Medicine. In this same timeframe, the genetic basis of the mammalian clock was identified as a transcription-translation feedback loop analogous to the *Per*/*Timeless* feedback loop of *Drosophila*. A homologous *Per* gene was identified in mammals, and *Cryptochrome* was identified as its co-regulator [37]. Furthermore, homologs of the *Clock* gene were identified as the transcriptional activator in both mammals and *Drosophila* [38, 39].

Since the identification of the key transcriptional pathways of the mammalian circadian clock, much effort has focused on elucidating the complex genetic architecture surrounding the clock [40, 41]. The circadian oscillator has been found to widely regulate transcription within mammals, and approximately 10% of all transcripts cycle with circadian periodicity [42]. This is perhaps unsurprising, as genetic evidence suggests that circadian rhythms evolved in concert with peroxiredoxin oxidation-reduction cycles [43]. Because cycles in metabolic regulation may have enabled archaic organisms to survive oxidative stress cycles in a newly-aerobic environment, circadian rhythms are deeply integrated within cellular and organismal metabolic networks.

Properties of the circadian clock

Circadian rhythms are distinguished from other periodic biological processes by several criteria [44]. First, circadian rhythms are endogenous, that is, they are self-sustained even in constant environmental conditions. Second, circadian clocks are entrainable and shift in phase or period to align with environmental cycles through cues referred to as *zeitgebers*[1]. Third, they are traditionally considered to be temperature-compensated, meaning oscillator period is insensitive to changes in temperature in the external environment. This property has recently drawn renewed scrutiny in the past 15 years following evidence that temperature cycles can entrain cell-autonomous circadian oscillators [45]. Finally, circadian rhythms have oscillatory periods of approximately, though often not exactly, 24 hours. Counterintuitively, a near-24h period may be more advantageous than an exactly-24h period, as it provides increased stability of entrained phase angle [44].

1.2 The mammalian circadian control system

In mammals, circadian rhythms are generated within individual cells by a network of interlocked genetic feedback loops [7, 46, 47]. These cell-autonomous clocks are responsible for regulation of genetic expression and metabolic processes in local tissue. For example, circadian regulation of glucose metabolism is localized to liver tissue, and the deletion of core clock genes in only liver tissue is sufficient to abolish circadian rhythms in expression of glucose regulatory genes [48]. This view is supported by studies demonstrating that rhythmic gene expression profiles are

---

[1] Trans. German: Time-givers

tissue-specific [49, 50]. Cellular rhythms are coordinated across tissues in the body and entrained to environmental rhythms through signals from the brain. The hypothalamic suprachiasmatic nucleus (SCN) is considered the "master clock" in mammals: it is responsible for entraining to light inputs and maintaining synchrony among the cell-autonomous oscillators in peripheral tissues throughout the body [9]. Peripheral tissues receive local inputs in addition to SCN signals, for example, cells in the liver may be entrained by rhythmic feeding independently of the SCN [51]. Finally, it is thought that peripheral clocks exert a degree of feedback into the SCN, though whether this is direct or indirect remains unknown [52].

A need for understanding and control of the clock

It is estimated that approximately 10% of all mammalian transcripts are under circadian regulation [42]. With such widespread influence, it is unsurprising that circadian rhythms play an important role in human health and disease. In particular, high amplitudes of circadian transcription factors in peripheral tissues are desirable for good metabolic health. Mice lacking circadian rhythms due to core clock gene knockouts, or with diminished circadian amplitude due to diet or age have been shown to develop diseases, including metabolic syndrome and diabetes [53–55]. Similarly, lifestyle factors such as shift work can cause misaligned circadian cues, resulting in diminished amplitude of circadian oscillation, and ultimately, adverse health outcomes [52, 56, 57]. Neurological diseases such as posttraumatic stress disorder (PTSD), depression, and addiction are also associated with circadian disregulation [58–60]. Thus, a general aim of the study of the circadian clock is the development of pharmacological or behavioral therapies for maintaining high-amplitude circadian rhythms, or easing the effects of circadian phase resetting during jet-lag or shift work. Relatedly, there is interest in how circadian rhythms affect drug metabolism and efficacy, especially with respect to cancer medication due to circadian control of cell cycles [61, 62]. To develop such therapies, the mammalian circadian clock must be investigated mechanistically as a dynamical system.

Circadian rhythms in mammals are generated within individual cells by interlocked transcriptional-translational feedback loops [46]. The cell-autonomous genetic clock is largely conserved across cell types, with the notable exception of red blood cells, which lack a nucleus and may compensate with a non-transcriptional clock [63]. Although the core clock is conserved, the genes under clock control may vary with cell type, creating a temporal architecture of gene expression across the body.

The cell-autonomous circadian clock

A schematic of the core clock is shown in Figure 1.1A. The interlocked positive (dotted lines) and negative transcriptional feedback loops (solid lines) are considered the primary source of circadian oscillation [46, 47]. Within the negative loop, isoforms of the *Period* (*Per1,2,3*) and *Cryptochrome* (*Cry1,2*) are transcribed and translated, and form heterodimers. PER-CRY heterodimers re-enter the nucleus, and repress transcription of Enhancer box (E box) genes including *Per* and *Cry* through sequestration of E box activator CLOCK-BMAL1 by dissociated CRY [64]. Over time, nuclear PER and CRY is degraded, allowing transcription to resume. This negative loop is balanced by an interlocked positive feedback loop regulating the expression of *Bmal1*. In this loop, E box-controlled genes *Rev-erbα* and *Rorα* repress and promote *Bmal1* transcription, respectively, through competitive binding to the ROR/REV-ERB Response Element (RRE) in the *Bmal1* promoter [65]. Collectively, the genes *Per*, *Cry*, *Clock*, and *Bmal1* are considered the core circadian clock.

It is important to note here that new evidence is emerging which downplays the primacy of transcriptional activity in circadian oscillation [66]. Recent studies have shown that limited oscillation may still occur in the absense of transcriptional oscillations of core clock genes, likely due to feedback loops involving phosphorylation of the products of core clock genes [67–69]. While this may yet become a monumental shift in our understanding of the clock, it is important to also note that the behavior of the clock, whether transcriptional or phosphorylational, exhibits the mathematical properties of a limit cycle oscillator, and so the approaches described herein may be applied analogously to such a phosphorylational system, should it be identified as the efficient cause of circadian oscillation.

The core clock regulates cellular transcription of clock-controlled genes (CCGs) via RREs, E boxes, and D boxes (DBP binding elements) [70]. Because the transcription factors corresponding to these elements peak at different circadian times, transcription of genes may be partitioned into various times of day. The core clock is also affected by a wide variety of cell type-specific transcription factors or posttranslational regulators. A genome-wide RNAi screen identified

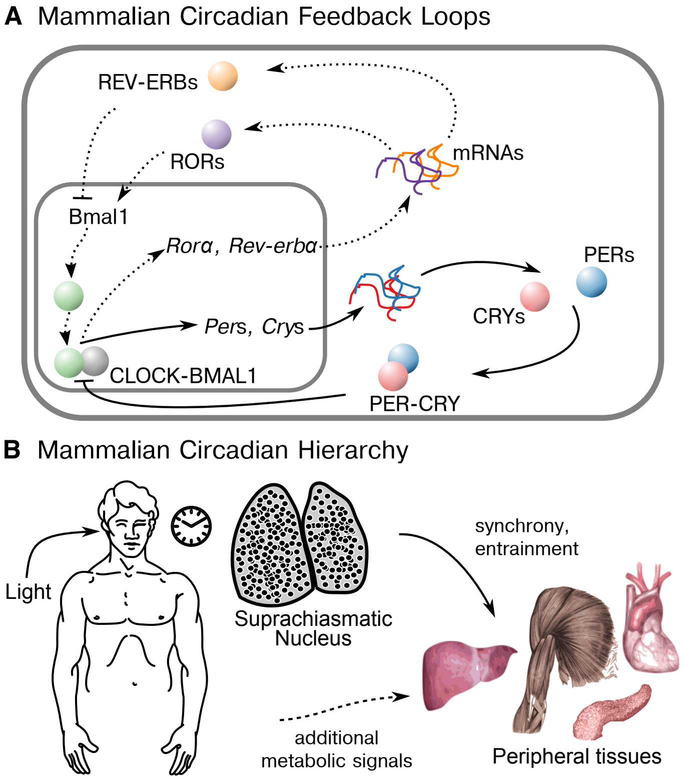

Figure 1.1: Schematic of the mammalian cell-autonomous clock and circadian system hierarchy. (**A**) Two interlocked feedback loops comprise the mammalian circadian oscillator: the PER-CRY negative feedback loop (solid lines), and the CLOCK-BMAL1 positive feedback loop (dotted lines). Diagram adapted from [46]. (**B**) The suprachiasmatic nucleus of the brain is the mammalian "master clock," responsible for entrainment to external light cycles and synchronizing peripheral oscillators such as those within the liver, muscle, heart, and pancreas. Within the SCN, neurons exchange neuropeptidergic and electrical signals to maintain synchrony.

Table 1.1: A non-exhaustive list of notable mammalian circadian models demonstrating the range in scale and scope of such models. While not specific to circadian oscillation, the structure of the Goodwin oscillator is a common framework for circadian analysis.

Reference	Dynamic States	Kinetic Parameters	Model Form
Goodwin 1965 [71]	3	6	general limit cycle ODE model
Kronauer *et al.* 1999 [11]	3	9	ODE limit cycle with light response
Leloup and Goldbeter 2003 [13]	16	53	mammalian mechanistic ODE model
Forger and Peskin 2005 [15]	73	36	mammalian mechanistic CME model
To *et al.* 2007 [16]	17/cell	62	multicellular mammalian ODE model

hundreds of genes with phenotypic effects on clock period or amplitude, indicating that clock pathways are highly interconnected with other, often tissue-specific metabolic pathways [40].

Stochasticity in the clock

Macroscale chemical processes may be approximated with continuous chemical kinetics, however, the low copy number of genes, transcripts, and proteins within an individual cell results in considerable deviation from continuous kinetics [72]. Stochasticity, or molecular noise, caused by the discrete nature of biochemical reactions, is referred to as *intrinsic* stochasticity. Although circadian rhythms are precise at the organism-scale, there is a significant degree of intrinsic stochasticity in circadian oscillation at the single-cell scale. The cycle-to-cycle variation in circadian period within a single cell is due to intrinsic stochasticity [73]. Intrinsic stochasticity may be captured computationally through the use of stochastic simulation algorithms [15, 20]. Cellular reactions are also subject to *extrinsic* stochasticity, caused by differences between cells or within the microscopic environment, including gradients in temperature, or differences in cell cycle phase, cell size, or organelle distribution. Extrinsic stochasticity may be simulated by introducing a variability in model parametrization. Intrinsic and extrinsic variability have been studied in the circadian clock experimentally [73, 74] and computationally [15, 18, 20, 21, 75–77]. Within the circadian system, communication between cells and tissues allows the maintenance of a precise circadian phase, and adaptation to environmental cues.

Hierarchy of clocks in the body

Mammalian circadian hierarchy, shown in Figure 1.1B, enables the coordination of circadian oscillation through the organism. The suprachiasmatic nucleus (SCN), the "master clock," consists of approximately 20,000 neurons within the hypothalamus. Neurons within the SCN synchronize spontaneously and therefore maintain tissue-scale oscillation indefinitely *in vitro*, whereas other tissues which lack intercellular communication display a damped oscillation likely due to gradual dephasing [74, 78]. SCN neurons exchange neuropeptidergic, neurotransmitter, and electrical signals to synchronize [9]. Molecular signals of primary importance are vasoactive intestinal peptide (VIP) and γ-aminobutyric acid (GABA) [79–82]. The SCN is commonly divided into two regions: a ventral "core" and a dorsal "shell," which differ in neuropeptide expression and response, and neuronal network structure [9, 81–85]. The SCN entrains through its core region receiving light input from the retinohypothalamic tract (RHT) [9]. The SCN then adjusts its phase of oscillation to match light cues, and the shell region outputs time of day cues to connected brain regions and ultimately the rest of the body [86].

Peripheral tissues sustain oscillation in the absence of a functional SCN, however, signals from the SCN are necessary to maintain a coherent phase [9]. These signals from the SCN include sympathetic and parasympathetic pathways, hormonal rhythms, and temperature [47]. In addition to signals from the SCN, peripheral tissues receive local metabolic cues which help to establish circadian phase. Glucose, glucocorticoids, insulin, and other common metabolic factors have been shown to influence the clock, and it is possible that multiple metabolic signals are simultaneously responsible for modulating peripheral clocks [52, 87]. Restricted feeding in rodents has been shown to effectively decouple liver cells from the SCN and shift circadian phase by nearly 180°, indicating that metabolic cues form an important component of the circadian system [88].

1.3 Quantitative analysis of circadian dynamics

In the past several decades, significant advances in understanding circadian rhythms have been made through the use of mathematical modeling. Here, we present an introduction to sensitivity analysis and modeling of the circadian clock, with a focus on ordinary differential equation models. Section 1.3 introduces the concept of a limit cycle oscillator, a dynamical system commonly used to describe circadian clockwork. Section 1.3 introduces a variety of quantitative tools for the analysis of a single limit cycle oscillator, and 1.3 expands upon these tools for the analysis of a population of oscillators. Sections 1.3 and 1.3 provide derivations of the tools introduced in 1.3 and 1.3, respectively, and comment on how these quantities may be calculated. For the casual reader, 1.3 and 1.3 may be omitted without loss of qualitative understanding.

Circadian clock dynamics are commonly modeled through coupled nonlinear equations. Broadly, clock models may be empirical (i.e., designed to capture clock behavior without regard for the underlying physical system), or mechanistic (i.e., comprised of the underlying species and their mathematical relationships). Furthermore, these models may consist of deterministic ordinary differential equations (ODEs) [11–13, 16, 17, 19, 89], a discrete stochastic chemical master equation (CME) [15, 18, 20, 76], or Langevin stochastic differential equations (SDEs) [90, 91]. Stochastic approaches are generally utilized in cases where intrinsic molecular noise is thought to be significant. A description and the dimensions of five notable circadian models are provided in Table 1.

Irrespective of these possibilities, the circadian clock is primarily modeled as a deterministic set of ODEs comprising a limit cycle oscillator. This is because the circadian oscillator exhibits limit cycle-like behavior: it has a self-sustained oscillation with stable waveform and amplitude, the oscillator manifold is attractive, and perturbations to oscillation result in a phase shift. The dynamics of a limit cycle oscillator are additionally useful for explaining entrainment and phase and amplitude response behavior of the circadian oscillator.

The limit cycle oscillator

Limit cycle oscillators are not unique to biology, for example, they have been utilized to describe oscillatory chemical reactions [92], electrical circuits [93], and earthquakes [94]. As such, some of the following tools were first conceptualized outside of the context of biological rhythms. For this work, we are exclusively interested in tools developed to describe attractive limit cycles. An attractive limit cycle oscillator consists of a set of coupled ODEs of the form:

$$\frac{dx}{dt} = f(x, t, p), \tag{1.1}$$

which satisfies:

$$\lim_{t \to \infty} [x(t) - x(t - T)] = 0. \tag{1.2}$$

The steady state limit cycle is therefore the closed oscillatory path $\Gamma \subset \mathbb{R}^n$ which is traversed with a period of T, where T is the smallest positive value for which (1.2) holds. For mechanistic models, $x \in \mathbb{R}^n$ is a vector of state concentrations, $p \in \mathbb{R}^m$ are kinetic parameters, and $\dot{x} = f(x, p)$ are differential material balance equations, of the form:

$$\frac{dx_i}{dt} = r_{x,in} - r_{x,out} + r_{x,generation} - r_{x,consumption} \tag{1.3}$$

for each of n species. The rate terms comprising the right hand side of (1.3) may follow mass-action, Michaelis-Menten, or Hill kinetics, providing an explicit mathematical analogy with the treatment of a continuous stirred tank reactor (CSTR) system. Here, the concentrations of mRNA and protein species correspond with the reactants and products in a CSTR, and the volume of the subcellular compartment in which each species resides corresponds to CSTR volume. However, concentrations are often provided in arbitrary concentration units for simplicity without loss of information. Empirical models need not conform to this physicality, and as such the Van der Pol oscillator is commonly used [11]. For simplicity, we will continue with our treatment of a mechanistic model, though the same tools apply to empirical models differing only in interpretation.

Each unique point x_0 on the stable limit cycle Γ corresponds to a unique phase $\phi_0 \in \mathbb{S}_{\mathbb{1}} = [0, 2\pi)$, with the corresponding mapping $\Phi : \Gamma \to \mathbb{S}^1$. Let $\gamma(t, x_0)$ denote the solution of system (1.1) with initial condition $x(0) = x_0 \in \Gamma$. Then, a time-dependent phase variable may be established

$$\phi(t) = \Phi[\gamma(t, x_0)]. \tag{1.4}$$

Intuitively, phase increases linearly with respect to time along the path Γ:

$$\frac{d\phi}{dt} = \omega, \tag{1.5}$$

where $\omega = 2\pi/T$ is the radial frequency. This yields particular solutions of the form

$$\phi(t) = \omega t + \phi_0 \qquad \mod 2\pi \tag{1.6}$$

where $\phi_0 = \Phi(x_0)$. Finally, let $x^0 \in \Gamma$ denote the arbitrary point on the limit cycle for which $\Phi(x^0) = 0$.[2]

Sensitivity analysis of limit cycle models

For oscillatory systems, most dynamic biological data are concerned with how the period of oscillation is affected by a permanent change in parameter values [19, 40], or how the phase or amplitude of oscillation is affected by temporary changes in state variable concentrations or parameter values [12, 95–97]. Sensitivity analysis of dynamical systems is traditionally concerned with how a solution to differential or differential-algebraic equations varies with respect to perturbations in initial state or parameter values, and these biological quantities may be described within a sensitivity analysis framework.

Biologically relevant oscillatory sensitivity metrics include: phase change in response to a state perturbation (for example, the one-time addition of a clock protein) $\frac{d\phi}{dx}$; phase change in response to a temporary parameter perturbation (for example, applying a light pulse to photosensitive cells) $\frac{d}{dt}\frac{d\phi}{dp}$; amplitude change in response to a state perturbation $\frac{dA}{dx}$; amplitude change in response to a temporary parameter perturbation $\frac{d}{dt}\frac{dA}{dp}$; period change in response to a permanent parameter change (for example, knockout of a clock protein isoform) $\frac{dT}{dp}$. The phase shift $\Delta\phi$ for a temporary change in parameter value converges asymptotically in time. However, because period T and orbit Γ are dependent on parameterization, a permanent change in parameter value will result in the phase change $\Delta\phi$ accumulating [22, 23]. The phase response of a system to state

---

[2] On notation: it is important to remember that x_0 is an arbitrary point on Γ, and x^0 is the particular point on Γ for which $\phi = 0$. Thus, trajectory $\gamma(t, x_0)$ is any arbitrary trajectory along Γ, but $\gamma(t, x^0)$ is the trajectory along Γ for which $\phi(0) = 0$.

or parameter perturbations occurring at different phases is commonly called a phase response curve (PRC), and its amplitude equivalent may be called an amplitude response cure (ARC).

By combining these sensitivity metrics with biological investigations, mathematical models may be used to guide experimentation, predict system behavior under new conditions, identify the roles of novel genes within the biological circuit, or uncover the mechanisms of drug action. In Section II, we additionally show how the infinitesimal parametric phase response curve $\frac{d}{dt}\frac{d\phi}{dp}$ may be used to exert control over the circadian system. Sensitivity analysis may be further expanded to describe changes in probabilistic behavior of discrete stochastic systems described by the chemical master equation [98]. These metrics are necessarily unique for stochastic systems, as higher moments of the proability distributions of each state may vary while the first moment does not.

Analysis of cellular populations

Thus far, we have treated the circadian clock as a single deterministic limit cycle oscillator. This limit cycle oscillator may be interpreted as representing the population-scale circadian oscillation, or alternately the oscillation within a single cell. Physically, each cell contains a noisy oscillator, which exhibits both intrinsic and extrinsic stochasticity. In some cases, simultaneously examining population-scale and single-cell dynamics through mathematical analysis of a population of limit cycle oscillators allows further insight into clock function or control.

In the SCN, coherent population-scale oscillation is self-sustained, due to intercellular communication driving synchrony [9]. In peripheral tissues, however, the lack of paracrine signalling results in a gradual damping of population-scale oscillation, as the cells comprising the population require external signals to maintain a synchronized phase [77]. Cultured circadian reporter cells similarly lack intercellular signalling, thus these cultures must be examined through the dual lens of population and single-cell effects. For example, a temporary perturbation to cultured reporter cells such as a light pulse will have two effects on the amplitude of bioluminescence: a cellular-scale effect due to the deviation from the limit cycle, and a population-scale effect due to the condensing or dispersing of cellular phases [99–101]. The single-cell effect will be transient, due to relaxation to the limit cycle, but the population synchrony effect will persist well after the pulse has ended.

These effects may be quantified through the use of previously-discussed sensitivity metrics. For example, a perturbation to cells within a region of negative slope of the single-cell PRC will result in increased population synchrony and thus increased population amplitude, whereas a positive slope will decrease population synchrony. Thus, the slope of the single-cell PRC dictates the angle of entrainment for a population of oscillators. Computational methods have been developed to distinguish between single-cell and population-scale effects on amplitude and phase [101], and a derivation of these methods is provided in Section 1.3.

Mathematical treatment and sensitivity analysis for limit cycle models

In this section, we provide derivations for the calculation of period, phase, and amplitude sensitivity, as introduced in 1.3. We begin by defining a local, first-order sensitivity matrix **S** as:

$$s_{i,j}(t,\alpha) = \frac{\partial x_i(t,\alpha)}{\partial \alpha_j} = \lim_{\epsilon \to 0} \frac{x_i(t,\alpha + \epsilon e_j) - x_i(t,\alpha)}{\epsilon} \tag{1.7}$$

where α may be any linear combination of model parameters and/or initial conditions, and e_j is the jth unit vector [22, 23]. The sensitivity matrix with respect to state initial conditions, $\mathbf{S_x} \in \mathbb{R}^{n\times n}$, may be computed directly, by integrating

$$\frac{d\mathbf{S_x}(t)}{dt} = \mathbf{J}(x)\mathbf{S_x}(t) + \frac{\partial f(x,p)}{\partial x(0)}, \tag{1.8}$$

where $\mathbf{J} \in \mathbb{R}^{n\times n}$ is the Jacobian matrix with element $J_{k,i} = \frac{\partial f_k(x(t),p)}{\partial x_i}$ and with initial condition $\mathbf{S_x}(0) = \mathbf{I}$, the $n \times n$ identity matrix [102]. The parametric sensitivity matrix (denoted $\mathbf{S_p} \in \mathbb{R}^{n\times m}$) may be solved similarly, by integrating

$$\frac{d\mathbf{S_p}(t)}{dt} = \mathbf{J}(x)\mathbf{S_p}(t) + \frac{\partial f(x,p)}{\partial p}, \tag{1.9}$$

with zero initial condition [23, 102]. In some cases, the direct solution of **S** may not be practical, and an alternate formulation using a Green's function approach yields advantages [102].

The parametric period sensitivity $\frac{dT}{dp}$ may be calculated by solving the boundary value problem:

$$\begin{bmatrix} \mathbf{M}-\mathbf{I} & f(x^0,p) \\ \frac{\partial f_i(x^0,p)}{\partial x} & 0 \end{bmatrix} \begin{bmatrix} \mathbf{S_{p,0}} \\ \frac{dT}{dp} \end{bmatrix} = \begin{bmatrix} -\mathbf{S_p}(T) \\ -\frac{\partial f_i(x^0,p)}{\partial p} \end{bmatrix} \tag{1.10}$$

where $x^0 \in \Gamma$ is the initial condition on the limit cycle as previously defined. Here, $\mathbf{M}$ is the monodromy matrix of the sensitivity system parameterized by p, $\mathbf{I}$ is the $n \times n$ identity matrix, and $\mathbf{S_p}(T)$ is the solution to (1.9) integrated to time T from initial condition $\mathbf{0}$. Solving this system yields the desired period sensitivities as well as the initial conditions for parametric sensitivities $\mathbf{S_{p,0}}$. For a detailed derivation of this result, I refer the reader to Ref. [23].

Phase response to state and parameter perturbations

Because a limit cycle oscillator is attractive, perturbations away from the limit cycle will eventually return to the closed path Γ. Thus, the concept of phase may be extended to any point within the region of attraction (excluding the stationary point for which $\frac{dx}{dt} = \mathbf{0}$). Let trajectory $\theta(t, x_a)$ be the time evolution of point $x_a \notin \Gamma$, with dynamics given by (1.1). The asymptotic phase of point x_a, denoted ϕ_a, is equal to the initial phase of the trajectory $\gamma(t, x_0)$ to which the trajectory $\theta(t, x_a)$ ultimately converges. This yields the asymptotic phase mapping $\Phi(x_a) \in [0, 2\pi)$. That is,

$$\phi_a = \Phi(x_a) = \Phi(x_0), \tag{1.11}$$

subject to

$$0 = \lim_{t\to\infty} ||\theta(t, x_a) - \gamma(t, x_0)||. \tag{1.12}$$

A phase response curve (PRC) may therefore be calculated by a method of small perturbations: applying an identical perturbation in species concentration or parameter at each phase, and calculating the resulting phase shift $\Delta\phi$. The infinitesimal PRC, the response to infinitesimal perturbations in species concentration or parameter value, is defined in [22] for species i:

$$\frac{d\phi}{dx_i} = \lim_{\Delta x_i \to 0} \frac{\Delta\phi}{\Delta x_i}, \tag{1.13}$$

or for parameter j:

$$\frac{d}{dt}\frac{d\phi}{dp_j} = \lim_{t_p, \Delta p_j \to 0} \frac{\Delta\phi}{t_p \Delta p_j}, \tag{1.14}$$

where t_p is the duration of the parameter perturbation. Usefully, these quantities are related [22]:

$$\frac{d}{dt}\frac{d\phi}{dp_j} = \frac{d}{dt}\frac{d\phi}{dx}\frac{dx}{dp_j} = \frac{d\phi}{dx}\frac{df}{dp_j}, \tag{1.15}$$

necessitating only the calculation of the state impulse PRC. This may be done through solving (1.8) using its Green's function formulation [102]. The homogeneous problem[3] is

$$\frac{d}{dt}\mathbf{K}(t,t') = \mathbf{J}(\gamma(t,x^0))\mathbf{K}(t,t'), \tag{1.16}$$

with $t > t'$ and initial condition $\mathbf{K}(t',t') = \mathbf{I}$, which admits the n linearly-independent solutions to (1.8) as the columns of the kernel $\mathbf{K}$. Since $t' \leq t$, an adjoint strategy is simpler than solving the integral form of (1.16) [103]:

$$\frac{d}{dt'}\mathbf{K}^*(t',t) = -\mathbf{K}^*(t',t)J(\gamma(t',x^0)), \quad \mathbf{K}^*(t,t) = I, \quad t' \leq t. \tag{1.17}$$

This system may integrated backwards from $t' = t$ to $t' = 0$ to solve for the adjoint matrix $\mathbf{K}^*$. The infinitesimal PRC is then found from:

$$\frac{d\phi}{dx_i} = \lim_{t \to \infty} \frac{K^*_{ki}(t',t)}{f(\gamma_k(t,x^0))}, \tag{1.18}$$

and thus we need only solve for one row of $\mathbf{K}^*$ [22, 103]. In the limit $t \to \infty$, (1.18) is T-periodic as it reaches the limit cycle. In practice, the adjoint solution approaches its limit cycle rapidly and this can be approximated by integration for three periods [22]. We note that as in [22], the sign of this phase shift is chosen to conform to circadian literature. By combining (1.15) and (1.18), we find the parametric infinitesimal PRC.

---

[3] On notation: I have chosen to use t and t' consistently with [102, 103], but note that our t is the equivalent of T, and our t' is the equivalent of t in [22]. T here, as in [102, 103], refers to the period of oscillation.

Amplitude response to perturbation

Perturbations away from the limit cycle result in changes in oscillatory amplitude $\mathbf{A} \in \mathbb{R}^n$ in addition to phase. Because perturbed trajectories eventually return to Γ, any change in amplitude for a single limit cycle oscillator occurs only in the transient region. We therefore define a reference trajectory $y(t)$ to be the limit cycle trajectory $\gamma(t, x_0)$ to which the oscillator asymptotically returns. This is explicitly given by shifting the initial condition to account for the accumulated phase shift ($\Delta\phi$) and the phase at which the perturbation is applied (ϕ_{appl}):

$$y(t) = \gamma(t + \frac{\Delta\phi + \phi_{appl}}{\omega}, x^0), \tag{1.19}$$

recalling that the phase at x^0 is 0. We call the perturbed trajectory $x(t) \in \mathbb{R}^n$, and note that it converges to the limit cycle reference trajectory $y(t)$ as $t \to \infty$, therefore, the total amplitude change for state i may be defined as in [101]:

$$\Delta A_i(x_i(t), y_i(t)) = \int_0^\infty (x_i(t) - \mu_i)^2 - (y_i(t) - \mu_i)^2 dt, \tag{1.20}$$

where μ_i is the mean value of state i:

$$\mu_i = \frac{1}{T}\int_0^T \gamma_i(t, x^0) dt. \tag{1.21}$$

Because $x(t)$ and $y(t)$ converge, the function ΔA does as well.

An infinitesimal amplitude response curve (ARC) may be defined in an analogous fashion to the infinitesimal PRC:

$$\frac{dA_i}{dx_j} = \int_0^\infty \lim_{\Delta x_j(0) \to 0} \frac{h_i(t)}{\Delta x_j(0)} dt, \tag{1.22}$$

where $h_i(t)$ is the integrand of (1.20). By Taylor expanding in $\Delta\phi$, and substituting terms derived previously [101], we arrive at an exact infinitesimal ARC for each state:

$$\frac{dA_i}{d\theta_j} = \int_0^\infty 2\left(s_{i,j}(t) - f_i(\gamma(t + \frac{\phi_{appl}}{\omega}, x^0))\frac{d\phi}{dx_j}\right)(\gamma(t + \frac{\phi_{appl}}{\omega}, x^0)) - \mu_i)dt, \tag{1.23}$$

where $s_{i,j}$ is an element of $\mathbf{S_x}$. The state impulse ARC may then be used to calculate the parameter infinitesimal ARC:

$$\frac{d}{dt}\frac{d\mathbf{A}}{dp_j} = \frac{d\mathbf{A}}{dx}\frac{df}{dp_j}. \tag{1.24}$$

Example phase and amplitude response curves for a limit cycle oscillator model are shown in Figure 1.2.

Mathematical treatment of limit cycle oscillator populations

A population of oscillators may be treated through a phase-density approach, as is common for phase-only models [100, 101]. Phase-only oscillator models use a single differential equation for the phase of each oscillator within a population, and capture population dynamics through coupling terms in these equations. To maintain consistency with these phase-only approaches, it is important to use the definition of phase $\phi \in [0, 2\pi)$. Furthermore, it is convenient to use the rescaling:

$$\tilde{t} = \omega t \tag{1.25}$$

$$\tilde{f} = f/\omega \tag{1.26}$$

$$\frac{dx}{d\tilde{t}} = \tilde{f}(x(\tilde{t}), p) \tag{1.27}$$

$$\tilde{\gamma}(\tilde{t}, x_0) = \gamma(t, x_0) \tag{1.28}$$

$$\tilde{\theta}(\tilde{t}, x_a) = \theta(t, x_a) \tag{1.29}$$

which yields a periodicity of $T = 2\pi$ to simplify circular statistics and maintain consistency with [101]. Importantly, this does not affect our phase mapping. The total number of oscillators is conserved, so

$$\int_0^{2\pi} p(\phi, \tilde{t})d\phi = 1. \tag{1.30}$$

The exact phase probability density function $\hat{p}(\phi, \tilde{t})$ following a perturbation may be calculated exactly by using a change of variables:

$$\hat{p}(\phi, \tilde{t})dg(\phi) = p(\phi, \tilde{t})d\phi, \tag{1.31}$$

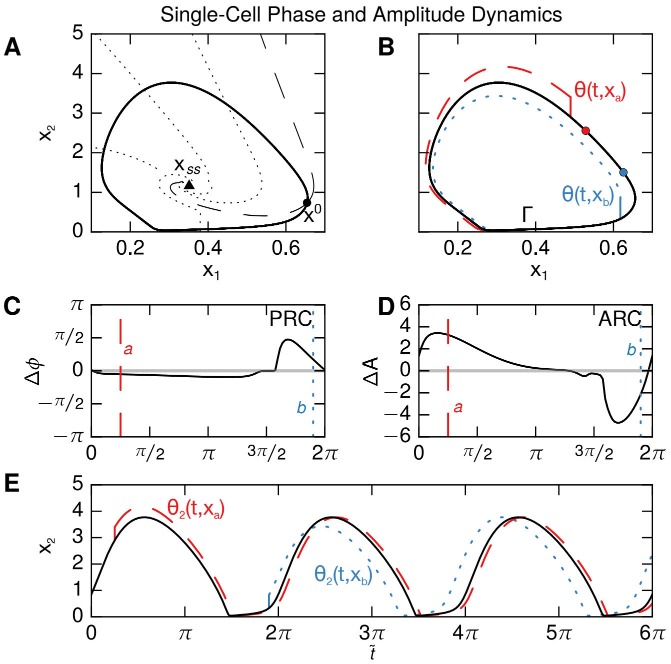

Figure 1.2: Phase and amplitude response curves for a single two-state limit cycle oscillator model (from [104]) describing oscillator response to perturbation. (**A**) Phase breakdown of state space, as visualized through isochrons: sets of points with constant phase within state-space [10]. The isochron with phase $\phi = 0$ is shown as the dashed line, with each subsequent (dotted) isochron at intervals of $\frac{T}{5}$. The fixed point (x_{ss}) and a reference point on the limit cycle (x^0) are shown with a triangle and a circle, respectively. (**B**) State-space response to an identical perturbation Δx at phases $\phi = 0.125T$ (trajectory $\theta_a(t, x_a)$, dashes) and $\phi = 0.95T$ (trajectory $\theta_b(t, x_b)$, dots). The final phase angle at which each trajectory returns to Γ are shown by circles, indicating a phase delay for θ_a and phase advance for θ_b. Perturbation a results in an amplitude increase (i.e. is perturbed to the outside of Γ), while b results in a decrease. (**C**) Phase and (**D**) amplitude response curves for the perturbation Δx. (**E**) Time-domain representation of state x_2, demonstrating phase and amplitude responses relative to limit cycle path $\tilde{\gamma}(\tilde{t}, x^0)$ (black solid line).

where $p(\phi, \tilde{t})$ is the phase probability density function prior to perturbation, and $g(\phi) = \phi + \Delta\phi$ is the phase transition curve, a mapping of oscillator phase before perturbation to phase following perturbation. However, in the limit of a large oscillator population ($n \to \infty$) it is simpler to map the distribution of phases in the population using a complex variable z, given by

$$\begin{aligned} z &= \rho \mathrm{e}^{i\bar{\phi}} \\ &= \frac{1}{N} \sum_{j=1}^{N} \mathrm{e}^{i\phi_j}, \end{aligned} \tag{1.32}$$

where $\bar{\phi}$ is the mean phase and ρ is called the Kuramoto order parameter, also called the synchronization index. The Kuramoto order parameter is related to the population variance and yields a simpler calculation at the expense of some detail regarding the exact distribution of phases (for additional detail, see [105]). For a perfectly synchronized population, $\rho = 1$, and for a population uniformly distributed on $[0, 2\pi)$, $\rho = 0$. The population phase and amplitude responses may be then calculated by

$$\Delta\bar{\phi} = \angle z - \angle \hat{z}, \tag{1.33}$$

and

$$\Delta\rho = |z| - |\hat{z}|, \tag{1.34}$$

respectively, where

$$z = \int_0^{2\pi} \mathrm{e}^{i\phi} p(\phi, \tilde{t}) d\phi, \tag{1.35}$$

$$\hat{z} = \int_0^{2\pi} \mathrm{e}^{i\phi} \hat{p}(\phi, \tilde{t}) d\phi = \int_0^{2\pi} \mathrm{e}^{ig(\phi)} p(\phi, \tilde{t}) d\phi. \tag{1.36}$$

Phase diffusion of uncoupled oscillators and population-scale mean expression profiles

Even for an identical population of oscillators, intrinsic cycle-to-cycle variability in period length will effect a gradual desynchronization over time. The drift of phases due to stochastic noise is approximately diffusive [20, 101, 106, 107], and so the evolution of the phase probability density function may be described through a Fokker-Planck equation:

$$\frac{\partial p}{\partial \tilde{t}} = \frac{\partial p}{\partial \phi} + D \frac{\partial^2 p}{\partial \phi^2}, \tag{1.37}$$

where $D\frac{\partial^2 p}{\partial \phi^2}$ describes phase diffusion about $[0, 2\pi)$ the with diffusion coefficient D, and $\frac{\partial p}{\partial \phi}$ describes convection of mean phase around $[0, 2\pi)$. Note that (1.37) has periodic boundary conditions and an initial condition $p(\phi, 0) = \Psi(\phi)$, yielding the solution as a convolution of the initial conditions with a wrapped normal distribution:

$$p(\phi, \tilde{t}) = \Psi(\phi) * f_{WN}(\phi; \tilde{t}, \sqrt{2D\tilde{t}}), \tag{1.38}$$

where f_{WN} is the wrapped normal distribution, $\tilde{t}$ is the mean phase (due to our rescaling), and $\sqrt{2D\tilde{t}}$ is the standard deviation of phase [101]. This convolution may be simplified by approximating $\Psi(\phi)$ as a normal distribution with mean μ_0 and standard deviation σ_0, to yield

$$p(\phi, \tilde{t}) = f_{WN}(\phi; \mu_0 + \tilde{t}, \sqrt{\sigma_0^2 + 2D^2\tilde{t}^2}). \tag{1.39}$$

The population-scale mean expression of state i, $\bar{x}_i(\tilde{t})$, for oscillators on the limit cycle Γ can be found through a weighted average of the phase probability density function:

$$\bar{x}_i(\tilde{t}) = \int_0^{2\pi} \gamma(\phi, x^0) p(\phi, \tilde{t}) d\phi \tag{1.40}$$

where x^0 is the point on Γ where $\phi = 0$. It is important to note that our rescaling leads to a linear relationship between ϕ and t, and thus integration from $\phi = 0$ to 2π is the equivalent of integration from $t = 0$ to T. For the case where limit cycle trajectory $\tilde{\gamma}(\tilde{t}, x^0) = \cos(\tilde{t})$, and where the phase probability density function evolves according to the convection-diffusion equation (1.37), then (1.40) yields an exponentially-damped sinusoidal result [101]:

$$\bar{x}_i(t) = \mathrm{e}^{-D\tilde{t}} \cos(\,\tilde{t}\,), \tag{1.41}$$

consistent with both experimental and computational studies [21, 74, 77]. Non-sinusoidal limit cycles will also approach this trajectory, as phase diffusion will damp higher frequency sinusoidal components of the limit cycle [101].

The population-scale mean expression after a perturbation may be calculated by decomposing the perturbed trajectory $\hat{x}_i(\tilde{t})$ into the steady-state perturbed trajectory $\hat{x}_{i,SS}$ resulting from the condensing or dispersing of phases along the limit cycle, and the transient population-scale deviations from the limit cycle $\hat{x}_{i,trans}$ which eventually converge to 0. The steady-state trajectory is

$$\hat{x}_{i,SS}(\tilde{t}) = \int_0^{2\pi} \tilde{\gamma}_i(\phi, x^0)\hat{p}(\phi, \tilde{t})d\phi, \tag{1.42}$$

where $\hat{p}(\phi, \tilde{t})$ must be calculated numerically for short times immediately following the perturbation, but may be approximated by (1.36) for sufficient damping. The transient trajectory necessitates the definition of the deviation trajectory:

$$\delta x_i(\phi, \tilde{t}) = \tilde{\theta}_i(\tilde{t}) - \tilde{\gamma}_i(\tilde{t} + \phi + \Delta\phi, x^0), \tag{1.43}$$

which represents the distance between the perturbed trajectory and the limit cycle trajectory to which it converges. The average transient affect can then be calculated by weighting the deviation term by the phase probability density prior to perturbation:

$$\hat{x}_{i,trans}(\tilde{t}) = \int_0^{2\pi} \delta x_i(\phi, \tilde{t})p(\phi, \tilde{t})d\phi. \tag{1.44}$$

Finally, the population-scale mean expression profile, $\hat{x}_i(\tilde{t})$, is

$$\hat{x}_i(\tilde{t}) = \int_0^{2\pi} \left(\tilde{\gamma}_i(\phi, x^0)\hat{p}(\phi, \tilde{t}) + \delta x_i(\phi, \tilde{t})p(\phi, \tilde{t})\right) d\phi, \tag{1.45}$$

as in [101]. Example population phase and amplitude response dynamics are shown in Figure 1.3.

1.4 Taking control of the clock

Control of biological systems may be studied as either "open-loop" optimal control in which system model behavior is optimized, or "closed-loop" feedback control in which feedback from sensing the process itself updates the actuation of the process. A coalescing of control engineering and systems biology has resulted in widespread use of open-loop and feedback control approaches in various biological and biomedical applications [108, 109]. These include identifying and modulating cellular behavior [110–112], treating diseases [113, 114], constructing

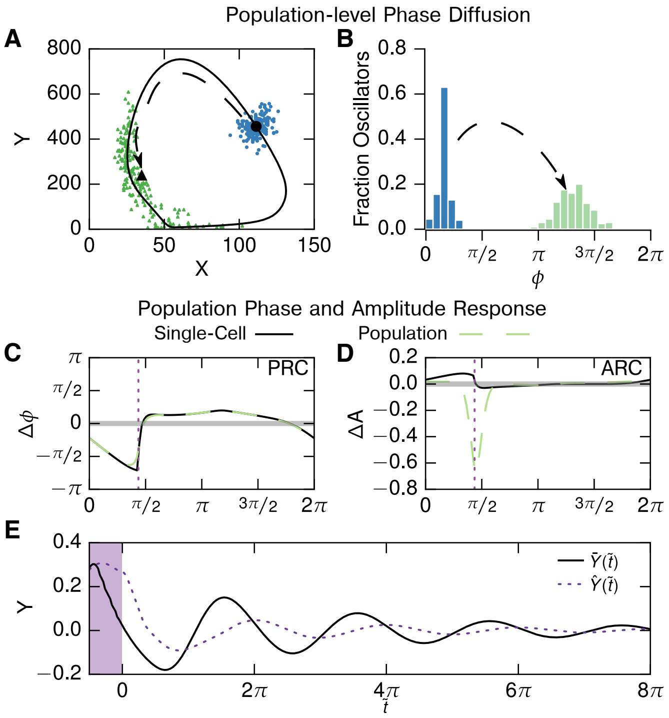

Figure 1.3: Phase and amplitude response dynamics for a population of two-state limit cycle oscillator models from [104]. (**A**) State-space representation of phase diffusion. An initial population of 200 oscillators (circles, blue) was simulated stochastically for $\frac{T}{2}$ resulting in a dispersion of final phases (triangles, green). The average molecular count of X and Y for initial and final conditions are shown in bold. The movement of the center of mass toward the inside of limit cycle orbit γ reflects amplitude damping due to desynchronization. (**B**) The diffusion of phases due to intrinsic noise is shown as a histogram of phases for the simulation from panel A. (**C** and **D**) Single-cell (solid line) and population (dashed line) PRC and ARC, for a temporary 40% increase in parameter k_2. (**E**) Population-scale mean expression profile $\hat{Y}(\tilde{t})$ resulting from perturbation at the phase indicated in panels B and C (dotted line in both panels). This results in a phase lag, and a loss of amplitude in comparison to the unperturbed trajectory $\bar{Y}(\tilde{t})$ due to the desynchronizing effect of the pulse, despite negligible changes in single-cell amplitude.

synthetic biological circuits [115, 116], optimizing biomanufacturing productivity [117, 118], and formulating targeted drug delivery systems [119–122]. Unlike open-loop systems that require manual intervention at critical times to prevent deleterious outcomes, closed-loop drug delivery systems enable effective regulation of targeted biological pathways by leveraging control-relevant models, systematic prediction, or decision-making based on clinical targets. Therefore, these approaches have found use in manufacturing and medical devices. Additional improvements in the quality of closed-loop drug delivery and adherence within society has been fueled by the invention of wearable sensors [123], minimally invasive actuators, and embedded decision-making platforms [124], along with novel drug delivery mechanisms [125] or input-output pairs [126].

Leveraging computational models of the circadian clock and the mathematical tools outlined previously, it is possible to formulate control approaches for the manipulation of clock phase, clock amplitude, or entrainment. For example, open-loop control has been applied to light resetting of the human clock *in silico* [28, 29]. Feedback control has also been implemented *in silico*, for example, on the drosophila clock [27, 127], or as proportional or proportional-integral feedback control laws derived from optimal control [128]. Figure 1.4 shows the overarching scheme by which the clock may be controlled either *in vivo*, *in vitro*, or *in silico*. In general, such a control system consists of a sensor tasked with observing the system state, an actuator by which control is exerted, and a control algorithm connecting these parts. Here, we briefly introduce the sensor and actuator components of a feedback control strategy. In Section II, I provide a more thorough review of the literature regarding design of circadian control algorithms and present two original studies of controller design for manipulating circadian phase and synchrony.

Sensor design

A critical component of a circadian control system is the design of a sensor which can accurately assess circadian phase while remaining minimally invasive. Current markers of human circadian phase are plasma or saliva melatonin, plasma cortisol, or core body temperature [129]. More recent works have utilized ambulatory monitoring approaches, using variables such as motion, respiration, light exposure, and ECG, and fitting a multivariate model, with some success [130]. However, these current approaches are likely too invasive for everyday use. Furthermore, single-dimensional recordings such as melatonin provide limited resolution for tracking phase, such as during daytime when melatonin concentration is negligible. Enabled by smartphone technology, another possible route to sensing circadian phase would be actigraphy in conjunction with a calculated light schedule [131]. However, these metrics would necessitate a robust control algorithm to compensate for potential sensor error. In general, the performance of any control algorithm would be highly subject to sensor accuracy, and choice of a sensor remains an open research question.

Actuator design

Photic actuation

The most common route to artificial control of the clock is through the natural control variable: light. This path is favorable as it is non-invasive and the mechanistic pathway is relatively well-understood. Historically, many studies have examined the role of light in entraining the clock. Recent studies have also begun to examine closing the loop between sensing and control of the clock by calculating an optimal light profile for reentrainment [28, 131]. Potential downsides to using light in clock control include delays in responsiveness, as the system is not evolutionarily optimized to respond to large shifts in phase rapidly; and loss of control during "dead zones," where light has little effect on circadian phase [44].

Pharmacological actuation

Small-molecule modulators of the circadian clock have gained significant recent attention [19, 132, 133]. Small-molecule pharmaceuticals are attractive due to facile delivery and uptake and ability to target specific proteins or complexes within the clock. Two such molecules, KL001 and Longdaysin, have been identified via high-throughput screening methods. Identifying the mechanistic action of these clock modulators presents a unique challenge, due to the inherent complexity of the gene regulatory network obscuring the direct effect. Neurotransmitters, or pharmaceuticals which modulate neurotransmitter expression, offer another possible path to control of the circadian oscillator. In particular, the neurotransmitters VIP and GABA have attracted attention, due to their preeminent role in synchronizing the SCN [134, 135]. However, these neurotransmitters are also implicated in a variety of non-circadian functions, and may not be sufficiently precise to target solely the clock. An important limitation on the potential of molecular clock modulators is that the oscillator appears to be optimized for high-amplitude high-precision rhythms, and very few clock modulations are able to simultaneously increase amplitude and precision for an extended duration [77]. This suggests that any long-term (i.e. many-cycle) clock modulation might be best accomplished by a dynamic approach, where circadian amplitudes are increased by precisely timing the administration of a clock-modulating therapeutic.

1.5 Conclusions

The mammalian circadian system is a natural, multi-scale, robust control system with widespread influence over metabolism and behavior. In the past two decades, a systems engineering approach has yielded great insight into the mechanistic function of the mammalian circadian oscillator. As technology for sensing and actuating circadian function continues to develop, control theory also will play an important role in developing novel clock therapies. Furthermore, design principles for generating stable control from sloppy biological components may yield improvements in the design of artificial control strategies, or in the design of artificial genetic circuits in synthetic biology.

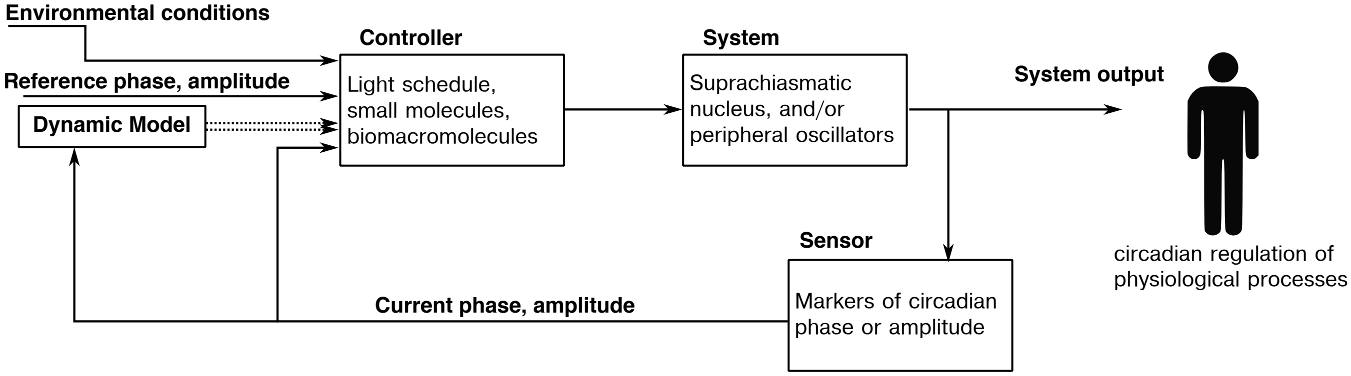

Figure 1.4: A generalized scheme for feedback control of the circadian clock identifying essential components and possible control variables. This diagram is generalizable to a variety of desirable control outcomes (optimal entrainment, phase shifting, amplitude) and control vectors (light, pharmaceuticals). A feed-forward scheme could be similarly implemented by shifting the clock in anticipation of a disturbance, such as light exposure during night.

Part I

Circadian Rhythms in the Suprachiasmatic Nucleus: Networks, Development, and Electrical Activity

Chapter 2

Inferring the functional network corresponding to synchrony in the suprachiasmatic nucleus

2.1 Introduction

Neurons in the SCN generate circadian oscillations through a transcription-translation feedback loop, and are known to synchronize by the timely release of vasoactive intestinal peptide (VIP) and γ-aminobutyric acid (GABA) neurotransmitters which modulate the oscillator through the transcription factor CREB [9, 79, 81, 83, 84]. While the single-cell oscillator and coupling pathways have been extensively researched, relatively little is known about the structure of the neuronal network driving synchronization in the SCN. Prominent modeling studies of the past decade have assumed a wide variety of network structures: nearest neighbor [16, 134], small-world [136], or mean-field [137, 138]; or combinations of these depending on coupling pathway [84], pointing to the high degree of uncertainty regarding the general connectivity of the SCN. There has been significant recent interest in attempting to elucidate the network structure and mechanisms driving synchrony the SCN, commonly through light-driven desynchronization assays [81, 82, 86, 139]. These methods have the advantage of reducing the SCN into large phase clusters of neurons, whose behavior can be easily tracked, and modeled with reduced approaches

---

Major portions of this chapter appear as J.H. Abel, K. Meeker, D. Granados-Fuentes, P.C. St. John, T. Wang, B. Bales, F.J. Doyle III, E.D. Herzog, and L.R. Petzold, "Functional network inference of the suprachiasmatic nucleus," Proceedings of the National Academy of Sciences of the United States of America, vol. 113, no. 16, 2016. DOI: 10.10173/pnas.1521178113. The discussion has been expanded to better fit the dissertation. All statistical, modeling, and mathematical analyses were performed by J.H. Abel, with the exception of neuron tracking by B. Bales. All experimental procedures were performed by members of the Herzog lab. All writing was by J.H. Abel, except for the description of neuron tracking by B. Bales and experimental protocols by E.D. Herzog.

[82]. This approach has had great successes in reconciling the roles of GABA and VIP [81–84]. A significant obstacle in developing a mechanistic understanding of synchronization in the SCN is the lack of single-cell resolution in these studies, preventing observation of the dynamics within these clusters. Furthermore, light is received primarily by the core SCN, and this asymmetry of input is entangled with observed SCN behaviors [83]. Thus far, only fast-scale (phasic) GABA connections have been mapped at a single-cell resolution [140], and this phasic GABA release is not thought to affect the core oscillator [84].

Here, we present a novel method for inferring the functional network of the suprachiasmatic nucleus during resynchronization at a single-cell resolution. Our strategy involved the application of tetrodotoxin (TTX) to disperse single-cell phases through inhibition of intercellular coupling while allowing continued cell-autonomous oscillation [141, 142]. TTX was then washed out, restoring coupling and allowing reorganization of the SCN over the following eight days. We applied the maximal information coefficient (MIC) statistic [143] to bioluminescence recordings during resynchronization in order to identify "functional connections" within the SCN at a single-cell resolution. Functional connections were defined between neurons which share a high degree of mutual information during resynchronization, characterized by a high MIC score. Although functional connections connote neither causation nor direct physiological connection [144], communication is necessary for SCN neurons to synchronize and maintain precise periodicity [145], resulting in a high mutual information between connected neurons. We used this method to infer networks within five mouse SCN explants. Results showed that the suprachiasmatic nucleus has a consistent resynchronization network with a small-world topology and an exponential node degree distribution in each sample. The most densely connected neurons, or "hubs," of each network were located in the central SCN. Unlike prior studies involving phase clusters, a second cluster of connected shell neurons was not found. Finally, we related our observed functional networks to the underlying physical network via stochastic simulation using two models of the coupled SCN [20, 76, 146].

2.2 Materials and methods

Cell culture and bioluminescence recording

SCN were obtained from 7-day old homozygous *Per2*^{Luc} mice (founders generously provided by J. Takahashi, University of Texas Southwestern) housed under a 12h:12h light:dark schedule. All procedures were approved by the Washington University Animal Studies Committee and complied with NIH guidelines. Bilateral SCN from 300 μm coronal sections of hypothalamus were cultured on Millicell-CM membranes (Millipore) in 400ml air-buffered Dulbecco's Modified Eagles Medium with two full-volume exchanges every 7 days. After 14 days *in vitro*, the culture was transferred to the stage of an inverted microscope (Nikon TE2000 fitted with a 20x objective and 0.5x coupler for a 10x magnification) inside a dark incubator (In Vivo Scientific). We add 0.15mM beetle luciferin (BioThema) to the medium and imaged bioluminescence at 36°C with an ultrasensitive CCD camera (Andor Ixon; 1x1 binning, 1 hour exposures). Cultures were then treated with 2.5μM tetrodotoxin (TTX, Sigma) as previously described [147]. TTX remained in the medium for 6 days while imaging continued. We then performed three full-volume exchanges of fresh medium and resumed recording for 8-12 days to monitor resynchronization of *Per2*^{Luc} rhythms. Bright field images before and after each recording were used to focus and align the culture with prior images.

Software was developed to locate and track neuron bioluminescence intensities in each image time series. In each frame, the software identified potential neurons using a standard difference of Gaussians blob detector. The algorithm took the set of neuron locations in each image and attempted to find spatial correspondences between them in the image time series. The correspondences were found by taking each potential neuron location and looking at previous images to find neurons in a nearby radius. Because neurons could be undetectable for multiple frames (when bioluminescence is low), the search was extended back in time multiple frames with a slowly increasing search radius. If the algorithm was able to connect a series of potential neuron locations through enough images, then it was assumed the sequence of locations represented a real neuron and the time series intensity was extracted from the images. If the algorithm could not form a sufficiently long sequence of locations, the neuron was discarded as noise. Results from automated neuron tracking were comparable to results obtained using manual tracking of neurons with ImageJ software [148].

Numerical methods

The MIC is calculated by partitioning a scatter plot of two variables (X and Y; here, these are bioluminescence recordings from two cells) into an n_x-by-n_y grid g that maximizes mutual information $I_g(X;Y) = \sum_{y \in Y} \sum_{x \in X} p(x,y) \log \left(\frac{p(x,y)}{p(x)\,p(y)} \right)$ normalized by the maximal mutual information, $\log \min\{n_x, n_y\}$, in g. The optimal grid is selected as in [143], by computing the normalized mutual information for a subset of all possible grids bounded in resolution by $n_x \times n_y < B$. Details regarding this partitioning algorithm appear as Section 3 of the supplement to [143]. As suggested in [143] we used binning parameter $B = N^{0.6}$, where N is the number of data points in each time series. The MIC was calculated through the minepy package for Python (with interfaces to C++, R, MATLAB, and Octave) [149]. The threshold for connectivity was selected based on receiver operating characteristic curves. Data analysis and processing was performed using Python. Network properties were calculated using the Networkx package [150]. Statistical tests for exponential and power law model fits were performed with the Python module powerlaw [151], in a manner according to [152]. Numerical optimization (rather than a continuous approximation) was used to fit discrete exponential and power law (zeta) models, and a likelihood-ratio test was applied to determine goodness-of-fit.

Stochastic simulation of circadian models, as detailed in the following subsection, was performed in Python with the StochKit2 implementation of the Gillespie algorithm in the GillesPy (http://github.com/gillespy) library [153, 154].

Network simulations

A stochastic three-state circadian oscillator with coupling through algebraic manipulation of *Period* promotion [20, 146], and a more detailed stochastic eleven-state circadian oscillator that explicitly captures VIP and CREB-based *Period* promotion for coupling [76] were selected for our simulations. The degree of stochasticity or noise within these models was fit as in [21, 101]: we captured the noise strength by tuning the volume parameter Ω for the stochastic models to fit the desynchronization rate for a population of uncoupled oscillators. This also captures the distribution of period lengths driven by intrinsic stochasticity [77]. Each cell within these networks was parameterized identically to reflect the primary importance of intrinsic variability in SCN neurons [145], and to ensure that this inference method can distinguish between connected and unconnected cells even in the case where all other parameters (amplitude, mean period, phase angle, noise intensity) are identical. Full equations and parameter sets for these simulations are included below.

Network resynchronization simulations were designed to reproduce the TTX-mediated resynchronization experiments. A population of cells, initially at an identical phase, was simulated stochastically with no coupling and allowed to desynchronize for six days, to mimic TTX inhibition of intercellular communication. Amplitude damping (as in the experiment) is observed only in the eleven-state model, due to the more mechanistically accurate coupling terms. After six days, coupling was restored with a predetermined network topology and simulation continued for an additional eight days. *Per* mRNA count was recorded in one-hour simulation intervals to reflect bioluminescence counts with one sample per hour. The MIC statistic was calculated as for the experimental data, using the resulting *Per* mRNA traces rather than bioluminescence. Representative simulations of the three-state and eleven-state models are shown in the following section.

Circadian models and parameters

Table 2.1 contains the equations and parameters for the three-state model of the mammalian circadian oscillator [20, 146]. Coupling is achieved in this model through the modulation of mRNA production rate, v_s. A cell with index j transcribes mRNA with maximum rate $v_s = v_s^0 + c_j$, where v_s^0 is the baseline maximum rate and c_j is the coupling term, which is dependent on the mRNA concentrations of connected cells. The coupling term c_j is bounded at 0. This reflects the fact that intercellular coupling is accomplished through *Per* promotion. To simulate stochastically, biomolecule concentrations were converted to populations, through use of a volume parameter, Ω. For this model, $\Omega = 40$ captured the correct degree of stochasticity as calculated in [21, 101].

Table 2.2 contains the equations and parameters for the eleven-state model [76]. In this model, coupling between neuron 1 and neuron 2 is achieved by VIP mRNA from neuron 1 being directly translated into VIP protein affecting cell 2, and vice-versa. So that each cell receives the same

Table 2.1: Ordinary differential equations and parameters comprising the three-state circadian model [20]. For these equations j indicates the index of the current cell, i indicates the indexes of cells coupled to cell j, and I is the total number of cells coupled to cell j.

State Variable	Symbol	Conservation Equation
mRNA	**M**	$\frac{d\mathbf{M}}{dt} = v_s \frac{K_1^n}{K_1^n + \mathbf{PN}^n} - \frac{v_m \mathbf{M}}{K_m + \mathbf{M}}$
Cytosolic protein	**PC**	$\frac{d\mathbf{PC}}{dt} = k_s \mathbf{M} - \frac{v_d \mathbf{PC}}{K_d + \mathbf{PC}} - k_1 \mathbf{PC} + k_2 \mathbf{PN}$
Nuclear protein	**PN**	$\frac{d\mathbf{PN}}{dt} = k_1 \mathbf{PC} - k_2 \mathbf{PN}$

Parameter	Description	Value	Units
v_s^0	Minimum mRNA transcription rate	0.82	[-]/hr
w	Weighting of connected cells	0.0050	Dimensionless
a	Coupling strength	2	1/hr
c_j	Coupling term for cell j	$a\left(\frac{\mathbf{M_j}+w\sum\mathbf{M_i}}{1+I\times w} - \mathbf{M_j}\right)$	
v_s	mRNA transcription rate	$v_s^0 + c_j$	[-]/hr
n	mRNA transcription Hill term	4.0	Dimensionless
K_1	mRNA transcription constant	1.0	[-]
v_m	mRNA degradation rate	0.42	[-]/hr
K_m	mRNA degradation constant	0.50	[-]
k_s	Protein translation rate	0.42	1/hr
v_d	Cytosolic protein degradation rate	1.2	[-]/hr
K_d	Cytosolic protein degradation constant	0.13	[-]
k_1	Cytosolic to nuclear protein rate	0.42	1/hr
k_2	Nuclear to cytosolic protein rate	0.50	1/hr

Table 2.2: Ordinary differential equations and parameters comprising the 11-state circadian model [76], continued on following page.

State Variable	Symbol	Conservation Equation
Per mRNA	**p**	$\frac{d\mathbf{p}}{dt} = \frac{v_{1pp}\mathbf{CREB} + v_{2pr}}{K_{1p} + \mathbf{C1P} + \mathbf{C2P}} - \frac{v_{3p}\mathbf{p}}{K_{2dp} + \mathbf{p}}$
Cry1 mRNA	**c1**	$\frac{d\mathbf{c1}}{dt} = \frac{v_{4c1r}}{K_{3c} + \mathbf{C1P} + \mathbf{C2P}} - \frac{v_{5c1}\mathbf{c1}}{K_{4dc} + \mathbf{c1}}$
Cry2 mRNA	**c2**	$\frac{d\mathbf{c2}}{dt} = \frac{v_{6c2r}}{K_{3c} + \mathbf{C1P} + \mathbf{C2P}} - \frac{v_{7c2}\mathbf{c2}}{K_{4dc} + \mathbf{c2}}$
VIP mRNA	**vip**	$\frac{d\mathbf{vip}}{dt} = \frac{v_{8vr}}{K_{5v} + \mathbf{C1P} + \mathbf{C2P}} - \frac{v_{9v}\mathbf{vip}}{K_{6dv} + \mathbf{vip}}$
Per Protein	**PER**	$\frac{d\mathbf{P}}{dt} = k_{1p}\mathbf{p} - \frac{v_{10P}\mathbf{P}}{K_{7dP} + \mathbf{P}} - v_{11aCP}\mathbf{P} \times \mathbf{C1} - v_{11aCP}\mathbf{P} \times \mathbf{C2}$ $+v_{12dCP}\mathbf{C1P} + v_{12dCP}\mathbf{C2P}$
Cry1 Protein	**C1**	$\frac{d\mathbf{C1}}{dt} = k_{2c}\mathbf{c1} - \frac{v_{13C1}\mathbf{C1}}{K_{8dC} + \mathbf{C1}} - v_{11aCP}\mathbf{P} \times \mathbf{C1} + v_{12dCP}\mathbf{C1P}$
Cry2 Protein	**C2**	$\frac{d\mathbf{C2}}{dt} = k_{2c}\mathbf{c2} - \frac{v_{14C2}\mathbf{C2}}{K_{8dC} + \mathbf{C2}} - v_{11aCP}\mathbf{P} \times \mathbf{C2} + v_{12dCP}\mathbf{C2P}$
VIP Protein	**VIP**	$\frac{d\mathbf{VIP_j}}{dt} = k_{3v}\sum_{i}^{I} w_i\mathbf{vip_i} - v_{15V}\mathbf{VIP_j}$
CRY1-PER Dimer	**C1P**	$\frac{d\mathbf{C1P}}{dt} = v_{11aCP}\mathbf{P} \times \mathbf{C1} - v_{12dCP}\mathbf{C1P} - \frac{v_{16C1P}\mathbf{C1P}}{K_{9dCn} + \mathbf{C1P} + \mathbf{C2P}}$
CRY2-PER Dimer	**C2P**	$\frac{d\mathbf{C2P}}{dt} = v_{11aCP}\mathbf{P} \times \mathbf{C2} - v_{12dCP}\mathbf{C2P} - \frac{v_{17C2P}\mathbf{C2P}}{K_{9dCn} + \mathbf{C1P} + \mathbf{C2P}}$
CREB Protein	**CREB**	$\frac{d\mathbf{CREB}}{dt} = \frac{v_{18V}\mathbf{VIP}}{K_{10V} + \mathbf{VIP}} - \frac{v_{19CR}\mathbf{CREB}}{K_{11dCR} + \mathbf{CREB}}$

Table 2.2: (Continued.)

Parameter	Description	Value	Units
v_{1pp}	CREB-induced *Per* mRNA promotion	0.235	[-]/hr
v_{2pr}	*Per* mRNA transcription	0.415	$[-]^2$/hr
v_{3p}	*Per* mRNA degradation	0.478	[-]/hr
v_{4c1r}	*Cry1* mRNA transcription	0.350	$[-]^2$/hr
v_{5c1}	*Cry1* mRNA degradation	1.44	[-]/hr
v_{6c2r}	*Cry2* mRNA transcription	0.124	[-]/hr
v_{7c2}	*Cry2* mRNA degradation	2.28	[-]/hr
v_{8vr}	*VIP* mRNA transcription	0.291	$[-]^2$/hr
v_{9v}	*VIP* mRNA degradation	1.35	[-]/hr
v_{10P}	*Per* protein degradation	13.0	[-]/hr
v_{11aCP}	PER-CRY dimer formation	0.493	$([-]\times \text{hr})^{-1}$
v_{12dcp}	PER-CRY dimer dissociation	0.00380	1/hr
v_{13C1}	*Cry1* protein degradation	4.12	[-]/hr
v_{14C2}	*Cry2* protein degradation	0.840	[-]/hr
v_{15V}	*VIP* protein degradation	0.723	1/hr
v_{16C1P}	PER-CRY1 dimer degradation	0.0306	[-]/hr
v_{17C2P}	PER-CRY2 dimer degradation	0.0862	[-]/hr
v_{18V}	CREB activation by VIP receptors	0.789	[-]/hr
v_{19CR}	CREB deactivation	1.27	[-]/hr
k_{1p}	PER translation	7.51	1/hr
k_{2c}	CRY translation	0.572	1/hr
k_{3v}	VIP translation	5.50	1/hr
K_{1p}	*Per* transcription constant	0.264	[-]
K_{2dp}	*Per* degradation constant	0.00795	[-]
K_{3c}	*Cry* transcription constant	0.156	[-]
K_{4dc}	*Cry* degradation constant	1.94	[-]
K_{5v}	*VIP* transcription constant	0.115	[-]
K_{6dv}	*VIP* degradation constant	0.110	[-]
K_{7dP}	*Per* protein degradation constant	0.0372	[-]
K_{8dC}	*Cry* protein degradation constant	4.23	[-]
K_{9dCn}	PER-CRY dimer degradation constant	0.0455	[-]
K_{10V}	CREB protein activation constant	1.46	[-]
K_{11CR}	CREB protein deactivation constant	1.01	[-]

total VIP input (to keep the model consistent), the VIP input is weighted by the total number of connections C. The weighting parameter w_i is therefore equal to $1/C$ for each connected cell. In this model, the volume parameter Ω was set to 400, as in [76].

For each model, cells which were not found to have functional connections were simulated with a weakened coupling to the mean field, to reflect the fact that these cells do eventually synchronize. This could be biologically indicative of weak coupling pathways, or simply that we did not detect their strong connections, as they did not exceed our threshold. For the three-state model, this was achieved by mean-field coupling with a weight parameter $w = 0.0025$. For the eleven state model, this was accomplished by mean-field VIP input with coupling strength $w_{i,weakfield} = 0.25k_{3v}$ and additional VIP input from the uncoupled cell itself $w_{i,self} = 0.75k_{3v}$ such that each cell receives an input of identical strength.

2.3 Results

Design of resynchronization experiment

To infer the SCN network, we observed five whole SCN mouse explants resynchronizing after decoupling by tetrodotoxin (TTX) (Figure 2.1). *Per2*^{Luc} knock-in SCN explants were cultured while under a microscope, allowing the capture of single-cell bioluminescence within the whole SCN. Bioluminescence counts were recorded each hour, and individual neurons were identified and tracked manually from the resulting images. These single-cell traces are shown in Figure 2.1A for SCN1. TTX was applied to the whole tissue explants for six days to inhibit intercellular coupling, while leaving physical connections within the tissue intact [141, 147, 155]. After six days, the TTX was washed out, and recordings continued for an additional 8 days as neurons in the network regained synchrony. In the synchronized SCN there was a strong correlation from cycle to cycle for single-cell relative peak times[141]. We demonstrate the loss of this hierarchy during TTX application and its restoration after TTX washout in Figure 2.1B. Pearson's r is shown for correlations between peak 0 pre-TTX, and peaks 1-4 at different experimental stages. By day 5 of TTX application (peak 2), all correlation with peak 0 was effectively removed. Shortly after TTX washout some correlation was restored, and correlation was completely restored by peak 4 (day 7 post-TTX). In Figure 2.1C, correlation with peak 0 for each day is shown. The restoration of

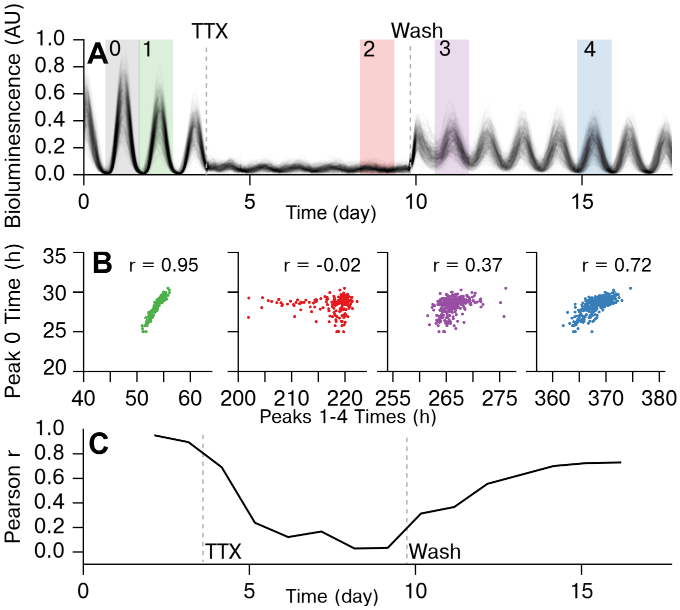

Figure 2.1: Experimental protocol demonstrating TTX-mediated resynchronization for SCN1. (**A**) Bioluminescence traces from individual cells within SCN1, showing pre-TTX, during-TTX, and post-TTX single-cell oscillations. (**B**) In the functioning SCN, peak times are highly correlated from cycle to cycle. We compare relative peak times 1 (pre-TTX), 2 (during-TTX), and 3-4 (post-TTX), to the first peak (0) in order show that a resynchronization is indeed taking place, and that the SCN network structure reverts to pre-TTX structure slowly after TTX wash. (**C**) Plot of Pearson *r* for correlating each peak to peak 0, showing the resynchronization. Pearson *r* does not completely return to pre-TTX levels due to inability to track cells accurately across TTX conditions.

correlation in peak times between pre- and post-TTX regions indicated that the original pre-TTX hierarchy was slowly restored over the course of several days post-TTX. Pearson's r returned to a maximum of ~ 0.7 due to imperfect cell tracking between pre-, during-, and post-TTX conditions. Approximately 40% of cells in each SCN explant lost observable rhythmicity during TTX application, corresponding with [147]. These cells were not included in this figure although they were included in the bioluminescence traces from the post-TTX resynchronization period used to infer network connectivity. A summary of rhythmcity, period distribution, and noise is included as Figure 2.2. This protocol resulted in ensembles of single-cell resynchronization traces from five biologically distinct SCNs each containing approximately 400 cells. This dataset is publicly available online at https://github.com/JohnAbel/scn-resynchronization-data-2016.

Inferring connections between SCN neurons

While fast-scale and electrical connections between individual neurons have been identified by methods such as mutual information, transfer entropy, directed transfer functions, Granger causality, or between-sample analysis of connectivity (BSAC) [140, 156–159], these methods are not suitable here due to nonstationary gene expression and the slow-scale nature of VIP and GABA feedback to the core oscillator, resulting in the damping of high-frequency signals [84, 159, 160]. High frequency GABA signals affect the firing of SCN neurons, and have been mapped previously [140], however, fast scale GABA is not thought to affect the core oscillator [84]. Additionally, due to the limitations of the $Per2^{Luc}$ bioluminescent reporter used to observe core clock gene expression, the most rapid sampling provides 30 minute sample intervals [81], insufficient for methods such as Granger causality [159].

We inferred connections within these samples using the maximal information coefficient (MIC) as our correlation metric [143]. MIC is effectively a continuous metric of mutual information, and is calculated by partitioning a scatter plot of two variables (in this case, raw bioluminescence recordings of two cells) in phase space into a grid that maximizes the mutual information. We selected this statistic because it readily captures relationships between noisy continuous random variables. MIC scores are high between cells which have identical periods and precise phase relationships, which is indicative of communication to resist the stochastic phase drift that occurs in uncoupled neurons. Strongly or directly connected cells will drift apart less in phase and have more precise periodicity than cells which are unconnected. This point, and the effects of sampling rate, cell amplitudes, and noise on MIC scores are examined via stochastic simulation in Figures 2.3 and 2.4. Because MIC partitions each pair of variables onto a grid, and computes the density of grid regions, it effectively performs a normalization of oscillation amplitude: scaling the amplitude of one or both cells will not affect the pairwise MIC score. Notably, MIC shows a bias toward oscillatory states with a small phase offset. To account for this, we repeated the entirety of the following analyses with a phase correction for each cell pair, and show that our results are consistent (following the main results, Figure 2.13).

We applied this correlation metric to pairs of bioluminescence traces from cells from all five SCNs. No detrending or other pre-processing was performed on this data. MIC was calculated using raw bioluminescence of each pair of cells. We then used a receiver operating characteristic (ROC) curve to determine if the method can differentiate between biologically distinct SCNs, and to establish a MIC connectivity threshold that rejects known false positives (Figure 2.5). SCN mean phases were aligned before computing MIC for this negative control in order to prevent biases due to misaligned phase. These five SCNs were cultured separately and bear no common influences, thus no connections should be found between them. A "possible positive" was defined to be an inferred connection within the same SCN (Figure 2.5A), whereas a false positive was a biologically-impossible inferred connection between two different SCNs. As it is only known *a priori* which connections cannot exist, we calculated a possible positive rate (PPR, connections within the same SCN) and false positive rate (FPR, connections between biologically-distinct SCNs), to validate that MIC preferentially detects physiologically-valid connectivity.

To infer the network structure within the SCN, we selected a critical MIC parameter, m_{crit}, from this control result. Pairs of cells that have a MIC score above m_{crit} were determined to be functionally connected. Our m_{crit} threshold was chosen to be 0.935, as this value has a 0.0032 FPR, while still capturing the strongest connections with PPR $= 0.036$. To account for slight variations in rate of synchronization between SCNs, we adjusted this threshold above m_{crit} for each SCN to normalize average node degree (average number of connections per cell) between networks. Because threshold values were raised, this results in a more conservative estimate of connectivity. For SCNs 1-5, threshold values were raised to 0.949, 0.935, 0.990, 0.968, and 0.969 to yield average node degrees or 4.44, 4.49, 3.94, 4.80, and 4.56, respectively.

SCN functional network displays a small-world exponential architecture

Networks inferred from the five SCN explants exhibit small-world characteristics as shown in Figure 2.6. Small-world networks are commonly found in biological systems, and are identified by the average path length L and clustering coefficient C^{Δ}, as defined in [161, 162]. A network G is determined to be small world if the average path length of G, L_G, is similar to the average path length L_{rand} for the equivalent random graph, and the clustering coefficient C^{Δ}_G is an order of magnitude greater than C^{Δ}_{rand}. That is:

$$L_G \approx L_{random} \text{ and } C^{\Delta}_G \gg C^{\Delta}_{random}, \tag{2.1}$$

where the equivalent random graph has the same number of vertices and edges. As shown in Figure 2.6, each SCN met the criteria for small-world architecture. Confidence intervals shown for random networks are determined by generation of 10,000 Erdos-Renyi equivalent networks for each SCN. Figure 2.8 demonstrates that these network characteristics are consistent across SCNs, and locally insensitive to the choice of connectivity threshold.

A semilog plot of the node degree distribution for each SCN is shown as Figure 2.7. Similarly to [140], our node degree distribution was best fit with a discrete exponential (geometric) distribution rather than a discrete power law (zeta or Zipf) distribution. The discrete exponential distribution, as defined in [152], is:

$$P(k) = C \exp(-\lambda k), \tag{2.2}$$

where the normalization constant C is:

$$C = (1 - \exp(-\lambda)) \exp(\lambda k_{min}), \tag{2.3}$$

λ is the inverse scale parameter, and k_{min} is the lower limit on the exponential scaling. For $k_{min} = 1$ (as in our case), the discrete exponential distribution is equivalent to a geometric distribution where the geometric "success probability" parameter $p = 1 - \exp(-\lambda)$. The λ parameter was fit via a numerical optimization of maximum likelihood, and the exponential distribution was found

Figure 2.2: Summary statistics for SCN slices during TTX application and during resynchronization. (**A, D**) Fraction of cells which displayed rhythmic circadian oscillation (A) during TTX or (D) during resynchronization. Not all cells observed during resynchronization could be tracked during TTX due to very low luminescence (as in [147]); cells which could not be tracked were classified as arrhythmic. We found that chemically uncoupled cells are nondeterministic, weak oscillators, in accordance with [147]. When re-coupled after TTX washout, nearly all cells observed became rhythmic. A cell was determined to be rhythmic if it exhibited a Lomb-Scargle periodogram peak between 18-32h period at $P < 0.05$ significance. Data was baseline detrended via discrete wavelet transform. (**B, E**) Period length histograms (B) during TTX application and (E) during resynchronization. As period varies cycle-to-cycle for decoupled oscillators and during resynchronization, we report each peak to peak period of oscillation for each cell, rather than finding the mean period of a cell through fitting a sinusoid. Peak times were identified by a discrete wavelet transform filtering for peaks with period between 16-32h. (**C, F**) Histograms of the fraction of oscillatory power in the circadian frequency range (16-32h) (C) during TTX or (F) during resynchronization, calculated via fast Fourier transform. Data was baseline detrended before FFT. We note that not all cells are observable during TTX due to low bioluminescence, and thus column (C) includes only rhythmic, observable cells. For all SCNs, the period distribution tightened and more oscillatory power was in the circadian range during resynchronization. As these effects and distributions are consistent across SCNs during resynchronization, a cross-comparison may be used to control false positive rate.

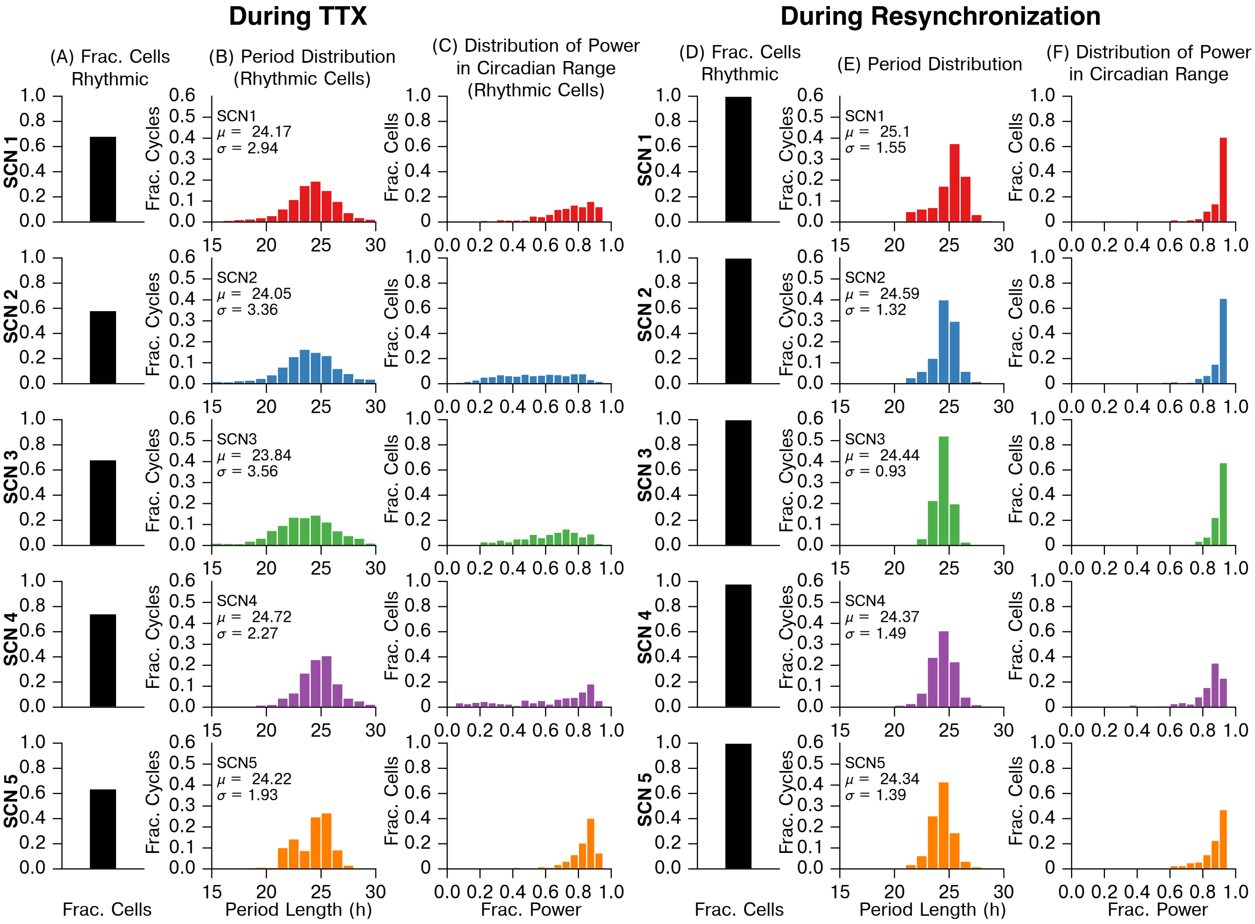

Figure 2.2: (Continued.)

Figure 2.3: MIC score for identification of network connections is largely invariant with respect to sampling rate and amplitude (continued from previous page). In A-C, we test the effect of sampling rate on the ability to distinguish between strongly and weakly coupled simulated cells. We use strongly and weakly coupled cells rather than coupled and uncoupled cells because the entire SCN is indirectly coupled, and therefore we are only interested in the strongest connections. In D-E, we show that the MIC binning procedure effectively normalizes amplitude, and therefore raw amplitude has no effect on MIC score. (**A**) Per mRNA traces for two weakly coupled cells (left, coupling strength parameter = 0.0033) and two strongly coupled cells (right, coupling strength parameter = 0.010). For both simulations in A-C, the discrete stochastic three-state model [146] was used, with volume parameter $\Omega = 40$, and the simulation sampling rate was set to 100 samples per hour. (**B**) Scatter plots and MIC values of Per mRNA for the cell pairs, downsampled to 1 hour intervals, or 6 hour intervals. (**C**) Effect of sample interval on MIC score. For sampling intervals shorter than approximately 2h, only marginal changes in MIC are seen, indicating that the MIC score is largely consistent with increased sampling rate. For sampling intervals longer than 2h (fewer than 10 samples/cycle), the MIC score becomes less accurate, and the ability to distinguish between connections of varying strength is reduced. (**D**) To demonstrate the effective normalization of cellular trajectories through MIC binning, we compared MIC values for strongly and weakly coupled cells, while scaling the peak-to-trough amplitude. For both simulations in D-E, the sampling rate was set to 1 sample per hour. Peak to trough amplitude of one of the resulting trajectories was scaled to $Amp = 10$ (top) or $Amp = 500$ (bottom) for visualization. (**E**) MIC score is completely invariant with respect to changes in amplitude of a simulated trajectory, as the gridding algorithm in MIC is effectively a normalization.

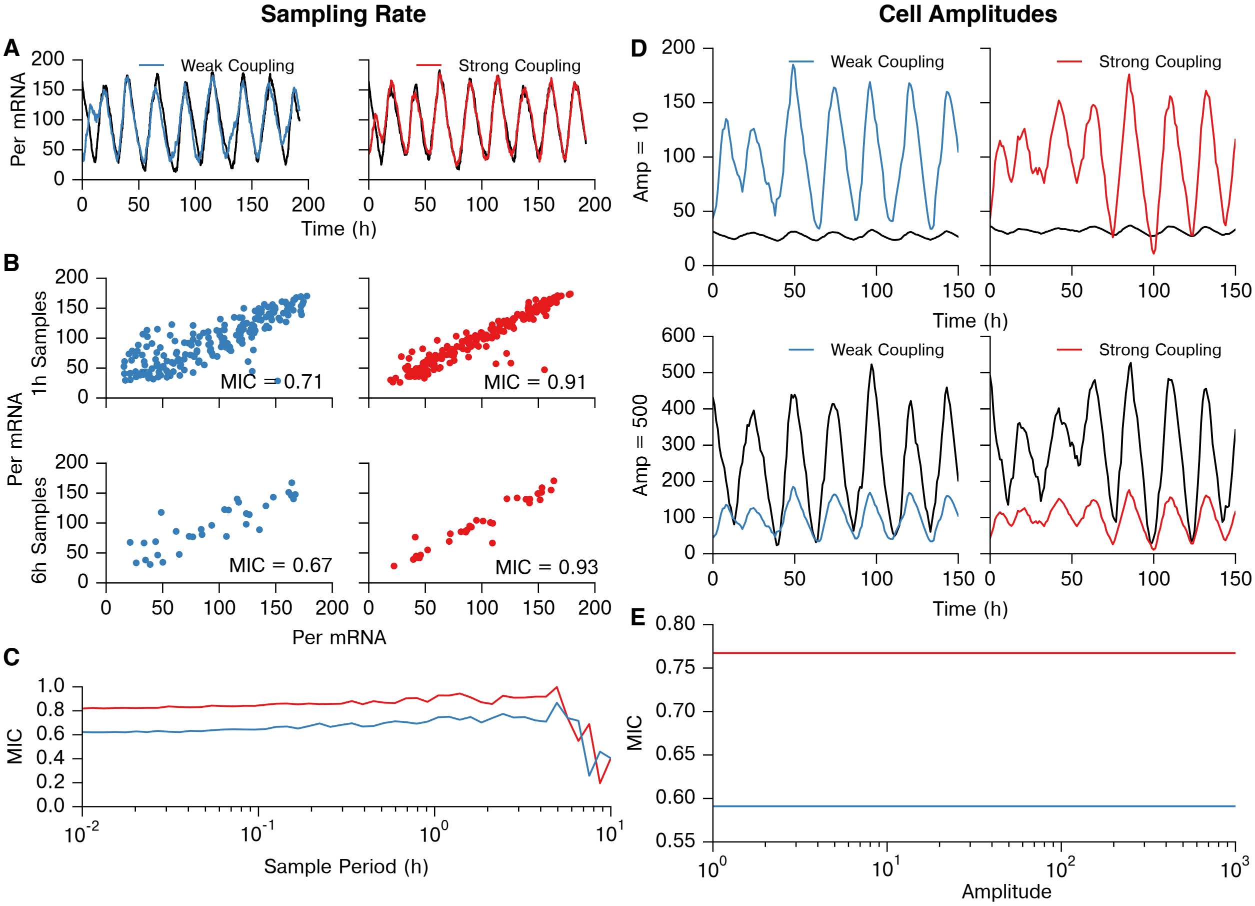

Figure 2.3: (Continued.)

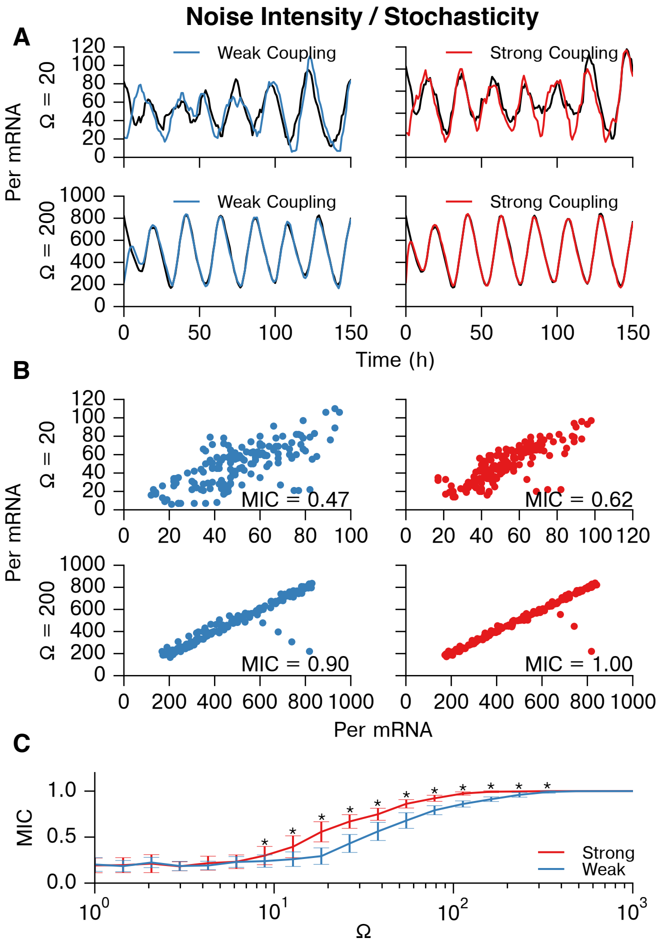

Figure 2.4: MIC is able to distinguish between strongly and weakly connected cells for a wide range of stochasticity. Stochastic noise in the three-state model [146] was tuned by changing the volume parameter Ω. Stochastic noise causes cells to drift in phase, and thus is essential for this inference. (**A**) Representative Per mRNA traces of weakly coupled (left, coupling strength = 0.0033) and strongly coupled (right, coupling strength = 0.010) cells resynchronizing for $\Omega = 20$ (top) and $\Omega = 200$ (bottom). For all simulations here, sampling intervals were 1h, as in the experiment. (**B**) Scatter plots and MIC values of Per mRNA for these representative cell pairs at $\Omega = 20$ and $\Omega = 200$. (**C**) Plot of mean ± S.D. MIC values for strongly and weakly coupled cell pairs vs. Ω (n = 33 cell pairs at each Ω). A broad range of stochasticity allows differentiation between strong and weak coupling (*$P < 0.05$, Wilcoxon sign rank test with Bonferroni correction). At very low Ω values, oscillation does not occur, and at very high Ω values, the MIC scores for both pairs approach 1.0. The experimentally-determined $\Omega = 40$ is well within the range for which MIC can distinguish between connections.

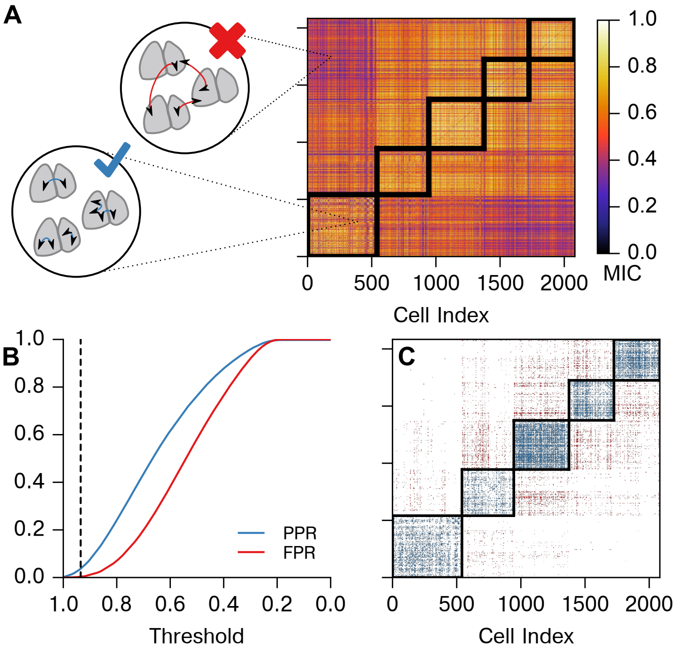

Figure 2.5: MIC identifies the strongest connections within a whole SCN sample. (**A**) Here, we calculate and plot pairwise MIC between neurons from all SCNs. We consider connections within the same SCN to be valid, whether between halves or within a single half. Connections between physiologically-distinct SCNs are invalid, as they are biologically infeasible. The block-diagonal regions outlined in black contain valid connections, and connections outside of this region are invalid. (**B**) False positive rate (FPR, red, inter-SCN connections) and possible positive rate (PPR, blue, same-SCN connections) are plotted for varying MIC threshold values. We choose an initial threshold of 0.935, for which FPR = 0.0032. (**C**) The connections identified by applying the threshold from (B) are shown to occur primarily in biologically-valid areas (blue), with few invalid connections found (red). Thus, the strongest functional connections within each SCN are identified.

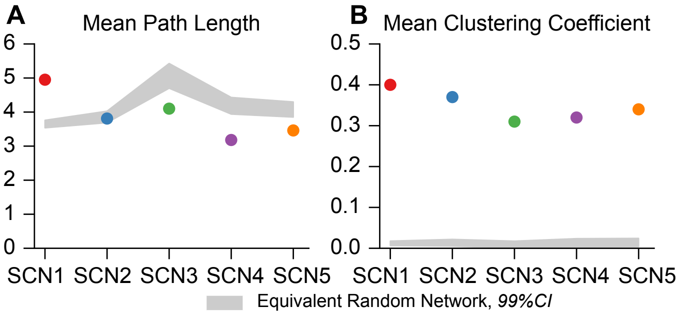

Figure 2.6: SCN functional networks display small-world structure. (**A**) Average path length is on the same order of magnitude of an equivalent random (Erdos-Renyi) network. (**B**) Clustering coefficient is a magnitude greater than that of equivalent randomly-generated networks. Confidence intervals determined by generation of 10,000 equivalent Erdos-Renyi networks for each SCN.

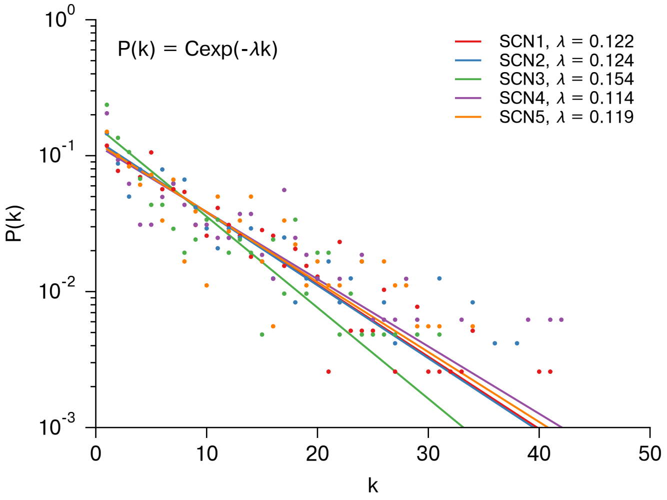

Figure 2.7: Node degree (k) distributions for SCNs 1-5 plotted on a semilog scale. The resulting discrete exponential distributions $P(k) = C\exp(-\lambda k)$ were fit via numerical optimization of the maximum likelihood, resulting in distribution parameters λ for each network. Each SCN is better fit by a discrete exponential distribution than a discrete power law distribution (likelihood-ratio test, $P < 0.0005$ for each SCN).

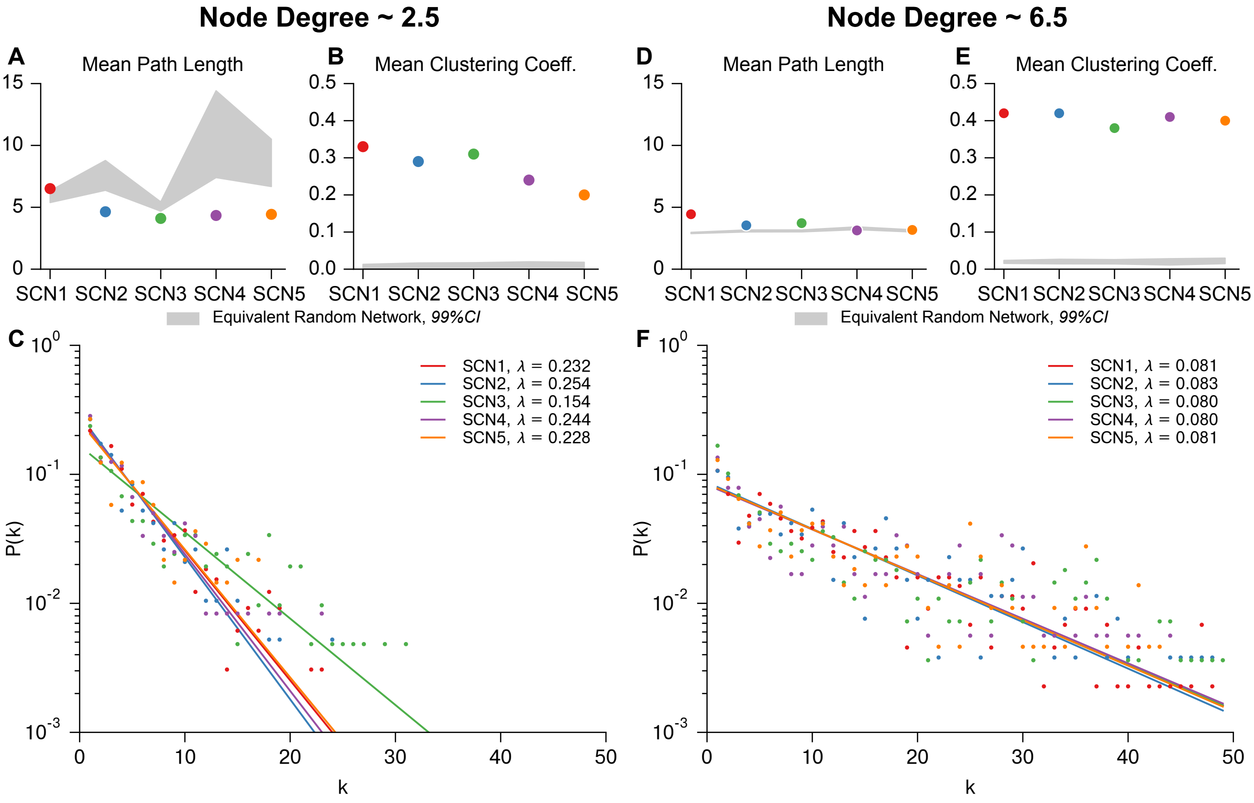

Figure 2.8: Small-world network characteristics and discrete exponential distribution of node degree is insensitive to selected MIC threshold. Threshold was altered for each SCN to yield an average node degree of approximately 2.5 (A-C) and 6.5 (D-F). (**A**,**D**) Average path length remains on the same order of magnitude as that of an equivalent random network (99% confidence interval taken from 10,000 randomly-generated networks). (**B**,**E**) Average clustering coefficient remains an order of magnitude higher than that of an equivalent randomly-generated network, confirming small-worldness. (**D**,**F**) Node degree distribution remains exponential for average node degrees of 2.5 and 6.5. As in Figure 4, the resulting discrete exponential distributions $P(k) = C\exp(-\lambda k)$ were fit via numerical optimization of the maximum likelihood, resulting in distribution parameters λ for each network. Each SCN is better fit by a discrete exponential distribution than a discrete power law distribution (likelihood-ratio test, $P < 0.0005$ for each SCN). SCN3 lacks sufficient resolution to lower node degree below ~ 4.0, and therefore shows slight deviation in λ for low average node degree.

Table 2.3: SCN Network Characteristics Threshold, average node degree (average connections per cell k), average path length L (average number of steps between cells in the network), and average clustering coefficient C^{Δ} [161, 162] of SCN networks. Average path length, and clustering coefficient for SCNs 1-5 show agreement and small-world network characteristics (high clustering coefficient). Connectivity threshold was raised above m_{crit} from Figure 2B to yield $ND \sim 4.5$ for each SCN.

Network	Threshold	Avg. k	Avg. L	Avg. C^{Δ}
SCN1	0.949	4.44	4.95	0.40
SCN2	0.935	4.49	3.81	0.37
SCN3	0.990	3.94	4.10	0.31
SCN4	0.968	4.80	3.18	0.32
SCN5	0.969	4.56	3.46	0.34

to perform better than a discrete power law distribution ($P < 0.0005$ for each SCN, likelihood-ratio test) [151, 152]. Figure 2.8C,F demonstrates that the exponential distribution of node degree is consistent across thresholds, with changes in λ. Thus, we identified a consistent small-world discrete exponential functional network arising from SCN resynchronization.

Coupling is strongest in and between core SCN regions

Commonly, studies of the SCN have revealed two clusters of cells: a ventral core region defined by excitatory (phase attractive) GABAergic connections, VIP production, and light input from the retinohypothalamic tract [9, 81, 83, 84]. To examine how this core-shell paradigm relates to the functional network, we examined the spatial hierarchy of the network. Figure 2.9A illustrates the spatial hierarchy of node degree distribution across a representative SCN. A lower node degree was observed in the shell region, relative to the higher node degree generally seen in the SCN core, obtained by our inference method. We note that in each SCN, a number (average 45%) of cells in the SCN displayed no functional connections. These cells are primarily located in the shell regions (Figure 2.9A). This does not indicate that there are no physiological connections, since shell neurons do resynchronize with the rest of the SCN. More likely, connections in this region are weaker and insufficient to rapidly resynchronize these cells above our functional connection MIC threshold. This structure is consistent even when accounting for phase lags between individual cells within the fully synchronized SCN (see Figure 2.13 following the main results). Strikingly, this result of one cluster and the *absence* of a second cluster differs from prior studies of the functional organization of the SCN, which identified two phase clusters of neurons [81].

The distribution of functional path distances (d) is shown in Figure 2.9B. The functional path distance is defined as the physical separation between two functionally-connected cells. This distribution also appears exponential for each network, where the likelihood of a connection existing at distance d exponentially decays with this d. These distributions are not strictly unimodal, rather, SCNs 1, 2, 4, and 5 display a second peak (identifiable via continuous wavelet transform peak detection) which corresponds to the physical separation between core regions. SCN3 lacks this second peak as the identified cores of each half lack spatial separation. The presence of this second peak indicates that core-core functional connections within a SCN are more prominent than average long-range functional connections. Furthermore, it indicates that core-core coupling is tighter than core-shell coupling.

Relationship between physical and functional networks via network resimulation

Since the physical connections between cells cannot be directly probed, we focused on obtaining the *functional* network structure. Here, we simulated the TTX experiment using stochastic circadian oscillator networks (using models from [20, 76, 146]) to determine how the functional network we infer is related to the underlying physical connectivity in the SCN. First, we tested the efficacy of this method for inferring simulated physical networks of 400 cells with either linear nearest neighbor, small world Watts-Strogatz [161], or random network topology. Next, we simulated the networks we inferred from SCN slices and show that our method can re-infer these physical networks with good accuracy. Details regarding these simulations are included in the Supplement.

In Figure 2.11, we show representative traces from these simulations and further demonstrate that our method is able to recapture the underlying physical networks (random, Watts-Strogatz small-world, nearest neighbor) with accuracy dependent on the density of connections. Functional networks inferred via our resynchronization and MIC method do not accurately recapture physical networks with dense random structure, as secondary indirect connections between nodes may be functionally identified as direct connections. To validate the consistency of specific network structures inferred from TTX experiments, we simulated the SCN networks discovered in the previous section and again inferred the network from these simulations. The resynchronization-MIC method performed well in recapturing simulated SCN networks, with an average area under the ROC curve (AUC) of 0.94 for the three-state model and 0.80 for the more complex eleven-state model. The ROC curves are plotted for each SCN in Figure 2.12. We note that the false positives are most often incurred in distinguishing between primary and secondary connections within dense regions, while disconnected nodes are easily identified. Thus, this methodology can distinguish well between regions with dense and sparse physical connections such as the core and shell, but is less apt at identifying the individual physical connections in each region.

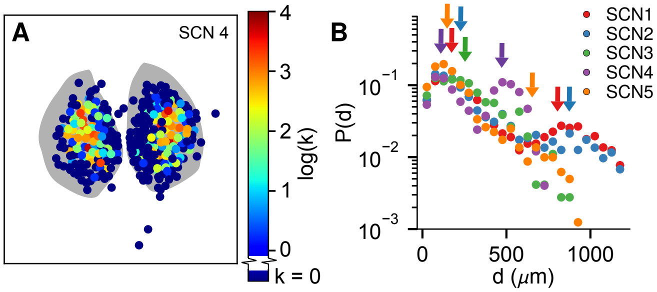

Figure 2.9: Hubs of the small-world network are located in the central SCN. (**A**) Heatmap of node degree (color $\propto \log(k)$) distribution for a representative SCN shows that hubs of the small-world network are preferentially located in SCN core regions. All SCNs are shown in Figure 2.10. (**B**) Connection length (d μm) distributions for SCNs 1-5 plotted on a semilog scale. Two peaks (arrows) are identifiable for SCNs 1,2,4,5: a "local" peak corresponding to connections between physically nearby neurons, and a second peak corresponding to the distance for functional connections between central SCN regions. For SCN3 these peaks are indistinguishable due to lack of spatial separation between cores.

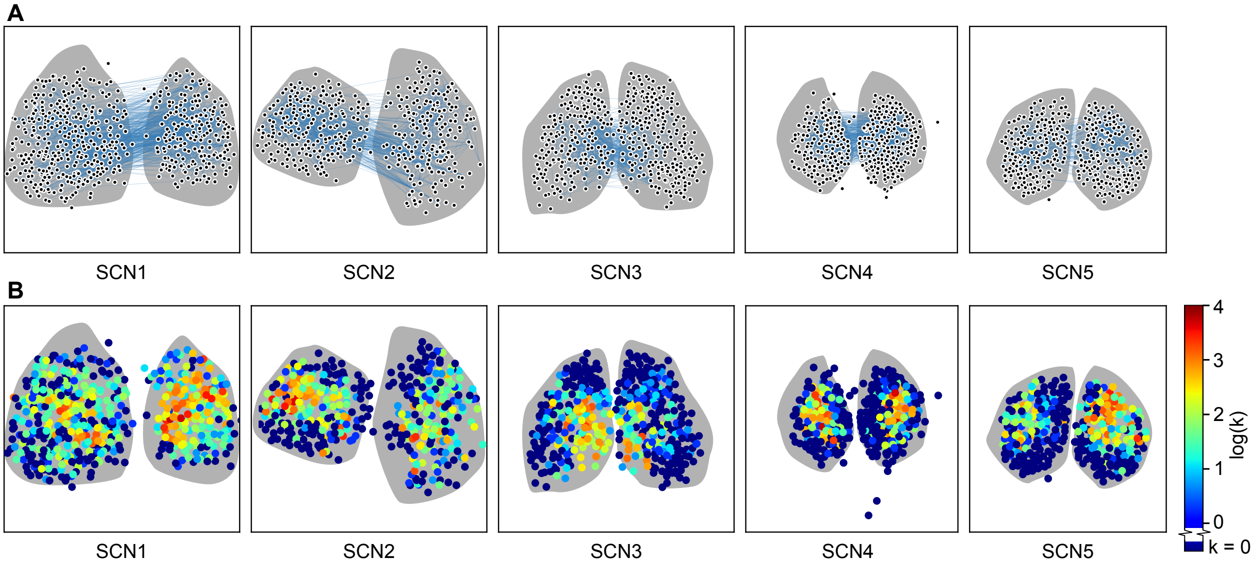

Figure 2.10: Hubs of the small-world network are located in the central SCN. (**A**) Inferred networks are shown overlaid on SCN tissue shape (gray). Connections between nodes are particularly dense in core regions and individual connections are difficult to distinguish. The 3rd ventricle is oriented at the top of each network. Strong functional connections between halves indicate that the core regions communicate to establish consistent phase to entrain the shell. Cells which have no or few functional connections are preferentially located in the outer SCN shell regions. (**B**) Heatmaps of node degree (color $\propto \log(k)$) distribution show that hubs of the small-world network are preferentially located in SCN core regions.

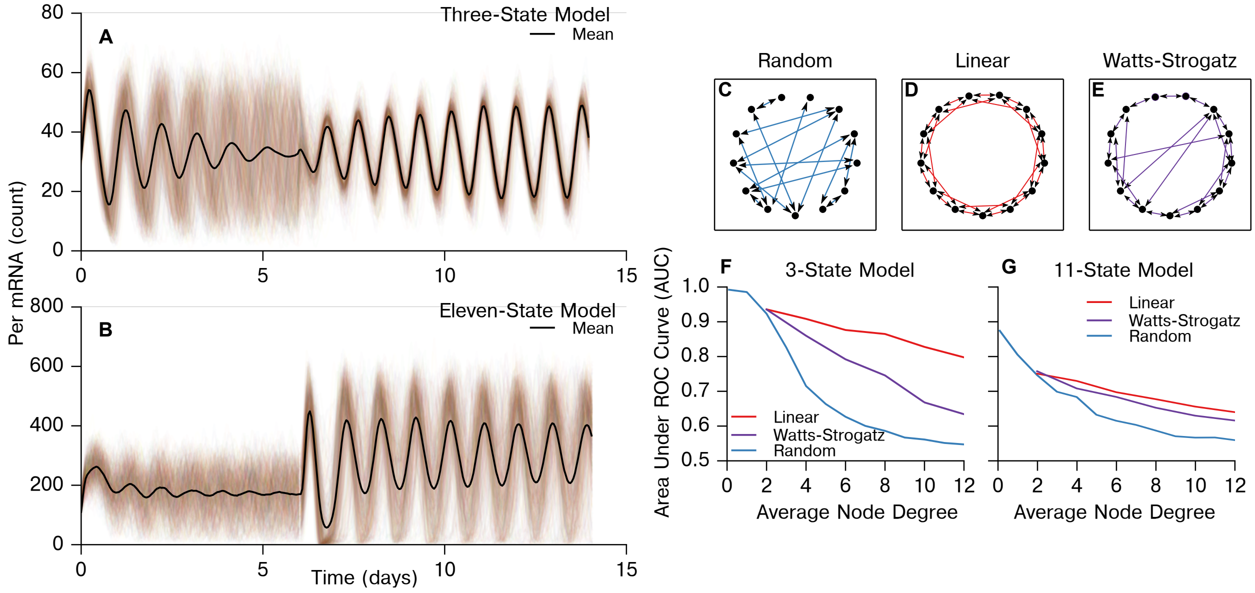

Figure 2.11: Accuracy of the MIC inference method depends on both network topology and average node degree. (**A**) and (**B**) show representative simulations capturing the TTX-mediated resynchronization for the three-state and eleven-state models, respectively. Next, MIC network inference was performed for simulated networks of three topologies: (**C**) random, (**D**), linear nearest neighbor, and (**E**) Watts-Strogatz small world ($\beta = 0.05$). These networks are only shown for visualization of network structure. Simulated networks each contained 400 cells to match SCN recordings, and the average AUC was calculated for 5 dynamically-generated networks of each node degree. The area under the ROC curve is plotted as a function of average node degree for the three-state circadian model [20, 146] (**D**) and the eleven-state circadian model [76] (**E**) for these network structures. We show that both node degree and network structure affect the accuracy of this method. In general, networks that have a shorter average path length and higher average node degree are more difficult to accurately infer, as it becomes increasingly difficult to differentiate between direct and indirect physical connections.

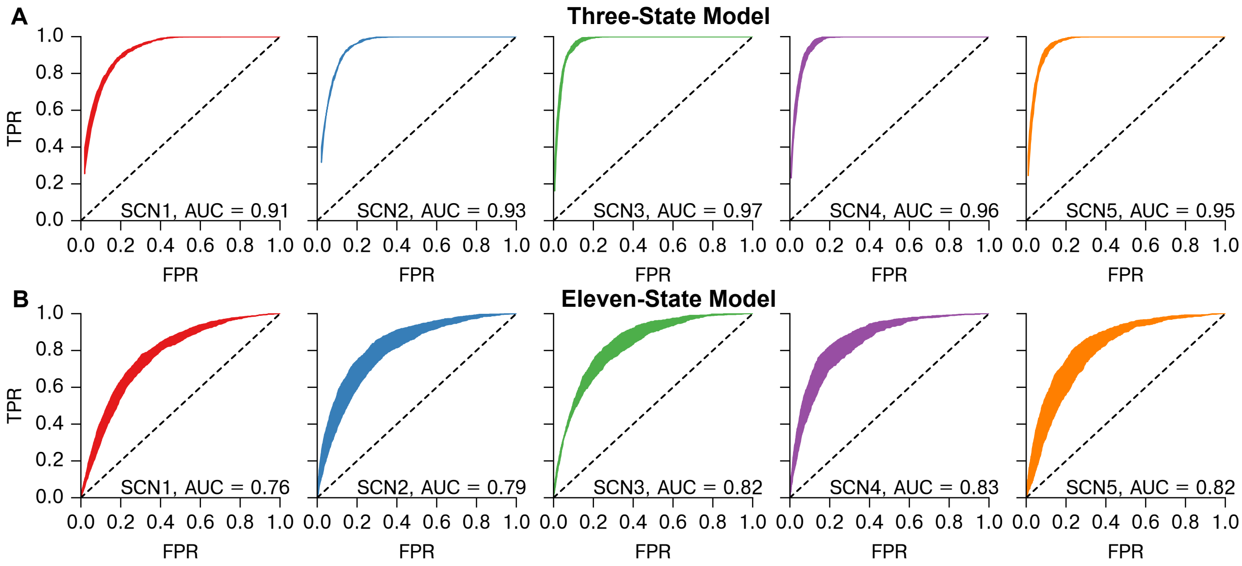

Figure 2.12: Receiver operating characteristic (ROC) curve ranges and mean AUC values for simulation and inference of the SCN networks with physical connections dictated by the functional network, using (**A**) the three-state [20, 146] and (**B**) the eleven-state [76] models. Shaded ranges were calculated from 7 simulations using unique random seeds. We note that all neurons are simulated, including those which are unconnected. Unconnected neurons do synchronize experimentally though at a slower rate. To reflect this, unconnected cells in simulation were connected to the mean field, but at a reduced coupling strength. Errors in this method are largely incurred by secondary connections within tightly coupled regions (i.e. physical connections of cell 1 → cell 2 → cell 3 often show the additional cell 1 → cell 3 functional connection). Thus, we may understand that errors are incurred by functional connections in regions of dense physical connectivity appearing more dense.

Figure 2.13: Effect of phase offset on MIC network inference. MIC is not phase-agnostic, and so the question arises of whether the inferred functional networks are driven by phase distributions in each SCN, similar to the phase clusters identified in [81]. First, we show how phase offset affects MIC score for pairs of synchronized oscillators. Next, we show that re-aligning out of phase trajectories and taking the maximum MIC reduces much of this bias. Finally, we examine how this affects the connections we identify in the five SCN tissues, and show that our results are consistent after applying this phase offset correction. (**A**) The MIC score varies with phase offset between two phase-locked oscillators. Each point on this plot was generated by simulating 50 pairs of strongly coupled cells, as in S2. Connected cells in this model synchronize to a phase offset of 0h because they are parameterized identically. One trajectory from each pair was phase-shifted in 0.1h increments up to 12h, to generate a range of phase offsets between the trajectories. The mean MIC score (y-axis) of the 50 pairs was then computed for each artificially-created phase offset (x-axis). As the phase offset between coupled cells is increased, the MIC score is reduced from its maximum at a 0h angle. This is considered the uncorrected case, where MIC is computed with no regard for the phase offset between trajectories. (**B**) Next, we took the phase-shifted trajectories from (A) and performed a correction to renormalize MIC, so that MIC score is not affected by the phase offset between cells which we originally added. The correction was performed by again shifting the trajectories 12h in either direction, this time in intervals of 1.0h to reflect experimental sampling rate, and calculating MIC scores at each of these shifts. We then selected the largest of the resulting values as the MIC score for the cell pair, as this maximum MIC corresponds to when phases are realigned. In comparison to the uncorrected method, the maximum MIC correction results in reduced sensitivity to the phase offset between cells, as the corrected MIC score (y-axis) is nearly flat with respect to the phase offset of the pair (x-axis). This method reduces power however, as some of the initial resynchronization period must be truncated in order to realign phases, resulting in a slight bias toward *larger* phase offsets. Thus, the uncorrected method (biased toward small phase offset) and corrected maximum MIC method (slightly biased toward large phase offset) form bounds on connectivity. (**C**) Scatter plot of MIC score vs. mean phase offset for all possible connections within each SCN. There is a clear bias against absolute phase offsets greater than $\sim$ 2h (left), in a similar form to (A). This bias is rectified by performing the maximum MIC correction (right). Phase offset (used only for plotting purposes) was calculated by a Hilbert transform after removing the trend via discrete wavelet baseline detrending. As the phase offset was unstable early during resynchronization, it was calculated after it had stabilized, during days 6-7.

Figure 2.13: (Continued.) (**D**) Plot of standard deviation of phase offset vs. mean phase offset for possible and identified connections within all five SCNs. Standard deviation of phase offset was calculated throughout the resynchronization period, and can be thought of as a measure of phase offset instability between two cells. As expected, MIC detects connections between cells with a low standard deviation in phase offset for both cases, with a wider range of mean phase offsets . Thresholds were raised for each of the five SCNs (to 0.980, 0.970, 0.999, 0.985, 0.985 respectively) after phase correction, as all MIC scores are increased by this method. Generally, cell pairs with a larger phase offset also had a less stable phase offset, such that even after phase offset correction most connections were between cells with an difference in phase of less than 2h. (**E**) Phase-corrected SCN networks maintained small-world characteristics, with a comparable mean path length and larger clustering coefficient than corresponding random networks. (**F**) Node degree distributions for each SCN remain exponential ($P<0.0001$ for each SCN, likelihood-ratio test comparison with power law fits), though λ changes corresponding to the increased average node degree for SCNs in which phases were aligned. SCN 3 deviates slightly from the others here, due to the high number of connections which yield saturated (1.0) MIC scores after re-alignment. (**G**) Connection length distributions for unaligned and phase-aligned networks. Despite the higher average node degree for aligned networks, these distributions continued to display two peaks: one for local connections within a core, and a second corresponding to core-core connections. (**H**) Similarly, core-shell hierarchy was maintained after phase-alignment. Additionally, many shell neurons remain functionally "unconnected," indicating a much slower resynchronization than neurons in SCN core regions. These neurons do synchronize, however, they are less tightly synchronized than cells which have identifiable connections.

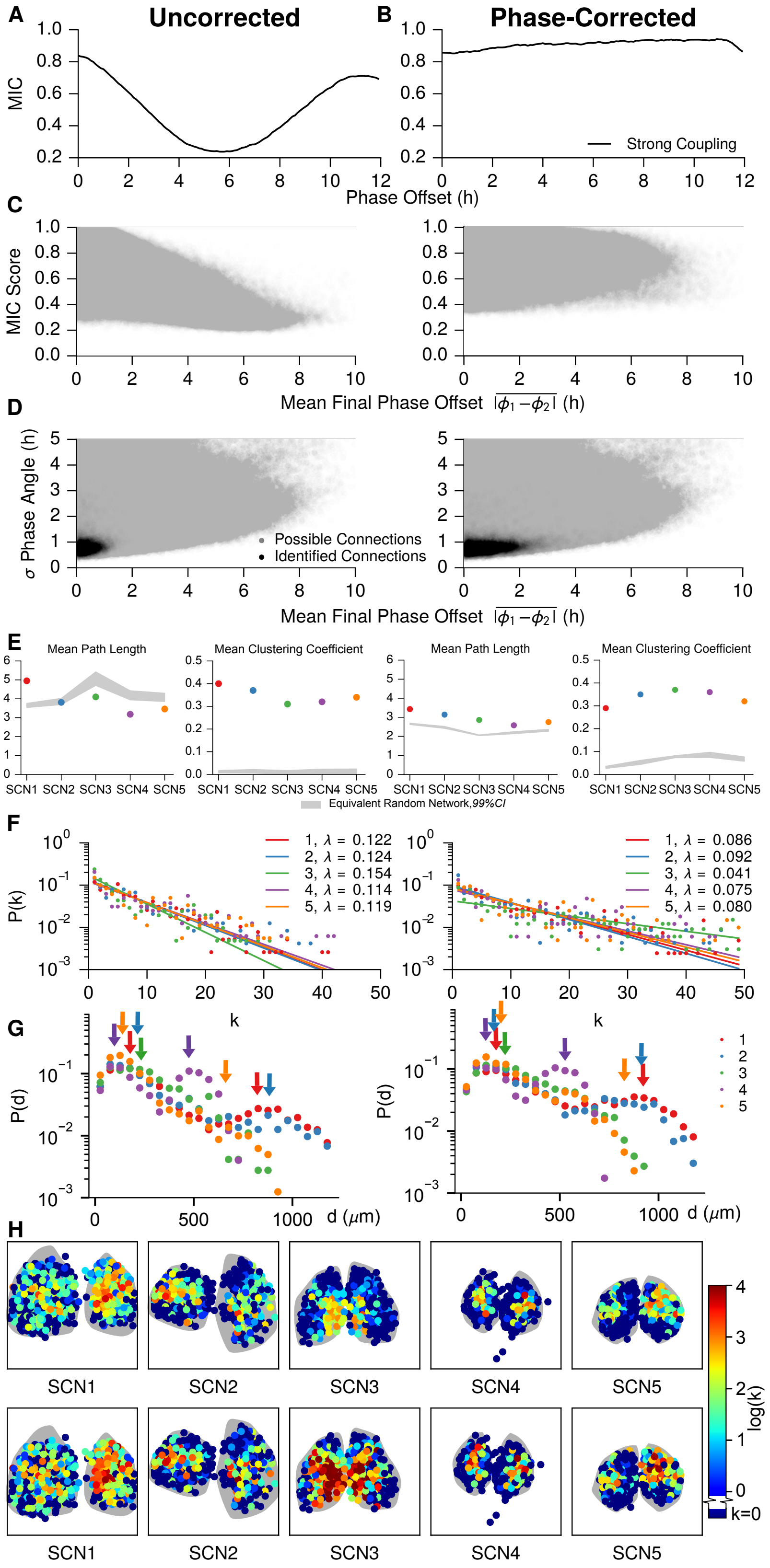

Figure 2.13: (Continued.)

2.4 Discussion

In this work, we inferred the functional network of the suprachiasmatic nucleus during resynchronization through the use of a TTX-mediated resynchronization and the maximal information coefficient. The functional networks we found were consistent across all samples, displaying small-world characteristics, a discrete exponential node degree distribution, and core-shell spatial hierarchy in which densely functionally-connected cores synchronize rapidly. Our results are consistent with previous studies which show differences in function and neurotransmitter activity between core and shell SCN neurons [9, 81–84, 86, 163–165]. However, in this work for the first time we probe connectivity within these clusters. This leads to two surprising results: a lack of a second functionally connected cluster in the shell region, and dense connections between SCN cores.

It is well-established that exposure to artificial long day or light:dark:light:dark frequency doubling conditions can split the SCN into core and shell phase clusters, which oscillate with a large phase lag and also result in behavioral splitting [81, 164, 165]. Although shell neurons form a phase cluster under these conditions, we found few functional connections within this region even when accounting for phase alignment, suggesting that the phase clustering is driven by a common response to light reception and mediated by the core SCN rather than driven by tight connectivity within the shell itself. This is one particular advantage of the TTX assay we employ: light-based approaches are unable to differentiate between cells which have identical responses to a common stimulus, and cells which communicate to establish similar behavior. A previous study of SCN reentrainment to shifted light exposure also showed that the ventral SCN reentrained rapidly, while the dorsal region took several days to reentrain [83]. It was proposed that the core entrained rapidly due to its receiving input from the retinohypothalamic tract (RHT), and showed that synchronization of the shell was mediated by the effect of excitatory GABA. As our resynchronization conditions are chemically-induced and do not involve light input, it was unexpected that a fast-resynchronizing core/slow-resynchronizing shell is a conserved feature between these studies. This consistency indicates that the underlying structure of the SCN, rather than simply RHT connection, drives the dominant role of the core SCN.

We did not attempt to identify connection directionality or the molecular mechanisms driving connectivity, and it is possible that multiple pathways are involved. It has been shown that excitatory GABA action drives reentrainment of the shell region in response to light phase shifts [83]. This was examined in depth in recent collaborative works [82, 84]; these studies demonstrated the encoding of day length through the GABA pathway, by the Cl^--dependent excitatory (core, phase-attractive) or inhibitory (shell, phase-repulsive) effects of slow-scale (tonic) GABA. Visually, the core regions identified in our networks overlap with the regions of excitatory GABA action [82]. In future studies, our TTX-based assay could be combined with VIP/GABA/glutamate agonist or antagonist application and repeated in order to identify the molecular mechanisms responsible for the identified connections. If GABA coupling affects differentiation between core hub neurons and shell neurons, this would result in significant seasonal plasticity of the functional network.

The functional networks we inferred contained a surprising number of connections between core regions of each suprachiasmatic nucleus. The SCN is often thought to be most tightly connected within each half, given the ability of the left and right SCN to oscillate in antiphase in animals exposed to constant light [166, 167]. However, tight bilateral coupling is reflective of previous studies which showed significant coupling between the halves and further implicates the glutamate receptor in this communication [168]. This is especially interesting, since the glutamate receptor has also been implicated in communication between the SCN and the RHT, which occurs in the core SCN region [169]. Thus, our results support the hypothesis that antiphasic oscillation between SCN halves in constant light is made possible by distinct signalling mechanisms in the SCN rather than a weaker coupling strength between halves [168, 170]. It is unclear if connections between halves are synaptic or diffusive.

Theoretical studies in network science as well as modeling studies specific to the circadian field have pointed to possible advantages and causes of a small-world network structure. Small-world exponential networks provide advantages in robustness due to having “hubs” of high node degree and many less-important nodes of low node degree. Networks with this topology are better able to maintain short paths of communication when randomly-selected nodes are removed [171], due to the redundancy and long-range connections provided by network hubs. This could occur during aging, as it is known that some brain regions lose mass during the aging process. Small-world topology has also been shown to enhance synchronization and amplitude properties of the SCN with a lower energy cost (fewer connections) when compared to random and nearest-neighbor networks [136, 172]. Theoretical studies have predicted that spatially embedded small-world networks, such as neuronal networks, would display an exponential node degree distribution as seen in our data [173, 174]. This distribution would result from growth of a small initial population of connected nodes. As more nodes are added, the neuron population is forced to move spatially and initial local connections ultimately become long-range, while new short-range connections form. In this context, it is striking to note that the fetal SCN forms as neurons are added to the core first and then shell regions. The connections we measure, therefore may reflect the ontogeny of synapse formation in the SCN. If, however, core-core long range connections are found to be diffusive rather than synaptic, this hypothesis would not apply. Future experiments could test whether the left and right SCN must form synapses to synchronize, for example, in co-cultures.

Our work presents both a new perspective on connectivity within the SCN and a new assay for observing communication between individual circadian neurons at high spatial resolution. A major difficulty in mapping the SCN and the brain as a whole lies partly in the multiple time and physical scales at play. One method alone is insufficient to map the whole SCN at all resolutions, necessitating multiple perspectives to achieve spatial, directional, and mechanistic specificity. In conjunction with light-driven desynchronization assays, antagonist/agonist application, genetic knockdowns, and mathematical modeling, this TTX assay with correlation metrics can be used to further probe connections within the SCN at a single-cell level, and between the SCN and other brain regions.

Finally, although we have presented results indicating heterogeneous network structure within the SCN, we have not proposed a means by which this structure arsises. Studies of the onset of circadian oscillation in the fetal SCN have been limited to whole-SCN analyses, in part due to the experimental challenge of explanting the fetal SCN and recording the activity of distinct neurons. In the ensuing chapter, we begin to approach questions of ontogeny of cell-autonomous circadian rhythms in SCN neurons, and how and when the network driving circadian synchrony arises. Importantly, the core-shell heterogeneity of the SCN observed in this study as well as others provides a marker for a “mature” SCN network.

Chapter 3

Ontogeny of circadian rhythms and synchrony in the suprachiasmatic nucleus

3.1 Introduction

How and when hypothalamic circadian rhythms arise during development is not known. More precisely, it has not been established when cell-autonomous circadian rhtyhms in the SCN arise, and how and when the network establishing intercellular synchrony first appears. Studies of whole-SCN circadian development do not make the distinction between single-cell and whole-tissue oscillation, further obscuring the development of the SCN network, which is necessary for synchronous oscillation.

In mice, it is well-established that neurogenesis of the SCN occurs between embryonic days 10-15 (termed E10-15, where E1 is the day when a vaginal plug is detectable), peaking between E12-14 and forming from ventrolateral to dorsomedial [175–177]. It is further known that a variety of transcription factors are expressed during differentiation of the SCN (e.g. *Lhx1*, *Shh*, *Six3*, *Six6*) [177–180]. Development also continues postnatally, and synaptogenesis has been found to occur primarily after birth [177, 181]. Although the SCN continues to develop after birth, numerous studies in rats have shown that circadian rhythms in fetal metabolism, and circadian

---

Major portions of this chapter appear as V. Carmona-Alcocer, J.H. Abel, T.C. Sun, L.R. Petzold, F.J. Doyle III, C.L. Simms, and E.D. Herzog, "Ontogeny of circadian rhythms and synchrony in the suprachiasmatic nucleus," Journal of Neuroscience, accepted. All statistical and mathematical analysis and modeling was performed by J.H. Abel. All experimental work was performed by members of the Herzog lab, primarily V. Carmona-Alcocer. This journal article, and thus a major portion of this chapter, was written collaboratively with V. Carmona-Alcocer and E.D. Herzog.

spontaneous electrical activity and clock gene expression within fetal SCN, begin before birth [182–187]. Studies of mice have yielded similar results to rat studies, with detectable fetal daily rhythms in *Per1* transcript levels at E17, and PER1 and PER2 proteins by E18 *in vivo* [188, 189]. *In vitro* studies of SCN explants have found circadian expression of the PERIOD2::LUCIFERASE ($Per2^{Luc}$) bioluminescent reporter in the whole SCN as early as E13 [190] or E15 [191]. Still, it remains unclear if these oscillations are self-sustaining and spontaneously synchronizing as in the mature SCN, or driven or coordinated by the circadian oscillator of the mother.

In the mature SCN, neurons exchange electrical and neurotransmitter signals to maintain identical periods and consistent phase relationships [192–194]. Among these signals, vasoactive intestinal peptide (VIP) has attracted significant attention for its essential role in SCN synchrony [79]. The absence of VIP or its receptor, VIPR2, reduces synchrony between neurons and consequently eliminates many daily rhythms, while exogenous application of VIP is able to restore synchrony to the $\text{VIP}^{-/-}$ SCN *in vitro* [79, 195–198]. It remains unknown when VIP is first expressed in the SCN, and whether its role in the fetal SCN is identical to that in the adult [199, 200]. For example, GABA, another neurotransmitter expressed in the SCN, is known to have very different effects in the fetal brain because of differing chloride potentials [201]. In this chapter, we used the $Per2^{Luc}$ bioluminescent reporter to study the onset of circadian rhythms in the SCN at at near-single-cell scale. We sought to identify the onset of self-sustained genetic circadian oscillations in individual cells, spontaneous synchronization within the explanted SCN, and other markers of the mature SCN including expression of neurotransmitters with circadian relevance.

3.2 Materials and methods

Animals

All mice were maintained on a C57BL/6JN background (WT) and housed in a 7am-7pm light-dark cycle in the Danforth Animal Facility at Washington University. The $Per2^{Luc}$ mouse line was generated by replacing the endogenous mouse *Period2* gene locus with a $Per2^{Luc}$ reporter construct [78]. For immunochemistry, we compared male and female homozygous $Per2^{Luc}$ pups to $Vip^{-/-}$ and $Vipr2^{-/-}$ pups as negative controls. Vaginal plugs confirmed overnight mating of each female. We designated the morning after mating as embryonic day 0.5 (E0.5) and the day of birth as postnatal age 0 (P0). All procedures were approved by the Animal Care and Use Committee of Washington University and followed National Institutes of Health guidelines.

Cultures and bioluminescence recording

Pregnant mice were euthanized with CO_2 and cervical dislocation and their embryos dissected into 4°C Hanks Buffered Saline Solution (Sigma). All surgeries started at 1:00 PM (Zeitgeber Time, ZT 06). We recorded bioluminescence from 300 μm coronal SCN slices from fetal (E13.5-E15.5 and E17.5) and postnatal (P2) homozygous $Per2^{Luc}$ mice [190]. Briefly, brains were embedded in a block of 4% low-melting agarose and prepared with a vibraslicer. SCN were dissected with scalpels from sections of the ventral hypothalamus and placed on 0.4 mm membrane inserts (Millipore) in sealed 35 mm Petri dishes (BD Biosciences) with 1 mL Dulbecco's Modified Eagle Medium (Sigma, pH 7.2), supplemented with 25 U/mL penicillin, 25 μg/mL streptomycin (Invitrogen), 10 mM HEPES (Sigma), 2% B27 (Invitrogen), 0.35 g/L NaHCO3 (Sigma) and 0.15 mM beetle luciferin (Promega). SCN explants were transferred to a light-tight incubator at 36°C (Onyx, Stanford Photonics). We collected images (XR Mega-10AW camera, Stanford Photonics) every 6 min (6 sec exposure) and then summed every 10 frames with ImageJ software (http://rsbweb.nih.gov/ij) to provide one image every hour. We applied adjacent frame minimization to each movie to filter out bright noise caused by the camera or cosmic rays.

Data analysis

We analyzed the $Per2^{Luc}$ rhythms of the developing SCN at the level of the whole tissue and with 30 μm (pixel) resolution. The statistical analysis for each experiment is described in detail in its respective section. We assessed rhythms measured as the integrated intensity of the SCN tissue with cosinor analysis (software from B. Meier and A. Kramer). We performed a pixel-based analysis of the same SCN movies. We excluded movies if the corners of the SCN slice moved (3 slices excluded at each of E15.5, 17.5 and P2). We measured periodicity of each pixel (1 px = 900 μm^2) and defined pixels as circadian if they had a dominant period between 18-32h with $P < 0.05$ by Lomb-Scargle periodogram analysis [202]; or a correlation coefficient greater than 0.6 in cosinor analysis. Because the two methods yielded 90 $\pm$ 0.02% (mean $\pm$ S.E.; n=30 brains) agreement in pixel classification, we reported results from the periodogram analysis only. The cycle-to-cycle variability in $Per2^{Luc}$ was evaluated by detrending rhythmic cells with a discrete wavelet transform [203] keeping only detail coefficients between 16-32h, and measuring the interpeak distance (h) of each cycle. We evaluated the synchrony index using the Kuramato method [105], with instantaneous phase calculated using a Hilbert transform of the detrended and denoised data.

A radial distribution of mean peak times was constructed for each SCN to identify the presence of core-shell structure. The time of the initial peak for each pixel was calculated following detrending. A radial distribution of peak times was constructed by binning individual cell peaks based on radial distance from a reference point in the left ventrolateral SCN. A null distribution of radial peak times was calculated by bootstrapping: reassigning peak time values at random to pixels within each SCN and recalculating the radial distribution using 10,000 bootstrap runs. An SCN was determined to have core-shell structure if the radial peak time distribution showed significant ($P < 0.05$) peaks for the shell region (early-peaking, middle distances) and at least one core region (late-peaking, near and far distances).

Software

Data analysis was performed in the Python language, using packages scipy and numpy [204], PyWavelets, Statsmodels [205], and Matplotlib [206]. Parallelization of data processing was achieved via iPython [207].

Immunocytochemistry

Brains of mice from ages E13.5-E17.5, P0 and P2 were removed and fixed in 4% paraformaldehyde in phosphate buffered saline (PBS) overnight at 4°C. We transferred them to 30% sucrose in PBS for 24 h at 4°C and sectioned in 30 μm thick coronal slices onto microscope slides. The sections were incubated for 1 h at 4°C in a blocking solution (10% not fat dry milk, 10% bovine serum albumin and 0.3% TritonX-100 in PBS) and then for 48 h at 4°C in an anti-VIP (1:1000, Imunostar) or anti-VPAC2R (1:1000, Abcam) rabbit polyclonal antibody diluted in 3% BSA and 0.35% TritonX-100 in PBS. After washing in PBS, the slides next were incubated at room temperature in a biotinylated goat anti-rabbit IgG (1:200; Vector) for 2 h and then ABC solution (1:200; Vectastain Elite ABC Kit, Vector) for 2 h. Finally, we incubated each slide in 50 mM Tris-HCl using 3,3-diaminobenzidine kit (Sigma). After each step, we rinsed 3 times for 15 minutes in PBS. Mounted sections were dehydrated through a series of ethanol and xylene washes. Slides were imaged (NanoZoomer microscope, Leica) and the integrated optical density of the SCN was measured using ImageJ software [148].

Drug treatments

All drugs were diluted in deionized water and they remained in the recording medium throughout the entire recording without further medium changes. VIP antagonist (200nM PG-99465) provided by Dr. P. Robberecht [208], GABA antagonist (100 μM Gabazine, TROCRIS), MEC (10 μM Meclofenamic acid, SIGMA), or TTX (2.5 μM tetrodotoxin).

3.3 Results

SCN cells become reliable circadian oscillators after E14.5

Recent in vitro studies have demonstrated the presence of circadian rhythms in PER2 expression in whole SCN explants at E13 [190] or E15 [191], around the times of peak or completed neurogenesis, respectively. To test if cell-autonomous oscillations appear prior to tissue-level rhythms, we imaged bioluminescence in fetal $Per2^{Luc}/Per2^{Luc}$ SCN slices. SCN explanted at E13.5 displayed no tissue-level circadian rhythms (n = 8 SCN from 2 litters; Fig. 3.1). At this stage, the ventricular zone of dorsal hypothalamus expressed high levels of PER2, sometimes in a circadian pattern (n = 2 of the 8 slices), but the bilateral SCN region had low to no PER2 expression and no circadian rhythms. In contrast, all tissues explanted on E14.5 or later displayed bilateral $Per2^{Luc}$ expression in the ventral hypothalamus, corresponding to the SCN. By E14.5, 45% of SCN were circadian (5 of 11 SCN from 4 litters). Notably, some E14.5 explants (n = 4 of 11) also displayed no rhythmic $Per2^{Luc}$ expression outside the SCN in the ventricular zone of the dorsal hypothalamus. By E15.5, no hypothalamic explants showed high PER2 expression outside the SCN region and nearly all SCN were circadian (n = 11 of 12 E15 SCN from 4 litters, 7 of 7 E17 SCN from 2 litters and 5 of 6 P2 SCN from 1 litter). We conclude that PER2 expression is localized to the SCN and becomes circadian on E14.5.

We next developed methods to culture and image the embryonic SCN for at least 5 days.

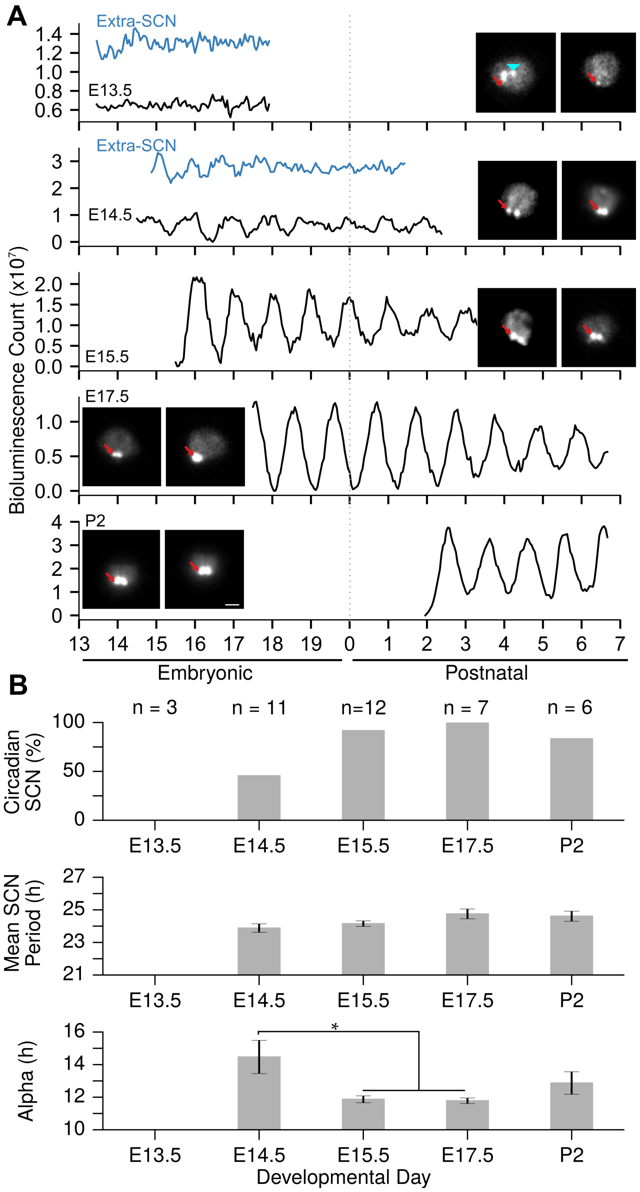

Figure 3.1: Circadian rhythms in the SCN during development. Long-term, real-time recordings of PER2 expression from SCN harvested after E14.5 showed reliable circadian periods between 18-32h. (**A**) Representative records of *Per2*^{Luc} bioluminescence from SCN starting on the day they were explanted. Note the weak circadian oscillations that were found in some E14.5 SCN. Insets show images of two representative SCN from each age. Some SCN harvested at E13.5 expressed *Per2*^{Luc} above the SCN region along the ventricular zone of dorsal hypothalamus (blue arrow head, n=5/8). All others harvested at this age and older reliably expressed high levels of PER2 in the bilateral SCN. Scale bar = 10 px = 300 μm. (**B**) Nearly all SCN expressed significant circadian rhythms when harvested on or after E15.5 (Upper panel), with periods close to 24 h (mean ± SEM; Middle panel) and durations of daily *Per2*^{Luc} expression above the mean close to 12 h (alpha; mean ± SEM, Lower panel; *P < 0.05, one-way ANOVA, Tukey's HSD). Note, 8 slices were examined at E13.5, however, we excluded 5 because they did not express detectable PER2 in the SCN region.

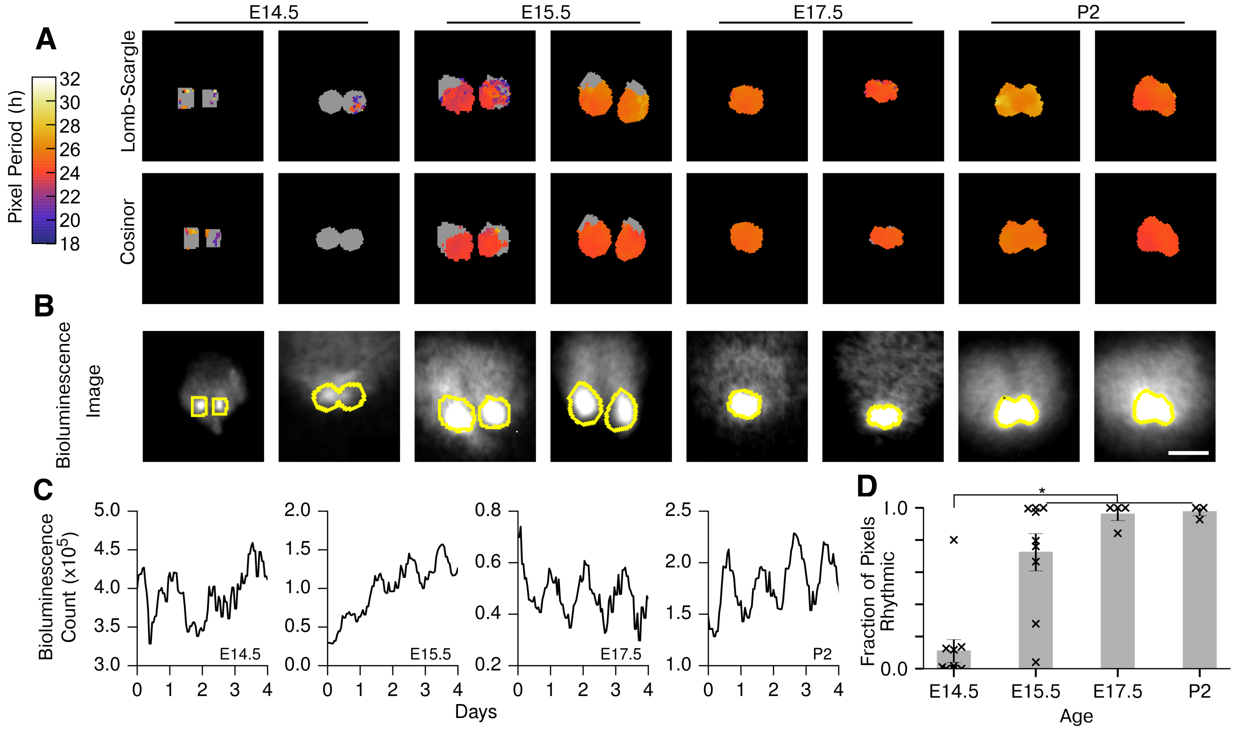

Figure 3.2: Embryonic SCN cells express PER2 rhythmically beginning around E14.5 in vitro. (**A**) Heat maps of two SCN explanted at each developmental stage show circadian pixels based on Lomb-Scargle periodogram (power above $P < 0.05$) and Cosinor analysis (correlation coefficient greater than 0.6). We therefore report results only from periodogram analyses for simplicity. (**B**) Representative Per2Luc bioluminescence images of the same SCN explants (1 h integration, 2 x 2 binning). Scale bar = 10 px = 300 μm. (**C**) Representative Per2Luc bioluminescence recordings from single rhythmic pixels from SCN cultured at different embryonic stages. Note the competence of the E15.5 SCN to generate and sustain circadian rhythms in PER2 protein expression. (**D**) The fraction of circadian pixels in each SCN (mean ± SEM,) was higher for explants at E15.5 and older (*$P < 0.05$, one-way ANOVA, Tukey's Honestly Significant Difference (HSD), n=at least 3 SCN at each age where age is reported as days post mating, E0.5, and post birth, E20.5=P0).

From these movies, we quantified local circadian rhythms where each pixel included approximately 10 or fewer cells (Fig. 3.2A-B). We found the fraction of circadian pixels (cells) increased approximately 7-fold from E14.5 (Fig. 3.2C-D; 0.10 ± 0.07, mean ± SEM; n=11 SCN from 4 litters) to E15.5 (0.72 ± 0.11; n = 9 SCN from 4 litters; *P < 0.05, one-way Kruskal-Wallis H(3)=10.62, with posthoc Tukey's Honestly Significant Difference). Nearly all regions were circadian in SCN explanted on E17.5 (0.96 ± 0.03; n = 4 SCN from 2 litters) and postnatal day 2 (P2, 0.97 ± 0.02; n = 3 SCN from 1 litter). The developmental increase in the number of circadian regions correlated with an increase in circadian period in the SCN (Fig. 3.3A-B). We conclude that a small number of SCN cells initiate endogenous circadian rhythmicity by E14.5, and by E15.5 SCN cells are rhythmic throughout the SCN.

To determine the precision of SCN rhythms during development, we measured the cycle-to-cycle difference in period for each pixel within the fetal SCN over three days of the recording. Interestingly the increase in the number of circadian oscillators correlated with an increase in circadian precision (Fig. 3.3C-D), suggesting that addition of circadian cells lengthens and stabilizes period in the SCN.

The phase wave typical of adult SCN appears around P2

In adults, PER2 expression progresses as a daily wave from dorsal to ventral across the SCN [141, 164, 209, 210]. We examined when this spatiotemporal patterning of circadian expression arises in the SCN. To do so, we identified the times of daily peak PER2 in each pixel of the SCN and tested for spatial organization of expression. We found reliable daily waves of PER2 from the dorsal to ventral SCN by P2, but not at earlier developmental stages (Fig. 3.4). We conclude that phase relationships among SCN cells continue to mature after birth.

Onset of synchrony and intercellular communication within the SCN

Synchronous circadian oscillations in the SCN are required to coordinate daily rhythms in behavior [79, 142, 167]. To test how synchrony develops, we measured the cycle-to-cycle variability in period length and the synchrony index (SI), a quantity that ranges from 1.0 (all oscillators peak together) to 0.0 (all cells peak at uniformly different times of day) from five days of recording. We found that synchrony tends to increase between E14.5 (Fig. 3.5; SI = 0.80±0.5, n = 6 SCN) and

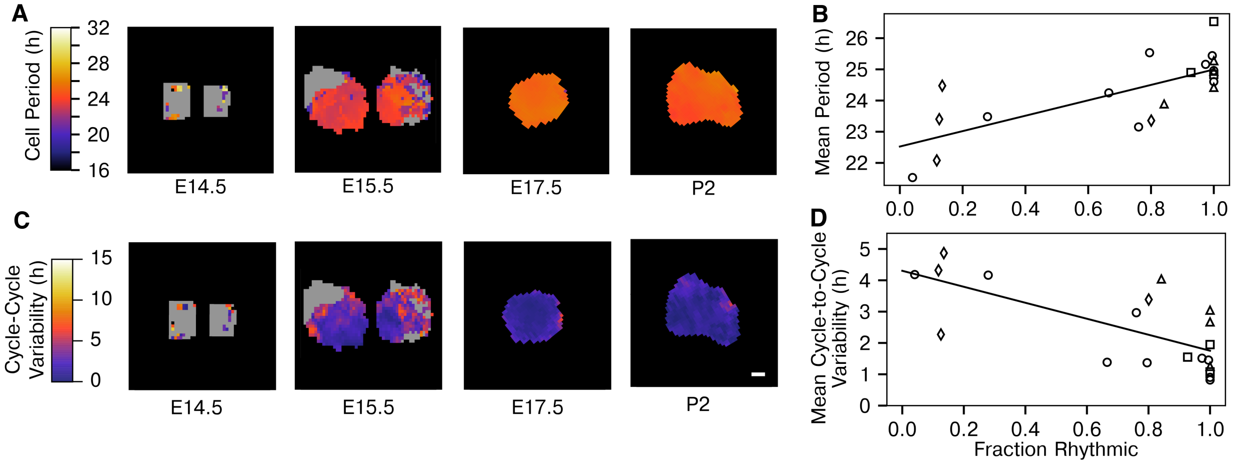

Figure 3.3: Circadian period and precision of SCN cells increased with development. (**A**) Heat maps from representative SCN show the mean period over 5 days of recording. (**B**) The fraction of rhythmic pixels correlated with an increase in the mean SCN period (Least-squares linear regression P = 0.00019, Pearson's r = 0.74. SCN with fewer than 5 circadian pixels were considered arrhythmic and excluded from this analysis. E14.5: diamonds, n=6 of 11, E15.5: circles, n=9 of 9, E17.5: triangles, n=4 of 4, P2: squares, n=3 of 3). (**C**) Representative mean cycle-to-cycle variability heat maps show the increase in circadian precision with age. Scale bar = 150 μm. (**D**) The average variability of the daily period across all rhythmic pixels within each isolated SCN inversely correlated with the fraction of circadian cells (least-squares linear regression P = 0.0006, Pearson's r = -0.70; symbols as in B), SCN with fewer than 5 circadian pixels were considered arrhythmic and excluded from this analysis.

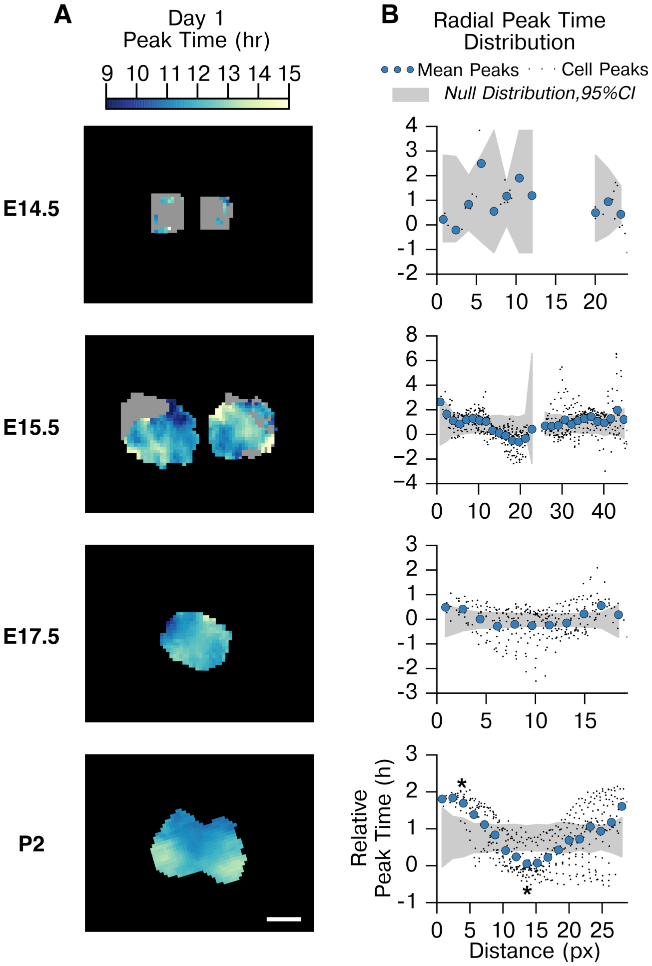

Figure 3.4: The phase wave of PER2 expression in the SCN appeared only after birth. (**A**) Heat maps of the time of peak PER2 expression across representative SCN. Note the dorsal-to-ventral distribution across the cells of the P2 SCN. Scale bar = 300 μm. (**B**) Radial distribution of peak times revealed a core-shell structure in the P2, but not younger, SCN explants. We compared the average differences in the times of peak PER2 expression as a function of distance from the ventral margin of each SCN with a null distribution of randomly shuffled peak times (shaded area=95% CI for mean peak time calculated from 10,000 resamples). At P2, PER2 peaked significantly later in the ventral core than the dorsal shell, as seen in this representative example.

E15.5 (SI = 0.87±0.05, n = 9 SCN) reaching a maximum around E17.5 (SI = 0.91±0.02, n = 4) and P2 (SI = 0.94±0.02, n = 3 SCN (one unilateral due to changes during recording between halves)). Although there is no significant differences in the SI between ages, SI was positively correlated with the fraction of SCN cells displaying daily rhythms, indicating that intercellular synchrony is developed simultaneously with increased endogenously generated cellular oscillation (Fig. 3.5C).

We next examined the signaling pathways that could enable synchronization of SCN cells starting around E15.5. VIP signaling is necessary for coordinated circadian rhythms among SCN cells and in behavior of adult mice [79, 195–198]. We measured the levels of VIP, and its cognate receptor, VIPR2, by immunocytochemistry between days E14.5 and P2 (Fig. 3.6). We found VIP (12.5±2.3, n = 7) and VIPR2 (15.0±5.6 relative optical density (ROD), n = 6) were detectable postnatally above baseline (immunolabeling in the P2 SCN of $Vip^{-/-}$ = 2.1±0.7 ROD, n = 5 brains and $Vipr2^{-/-}$ =3.8±2.1 ROD, n = 5, mean±SEM), but not earlier stages. To further explore this surprising result, we found that a VIP antagonist did not affect synchrony of the E15.5 SCN (Fig. 3.7). Consistent with prior publications, we found that addition of the VIPR2 antagonist reduced the fraction of circadian cells in the isolated adult SCN to 30% from 84% (n = 1 adult SCN; [79, 208]. We conclude that VIP and its receptor VIPR2 appear in the SCN after the initiation of circadian rhythms and are not required for circadian synchrony among embryonic SCN cells.

We then performed further pharmacological experiments to test if GABA and/or gap junctions, other candidate coupling mechanisms, might drive synchrony in the SCN before VIP expression begins. Remarkably, antagonists against either or both GABA and gap junctions did not reduce the synchrony index of the E15.5 SCN (Fig. 3.7).

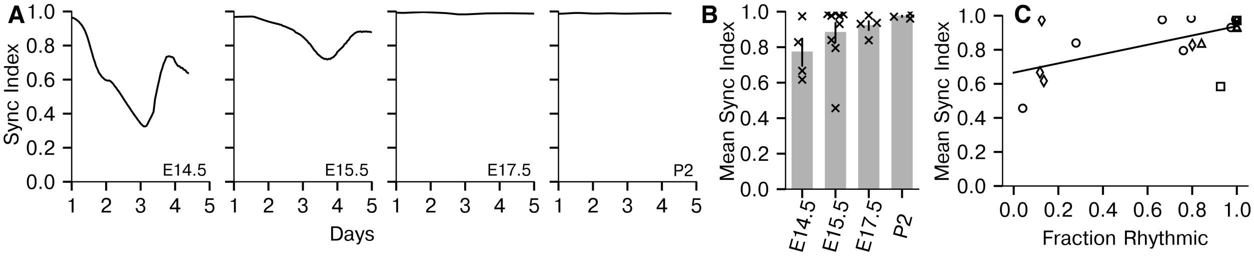

Figure 3.5: The synchrony between SCN cells increased and became more stable as the fraction of circadian cells increased. (**A**) Representative traces of the synchronization index (also called the Kuramoto order parameter or Rayleigh Statistic, r) among regions within the cultured SCN at different ages. (**B**) The average synchronization index of SCN slices (mean ± SEM, 24 h excluded from either end of analysis) did not reliably increase with age, but (**C**) correlated with the fraction of circadian cells in the SCN (symbols as in prior figure, Least-squares linear regression P = 0.004, Pearson's r = 0.61, n=at least 3 SCN at each age).

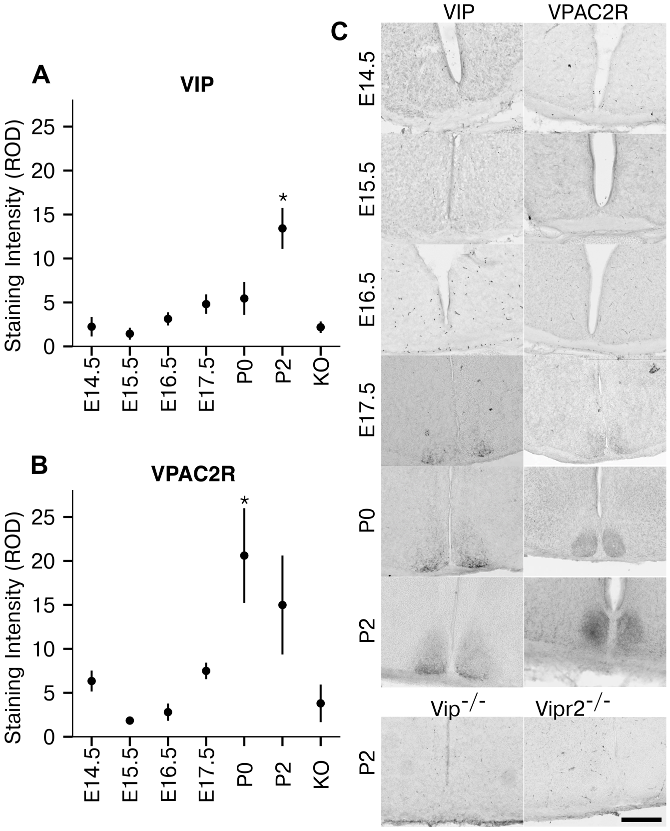

Figure 3.6: VIP and VPAC2R expression matured in the postnatal SCN. (**A**) Immunostaining intensity (Mean relative optical density ± SEM, n=9, 5, 7, 6, 7 and 7 brains at each age, respectively) of VIP in the SCN was significant by P2 compared to Vip-knockout controls (n=5, *P < 0.05, one-way ANOVA with Tukey's HSD). (**B**) Immunostaining intensity (Mean ± SEM) of VPAC2R (n=6, 6, 5, 5, 7, and 6 brains, respectively) was significant by P0 compared to Vipr2-knockout controls (n=5, *P<0.05, one-way ANOVA with Tukey's HSD). (**C**) Representative coronal SCN sections show the VIP (left panel) and VPAC2R (right panel) immunoreactivity at different ages. Scale bar = 200 μm.

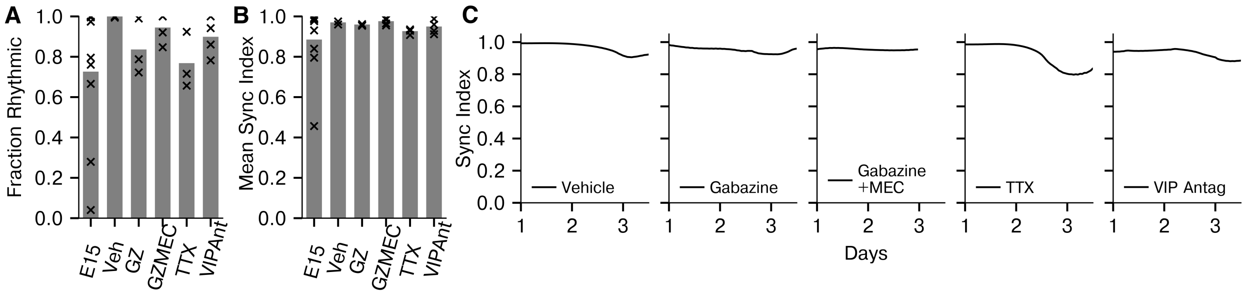

Figure 3.7: Antagonists of GABA or VIP signaling, gap junctions or neuronal firing did not disrupt circadian synchrony in the developing SCN. Drugs applied during the first day of culture of E15.5 SCN explants did not change (**A**) the fraction of pixels with circadian *Per2*^{Luc} (grey bars show the means across all SCN recorded at each developmental stage), or (**B**) the mean sync index over the 5 days of recording. (**C**) The synchronization index within a representative cultured E15.5 SCN treated with Veh (Vehicle), Gz (100 μM Gabazine), MEC (10 μM Meclofenamic acid), VIP antagonist (200 nM PG-99465), or TTX (2.5 μM tetrodotoxin).

3.4 Discussion

Our results indicate that E15.5 is a critical time in the maturation of the SCN. The clock gene, PER2, is first expressed on E14.5 in the SCN and approximately 10% of these SCN cells are weakly circadian. By E15.5, nearly all cells within the SCN show circadian oscillation in gene expression. Previous studies have identified E15.5 as the end of neurogenesis [175–177], and transcription factors Lhx1 and RORα are widely expressed across the SCN [178]. In particular, RORα deserves further study, as it is known to be a core component of the mammalian circadian oscillator. RORα is a positive regulator of *Bmal1* expression [211], and *Bmal1* is an essential transcription factor and activator of *Per* gene expression [41, 212]. RORα knockout adult mice showed slight behavioral abnormalities in circadian rhythms. We therefore speculate that expression of RORα or another transcription factor in the SCN at E15.5 induces the onset of autonomous circadian oscillations in SCN cells.

Consistent with a prior publication [190], we found no evidence that development occurs *in vitro*: on average we did not find increases in the number of oscillatory cells or SCN-wide synchrony as a recording progressed. For example, SCN explanted on 13.5 were arrhythmic and did not show an increase in the fraction of rhythmic pixels over the course of the experiment. SCN isolated at E14.5 or E15.5 similarly did not show changes in the amplitude, period, variability or fraction of circadian cells during 7-day recording. Although we cannot rule out that arrhythmic, fetal SCN cells cultured longer than 7 days might develop daily cycling, our results indicate that the transition from arrhythmic to circadian is rapid and likely requires signals from outside the fetal SCN. Other studies have found that stem cells exhibit autonomous oscillations after inducing differentiation with retinoic acid [213, 214]. Our result suggest that this signal, if it indeed initiates oscillation, does not originate spontaneously within the SCN.

Interestingly, we found that PER2 was first expressed outside the SCN. At E14.5, extra-SCN PER2 expression was high and occasionally circadian, but was nearly completely eliminated by E15.5. It is not clear whether these PER2-expressing cells move into the SCN or remain in the dorsal hypothalamus while reducing their PER2 expression. Anecdotally, it appeared that neuronal migration into the SCN region may explain this extra-SCN PER2 expression. Further study with more rapid imaging than 1/hr would be needed to examine this possibility. Still, rhythmic bioluminescence in these extra-SCN regions could explain the discrepancy between previous studies reporting the onset of PER2 daily oscillations in hypothalamic explants at E13 or E15 [190, 191]. The correlations between increasing fraction of rhythmic cells, increasing circadian period, and increasing period precision during this time could reflect the consequences of cell-cell communication [147] or differential expression of molecular components of the circadian oscillator [178, 200]. Together, these data support the onset of cell-autonomous circadian oscillation between E14.5 and E15.5, with intercellular communication developing shortly thereafter.

The SCN in adult mice displays a dorsal to ventral phase wave in clock gene expression [141, 209, 210, 215]. Because this phase wave is not a fixed property (e.g., it can adopt a different pattern after a temperature manipulation *in vitro*) [216], it is important to consider whether the results from the isolated SCN reflect its *in vivo* circadian properties, or are simply reflective of its environment. Our results indicate that under the constant conditions we employed, the SCN phase wave first appears after birth. SCN explant procedures were performed at identical times of day, so although surgery has been shown to strongly reset circadian phase [190, 191], it is unlikely to cause spatial wave seen in the more mature SCN. Furthermore, it is unlikely that surgery can start circadian oscillation in cells lacking critical clock components, as demonstrated by the lack of oscillation on E13.5 and E14.5. Postnatal maturation of the SCN network likely involves synaptogenesis to allow direct neurotransmission. Synaptogenesis peaks near P2, corresponding to the time at which we first found the core-shell phase wave [217]. This provides indirect evidence, therefore, that synaptic network topology contributes to the core-shell differentiation and the phase relationships among SCN cells [85, 218]. I speculate that neurotransmission for synchrony might be undirected before synaptogenesis, and then may be synaptic in postnatal days. The directed nature of neurotransmission through synapses would then enable the phase wave to develop, as there could then be distinct classes of neurons “sending” or “receiving” neurotransmission to establish synchrony.

Though the network continues to mature after birth, we found that SCN intercellular synchrony is established before synaptogenesis peaks. Surgeries can reset SCN rhythms [190], and we found that synchrony of E14.5 and immature E15.5 SCN decreased over the course of the recording, indicating weak or no spontaneous synchronization between cells. Intuitively, prior studies have also related increases in period variability with lower intercellular synchrony

[147, 219]. Our data likewise showed an increase in synchrony by E15.5 (Fig. 3.3) that corresponded with a decrease in cycle-to-cycle period variability. This synchrony in adults is at least in part established by the neurotransmitter VIP and its receptor VIPR2 [79, 195–198]. In rats, *Vip* mRNA is detected by E18 [187, 220], but VIP protein expression has only been examined postnatally [221]. Our results showed that VIP protein is undetectable by immunochemistry before birth. While this may seem startling, this result corresponds well with a prior study in which embryonic SCN explants from VIP$^{-/-}$ mice maintained circadian oscillations at the tissue level [191], indicative of intercellular synchrony. Our results further demonstrate that synchrony is achieved near E15.5, at least several days before significant expression of VIP or its receptor VIPR2. Finally, that VIP antagonist does not interfere with synchrony or cell-autonomous oscillation suggests that other neural signals are sufficient to sustain synchrony before the maturation of the SCN.

The increase in synchrony in the SCN at E15.5 does coincide with Lhx1 expression across the SCN [178]. This transcription factor is important for the expression of diverse neuropeptide coupling signals aside from VIP, such as GRP or AVP [180]. Because these signals can mediate the synchrony in adults [222, 223] and in postnatal ages [200], they are candidates for sustaining spontaneous SCN synchrony during embryonic development.

It has long been recognized that the accumulation of intercellular calcium, through opening voltage-gated Ca^{2+} channels during action potentials, is the trigger for neurotransmitter release [224, 225]. In this chapter, we did not seek to determine the onset of neuronal firing within the SCN, or its interaction with the expression or release of small neurotransmitters such as GABA or large neuropeptides such as VIP [226]. This interaction is compounded by the release of VIP from large dense-core vesicles, rather than the relatively well-understood small clear-core vesicles [227]. This topic would make for an interesting follow-up study, as it would shed light on the role of membrane potential in cell-autonomous and tissue circadian rhtyhms, as well as on neurotransmitter and neuropeptide release more broadly. For example, it is unclear if neuronal excitability should be considered a clock output, input, or core feature. In the following chapter, we begin to address these open questions by identifying firing patterns within the mature SCN, and how these firing patterns relate to neuronal class as determined by VIP expression.

Chapter 4

The role of neuronal firing patterns in VIP and non-VIP neuronal populations of the suprachiasmatic nucleus

4.1 Introduction

In this chapter, we sought to address questions of the role of VIP and neuronal firing in the entrainment of daily rhythms in gene expression and activity. The mature SCN expresses a broad range of small neurotransmitters (such as GABA and glutamate) and larger neuropeptides (such as VIP, pituitary adenylate cyclase-activating polypeptide (PACAP), and vasopressin (AVP)), many of which have been implicated in shifting SCN circadian phase or modulating light input [226, 228–233]. In mammalian nervous systems, the release of molecules involved in neuronal signaling is regulated by calcium (Ca^{2+}) influx during cellular action potentials. In line with these observations, a recent study of the SCN found that periodic optogenetic stimulation of all SCN neurons was sufficient to phase shift and entrain circadian rhythms in gene expression *in vitro* and behavior *in vivo* [234]. However, due to the menagerie of signaling occurring in the SCN, the mechanism or mechanisms driving this result have not been elucidated. More broadly, little is known about the respective roles of neurotransmitters in entraining the neuronal population of the SCN to daily rhythms in the environment.

The results in this chapter are in revision as C. Mazuski, J.H. Abel, S.P. Chen, T.O. Hermanstyne, F.J. Doyle III, and E.D. Herzog, "VIP neurons of the SCN entrain circadian rhythms with distinct firing patterns,." Spike sorting, identification of neuronal firing patterns, analysis of *in vivo* optogenetic experiments, and statistical analyses for results in Figures 4.2, 4.5, 4.11, and 4.12 were performed by J.H. Abel. All experimental work was performed by members of the Herzog lab, primarily C. Mazuski. The text of this chapter is original, however, the materials section, figures, and captions are identical to the drafted text of the revised manuscript.

The neuropeptide VIP has been previously implicated in establishing synchrony among SCN neurons [79, 197, 235], and thus is a candidate pathway for partial mediation of the entrainment observed in [234]. Though VIP is expressed in only approximately 10% of SCN neurons, a majority of SCN neurons expresses its receptor VIPR2 [236]. VIP is thought to affect the transcriptional oscillator directly through the VIPR2 G-protein coupled metabotropic receptor (GPCR), which activates a signaling cascade resulting in the promotion of *Per* transcription [237, 238], possibly through CREB [16, 238, 239]. Genetic loss of VIP or its receptor results in asynchronous circadian activity among SCN neurons, which may be rescued by exogenous VIP application [79]. Though other neurotransmitters are known to modulate SCN synchrony or phase responses to light [82, 232], VIP is currently the only neurotransmitter thought to be essential for synchronous oscillation.

Though its pathway and mechanism has been well-studied, the release of VIP is not well understood. VIP is released from large dense-core vesicles, and though it is known that increases in cytosolic Ca^{2+} results in neuropeptide release from large-dense core vesicles [240], the dynamics of this process remain largely uncharacterized [227]. Furthermore, it is unclear what firing patters or frequencies are present in the SCN, or if these patterns correspond in any way to cellular neurotransmitter or neuropeptide content and release. It is known, however, that SCN neurons exhibit circadian rhythms in spontaneous electrical activity [241], thus forming a potential link between these patterns of action potentials in the SCN, VIP or other neurotransmitter release, and the entrainment of circadian rhythms in gene expression and behavior.

We sought to answer questions of how neuronal firing and VIP release affect SCN function through cells to circuits to behavior approach. First, we developed a Cre-lox system to target optogenetic stimulation to solely VIP neurons of the SCN. Next, we used this system to record and identify multiday patterns of spontaneous electrical activity in VIP and nonVIP SCN neurons. We then applied optogenetic stimulation to only VIP neurons at physiologically relevant frequencies both *in vivo* and *in vitro* to test the role of firing patterns in these neurons in evoking the circadian responses observed in [234], and ultimately in entraining genetic circadian oscillation in the SCN.

4.2 Materials and methods

Animals

VIPCre knock-in mice (VIP$^{\text{tm1(cre)Zjh}}$, Jackson Laboratories), floxed ChR2 (Ai32, Gt(ROSA)26Sor$^{\text{tm32(CAG-COP4*H134R/EYFP)Hze}}$, Jackson Laboratories) and *Per2::Luc* [78] knock-in mice (founders generously provided by Dr. Joseph Takahashi, University of Texas Southwest Medical Center) were housed in a 12h:12h light:dark cycle in the temperature and humidity controlled Danforth Animal Facility at Washington University in St. Louis. All animals were congenic on a C57BL/6JN background. Combinations of these genotypes were used for all experiments, with VIPChR2 animals being heterozygous for both VIPCre and floxed-ChR2 and controls being littermate animals heterozygous for only VIPCre or floxed-ChR2. Mice were genotyped by PCR before and by presence (ChR2-positive) or absence of eYFP fluorescence microscopy following each experiment. All procedures were approved by the Animal Care and Use Committee of Washington University and followed National Institutes of Health guidelines.

Multielectrode array cell electrophysiology

Homozygous VIPCre-J mice were crossed with homozygous floxed-ChR2 mice to generate heterozygous litters expressing ChR2 solely in VIP+ neurons (VIPChR2). Extracellular recordings were made from multielectrode arrays (Multichannel Systems, Reutlingen, Germany) plated with SCN cells as previously described [79, 140, 242]. Briefly, following decapitation, the brains were rapidly removed from postnatal day 4-5 (P4-P5) VIPChR2 pups. We dissected the bilateral SCN from 250 μm thick coronal brain slices, papain-dissociated and dispersed the cells at high density onto sixty, 30 μm diameter electrodes (200 μm spacing) pre-treated with poly-D-lysine/laminin. Cultures were maintained in Air-DMEM (Dulbecco's Modified Eagles Medium, DMEM, supplemented with 10% fetal bovine serum for the first week of recording) for 3 weeks prior to recording.

Multielectrode arrays were covered with a fluorinated ethylene-polypropylene membrane before transfer to a recording incubator maintained at 36°C. We waited 24h before the start of digitization to ensure culture health and stability. For extracellular recordings, spikes that exceeded a manually set threshold (3-4 standard deviations from noise level) were digitized (1 ms before and after crossing the threshold; MC-Rack software, Multichannel Systems) at 20,000 Hz sampling. Subsequently, the culture was stimulated with 15 ms pulses of light from a high-power 470 nm LED (Cree XLamp XP-E2 Blue High Power LED, LEDsupply) at frequencies between 2-20Hz for 1 h. Culture light intensity was verified to fall between 5 – 1 mW.

Whole-cell patch clamp electrophysiology

Whole cell patch clamp recordings from SCN neurons were obtained using the procedures described in Hermanstyne *et al.* [243]. Specifically, SCN slices were prepared from 3 month old adult VIPChR2 heterozygous mice. After anesthesia with 1.25% Avertin, brains were removed into a cold cutting solution (in mM: 240 sucrose, 2.5 KCL, 1.25 NaH_2PO_4, 25 $NaHCO_3$, 0.5 $CaCl_2$ and 7 $MgCl_2$, saturated with 95% $O_2/5\%CO_2$). 300μm coronal slices were cut on a Leica VT1000S vibrating blade microtome and incubated in oxygenated artificial cerebrospinal fluid (in mM: 125 NaCl, 2.5 KCL, 1.25 NaH_2PO_4, 25 $NaHCO_3$, 2 $CaCl_2$, 1 $MgCl_2$, 25 dextrose, saturated with $95\%O_2/5\%CO_2$) for at least 1 h. Using glass pipettes (4-7 Mω) containing an intracellular solution (in mM: 120 $KMeSO_4$, 20 KCl, 10 HEPES, 0.2 EGTA, 8 NaCl, 4 Mg-ATP, 0.3 Tris-GTP, and 14 phosphocreatine), a “loose patch” cell-attached recording was obtained. A gigaOhm seal (>2 GΩ) was formed and spontaneous firing was recorded for approximately 1 min. We then evoked firing in ChR2-positive neurons with 15 ms pulses from a 465 nm laser (DPPS MDL-III-447 100 mW, 5% stability, Information Unlimited) positioned over the slice controlled by a TTL input from a Grass stimulator (S88, Grass Instrument Company, Quincy, MA) at the desired frequency (2 to 15 Hz). Electrophysiological data were compiled and analyzed using ClampFit, Mini Analysis, and Prism 7.0 (Graphpad Software, La Jolla, California).

Isolation of individual neuronal firing patterns

Software was created for semi-automated spike sorting to allow discrimination of neuronal activity from MEA recordings across multiple days. Time-stamped spikes from a given electrode were separated into 24 h epochs, subsampled by taking a random 10% of the total spikes from each epoch, and then sorted based on principal component analysis (PCA) and fitting a Gaussian mixture model (GMM) to the principal components that contained >10% of the explained variance using a Bayesian information criterion (BIC) cutoff. The recording noise was identified as the cluster with the average spike shape with the lowest magnitude as shown in Figure 4.1. The data was split into the remaining clusters. PCA, GMM clustering, and splitting was then applied recursively until each cluster could not be split further based on the BIC cutoff. This allowed for the identification of neurons with fewer total recorded spikes. We used the Mahalanobis distance to keep only spikes sufficiently close to the center of the GMM. The PCA components and GMM parameters used to sort the subsampled day of spikes were saved and used to sort all spikes on that electrode from that day. The spike trains identified on each electrode were then combined across days by correlating spike shapes (Pearson $r > 0.95$) to recover the activity of a single neuron throughout the multiday recording. If neuronal firing could not be connected across more than one day, it was excluded from subsequent analysis. Firing activity during optogenetic stimulation was similarly sorted and matched to the third day of spontaneous firing to identify VIP+ neurons.

This procedure was automated using the Python language, using packages scipy [204], and scikit-learn [244] for sorting, and neuroshare for reading raw MEA data files. All scripts used in spike sorting are publicly available at: http://github.com/JohnAbel/spikesort. This method produced similar numbers of circadian neurons and spike times to manual sorting performed as in [140] in approximately 90% less time. To calculate circadian rhythmicity, we binned the average firing rate of each neuron over 10 min intervals. Using the MetaCycle package [245], we calculated circadian rhythmicity using JTK cycle and Lomb-Scargle periodogram analysis (range 20 to 28h). If a neuron was deemed rhythmic with $P < 0.05$ after controlling for multiple comparisons on both methods, we considered that neuron to be circadian.

Classification of individual neuronal firing patterns

Neuronal firing patterns from the three days of spontaneous activity were identified in Python using scipy hierarchical clustering of interspike interval histogram (ISIH) over 1.5 s with 100 bins, using dynamic time warping [246] as the correlation metric, and complete linkage. Varying ISIH bin size (0.005 s to 0.05 s) did not alter results significantly. The threshold for dendrogram cluster identification was set to 70% of the maximum distance between data points (default scikit-learn setting). Following clustering, DFIR was identified with a bin size of 0.001 s to construct summary statistics with high temporal resolution. In-slice recording and whole-cell patch clamp recording data were analyzed in an identical fashion, except ISIH bin size was changed to 0.05 s for patch clamp recording due to the short 60 s recording interval.

Recording and analysis of real-time clock gene expression

To record circadian PER2 protein expression, we crossed heterozygous VIPChR2 and *Per2*^{Luc} mice. Control mice were littermate animals lacking either VIPCre or floxed-ChR2. Adult (> P15) mice of both sexes were sacrificed with CO_2 and 300 μm coronal brain slices were sectioned. The bilateral SCN was dissected out and cultured on Millicell-CM inserts (Millipore, Billerica, MA) in pre-warmed culture medium (AirDMEM supplemented with 10 mM HEPES and 100 μM beetle luciferin, Promega, Madison, WI). The sealed 35 mm Petri dishes (BD Biosciences, San Jose, CA) were transferred to a light-tight incubator kept at 36°C. As described previously [79, 140], bioluminescence from the Luc reporter was counted with a photomultiplier tube (PMT; HC135-11 MOD, Hamamatsu Corp., Shizuoka, Japan) in 6 min bins for at least three days prior to optogenetic stimulation. PMT recordings were paused during 1 h of optogenetic stimulation between CT9-12 for either one day or three consecutive days. Using a custom-made LED array (Cree XLamp XP-E2 Blue Color High powered LEDs, LEDsupply, Randolph, VT) that delivered light flashes (15 ms, 5 mW, 470 nm) per dish, SCN were stimulated for 1 h at either high (20 Hz pulses at 2 Hz) or low instantaneous frequencies (4 Hz). The LED array was powered by a supply (LEDD1B high-powered LED driver, Thorlabs, Newton, NJ) under TTL control from a stimulator (S88, Grass Instrument Company, Quincy, MA). Care was taken to minimize any mechanical disturbance to the SCN, and during stimulation, the temperature underneath the LED array remained at 36°C. After stimulation, the dishes were repositioned underneath their PMT and recording continued for at least four days.

For pharmacology experiments we stimulated VIPChR2 *Per2*^{Luc} slices in the presence or absence of 10μm VPAC2R antagonist in AirDMEM([D-p-Cl-Phe6,Leu17]-VIP, Tocris Bioscience, Bristol, UK). Following 1 h of stimulation with HIF frequency, all slices were transferred briefly into a fresh, prewarmed dish of AirDMEM and then transferred back into their original dishes and placed back underneath their PMT channels. All data were analyzed blinded to genotype. SCN traces that did not retain rhythmicity due to media evaporation or fungal infection were excluded ($N = 4$), and all other data were analyzed in a stereotyped manner. In addition, due to inherent variability in period and amplitude within our PMT systems, all comparable experiments were performed in the same incubator. Each experiment (HIF stimulation, LIF stimulation, and antagonist treatment) represents at least 3 separate runs with control and experimental conditions run in parallel. Raw counts from the PMT were detrended using a running 24-hour smooth, discarding the first and last 12 h of the recording as previously described [193]. For single-pulse experiments, the data from the day of stimulation also was excluded from analyses. Circadian period was calculated from a linear fit to times of the daily acrophase of PER2 expression (baseline= second through fourth days of recording; after-stimulation= fifth through seventh days; Clocklab, Actimetrics). The difference between the baseline-extrapolated and observed acrophases in the three days following stimulation was reported as the phase shift. For PMT traces stimulated for three consecutive days, we used the rising phase as a stable phase marker. Given the natural spread of PER2, we normalized the data based on the rising phase on the day before stimulation.

In vivo stimulation of VIP neurons

To stimulate VIP neurons *in vivo*, mice underwent stereotactic surgery to implant a fiberoptic cannula capable of delivery light to the bilateral SCN. Specifically, anesthetized mice (2% Isoflurane) were placed into a stereotaxic device and implanted with a sterilized fiber-optic cannula (5.8 mm in length, 200 μM diameter core, 0.39 NA; Thorlabs, Newton, NJ). The cannula was implanted at +0.4mm anterior, +0.0 mm lateral and -5.5 mm ventral to Bregma. Mice received analgesic treatment during recovery. Following recovery, mice were enucleated as previously described [243, 247] so that mice did not respond to ambient light. Additionally, mice were tethered to a flexible fiberoptic cable (Thorlabs, Newton, NJ) attached to a laser (465 nm, 100 mW, 5% stability, DPPS MDL-III-447, Information Unlimited) and allowed to freely roam with ad lib access to food, water and an open-faced wheel in a custom-built cage. Wheel revolutions were counted with a reed switch (Clocklab, Actimetrics). After free-running locomotor behavior returned to pre-enucleation levels, mice were stimulated for up to 40 days with different frequency patterns (HIF or LIF). Mice that received both stimulation patterns had the order randomized and separated by at least four days without stimulation.

Immunohistochemistry

To test for neuronal activation, we measured cFOS protein induction in mice implanted with a fiberoptic aimed at the SCN after 1 h of stimulation (15 Hz, 15 ms pulses) during early subjective night (CT 13). Immediately following stimulation, mice were anesthetized with 1.25% Avertin (2,2,2-tribromoethanol and tert-amyl alcohol in 0.9% NaCl; 0.025 ml/g body weight) and transcardially perfused with phosphate-buffered saline (PBS) and 4% paraformaldehyde (PFA). The brain was rapidly dissected and transferred to 30% sucrose following 24 h in 4% PFA. Frozen coronal sections cut at 40 μm were collected in three separate wells. cFOS immunofluorescence or avidin-biotin immunohistochemistry was performed using two using a rabbit anti-cFOS antibody (Santa Cruz Biotechnology, Santa Cruz, CA). For immunofluorescence, free-floating sections were washed for 1 h in PBS, incubated overnight at 4°C in anti-rabbit cFOS antibody (1:1000 in PBSGT). Slices were washed again and incubated for 2 h at room temperature in donkey anti-rabbit Cy3 secondary antibody (1:500 in PBSGT). Sections were washed again in PBS for 30 min, mounted, and cover-slipped with DABCO (1,4-Diazobicyclo[2,2,2]-octane) mounting medium. Sections were imaged in 4-μm z-stacks on a Nikon A1 Confocal microscope. Two independent investigators quantified the fraction of ChR2-eYFP positive neurons that also expressed nuclear cFOS and results differed by less than 10% per brain. For DAB immunohistochemistry, free-floating sections were incubated for 72 h in rabbit c-Fos antibody (1:2500). Subsequently, sections were processed with the avidin-biotin method for immunohistochemistry. Tissues were reacted in diaminobenzidine with 0.01% H_2O_2, mounted, dehydrated and cover-slipped. Sections were imaged using the Alafi Nanozoomer at Washington University in St. Louis Medical School. Tissues were always processed together and mid-SCN sections were selected from all animals for quantification. An investigator blinded to the genotype of the mouse quantified the number of cFOS positive cells within the SCN using ImageJ software. The SCN was located and boundaries were drawn to demarcate the ventral and dorsal SCN in each animal (250 μm x150 μm, ventral SCN per side, 150 μm x 150 μm, dorsal SCN per side).

Locomotor analysis

We identified the daily onset of locomotor activity from wheel running data in 15 min bins as the zero-crossing of the continuous wavelet transform using the Mexican Hat wavelet, as described for temperature rhythms in [248]. We calculated the phase response curve by identifying the change in activity onsets evoked by optogenetic stimulation compared to the mean time between onsets in the same mouse under free running conditions, to account for inter-individual differences. Calculating phase change in comparison to the same mouse under free-running conditions (rather than comparison with a separate control group) allowed inclusion of mice with visibly different periods. To measure the time to entrainment, we constructed Rayleigh plots of activity onset for days 2-10 of optogenetic stimulation and calculated the Kuramoto parameter (i.e. synchronization index) [105]. Finally, we measured optogenetically induced activity suppression by comparing wheel revolutions during the stimulated hours between CT 12 – 16 and equivalent time bins from free-running days with no stimulation.

4.3 Results

Identifying spontaneous electrical activity of VIP neurons

The aim of our first experiment was to identify relevant firing patterns and frequencies within the SCN, and to test the hypothesis that the subset of SCN neurons that express VIP exhibit also form a coherent electrophysiological class of neurons. To characterize the firing of these neurons across multiple days, we recorded from high-density SCN neuronal cultures plated on multielectrode arrays (MEAs) for three days. Extracellular recording from MEAs allowed the recording from dozens of individual neurons within an SCN culture, and prior studies have shown that neuronal activity in high-density SCN cultures corresponds well with recordings from SCN slices *in vitro* and the intact SCN *in vivo*. As described in the methods, channelrhodopsin-2 (ChR2) was expressed solely in VIP neurons by crossing a floxed-ChR2 mouse line with a VIPCre mouse line. Following the recording of spontaneous electrical activity, each culture received optogenetic stimulation, so that, by identifying which neurons respond to stimulation, we were able to retroactively classify neuronal identity by VIP content. The schematic in Figure 4.2a

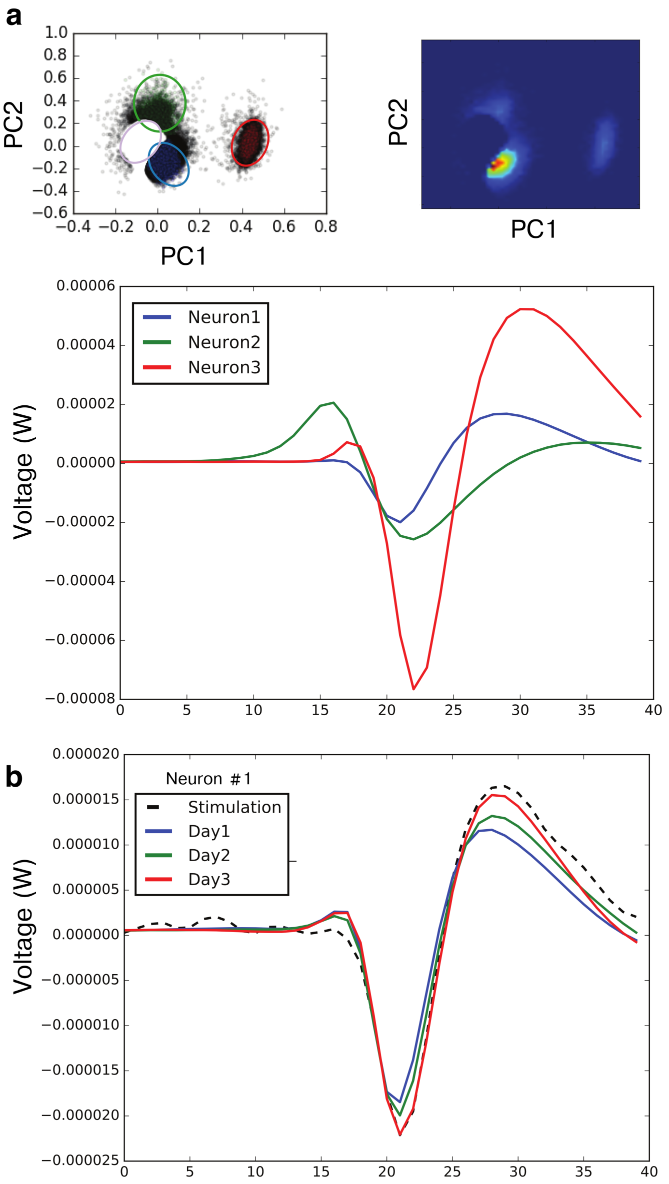

Figure 4.1: Spontaneous electrical firing from individual neurons can be reliably tracked across multiple days. We used a recursively applied PCA with Gaussian mixture model (GMM) clustering to discriminate firing from single SCN neurons across multiple days on multielectrode arrays before and during optogenetic stimulation. The automated analysis was performed blinded to the identity of the neuron (VIP or non-VIP). (**a**) On this representative electrode, we identified 3 clusters (circled in top panel) and their corresponding average extracellular waveforms (bottom panel). The purple circle is the noise cluster which was identified and removed from analysis. (**b**) Neuron1 from the above analysis was identified as VIP-positive. The spike waveform during optogenetic stimulation (dashed line) correlated with the mean spontaneous activity waveforms recorded from each of the prior three days from the same electrode.

shows the experimental procedure for obtaining multiday recordings from MEAs containing VIP and nonVIP neurons. Figure 4.2b demonstrates the method for identifying VIP neurons retroactively. The interspike interval histograms for a VIP neuron and a nonVIP neuron during a 4 Hz stimulus demonstrate that the VIP neuron responded by firing precisely in response to the stimulation pattern. To further confirm that VIP neurons responded by firing synchronously, we cross-correlated spike times between pairs of SCN neurons (Figure 4.2c). As expected, only VIP neurons fired synchronously (with no lag) in response to optogenetic stimulation. Furthermore, some nonVIP neurons responded with reductions in firing for approximately 10-20 ms following each stimulation, consistent with inhibitory signaling from VIP neurons.

Using this information, we retroactively classified the three prior days of spontaneous activity as VIP or nonVIP and in total, 8 MEAs resulted in multiday recordings from 40 VIP and 543 nonVIP SCN neurons. Prior studies have relied on brief 1-30 min snapshots of VIP neuron firing, and reached opposing conclusions as to whether VIP neuron firing is circadian [243, 249]. By tracking VIP neurons continuously across multiple days, we found that the majority ($81.5 \pm 4.0\%$, mean ± SEM, Figure 4.2d-e) of VIP neurons in each culture were circadian, i.e. met the criteria for circadian oscillation as described in the methods. In contrast, about half ($51.7 \pm 8.5\%$, mean ± SEM) of nonVIP neurons were circadian.

We performed additional experiments to test our assumptions that VIP neurons selectively and consistently responded to ChR2 stimulation. First, we tested if ChR2 stimulation reliably triggered responses in ChR2 neurons by identifying VIPChR2 neurons via yEFP expression and using a whole-cell patch clamp recording technique (Figure 4.3). We found that only VIPChR2 neurons increased their firing rate to match that of the stimulus, and that these neurons reliably responded for frequencies between 2 and 15 Hz. Next, we used a post-stimulus time histogram (PSTH, Figure 4.4) to validate that these responded occurred within 5 ms of the stimulus. Together, these results demonstrate a highly reliable optogenetic system for triggering firing of solely VIP neurons.

Figure 4.2: Characterizing multiday spontaneous firing activity of identified VIP SCN neurons within a multielectrode array culture. (**a**) SCN neurons were categorized as VIP-positive (VIP) or –negative (non-VIP) by optically tagging VIP neurons using optogenetic stimulation after 3 days of spontaneous activity recording. Multiday firing was sorted from 583 SCN neurons identified on 8 multielectrode arrays plated and cultured for 3 weeks from VIPChR2 mice. Raster plots of five representative SCN neurons show how their spike times over one minute differed in mean rate and pattern. (**b**) The inter-spike interval histograms during optogenetic stimulation illustrate how a representative VIP (top) neuron fired at the stimulation frequency (4 Hz) with a precision of <10ms (top right inset) and a non-VIP neuron (bottom) fired in a ChR2-independent pattern. (**c**) To further characterize the evoked firing of VIP neurons, we cross-correlated spike times between concurrently recorded SCN neurons during optogenetic stimulation. A VIP reference neuron (top left panel) fired synchronously with 3 other representative VIP (top panels), but not 4 representative non-VIP neurons (bottom panels). Note that some non-VIP neurons (#2 and #3) decreased their firing following stimulation of VIP neurons, indicative of postsynaptic inhibition. (**d**) Four representative VIP (top) and non-VIP (bottom panels) SCN neurons showing circadian firing patterns over the three days of recording. (**e**) A greater fraction of VIP neurons were circadian ($81.6 \pm 4.7\%$) compared to non-VIP neurons ($51.7 \pm 8.5\%$, Chi-squared test $^{**}P < 0.00001$). (**f**) eYFP fluorescence (green) reveals the subset of SCN neurons expressing ChR2 near 4/60 electrodes.

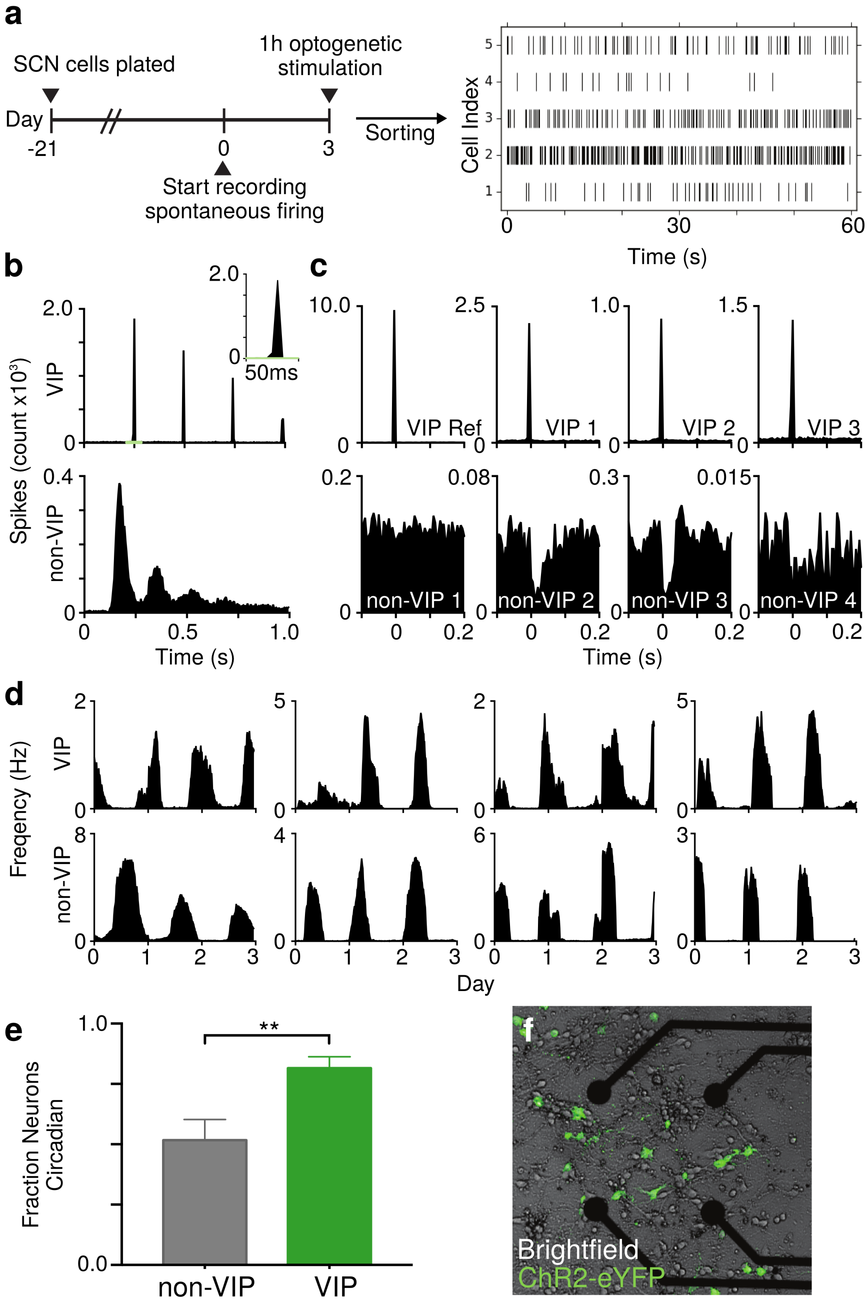

Figure 4.2: (Continued.)

VIP neurons exhibit multiple distinct firing patterns

Prior studies have focused on circadian variations in mean firing rates through binning electrical activity into seconds-to-minutes long epochs. However, it is millisecond-to-second firing patterns and short-term firing frequency that have been implicated in neurotransmitter release probability and changes in calcium transients [250, 251]. Therefore, we analyzed the resulting circadian neurons ($n = 268$ nonVIP and $n = 33$ VIP) to characterize the physiologically relevant instantaneous firing frequencies.

Using the spike timing (or interspike interval histogram (ISIH) of the entire recording) and a hierarchical clustering, we found three distinct classes of firing pattern, similar to those observed in [252]. These classes were tonic (i.e. characterized by a highly regular timing between spikes), irregular (i.e. characterized by a wide variability in spacing between spikes), and bursting (i.e., characterized by infrequent bursts of several spikes at frequencies in excess of 50 Hz). Contrary to our expectation, VIP neurons were classified into multiple categories of firing pattern, indicating that they are an electrophysiologically heterogeneous group of neurons. This result is shown in Figure 4.5a-b. We note that our classification scheme does not indicate that, for example, an irregular neuron could never burst, but instead that irregular spiking represents the dominant mode of its electrical activity. For each neuron, we then identified the dominant instantaneous firing rate (DIFF): the firing frequency associated with the peak of the ISI histogram (Figure 4.5d).

Intriguingly, we did not observe day-to-day changes in neuronal firing class despite drastic changes in mean firing rate across the circadian day (Figure 4.5e). That is, a tonic neuron may be silent for its subjective night, but will resume tonic firing the next day with ISI corresponding to that of the previous day. To determine if these patterns were consistent with *in vivo* neuronal function, we analyzed the data from [243] using an identical hierarchical clustering. These VIP data were also classified as electrophysiologically heterogeneous, with clusters corresponding to the tonic and irregular clusters identified from MEA recordings. Representative 60 s firing from each of the electrophysiological classes are shown in Figure 4.6. In sum, we found that VIP neurons, despite being a small subset of the SCN, are members of distinct and consistent electrophysiological classes and largely fire with tonic or irregular spike timing, at peak frequencies of approximately 2-10 Hz.

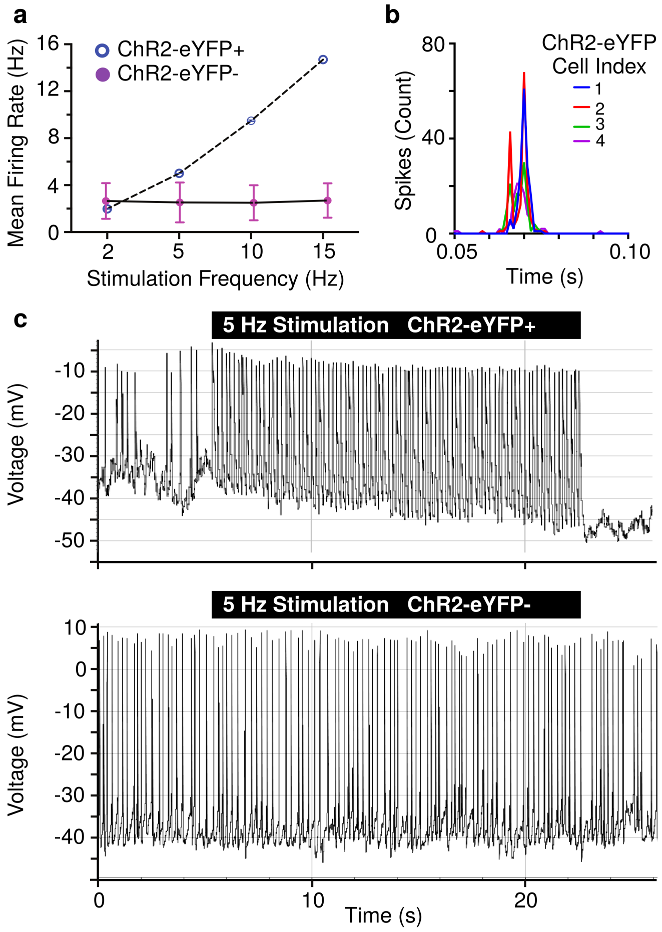

Figure 4.3: Only ChR2 positive SCN neurons increase firing in response to optogenetic stimulation. (**a**) Using whole-cell patch clamp, we recorded from neurons within VIPChR2 SCN slices while stimulating at 2, 5, 10, or 15 Hz. ChR2-eYFP positive neurons ($n = 5$) matched their firing to the stimulation frequency, while ChR2-eYFP negative neurons ($n = 5$) in the same SCN slice did not. (**b**) ChR2-eYFP positive neurons followed the stimulation frequency within 10 ms as revealed by the interspike interval histogram (15 Hz stimulation, $n = 4$ neurons). (**c**) Representative traces show a ChR2-eYFP positive neuron that increased its firing rate in response to 5 Hz stimulation, while ChR2-eYFP negative firing did not change. These results indicate that the presence of ChR2 is necessary for light-evoked increases in firing.

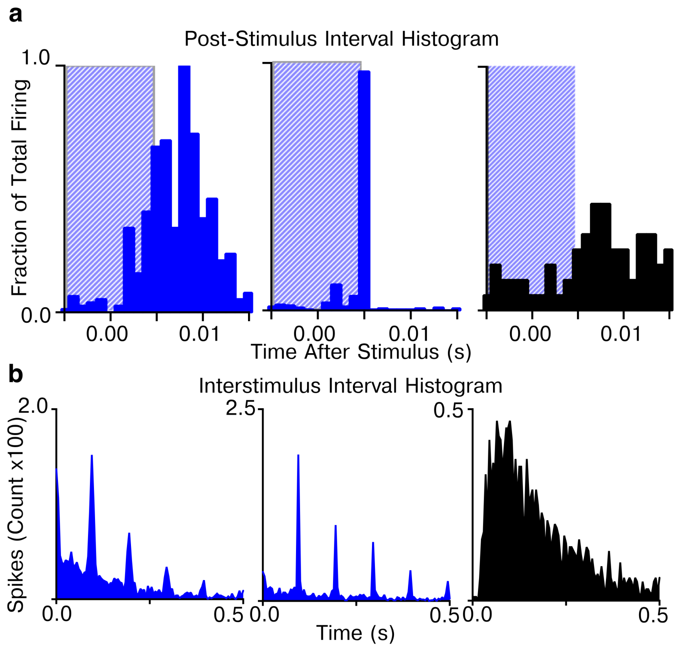

Figure 4.4: VIPChR2 neurons fire within 10 ms of stimulation. (**a**) The post-stimulus histogram (PSTH) of SCN neuronal firing following a 10 ms laser flash (blue box) showed that 100% of neurons identified as VIPergic (blue) fired reliably within 10ms of the stimulation, while non-VIP neurons (black) did not respond to the flashes. (**b**) Corresponding ISIH for two VIP (blue) and one non-VIP (black) neurons during 10 Hz stimulation. The VIP neuron fired at 0.1 s intervals whereas the non-VIP neuron (black) did not. Thus, the ISIH or the PSTH accurately identified VIP neurons on multielectrode arrays.

Figure 4.5: VIP-expressing SCN neurons exhibit tonic or irregular circadian firing patterns. (**a**) Hierarchical clustering sorts SCN neuron recordings from multielectrode arrays into one of three different daytime firing patterns: Tonic (TON), irregular (IRR) or bursting (BUR). Identification of VIP neurons (black lines) reveal that they are a heterogeneous class of neurons that exhibit either tonic or irregular firing. (**b**) Representative interspike interval histograms (ISIH) for each identified class of neurons. The dominant instantaneous firing frequency (DIFF, black triangle) measures the most common firing interval for an individual neuron. (**c**) The total ISIH for VIP and nonVIP neurons. (**d**) Quantification of the DIFF from each class (n = the number of neurons recorded within each class; median interquartile range in Hz: TON VIP 5.3 ± 2.8, IRR VIP 3.9 ± 3.7, TON Non-VIP 6.2 ± 3.6, IRR Non-VIP 4.1 ± 4.1, BUR Non-VIP 101.0 ± 73.6). (**e**) Short-term firing patterns were stable across multiple days shown by three representative SCN neurons. Note that the daily appearance of multiple bands during tonic firing corresponds to harmonics resulting from skipped spikes. (**f**) Daytime firing VIP neurons recording using whole-cell patch clamp (data previously published in [243]) similarly exhibit tonic or irregular firing. (**g**) Representative ISIH from these neurons. (**h**) Dominant instantaneous firing rate was calculated for each neuron from the ISIH peak, and a boxplot of dominant frequency is shown for each neuron class (tonic/irregular). Observed DIFF fell predominantly between 2 Hz and 10 Hz (tonic VIP 4.5 ± 1.4 Hz; irregular VIP 2.8 ± 1.4 Hz; all values median ± interquartile range).

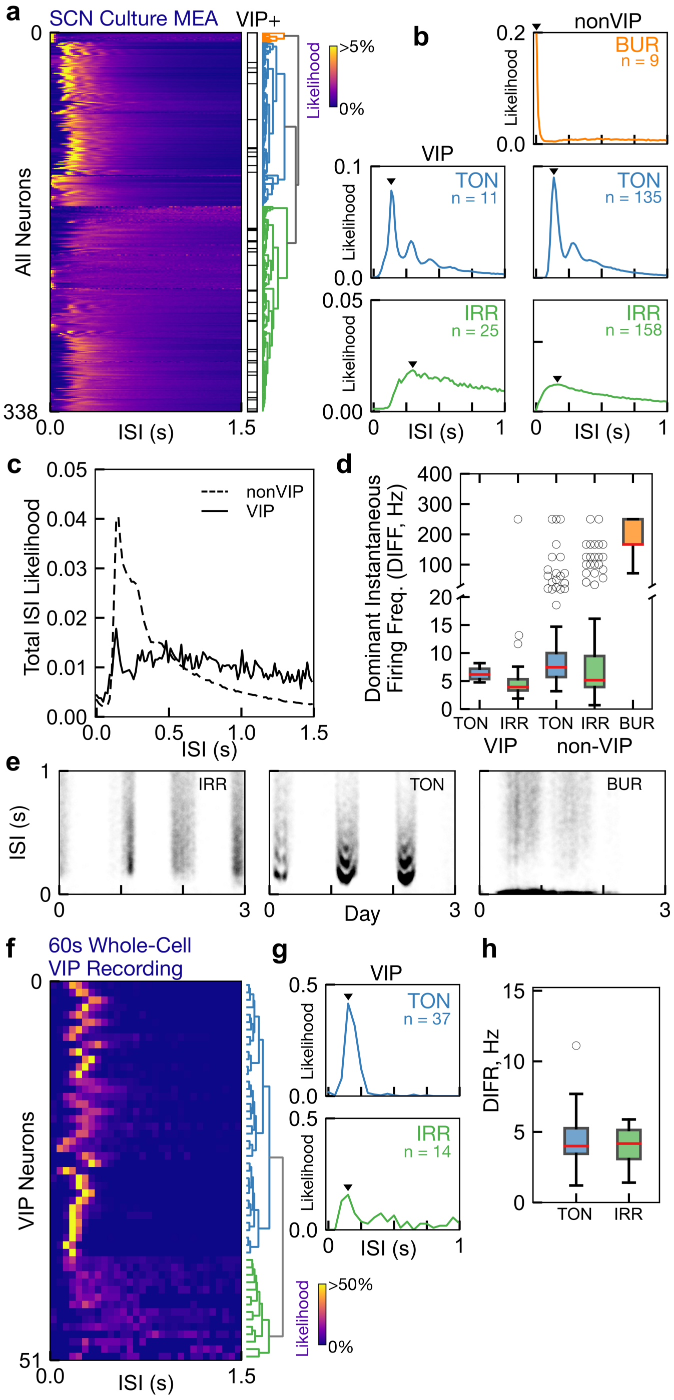

Figure 4.5: (Continued.)

High frequency stimulation of VIP neurons shifts genetic circadian rhythms *in vitro*

We next sought to test the role of the electrical activity we have identified within the SCN. To do so, we optogenetically stimulated VIP neurons within SCN explant slice cultures and recorded circadian gene expression through the $Per2^{Luc}$ bioluminescent reporter, which directly reports PER2 protein abundance). We selected two firing patterns for the stimulation: low instantaneous frequency (LIF, 4 Hz), and high instantaneous frequency (HIF, 20 Hz doublets applied at 2 Hz). These patterns share a mean firing rate across each second (4 Hz), but differ in spike timing.

Following several days of baseline recording, we stimulated VIP neurons with these patterns for 1 h near the peak of PER2 bioluminescence, corresponding to circadian time (CT) 9-12, since this time is associated with the largest response to exogenous VIP application [253] When applied to MEA SCN cultures, we found that 1 h stimulation did not result in depolarization block or habituation (Figure 4.7). We found that HIF stimulation resulted in phase delays of approximately 1.5 h, whereas LIF stimulation or stimulation of the control group did not (Figure 4.8a-b). Furthermore, we found that stimulation in the presence of VIP antagonist significantly reduced the resulting phase shift (Figure 4.8c). Repeated stimulation for three days yielded similar results (Figure 4.9. Our results indicate that the phase of circadian gene expression is mediated through VIP release, which in turn is dependent upon firing frequency of VIP neurons.

High frequency stimulation of VIP neurons induces cFOS expression throughout the entire SCN *in vivo*

Next, we sought to determine if VIP neuronal stimulation resulted in neurotransmission throughout the SCN. VIP neurons are predominantly located in the ventrolateral SCN, though they densely innervate the rest of the SCN, and the VPAC2R VIP receptor is expressed throughout the SCN [236]. Consistent with our expectation, we found that *in vivo* stimulation of VIP neurons increases expression of cFOS, a marker of neuronal activation, throughout the SCN (Figure 4.10). Expression of cFOS increased approximately 5-fold in the ventral SCN, and 4-fold in the dorsal SCN compared to controls. Thus, *in vivo* stimulation of VIP neurons increases the electrical activity in both VIP and nonVIP subpopulations of the SCN.

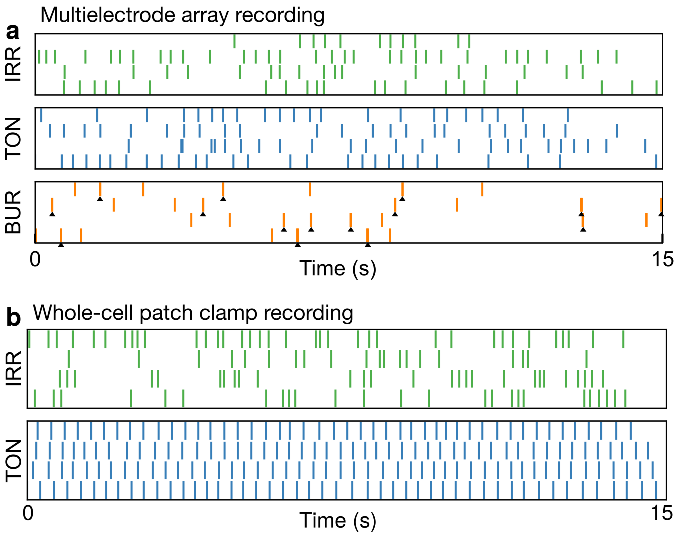

Figure 4.6: Examples of SCN firing classes identified through hierarchical clustering (**a**) Representative examples of irregular, tonic and bursting firing in multielectrode array recordings. (**b**) representative examples of irregular and tonic firing in whole-cell patch clamp recordings from Hermanstyne *et al.* [243].

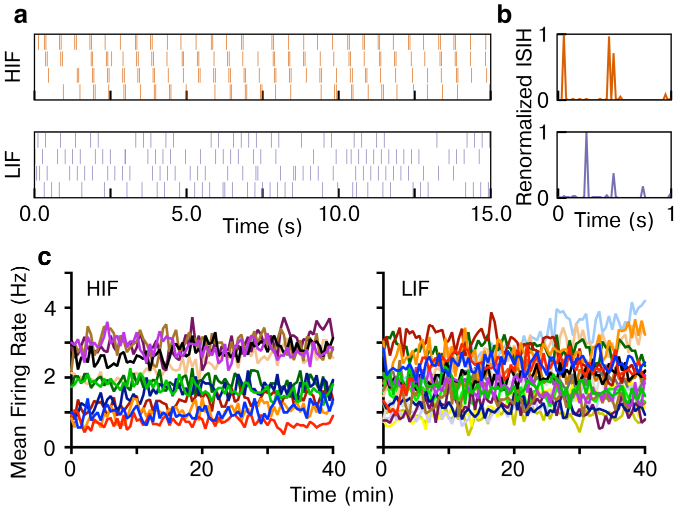

Figure 4.7: VIPChR2 neurons fire reliably in response to 40 min of HIF or LIF stimulation. To test whether VIP neurons reliably fire at HIF and LIF frequencies, we stimulated VIPChR2 MEA cultures for 40 min with either frequency. (**a**) 60 s raster plots of two representative VIP neurons firing at HIF and LIF frequencies. The MEA recordings occasionally miss spikes (due largely to the proximity of a neuron to the electrode and the conservative clustering method) but the pattern of spike timing is consistent with the stimulation (**b**) as illustrated by the ISIH. (**c**) VIP firing binned at 30 s showed no change over a 40 min period with either HIF or LIF indicating that individual neurons show no evidence of habituation or depolarization block in response to HIF and LIF stimuluses. The neuron-to-neuron variability in mean frequency is likely primarily due to missing spikes on the multielectrode array.

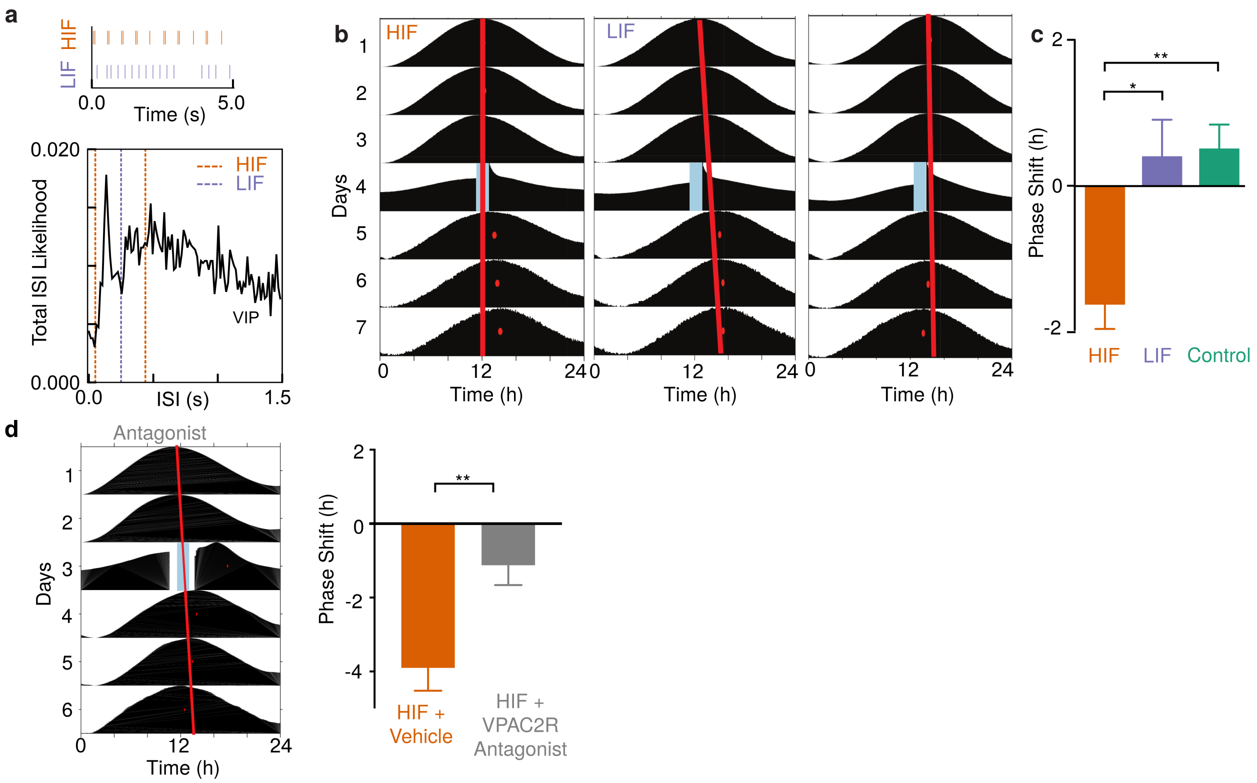

Figure 4.8: High Frequency Optogenetic Stimulation of VIP SCN neurons phase delays circadian rhythms in PER2 expression. (**a**) Optogenetic stimulation was selected from physiological relevant firing frequencies observed in VIP- specific multi-day multielectrode array recordings and whole-cell slice recordings. High instantaneous frequency stimulation (HIF) and low instantaneous frequency stimulation (LIF) evoke similar numbers of action potentials with dramatically different interspike intervals. (**b**) Representative *Per2*^{Luc} actograms from three SCN slices. In the top two traces, ChR2 expressed in VIP neurons was activated for 1 h (blue bar) on the fourth day of recording with high (HIF) or low (LIF) frequencies. Control SCN received either HIF or LIF stimulation, but lacked ChR2. Note the large delay in the time of the daily PER2 (red dots) on the days after HIF stimulation relative to the extrapolated unperturbed phase (red line). (**c**) HIF stably delayed PER2 rhythms compared to either LIF or control conditions (-1.6 ± 0.3 h, HIF, 0.4 ± 0.5, LIF, 0.5 ± 0.3, control; $^{*}P < 0.05$ and $^{**}P < 0.01$, one-way ANOVA with Tukey's posthoc test, n= 9, 10 and 32 SCN slices, respectively). (**d**) VPAC2 antagonist treatment during HIF stimulation reliably reduces the resulting phase shift, shown by a representative actogram (left) and the group summary. (-3.902 ± 0.6178 HIF + Vehicle, -1.124 ± 0.5381 HIF + VPAC2R Antagonist; $^{**}P < 0.01$, unpaired t-test, $n = 7,7$ SCN slices, respectively).

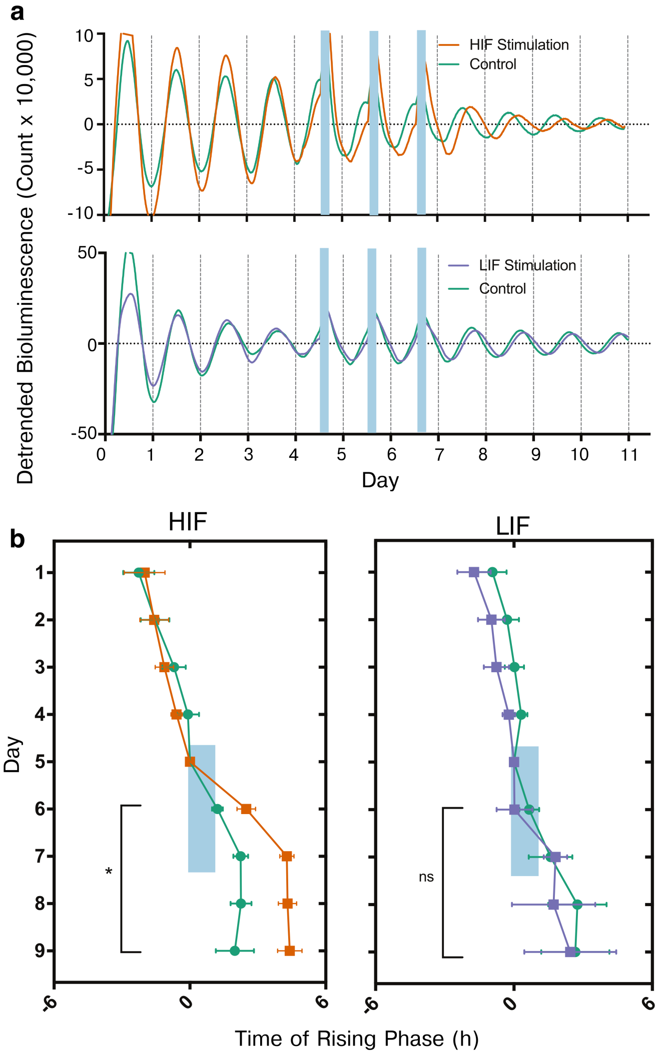

Figure 4.9: HIF but not LIF stimulation of VIP neurons shifts clock gene rhythms in SCN slices. (**a**) Representative bioluminescence traces show that daily HIF stimulation (blue bars) phase delayed PER2 circadian rhythms compared to control SCN explants, while LIF stimulation did not. (**b**) Using the rising phase as a reliable phase marker, we found that HIF stimulation sufficed to change the phase of PER2 expression compared to controls (n = 8 VIPChR2, and n = 7 control, Watson-Williams test for days 6 – 9, *$P < 0.05$). LIF stimulation failed to phase shift PER2 gene expression (n = 5 VIPChR2 SCN, and n = 10 control SCN, Watson-Williams test for days 6-9, $P = 0.5$).

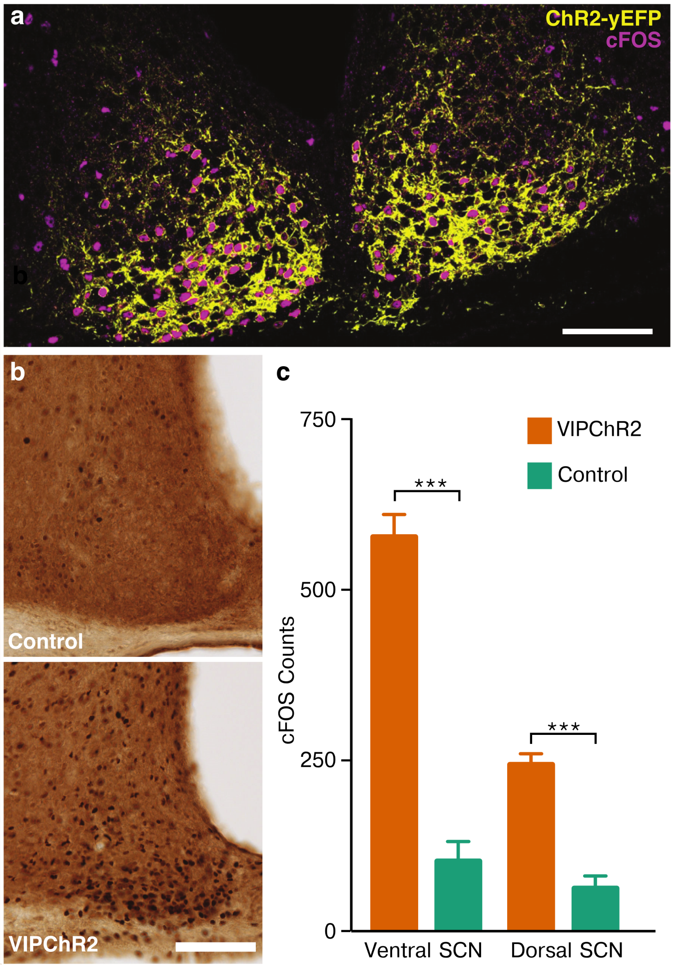

Figure 4.10: Activation of SCN VIP neurons in vivo induces cFOS expression throughout the SCN. (**a**) Representative image of the bilateral SCN showing cFOS induction (magenta) within VIPChR2 neurons (yellow) after 1 h of 15 Hz stimulation in vivo at CT13 (scale bar = 100 μm). (**b**) The number of SCN cells expressing cFOS protein was higher in VIPChR2 (bottom) than control (top panel) mice after 1 h of 15 Hz stimulation at CT13. *In vivo* optogenetic stimulation of VIP neurons increased cFOS expression throughout the SCN (577.8 ± 33.0 Ventral SCN VIPChR2, 103.0 ± 56.9 Ventral SCN Control, 244.5 ± 15.6 Dorsal SCN VIPChR2, 63.0 ± 17.9 Dorsal SCN Control; unpaired Student's t-test $^{***}P < 0.001$, $n = 4$ mice for each condition).

High and low frequency stimulation of VIP neurons entrains daily locomotor rhythms *in vivo*

Next, we used daily wheel running activity as a marker for circadian phase to investigate the role of VIP neuronal firing and frequency on behavioral circadian rhythms *in vivo*. Control and VIPChR2 mice were enucleated to prevent response to ambient light input, and a fiber optic cannula was implanted to deliver light for optogenetic stimulation of VIP neurons in the SCN. Enucleated mice, as in darkness, display a free-running circadian rhythm with a near-24 h periodicity (period $= 23.4 \pm 0.1$, $n = 7$ VIPChR2, period $= 23.4 \pm 0.2$, $n = 4$ control).

To first test if stimulation of VIP neurons alone was sufficient for entrainment, two VIPChR2 and one control mice were delivered 1 h of optogenetic stimulation each day for up to 30 days with a HIF pattern (Figure 4.11a), resulting in entrainment only in the case of the VIPChR2 mice. Next, HIF and LIF stimulation was applied for 1 h each day for a minimum of four days in a randomized order (HIF then LIF, or LIF then HIF), with four days of no stimulation and free-running circadian behavior between HIF/LIF patterns. From these data, we calculated a phase response curve for the 1 h stimulus (combined HIF and LIF, Figure 4.11b). Control mice showed no response, whereas VIPChR2 mice displayed solely phase delays primarily in the early to mid subjective night (CT10-18), which were sufficient for entrainment. Interestingly, optogenetic stimulation in VIPChR2, but not control, mice resulted in an acute reduction in wheel running activity during the early subjective night (CT12-18, mouse activity primarily occurs during these times and so stimulation effects of acute activity at CT0-12 and CT18-24 could not be tested). Light evokes similar suppression of mouse activity in subjective night, though the mechanism by which this occurs is unknown.

Finally, we compared the ability of HIF and LIF to entrain mouse behavior (Figure 4.12). We found that although both HIF and LIF were able to entrain locomotor activity, mice under HIF condition entrained more rapidly. In conjunction with our *in vitro* assessment of circadian phase shifting, we conclude therefore that firing frequency affects the magnitude of phase shifting possibly through altering the likelihood of VIP release.

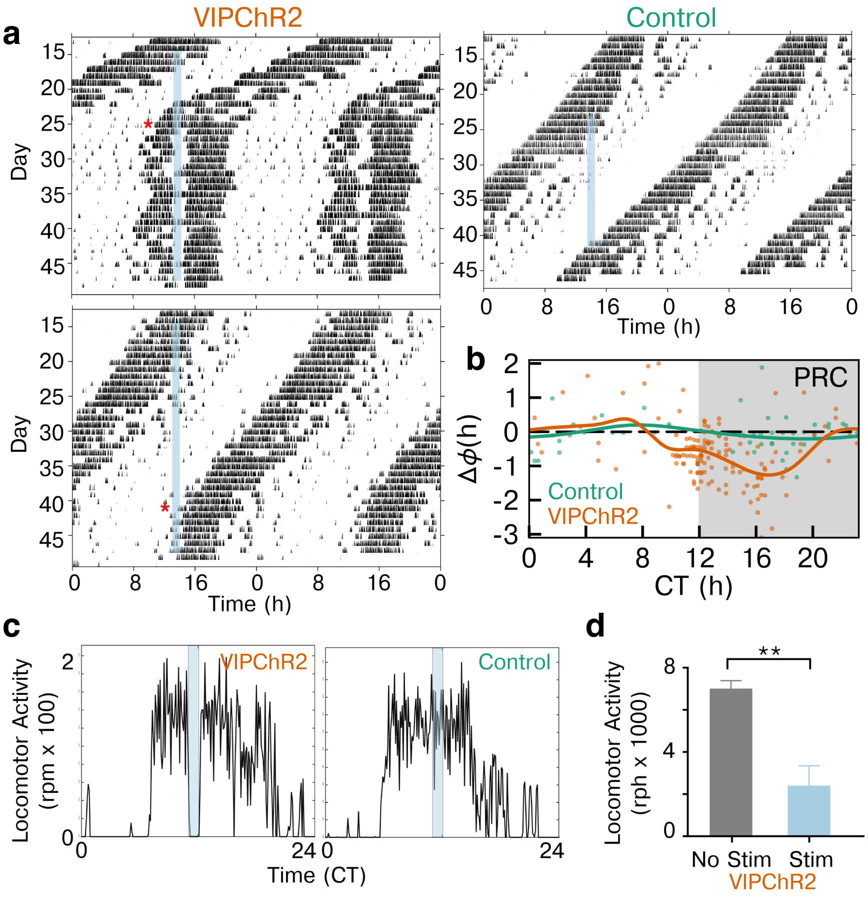

Figure 4.11: Optogenetic stimulation of only VIP neurons *in vivo* entrains locomotor activity. (**a**) Daily locomotor activity of two representative mice entrained to HIF stimulation of SCN VIP neurons (blue bar) compared to a control mouse lacking ChR2. Actograms show wheel revolutions per 6 min (black bars) recorded from enucleated mice for almost 50 days. Note that the two VIPChR2 mice, with slightly different periods, reached stable entrainment (*) only when the stimulation occurred around early subjective night. (**b**) Average phase response curves for HIF and LIF stimulation of VIPChR2 (orange, $n = 7$) and control mice (green, $n = 4$) show the change in phase (dots) on the day after stimulation at different circadian times. Note that activation of VIP neurons entrained daily locomotor rhythms through phase delays when delivered during the late subjective day and early subjective night. (**c**) Representative activity profiles of 2 mice show that HIF stimulation of VIP neurons acutely reduced running wheel activity in VIPChR2 (left), but not control (right), mice. (**d**) Wheel revolutions during optogenetic stimulation (CT 12-18, 1 h of HIF) decreased nearly four-fold compared to baseline in VIPChR2 mice (2355.0 ± 981.1 during stimulation vs. 6958.0 ± 418.9 with no stimulation, $n = 6$ mice, paired Student's t-test $^{**}P < 0.01$).

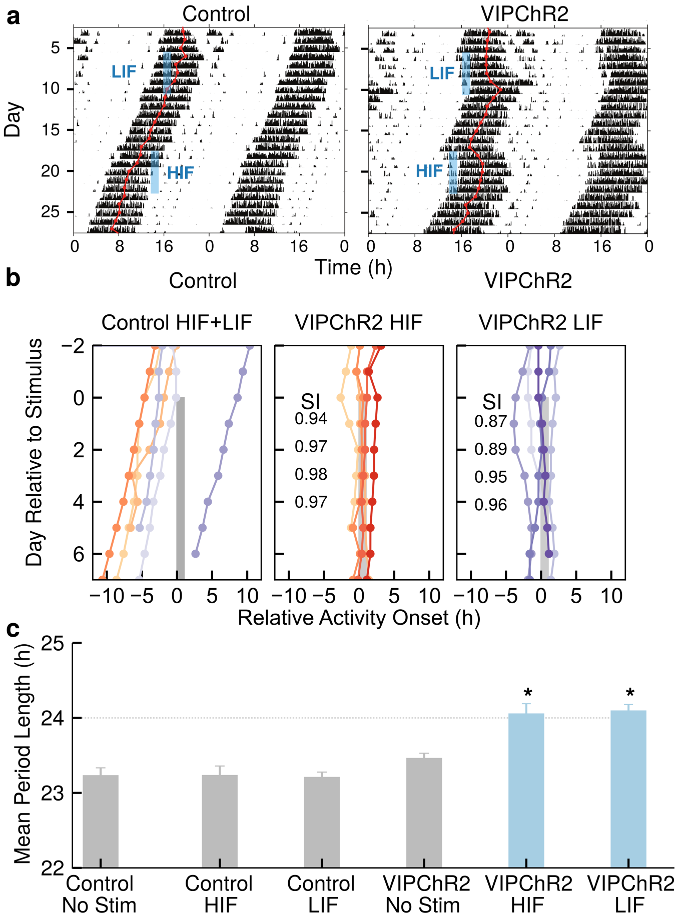

Figure 4.12: Instantaneous firing pattern affects locomotor rhythm entrainment. (**a**) Representative actograms show how daily optogenetic stimulation with HIF or LIF (blue bar) differentially entrained VIPChR2, but not control, mice. The daily acrophase (red circles and lines) of control mice in constant darkness free-ran through the days of stimulation. In contrast, daily HIF stimulation produced a large delay and rapidly entrained locomotor rhythms. Daily LIF stimulation, though having smaller effects on phase, also entrained activity. (**b**) Daily stimulation entrained daily activity onsets to within 2 h of the stimulation in both HIF and LIF but not in control mice. HIF stimulation immediately resulted in tight clustering fo activity onsets, as shown by the higher synchrony index (SI), while LIF stimulation more gradually entrained to the stimulation, as seen by the gradually increasing SI. (**c**) Daily HIF or LIF stimulation shifted the period of locomotor rhythms to 24 h in VIPChR2, but not control, mice (one-way ANOVA with posthoc Tukey HSD *$P < 0.05$). Note that VIPChR2 mice displayed a period identical to controls while stimulation was off, indicating that it was activation of VIP neurons causing a 24 h period rather than simply the genotype.

4.4 Discussion

In this chapter we sought to relate electrophysiological properties of a distinct subset of SCN neurons with their previously-known neurotransmitter content and role in SCN synchrony and entrainment. Most intriguingly, we found that there are further subclasses of neurons within the subset of SCN neurons that express VIP, as identified by spontaneous firing patterns. The persistent and heterogeneous firing patterns within this subpopulation suggests multiple specific roles for these firing patterns in SCN function. Other studies have presented some evidence for multiple subpopulations of VIP-expressing SCN neurons that arise at different times in development [220], however it is unknown if these developmental subpopulations correspond to the electrophysiological subpopulations we have identified. It is possible that these patterns are reflective of differing connectivity, such as receiving retinal input or projecting within or outside of the SCN to establish synchrony or entrainment. Further study is needed to characterize the projections from VIP SCN neurons, and determine how this might be correlated with firing pattern and thus neuropeptide release.

The phase responses we observed following stimulation of VIP neurons only partially recaptures the phase responses observed during whole-SCN optogenetic stimulation [234]. This is unsurprising, as there are numerous pathways of neurotransmission in the SCN, and the phase response curves calculated by Jones *et al.* are likely the dynamic response to the simultaneous activation of many pathways. Because approximately half of nonVIP neurons we tracked were found to also have circadian rhythms in electrical activity, it remains an open question as to which neurotransmitters are released at which phases in the course of a normal day of circadian oscillation *in vivo*, and what their effects might be. Based on our observation that VIP stimulation evoked only phase delays, we speculate that each subpopulation of SCN neurons may play differing roles in maintaining the stability of phase relationships and entrainment in the SCN. Further evidence for this idea has recently been presented by studies of AVP-expressing neurons of the SCN [232]. Though the numerous pathways present in the SCN at first may seem divergent in roles and thus imposing to characterize, there is some hope that they ultimately may be understood by their effect on phosphorylational states of clock products and clock inputs such as CREB [80, 217, 233, 238, 239, 254].

Interestingly, stimulation of VIP neurons also resulted in acute cessation of locomotor activity. This is consistent with a previous study showing that SCN electrical activity was correlated with locomotor inactivity [255]. There, the authors suggested that it was activity that suppressed SCN firing and thus activity could be considered an input into the clock. Here, we found a causal relationship in the opposite direction: stimulation of the SCN resulted in suppression of activity, rather than activity resulting in the suppression of SCN firing. Furthermore, how VIP neurons connect to behavioral circuits remains unknown.

We also found that the instantaneous firing frequency affects the phase shifts caused by VIP neurons. Importantly, quantification of the actual release of VIP within the SCN in response to stimulation at different frequencies remains a significant experimental challenge. Prior studies studies have shown that neuropeptide release can be caused by increases in either cytosolic Ca^{2+} as well as local Ca^{2+} influx in microdomains of the synaptic terminal [240]. Thus, it is possible that instantaneous frequency affects the total local or cytosolic Ca^{2+} concentration, and thus the amount of VIP released. A potential approach to address this question is through the use of a VIP-sensing fluorescent reporter (VIP-SnFR) as has been done previously for glutamate [256]. Another potential approach is to perform two-cell patch clamping with Ca^{2+} imaging to quantify differences in vesicle release caused by the differing Ca^{2+} transients resulting from stimulation patterns. Because vesicle release is a highly nonlinear function of local or cytosolic Ca^{2+} concentration, quantification of the neuropeptide release itself may be necessary, rather than simply recording calcium currents. Ultimately, this further study is necessary to identify how exactly the observed frequency-dependence of phase shifting is achieved.

An additional unanswered question involves identification of the mechanisms driving the daily variation in firing pattern, especially the silencing of circadian SCN neurons at night. VIP acts primarily though the Gq (or possibly Gs) GPCR [257], which drives excitatory responses and neuronal firing. The Gi GPCR, on the other hand, is involved in inhibitory signaling and nighttime silencing of SCN firing [80]. Importantly, inhibition of the Gi pathway results in desynchrony, possibly due to the lack of silencing at night and therefore arrhythmic release of VIP and other neurotransmitters. An interesting approach to characterizing the effects of inhibitory neurotransmission might involve anionic optogenetic techniques that result in inhibition rather than excitation [258]. This points further to the intricate balance of excitation and inhibition necessary for SCN function and the normal Ca^{2+} rhythms and release of neurotransmitters [135, 259]. Thus, the interaction of metabotropic receptors, their agonists, and the downstream interaction with the core circadian TTFL should continue to be a fruitful field of study in circadian function. To that end, I pose specific questions regarding the organization of the SCN, and potential directions for answering these, in the following chapter.

Chapter 5

Summary and future directions: proposed study of the suprachiasmatic nucleus

The prior three chapters discussed new results in understanding the network structure of the SCN, the development of the SCN, and how electrical signals transmitted within the SCN function to set the circadian clock. These results have generally shown that the SCN is highly heterogeneous and integrates numerous signaling pathways into its function. Although many researchers have discovered much about the structure and function of the SCN over the past decade, many fundamental questions remain, especially in quantitatively linking our understanding of the SCN across timescales. In this chapter, I present two potential avenues for further study of the SCN and its properties.

5.1 Role of dimerization in circadian rhythm stability

Dimerization is a common motif in circadian oscillation, and heterodimeric transcription factors have been identified in many species including the mouse [46], *Drosophila* [39], and *Arabidopsis* [30]. Why might this be? One possible reason is that dimerization may provide a means of resistance to stochastic fluctuations in molecular species count, and thus increases circadian precision. Dimerizaton reactions are fast relative to transcription, and are reversible, and so the dimerization reaction could function as a buffer against large-amplitude but ultradian (i.e. shorter than 24 h timescale) fluctuations in individual clock products. A conceptually-similar structure for stabilizing ATP availability has recently been studied using a controls approach [260], which could provide a blueprint by which to approach this question. Although, as stated in [260], the fast kinetics of the buffering (here, dimerization) can lead to high-frequency noise, this noise would likely be rapidly damped out by the subsequent low-pass filtering of downstream metabolic pathways or the slow transcriptional dynamics.

Although the approach of [260] would be of use here, the mathematical techniques rely on a linearization about a stable fixed point. This would be a shaky assumption for the circadian oscillator, as the durations of stochastic fluctuations are not necessarily much shorter than circadian oscillation. Thus, a potentially useful tool in approaching this question would be the ability to isolate a single reaction or pathway within a model to determine how its structure affects the precision of an emergent property of the system, such as oscillatory period. This is particularly challenging for complex stochastic systems, as nonlinear interactions between system components invalidates some assumptions commonly used in sensitivity analysis of stochastic systems. The isolation of this pathway could be achieved by incorporating a single stochastic reaction pathway in an otherwise deterministic model. The prospect of building such a hybrid stochastic-deterministic solver has been discussed with Professor Brian Drawert (UNC Asheville, formerly postdoctoral researcher at UC Santa Barbara) and is currently under construction as part of the GillesPy2 software package for stochastic simulation, an updated version of the package we have previously released [154]. Using this hybrid solver, one could feasibly compare the oscillatory precision of an oscillator with only a single stochastic reaction pathway. For example, a circadian model could include only stoachastic translation and dimerization, with all other reactions deterministic, in order to directly attribute the resulting precision to the structure of that single pathway. In this manner, the precision could be compared between monomeric, homodimeric, or heterodimeric methods of transcriptional repression. By keeping the total species counts constant between monomeric, homodimeric, and heterodimeric structures, one could directly test if heterodimerization provides benefits in oscillatory precision in comparison to alternate reaction structures while maintaining identical cellular energy consumption for transcription and translation.

By a combination of these techniques, we may then determine if dimerization is able to buffer against stochastic fluctuations in molecule count. While a positive result would not prove conclusively that this is the impetus for this convergent motif in circadian oscillation, it might provide an additional tool in the design of precise synthetic biological oscillators [261].

5.2 Quantification of neurotransmitter release and dynamics in the suprachiasmatic nucleus

As mentioned in the prior chapter, despite the well-known role of VIP in circadian oscillation, there is relatively little known about the numerous other pathways of neurotransmission that contribute to the circadian oscillations of the SCN. There is ample opportunity to quantify neurotransmission by standard neurobiological techniques for relating electrical activity with neurotransmitter release, and ultimately with phase shifting and entrainment in the clock. These results could be then related by modeling approaches to better understand circadian function. I believe this work is ultimately necessary for understanding population dynamics of the SCN, as there is currently a plethora of fundamental unanswered questions regarding SCN intercellular communication. Here, I will attempt to present an approach for addressing some of these questions with experiments and modeling.

Experimental approach

A thorough experimental approach would possibly involve dual whole-cell patch clamp recordings of neuronal membrane potential within an SCN culture, similar to approaches in [249]. Notably, Fan *et al.* found that VIP and AVP neuronal populations project similarly within the SCN, indicating that there may be a general rule for how circadian neurotransmission networks are structured. Techniques such as the optical tagging used in the previous chapter could be used to identify the neurotransmitter content of the presynaptic cell, and the patch clamp could then be used to observe the postsynaptic electrophysiological response to presynaptic action potentials and neurotransmitter release. This would further differentiate between neurotransmitters that elicit primarily ionotropic responses (neurotransmitter release and uptake that directly results in cellular depolarization) or primarily metabotropic responses (that which indirectly changes membrane excitability through metabolic intermediates). It is highly likely that ionotropic and metabotropic signaling work in concert to drive circadian synchrony, though the exact relationship between these systems is uncharacterized. Unfortunately, these experiments are extremely time consuming, especially due to the wide variety of neurotransmitters in the SCN, and the likelihood of corelease clouding the effect of signaling between individual cells [233].

An alternate approach might involve more thoroughly analyzing electrical activity in SCN cultures using calcuim fluorescence to track subthreshold electrical activity. It would be ideal in this case to analyze shorter (1-2h) recordings that are not limited to spiking alone, to correlate subthreshold excitatory or inhibitory postsynaptic potentials (EPSPs or IPSPs) with presynaptic neuronal firing events. This approach would still require identification of the neurotransmitter content of each neuron by optical tagging, or more simply applying a potent mix of antagonists for each undesired receptor. Furthermore, ionotropic and metabotropic postsynaptic responses could be differentiated by observing the timescale at which each occurs: ionotropic signaling lasts approximately 10-20 ms following a presynaptic action potential, whereas metabotropic signals last for in excess of 100 ms [201]. Subthreshold recording of simultaneous electrical activity from numerous cells via fluorescent calcium reporters is still in a nascent stage [262], but has strong potential for improving understanding of the SCN.

Ionotropic neurotransmission may modify instantaneous neurotransmitter release, but direct modulation of transcriptional activity or phosphorylational states of clock products is governed by the downstream mediators of metabotropic pathways. Only metabotropic pathways directly affect the circadian clock. It is important to identify the specific GPCR pathways that mediate response to each neurotransmitter, because each involves differing response dynamics, effectors, secondary messengers, and mediators. GPCR pathways can be differentiated by already-established techniques in neurobiology (e.g. inhibition of specific GPCRs such as G_i inhibition by pertussis [80]; or blockade of downstream effectors such as adenylyl cyclase and phosholipase C [253]). The diversity of pathways by which GPCRs affect cellular metabolism might immediately suggest that these pathways are therefore divergent. However, GPCR signaling is thought to be generally convergent [201], and signals to the clock likely converge in phosphorylation or dephosphorylation of clock transcription factors such as CREB, or clock products themselves. These phosphorylation responses can be studied directly, or inferred from previously-collected data about the downstream paths of metabotropic signaling specific to the SCN or the hypothalamus in general. Most encouragingly, some of these data have already been collected. Prior studies have identified adenylyl cyclase and phospholipase C as the primary effectors of VIP, though, confusingly, these are generally thought to be part of the independent G_s and G_q pathways [201, 253]. However, both pathways result in downstream phosphorylation, closing of voltage-gated potassium channels, and ultimately excitation of the cellular membrane. In a similarly confusing fashion, the neurotransmitter GABA is thought to have both excitatory and inhibitory effects in the SCN, depending on local chloride concentration [84]. Clearly, further study is needed here to more exactly resolve the roles of these pathways, despite their being the most thoroughly studied paths of neurotransmission in the SCN.

Finally, the timing of the neurotransmitter release will play an important role in phase shifting and entrainment. Therefore, it is important to study the excitatory and inhibitory signals that result in the persistent electrical activity of the circadian day in SCN neurons, and silencing during circadian night. Nighttime silencing is likely mediated by metabotropic pathways and the circadian clock itself, since the timescale of ionotropic signalling is very short. These experiments would be best approached hand-in-hand with modeling of the signal transmission pathways.

Modeling approach

While the suggested experimental work is technically simple but time-consuming, a particular challenge will be in quantifying the relationships between neurotransmission pathways, and thus being able to use these to better understand the overall population dynamics of the SCN. For example, while it is feasible to identify the pathway by which each neurotransmitter acts, it is infeasible to do so at every circadian phase or under every condition of transmitter co-release. Here, computational approaches may be of use. One further computational challenge will be in relating circadian dynamics (i.e. dynamics at at 24 h timescale) with electrical dynamics, which have millisecond resolution. The challenge of computational power could be resolved simply by finding the power to perform such extreme simulations. This approach has recently yielded some results in linking the circadian and electrical timescales [84]. Clever uses of modeling and system identification tools could also greatly simplify this problem.

In general, the transient change to neuronal internal state resulting from a single action potential decays rapidly and returns to baseline in less than 1 s. Transcription would therefore function as a low-pass filter mediating this process, and only sustained firing (and thus sustained neurotransmission) has the potential to appreciably phase shift the circadian clock. Intuitively, a potential simplification to the simultaneous modeling of these pathways could be achieved, then, by searching for timescale separations between processes and performing frequency domain analysis on neurotransmission pathways to determine their effects on clock gene transcription. To perform this analysis, one must linearize about a steady or pseudo-steady state, which is generally a poor assumption due to the oscillatory nature of the clock. However, it could be possible instead to perform multiple linearizations corresponding to different circadian phases, and thus identify a range of dynamic responses to input stimuli. The results of this analysis will then dictate the level of modeling detail needed to accurately capture intercellular communication dynamics. Importantly, this would allow the use of a slow dynamic state corresponding to general cellular firing rate in models of circadian dynamics, rather than modeling each individual spike, as has been previously done. Modeling each spike is particularly onerous due to the extreme stiffness of models such as Hodgkin-Huxley.

A path to control the SCN

The proposed modeling approaches of the prior section may also yield advances toward control of circadian rhythms. From an engineering and medical perspective, GPCRs in particular provide enticing targets for pharmaceutical intervention, due to their high selectivity for their agonists, and the ability to target GPCRs expressed by small subclasses of neurons [263, 264]. In a conceptually similar fashion, VIP application (targeting the VPAC2R VIP receptor) has been used to speed entrainment *in vivo* following shifts in environmental phase [134]. The further elucidation of the roles of these pathways will likely enable the precise targeting of new pharmaceutical inputs to the core circadian clock. An open theoretical question, then, is how best to dose these drugs to achieve the desired dynamic response, as we have seen that stimulation of VIP neurons results in drastically different effects at different times of day. Control theory provides a mathematical framework for broadly approaching this question. In Section II, I begin to approach this question by formulating phase control of the circadian clock as an optimal control problem.

Part II

Control of the Mammalian Circadian Oscillator

Chapter 6

Pharmaceutical-based entrainment of circadian phase via nonlinear model predictive control

6.1 Introduction

Since environmental signals (such as ambient light) set the time of this biological clock, mistimed environmental cues may result in adverse changes to these rhythms, and consequently, a loss of temporal regulation of the genetic architecture, and psychological and physiological pathologies [265]. In recent years, small-molecule pharmaceuticals have gained significant interest as a path toward modulating the circadian clock to reduce the effects of circadian disturbances [19, 132]. Small-molecule pharmaceuticals present critical benefits over the use of light for clock resetting including avoiding the daytime "dead-zone" where light evokes a minimal phase response, and reducing the impractical and burdensome challenge of attempting to tightly control one's light environment. For example, light-based regulation would necessitate sustained periods of time wearing low-transmission glasses or light visors [28]. Most importantly, light dosing strategies typically take several days to reset circadian rhythms: hence the prevalence of sustained jet lag following long trips across time zones. Even state-of-the-art optimal control policies involving light necessitate as much as eight days to complete a phase resetting when allowing for regular sleep [266].

Pharmaceuticals are expected to enable direct manipulation of sensitive control targets within

---

Major portions of this chapter will appear in a journal article, currently submitted for peer review as J.H. Abel, A. Chakrabarty, and F.J. Doyle III, "Pharmaceutical-based entrainment of circadian phase via nonlinear model predictive control."

the clock, allowing more rapid clock resetting [27]. The complex nature of the circadian oscillator necessitates a control approach toward dosing strategies for these drugs, as identical stimuli applied at different times of the day may have drastically disparate effects on the clock. Modeling approaches such as those described in [133] have been employed to identify the underlying mechanistic action of these drugs. Such models may, in turn, be used to inform advanced model-based control strategies such as model predictive control (MPC) for circadian regulation.

Prior studies employing models of circadian dynamics have independently investigated optimal control-based approaches for manipulating the circadian clock. For example, nonlinear MPC and multi-target MPC for light-resetting a *Drosophila* circadian clock model was demonstrated in [27, 127], and complementary phase response curves (PRCs) were leveraged to identify potential control targets. Other studies using nonlinear *Drosophila* clock models [267, 268] proposed more efficient procedures to obtain light-based optimal control trajectories by relaxing the nonlinear control problem into a mixed-integer formulation. Recent work has extended the concept of using light-based feedback control to investigate re-entrainment of clocks in humans. Attempts have been made to pose this complex problem as a scheduling problem to obtain the best bang-off-bang strategy [28] for light inputs. Recently, the authors in [29] used lower harmonics to formulate an approximate model of the circadian oscillations in humans, and exploited the structure of the co-state equation to propose an efficient line-search algorithm to obtain optimal control sequences. Although these methods are elegant and have been demonstrated to be effective through numerous simulation studies, a significant drawback of optimal control approaches is that they are rarely immune to measurement inaccuracies, exogenous noise, or plant-model mismatch. Furthermore, without model approximation, deriving optimal control sequences remains computationally prohibitive, if not intractable, for complex high-dimensional nonlinear models [268].

The use of feedback in circadian entrainment remains a relatively unexplored problem. A notable exception is [128], where the authors developed a framework for control of circadian rhythms using short-duration pulses to shift the phase, via proportional-integral-derivative (PID) control by exploiting a low-dimensional approximate predictive model of the phase dynamics, known as a *phase response curve* (PRC). This low-dimensional representation of pertinent phase information and the predictive power of a PRC enables the construction of MPC algorithms that are well-known to be inherently robust to noise/plant-model mismatch. A pair prominent recent study derived a feedback control law for circadian entrainment using lookup tables from the optimal control [269]. This study focused on a light input which may be switched on and off at will, and although highly effective for light, thus pharmaceutical delivery under this policy would incur errors. More importantly, the main result proven in this chapter bounds the nearness of their feedback control approach to their optimal control law. Previously, we performed preliminary investigations of MPC in circadian control with pharmaceuticals [270, 271], which demonstrated MPC of mammalian circadian rhythms via KL001, a small-molecule pharmaceutical that was recently used to manipulate (*in vitro*) the circadian clock in mammals [19, 132]. Although our previous investigations have revealed the importance of carefully selecting prediction horizon and controller sampling time of the MPC to reset the circadian oscillator, no systematic method of selecting these design variables has been derived.

This chapter seeks to answer three fundamental questions:

1. What does the optimal control policy for pharmaceutical-driven circadian phase resetting look like?
2. What design considerations should be made in implementing feedback control of circadian phase? More specifically, how does the selection of sampling or switching times and the prediction horizon affect the optimality of the applied control?
3. How can these design considerations shape our selection of circadian therapeutics?

In answering these questions, this chapter presents a systematic framework for constructing PRC-based nonlinear MPC formalisms capable of manipulating mammalian clocks using small-molecule pharmaceuticals.

6.2 Phase-reduced model and optimal phase shifting

Here, we reintroduce some formalisms developed in Chapter 1 for their application to the phase control problem.

Circadian oscillator model

Circadian dynamics are most commonly represented by limit-cycle oscillators. These oscillators are generally modeled using a class of smooth nonlinear dynamical systems of the form

$$\frac{dx}{dt} = f(x, p, u), \tag{6.1}$$

where $x(t) \in \mathbb{R}^n$ denote states such as mRNA or protein concentrations, $p \in \mathbb{R}^m$ denote kinetic parameters, and $u(t) \in \mathbb{R}^l$ denote control inputs. The zero-input system $\dot{x} = f(x, p, 0)$ comprises an exponentially-attractive limit cycle $\Gamma \subset \mathbb{R}^n$ that satisfies

$$\lim_{t \to \infty} [x(t) - x(t - T)] = 0, \tag{6.2}$$

with period T and radial frequency $\omega = 2\pi/T$. A two-dimensional limit cycle with states $x = [x_1, x_2]$ is visualized in Fig. 6.1A.

This chapter is concerned with dynamics of the phase of oscillation, and so we first map every unique point on the limit cycle $x_0 \in \Gamma$ to a unique scalar phase $\phi_0 \in \mathbb{S}^1 = [0, 2\pi)$. Let $\Phi : \Gamma \to \mathbb{S}^1$ denote the corresponding map relating x_0 to oscillator phase $\phi_0 = \Phi(x_0)$.

Let $\gamma(t, x_0)$ denote the solution of system (6.1) with initial condition $x(0) = x_0 \in \Gamma$. Thus a time-dependent phase variable

$$\phi(t) = \Phi[\gamma(t, x_0)] \tag{6.3}$$

may be established. Considering that the unperturbed oscillator traverses the limit cycle at the constant rate ω, the system phase evolves in time according to:

$$\phi(t) = \omega\, t + \phi_0 \mod 2\pi. \tag{6.4}$$

The application of an exogenous input (such as a control action) will divert the state of an oscillatory system away from the limit cycle Γ. In order to ascertain the phase shift incurred by such an input, we must assign a phase to points that are not on the limit cycle Γ, but that are exponentially attracted to Γ. This can be done by assigning them the phase of the trajectory to which they ultimately converge. The trajectory denoted $\theta(t, x_a, u)$ is the time evolution of point

$x_a \notin \Gamma$, with dynamics given by (6.1) and control input u. For the zero-input case ($u = 0$), the state x_a may be assigned the phase of the initial condition of the trajectory $\gamma(t, x_0)$ to which the trajectory $\theta(t, x_a, 0)$ ultimately converges. The asymptotic phase of x_a, denoted ϕ_a, is equal to the phase ϕ_0 of point $x_0 \in \Gamma$, subject to

$$0 = \lim_{t \to \infty} ||\theta(t, x_a, 0) - \gamma(t, x_0)||. \tag{6.5}$$

This relationship yields the asymptotic phase map $\phi_a = \Phi(x_a)$. The asymptotic phase map may be used to formulate a time-dependent asymptotic phase variable for the zero-input case

$$\varphi(t, 0) = \Phi[\theta(t, x_a, 0)] \tag{6.6}$$

for the zero-input case. The trajectories γ and θ with identical phase, and their asymptotic convergence, are shown schematically in Fig. 6.1B.

This formulation yields phase dynamics identical to the case for ϕ, with particular solutions of the form $\varphi(t, 0) = \omega\, t + \phi_0$ with initial phase ϕ_0. The following subsection described how the concept of an asymptotic phase variable can be extended for the more challenging and useful case of non-zero control input u.

Infinitesimal parametric phase response curves and the phase-reduced model

For an oscillator in the neighborhood of Γ, the phase dynamics resulting from a control input may be derived by the chain rule:

$$\frac{d\varphi(t,u)}{dt} = \omega + \frac{\partial}{\partial t}\frac{\partial \Phi[\gamma(t, x_0)]}{\partial u} u(t) \tag{6.7}$$

which yields a first-order approximation of phase dynamics for a nonzero control input.

Pharmaceutical manipulations of the clock are generally considered to be mediated by temporary changes in one or more parameter values (e.g. increased degradation of a protein, or decreased transcriptional rate) [19, 272]. Input $u(t)$ is incorporated into the ODE model as a time-dependent modification of parameters p

$$p(t) = p_0 + u(t). \tag{6.8}$$

Substituting this into (6.7) yields

$$\frac{d\varphi}{dt} = \omega + \frac{\partial}{\partial t}\frac{\partial \Phi[\gamma(t, x_0)]}{\partial p} u(t), \tag{6.9}$$

where $\frac{\partial}{\partial t}\frac{\partial \Phi[\gamma]}{\partial p}$ is the infinitesimal parametric PRC (ipPRC) for the oscillator on the limit cycle [22]. The formulation (6.9) is valid up to the first-order approximation in both duration and magnitude of the control, and is referred to as the *phase-reduced model*. The one-dimensional phase equation is therefore given by:

$$\frac{d\varphi}{dt} = \omega + B(t, \varphi) \cdot u(t), \tag{6.10}$$

where $B(t, \varphi)$ is the ipPRC and $u(t)$ is the parametric perturbation.

Assumption 1. *The ipPRC $B(\cdot)$ is fully known and dependent only on the asymptotic phase $\varphi(t)$.*

The ipPRC can be calculated numerically from mechanistic models of the clock for a known control input as above, or alternately could be characterized experimentally [22, 273]. A prior method of formulating asymptotic phase dynamics assumed short pulses of control inputs that relax completely to the limit cycle after each pulse [128], and thus the phase sensitivity on the limit cycle may be used. Assumption 1, rather, implies that the phase response dynamics are constant along isochrons (state-space regions of constant phase). This assumption is violated as the oscillator becomes more distant from its limit cycle, or closer to the fixed point at the center of the limit cycle. Identifying violations of this assumption may be studied in the future, and in these cases, the model should be simulated in full. This assumption has been used in prior studies as well [266, 269]. Our assumption yields a few practical advantages when implementing pharmaceutical inputs. Short pulses are less able to evoke significant phase shifts, as the realized phase shift is determined by integration of the ipPRC. Thus, the ipPRC must be of extreme magnitude to yield appreciable shifts for short pulses. Pharmaceutical inputs to the clock are not likely to have the extremely rapid pharmacokinetics needed to be approximated as short pulses.

Assumption 2. *The ipPRC map is continuous on* $[0, 2\pi]$ *and has exactly two zero crosses in that interval; the derivatives of the ipPRC at the zero crosses have opposite sign.*

This PRC form is readily found in the literature, and for stimuli of a finite duration is commonly referred to as a type 1 phase response [273, 274]. Methods for calculation of the ipPRC using limit-cycle oscillator models are described elsewhere [22]. The other phase response observed (solely) for finite-duration stimuli, a type 0 phase response, contains a discontinuity. This form is associated with strong and extended stimulus or multiple stimuli over several days, and therefore does not correspond to the ipPRC [11, 273, 274]. Furthermore, a type 0 phase response may be generated from an ipPRC that conforms to Assumption 2 by applying a long-duration stimulus.

The phase resetting problem and optimal phase resetting via Pontryagin's maximum principle

The phase-resetting problem involves tracking a reference oscillator with phase given by $\varphi_r(t) \in [0, 2\pi)$, with the oscillator $\varphi(t, u)$ which obeys (6.10), and with control input bounded by $u \in [u_{\min}, u_{\max}]$. The phase of the reference oscillator is given by:

$$\varphi_r(t) = \omega_r \, t + \varphi_r(0) \mod 2\pi.$$

Assumption 3. *The reference angular velocity is identical to the angular velocity of the oscillator, that is,* $\omega \equiv \omega_r$*.*

Assumption 4. *The oscillator is not perturbed by exogenous inputs other than control actions.*

Through these assumptions we seek to achieve a phase shifts rather than entrain to a dynamic phase angle or an environment that also phase shifts oscillation. The more complicated case, in which small differences in the human circadian period (see [275]) and dynamic light input are accounted for, may be approached by future studies. This simple case of achieving a static phase shift more simply yields optimal control policies that are sufficient to provide understanding for feedback controller design.

The phase difference between the reference oscillator and the oscillator under control is:

$$\chi(t) = \varphi(t) - \varphi_r(t) \mod 2\pi.$$

The total desired phase shift is such that $\chi(t_f) = 0$, and therefore

$$\Delta\phi_f = -\chi(0) \mod 2\pi.$$

In an ideal case where pharmaceutical inputs can be continuously dosed, one can derive an optimal control trajectory for entrainment via Pontryagin's Maximum/Minimum Principle [276]. The optimal control problem may be formulated with state dynamics

$$\begin{aligned} \dot{\varphi} &= \omega + B(\varphi) \cdot u(t) \\ \varphi(0) &= \phi_0, \end{aligned} \tag{6.11}$$

and cost functional

$$J[u(t)] = \int_0^{t_f} 1\,dt. \tag{6.12}$$

This yields a free-time fixed-endpoint problem, which can be solved using standard optimal control approaches [269, 276]. The Hamiltonian

$$H(\varphi, \lambda, u) = (\omega + B(\varphi) \cdot u) \cdot \lambda + 1 \tag{6.13}$$

is formulated with λ is the dynamic costate with terminal condition $\lambda(t_f) = 0$. Using Pontryagin's Maximum Principle with constrained control inputs in the range $[u_{\min}, u_{\max}]$ we can write

$$\begin{aligned} \max_u H(\varphi, \lambda, u) &= \max_{u_{\min} \le u \le u_{\max}} \{(\omega + B(\varphi) \cdot u) \cdot \lambda + 1\} \\ &= \omega \cdot \lambda + 1 + \max_{u_{\min} \le u \le u_{\max}} \{B(\varphi) \cdot u \cdot \lambda\} \end{aligned}$$

which yields the optimal "bang-bang" control policy

$$u^\star(t) = \begin{cases} u_{\max} & \text{if } B(\varphi) \cdot \lambda > 0 \\ u_{\min} & \text{if } B(\varphi) \cdot \lambda \leq 0 \end{cases}. \tag{6.14}$$

Here, the terminal condition of the costate, $\lambda(t_f) = 0$, forces the costate to be either positive or negative for any given initial condition for all time, and so for a specific initial condition the control input depends exclusively on the sign of $B(\varphi)$, c.f. [269].

This implies that the oscillator should be shifted in only either the negative or positive direction toward its final phase shift, but not both. For an oscillator with desired phase shift $\Delta\phi_f$ and initial phase ϕ_0, the optimal control input $u^\star$ is one of two admissible trajectories: either that for achieving the positive phase shift

$$u_+^\star(t) = \begin{cases} u_{\max} & \text{if } B(\varphi) > 0 \\ u_{\min} & \text{if } B(\varphi) \leq 0 \end{cases} \tag{6.15}$$

or the negative phase shift

$$u_-^\star(t) = \begin{cases} u_{\min} & \text{if } B(\varphi) \geq 0 \\ u_{\max} & \text{if } B(\varphi) < 0 \end{cases}. \tag{6.16}$$

Which of these two trajectories is optimal depends upon which reaches $\Delta\phi_f$ more rapidly, where $\Delta\phi$ accumulates according to

$$\Delta\phi = \int_0^t B(\varphi(t')) \cdot u(t') dt' \mod 2\pi. \tag{6.17}$$

A decision boundary between advances and delays is denoted $\Delta\phi_b$ (i.e., $\Delta\phi_f > \Delta\phi_b$ indicates that delays are preferable, and $\Delta\phi_f < \Delta\phi_b$ indicates that advances are preferable). Correspondingly, that boundary for the continuous time optimal control is denoted $\Delta\phi_b^\star$. Thus, the two admissible trajectories may be calculated and compared to determine optimality.

This concept is illustrated for small-molecule pharmaceutical KL001 input in Fig. 6.2 and Fig. 6.3. First, we selected the model from [19, 133] to capture circadian oscillator dynamics because it was created to identify the effect of the small-molecule KL001 on the mammalian oscillator. Model states and reactions are shown schematically in Fig. 6.2A, and the equations and parameters comprising this model are shown in Table 6.1. The control input was included as a reduction of parameter v_{dCn}, as identified in [133], leading to the ipPRC of Fig. 6.2B. Next, the optimal control law was applied in Fig. 6.3.

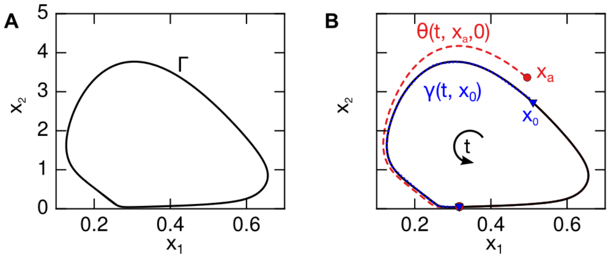

Figure 6.1: Schematic of limit cycle dynamics for arbitrary states x_1 and x_2. (**A**) The limit cycle Γ in state space. (**B**) Schematic of trajectories γ and θ. These points may be assigned identical phases ($\phi_a = \phi_0$), as the trajectories originating at these points converge asymptotically.

Table 6.1: Model equations and parameters for the core clock feedback loop from [101], continued on the following page.

State Variable	Symbol	Conservation Equation
Per mRNA	**p**	$\frac{d\mathbf{p}}{dt} = \frac{v_{\text{txn},\mathbf{p}}}{k_{\text{txn},\mathbf{p}}+(\mathbf{C1N}+\mathbf{C2N})^3} - \frac{v_{\text{deg},\mathbf{p}}\ \mathbf{p}}{k_{\text{deg},\mathbf{p}}+\mathbf{p}}$
Cry1 mRNA	**c1**	$\frac{d\mathbf{c1}}{dt} = \frac{v_{\text{txn},\mathbf{c1}}}{k_{\text{txn},\mathbf{c}}+(\mathbf{C1N}+\mathbf{C2N})^3} - \frac{v_{\text{deg},\mathbf{c1}}\ \mathbf{c1}}{k_{\text{deg},\mathbf{c}}+\mathbf{c1}}$
Cry2 mRNA	**c2**	$\frac{d\mathbf{c2}}{dt} = \frac{v_{\text{txn},\mathbf{c2}}}{k_{\text{txn},\mathbf{c}}+(\mathbf{C1N}+\mathbf{C2N})^3} - \frac{v_{\text{deg},\mathbf{c2}}\ \mathbf{c2}}{k_{\text{deg},\mathbf{c}}+\mathbf{c2}}$
Per Protein	**PER**	$\frac{d\mathbf{P}}{dt} = k_{\text{tln},\mathbf{p}}\ \mathbf{p} - \frac{v_{\text{deg},\mathbf{P}}\ \mathbf{P}}{k_{\text{deg},\mathbf{P}}+\mathbf{P}} - v_{\text{a},\mathbf{CP}}\ \mathbf{P\ C1} + v_{\text{d},\mathbf{CP}}\ \mathbf{C1N}$ $-v_{\text{a},\mathbf{CP}}\ \mathbf{P\ C2} + v_{\text{d},\mathbf{CP}}\ \mathbf{C2N}$
Cry1 Protein	**C1**	$\frac{d\mathbf{C1}}{dt} = \mathbf{c1} - \frac{v_{\text{deg},\mathbf{C1}}\ \mathbf{C1}}{k_{\text{deg},\mathbf{C}}+\mathbf{C1}} - v_{\text{a},\mathbf{CP}}\ \mathbf{P\ C1} + v_{\text{d},\mathbf{CP}}\ \mathbf{C1N}$
Cry2 Protein	**C2**	$\frac{d\mathbf{C2}}{dt} = \mathbf{c2} - \frac{(v_{\text{deg},\mathbf{C2}} - u(t))\ \mathbf{C2}}{k_{\text{deg},\mathbf{C}}+\mathbf{C2}} - v_{\text{a},\mathbf{CP}}\ \mathbf{P\ C2} + v_{\text{d},\mathbf{CP}}\ \mathbf{C2N}$
CRY1-PER Dimer	**C1N**	$\frac{d\mathbf{C1N}}{dt} = -\frac{(v_{\text{dCn}-u(t))}\ \mathbf{C1N}}{k_{\text{deg},\mathbf{CP}}+\mathbf{C1N}+\mathbf{C2N}} + v_{\text{a},\mathbf{CP}}\ \mathbf{P\ C1} - v_{\text{d},\mathbf{CP}}\ \mathbf{C1N}$
CRY2-PER Dimer	**C2N**	$\frac{d\mathbf{C2N}}{dt} = -\frac{(v_{\text{dCn}}\ m_{\mathbf{C2N}})\ \mathbf{C2N}}{k_{\text{deg},\mathbf{CP}}+\mathbf{C2N}+\mathbf{C1N}} + v_{\text{a},\mathbf{CP}}\ \mathbf{P\ C2} - v_{\text{d},\mathbf{CP}}\ \mathbf{C2N}$

Table 6.1: (Continued.)

	Parameter	Description	Value
1	$v_{\mathrm{txn},\mathbf{p}}$	*Per* Transcription rate	0.195
2	$v_{\mathrm{txn},\mathbf{c1}}$	*Cry1* Transcription rate	0.131
3	$v_{\mathrm{txn},\mathbf{c2}}$	*Cry1* Transcription rate	0.114
4	$k_{\mathrm{txn},\mathbf{p}}$	*Per* Repression constant	0.425
5	$k_{\mathrm{txn},\mathbf{c}}$	*Cry1/2* Repression constant	0.259
6	$v_{\mathrm{deg},\mathbf{p}}$	*Per* Max degradation rate	0.326
7	$v_{\mathrm{deg},\mathbf{c1}}$	*Cry1* Max degradation rate	0.676
8	$v_{\mathrm{deg},\mathbf{c2}}$	*Cry2* Max degradation rate	0.608
9	$k_{\mathrm{deg},\mathbf{p}}$	*Per* Degradation constant	0.011
10	$k_{\mathrm{deg},\mathbf{c}}$	*Cry1/2* Degradation constant	1.149
11	$v_{\mathrm{deg},\mathbf{P}}$	Max PERc degradation rate	2.970
12	$k_{\mathrm{deg},\mathbf{P}}$	PERc degradation constant	0.034
13	$v_{\mathrm{deg},\mathbf{C1}}$	Max CRY1c degradation rate	1.523
14	$v_{\mathrm{deg},\mathbf{C2}}$	Max CRY2c degradation rate	1.686
15	$k_{\mathrm{deg},\mathbf{C}}$	CRYc degradation constant	2.017
16	v_{dCn}	CRYn degradation rate	0.101
17	$m_{\mathbf{C2N}}$	CRY2n degradation multiplier	3.318
18	$k_{\mathrm{deg},\mathbf{CP}}$	CRYn degradation constant	0.053
19	$v_{\mathrm{a},\mathbf{CP}}$	CRYn association rate	0.041
20	$v_{\mathrm{d},\mathbf{CP}}$	CRYn dissociation rate	0.002
21	$k_{\mathrm{tln},\mathbf{p}}$	PER translation rate	3.000

We may visualize the two admissible trajectories as two oscillators $\varphi^{+}(t)$ and $\varphi^{-}(t)$ receiving control inputs $u^{\star}_{+}(t)$ and $u^{\star}_{-}(t)$, respectively, causing the accumulation of phase shifts $\Delta\phi^{+}(t)$ and $\Delta\phi^{-}(t)$ moving in opposite directions around the circle of all phase shifts $\Delta\phi \in [0, 2\pi)$ starting at $\Delta\phi = 0$. The time $t^{\star}_{b}$ at which these oscillators meet therefore achieves any phase shift on $[0, 2\pi)$. This time may be found for any initial phase $\varphi(0) = \phi_0$ by solving the coupled equations (6.10) and (6.17) for inputs $u^{\star}_{+}(t)$ and $u^{\star}_{-}(t)$, with the terminal condition of $\Delta\phi^{+}(t^{\star}) = \Delta\phi^{-}(t^{\star})$.

Thus, $\Delta\phi^{\star}_{b}(\phi_0)$ is defined as the phase shift at which $\varphi^{-}(t)$ and $\varphi^{+}(t)$ meet. The maximum time to achieve *any* phase shift starting from ϕ_0 is given by $t^{\star}_{b}(\phi_0)$, and $\Delta\phi^{\star}_{b}(\phi_0)$ (depicted as a solid black line in Fig. 6.3D) yields the boundary between where a positive shift and negative shift are optimal to reach a desired $\Delta\phi_f$ from phase ϕ_0. The optimal control input for a given ϕ_0

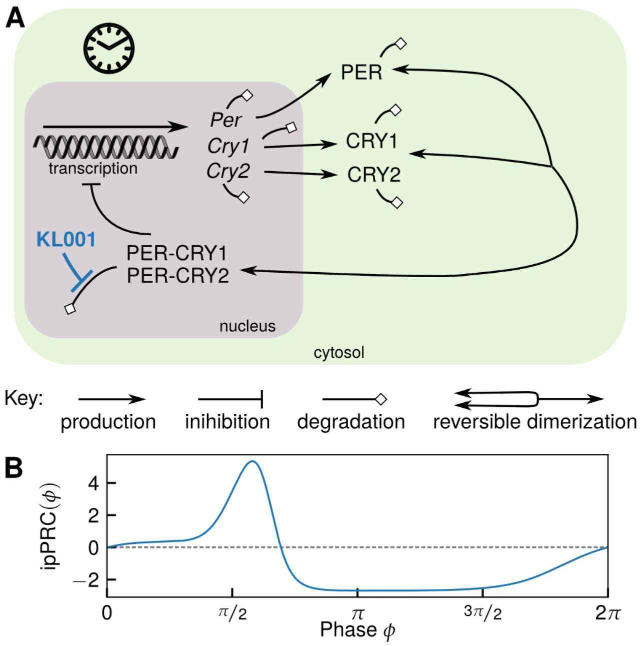

Figure 6.2: Schematic of the core circadian gene regulatory network and effect of small molecule KL001. (**A**) The core circadian negative feedback loop. KL001 stabilizes nuclear CRY by reducing its degradation rate, as shown in blue. All reactions in the figure are explicitly incorporated in the clock model used [101], and the full equations are provided in Table 6.1. (**B**) Infinitesimal parametric phase response curve (ipPRC) for KL001-mediated stabilization of nuclear CRYs as calculated from the model.

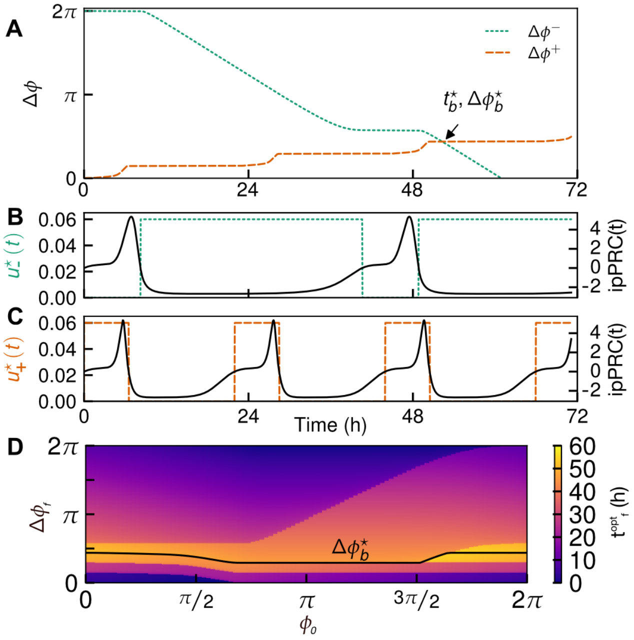

Figure 6.3: Optimal control of the circadian clock by use of the ipPRC shown in Fig. 6.2B. (**A**) Maximal phase advances $\Delta\phi^{\star}_{+}(t)$ and delays $\Delta\phi^{\star}_{-}(t)$ for the ipPRC, with $\phi_0 = 0$ and $u_{\max} = 0.06$, $u_{\min} = 0.00$. The respective maximal phase shifts meet at time $t^{\star}_{b}$ and phase shift $\Delta\phi^{\star}_{b}$ as marked on the graph. All phase shifts may be achieved in time less than or equal to $t^{\star}_{b}$. Note that $t_f^{\mathrm{opt}}(0, \Delta\phi_f)$ can be found on this plot by seeking the minimum time at which the oscillator crosses the desired $\Delta\phi_f$ (for example, $t_f^{\mathrm{opt}}(0, 3\pi/2) \approx 20$ h, and is achieved by a phase delay). (**B,C**) Plot of optimal inputs $u^{\star}_{-}(t)$ and $u^{\star}_{+}(t)$, respectively, for the phase delay and advance shown in A. (**D**) Heatmap of optimal time to reset the clock t_f^{opt} as a function of initial phase as desired shift. Note that $\Delta\phi^{\star}_{b}$, the boundary between advances and delays, is dependent on ϕ_0.

and $\Delta\phi_f$ is therefore defined as:

$$u^\star(t) = \begin{cases} u^\star_+(t) & \text{if } \Delta\phi_f < \Delta\phi^\star_b(\phi_0) \\ u^\star_-(t) & \text{if } \Delta\phi_f \geq \Delta\phi^\star_b(\phi_0) \end{cases}. \tag{6.18}$$

Therefore the optimal shift time $t_f^{\text{opt}}(\phi_0, \Delta\phi_f)$ may be calculated by applying this continuous time optimal control until $\Delta\phi = \Delta\phi_f$. One can formally write $t^\star_b$ as

$$t^\star_b(\phi_0) = \sup_{\Delta\phi_f} t_f^{\text{opt}}(\phi_0, \Delta\phi_f). \tag{6.19}$$

Remark. A bang-bang optimal control policy for light entrainment was shown previously in [28] and [29]. Applying these solutions, however, necessitated either a line search or a search for switching times due to the nonlinear temporal relationship between light input and driving force on the oscillator. Because pharmaceutical control of the clock can be parameterized directly within the limit cycle model, this formulation provides a simple way to compute the theoretical optimal phase resetting policy. Therefore, this provides a means for determining the relative efficacy of any applied control policy.

6.3 Closing the loop: designing a PRC-based nonlinear MPC

Motivation

Model predictive control is generally implemented by solving a finite-horizon optimal control problem at discrete sampling times, that is, for $t = 0, \tau, 2\tau, \cdots$ where τ is the sampling time. This section will demonstrate that time discretization causes a loss of optimal control in regions where the step includes a zero cross of the ipPRC, as the input cannot be adjusted during the step and the continuous-time optimal control policy will be violated (visualized in Fig. 6.4). Additionally, care must be taken to ensure that a controller selects the optimal direction of phase shifting (e.g., 8h advance vs. 16h delay) when only observing a finite portion of the future PRC. For the continuous time optimal control, that boundary is known to be $\Delta\phi^\star_b$, however, this is unlikely to be the correct boundary for the sampled-time case. Further, there is no guarantee that this boundary will appear from simply solving the finite-horizon optimal control.

This section explores how the formulation of the finite-horizon optimal control problem for MPC affects our ability to control the clock. For example, consider an ipPRC with a small positive lobe. A large sampling time in this case may result in a controller unable to access the positive ipPRC region due to the surrounding negative region being included in each step, and the inadvertent delays canceling the desired advance. This would force such a controller to use phase delays to achieve even small positive phase shifts.

It is therefore useful to compare the performance of a controller with piecewise constant control and uniformly spaced steps in sampling and switching time (the *sampling-time control*) to the continuous-time optimal control case to identify where inefficiency accumulates. This technique can be used to find a balance between high performance and the computational cost and physical impracticality of frequently updating the algorithm via measurement of physiological phase markers.

Additionally, the controller design will inform the suitability of a specific pharmaceutical for use. For example, a drug with a small positive ipPRC lobe will not be an appropriate choice for achieving large phase advances if an alternative drug with a larger positive ipPRC lobe exists. Alternately, the drug with the larger positive ipPRC lobe may be unsuitable if its pharmacokinetics are slow, such that sampling times must be very long to allow drug clearance between adjusting the dose.

Exploiting the ipPRC to choose MPC sampling time

Consider the more practical scenario of implementing control inputs parameterized as piecewise constant signals with equispaced time intervals between the knots of the control parameterization trajectory. This is commonly done when solving and applying MPC in continuous-time. The control input is defined as constant across time steps of uniform duration in a finite horizon, as commonly done for MPC:

$$u(t) = u_i \text{ for } t \in [t_{i-1}, t_i), \tag{6.20}$$

where t_i are the discrete sampling times, with $i = 1, \cdots, N_p$ where N_p is the number of steps in the prediction horizon (and control horizon, in this chapter). Then, $u_i \in [u_{\min}, u_{\max}]$ is a scalar constant, and $\tau = t_i - t_{i-1}$ is the sampling time for the controller.

The error incurred due to piecewise constant control actions at discrete sampling times is quantified via two metrics, the first of which is described in the following definition.

Definition 1. *The* ***residual phase error*** *(E_τ^ϕ) is the phase error remaining at sampling time t_k, the first sampling time for which the continuous-time optimal control would have first completed the reset.*

Recall that t_f^{opt} is the time at which $\chi(t) = 0$ under the optimal control and so

$$k = \arg\min_{i \in \mathbb{N}} i \;\; \text{subject to: } \; t_i \geq t_f^{\text{opt}}. \tag{6.21}$$

Based on Definition 1, the residual phase error is given by

$$E_\tau^\phi = \chi(t_k). \tag{6.22}$$

First, we provide bounds on these two metrics and demonstrate that these bounds are solely dependent on the sampling time τ and the ipPRC specific to the pharmaceutical being used.

Theorem 1 (Bounding of E_τ^ϕ)**.** *Suppose Assumptions 1-4 hold. Let n_{cyc} be the number of 2π cycles required to achieve the continuous time optimal control resetting using the optimal control policy* (6.18)*. The residual phase error incurred by the sampled-time control* (6.20) *satisfies*

$$E_\tau^\phi \leq (n_{\text{cyc}} + 1)(E_\tau^{0,-} + E_\tau^{0,+} + E^s)$$

where $E_\tau^{0,-}$, $E_\tau^{0,+}$, and E^s are the errors incurred at the negative zero cross, the positive zero cross, and a correction for phase advance cases, respectively.

Proof. Note that the sampling-time control is able to identically track the continuous-time optimal control except where consecutive sampling times occur on either side of a zero-cross of the ipPRC.

By Assumption 2, the ipPRC has two zero-crosses in each $[0, 2\pi)$ cycle and so this occurs at most twice per cycle. A zero cross occurs at $t = t^0$ (where $t_{i-1} < t^0 < t_i$). The maximal loss of phase advance or delay is incurred if the switching times are positioned such that the shift incurred over that time step $\Delta\phi_i(u_i) = 0$, where

$$\Delta\phi_i(u_i) = \int_{t_{i-1}}^{t_i} B(\varphi(t')) \cdot u_i \, dt', \tag{6.23}$$

which must be solved numerically with (6.10) to provide $\varphi(t')$. Based on the arguments made in the previous section using Pontryagin's principle, we know that u_i is either $u_{\max}$ or $u_{\min}$.

The maximal loss in phase shift is of equal magnitude in the positive and negative directions because competing advances and delays of identical magnitudes cancel. The maximal error incurred at a given zero-cross is

$$E_\tau^0 = \max_{t_{i-1},u} \left| \int_{t_{i-1}}^{t^0} B(\varphi(t')) \cdot u \, dt' \right| \tag{6.24}$$

and the error for the positive or negative zero-cross is denoted $E_\tau^{0,+}$ and $E_\tau^{0,-}$, respectively. The maximal phase error incurred for each cycle is the sum of the maximal error from each zero-cross, all other steps are identical to the continuous-time optimal control. A demonstration of the phase-shift cancellation by competing advances and delays is shown in Fig. 6.4.

For phase advances, additional error is incurred by phase advances accumulating less due to the zero crosses, thus, the oscillator phase will reach the next positive ipPRC lobe later than it would if it could achieve the full phase advance. The additional error accumulated is equal to the maximal shift that could be achieved in the extra time that it takes to reach the positive lobe. The time lost per cycle for phase advances is:

$$t_E = \frac{T}{2\pi} \cdot (E_\tau^{0,+} + E_\tau^{0,-}) \tag{6.25}$$

which results in an additional residual phase error per cycle of

$$E^s = \begin{cases} \max\limits_{0 \le t \le T} \int_t^{t+t_E} B(\varphi(t')) \, dt' & \text{if } \Delta\phi_f < \Delta\phi_b \\ 0 & \text{if } \Delta\phi_f \ge \Delta\phi_b \end{cases}, \tag{6.26}$$

where $\Delta\phi_b$ is the decision boundary between phase advances and delays. In the case of phase delays, this quantity is 0, since the oscillator phase will reach the next negative lobe more rapidly due to achieving less phase delay. Thus, we can bound the residual time phase error

$$E_\tau^\phi \leq (n_{\text{cyc}}(\Delta\phi_f, \phi_0) + 1)(E_\tau^{0,-} + E_\tau^{0,+} + E^s) \tag{6.27}$$

for a given τ, which concludes the proof. ■

The bound E_τ^ϕ may be thought of as the maximal value of $\chi(t_k)$ for optimal control with sampling time τ.

Remark. At first glance, it may seem that this bound is loose for the case of arbitrarily large n_{cyc}, the number of cycles to achieve any reset is bounded by the finite scalar

$$n_{\text{cyc}}^{\max} = \max_{\Delta\phi_f, \phi_0} n_{\text{cyc}}(\Delta\phi_f, \phi_0)$$

the maximum number of number of cycles to achieve any continuous time optimal reset. Applying this value in (6.27), we may bound the residual time phase error for any sampling-time optimal reset.

Fig. 6.5 shows how the residual phase error bounds evolve over time for phase advances or delays, $\phi_0 = 0$, and $\tau = 2$ h. This corresponds to the actual residual phase error incurred, by numerically calculating the optimal control. Although the error bound increased identically for each cycle, the actual residual phase error varies each cycle, depending upon how each zero-cross aligns with the sampling times.

Fig. 6.6A-B demonstrates this bound for KL001 under $\tau = 1, 2, 4$ h, for $\phi_0 = 0$. The number of cycles to achieve each reset for phase advances or delays $\Delta\phi_f \in [-2\pi, 2\pi]$ (to explicitly show advances and delays) and $\phi_0 = 0$ under the continuous-time optimal control for KL001 is shown in Fig. 6.6A. The region of this plot that corresponds to the phase resetting directions selected by the continuous-time optimal control (advances for $\Delta\phi_f < \Delta\phi_b^\star$, delays for $\Delta\phi_f \geq \Delta\phi_b^\star$) are denoted between the dashed lines. Notably, the number of cycles to achieve phase advances accumulates more rapidly due to the smaller positive lobe of the PRC, and as such, error will incur more quickly in phase advance regions. Fig. 6.6B shows the bounds on the residual phase error for $\tau = 1, 2, 4$ h, and the actual residual phase error incurred for numerically calculating the optimal control for each shift and sampling time. As observed, the calculated residual phase

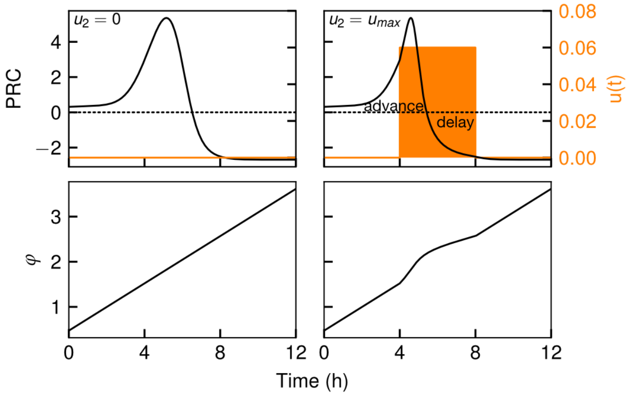

Figure 6.4: Error in applying the optimal control policy occurs at the zero-crosses of the ipPRC. For a sampling time of 4 h, the zero-cross occurs in the second step $t_1 < t^0 < t_2$, and so u_2 will necessarily violate the continuous-time optimal control law. For the cases shown here, $\Delta\phi_2(u_{\max}) = \Delta\phi_2(u_{\min}) = 0$, and the resulting phase is identical due to cancellation of the advance by the delay. Finally, it is noteworthy that this single pathological step consumes most of the positive lobe of the PRC, suggesting that $\tau = 4$ h is a poor choice for sampling time if phase advances are desirable.

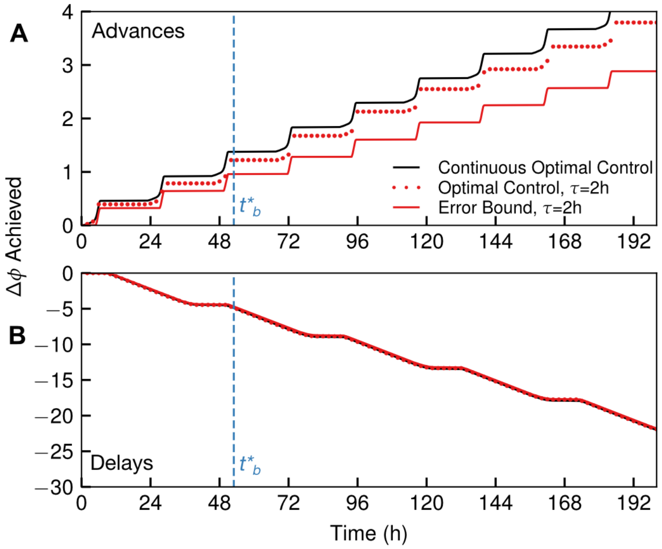

Figure 6.5: The bound on residual phase error (red line) and the actual residual phase error (red dots) plotted as a function of time, in comparison to the continuous-time optimal control (black line), for $\tau = 2$ h and $\phi_0 = 0$. Phase advances (**A**) and delays (**B**) are shown explicitly. The bound deviates further from the optimal control at each completed cycle, however, only the shifts that occur before $t_b^\star$ (dashed line) are attempted under the optimal control policy. Additionally, the error is more severe for phase advances, due to the relatively smaller positive region of the ipPRC, and the proximity of that positive region to a large negative region. For panel B, these lines are nearly on top of one another. The numerically-calculated optimal control for $\tau = 2$ h indeed obeys the bounds derived in Theorem 1 from the continuous time optimal control.

errors fall within the computed bounds.

In addition to the residual phase error, it is useful to determine how much additional time it would take to reach a complete reset. Effectively, we aim to find t^{add} for $\chi(t_f^{\text{opt}} + t^{\text{add}}) = 0$. Finding or bounding t_e is complicated, as finding it necessitates knowledge of the entire optimal control trajectory for each ϕ_0 and $\Delta\phi_f$. An abstraction is used to gather data about this additional time, described in the following definition.

Definition 2. *The* ***number of additional cycles to complete reset*** *($n_\tau^{\text{add}} \in \mathbb{N}$) is a positive scalar that enforces the constraint*

$$\chi(t_f + n_{\text{cyc}}^{\text{add}} T^{+,-}) = 0,$$

where $T^{+,-}$ is the accelerated/decelerated period of the oscillator induced by a phase advance/delay, respectively.

Remark. Clearly, $T^+ < T < T^-$, and by virtue of being on a limit cycle yields

$$\lim_{t\to\infty} [x(t, p, u_+) - x(t - T^+, p, u_+)] = 0$$

and

$$\lim_{t\to\infty} [x(t, p, u_-) - x(t - T^-, p, u_-)] = 0$$

where u_+ and u_- are control inputs resulting in phase advances or delays, respectively.

The following upper bound is proposed on the number of additional cycles to complete reset.

Theorem 2 (Bounding of $n_{\text{cyc}}^{\text{add}}$). *Let $\Delta\phi_{g,\tau}^-$ and $\Delta\phi_{g,\tau}^+$ be the maximum phase delay and advance that is guaranteed to be achievable in a cycle of 2π, respectively. Recall that $\Delta\phi_b$ is the decision boundary between phase advances or delays. The number of additional cycles to correct for the residual phase error incurred by the sampled-time control* (6.20) *is bounded above by*

$$n_{\text{cyc}}^{\text{add}} \leq \begin{cases} \lfloor E_\tau^\phi / \Delta\phi_{g,\tau}^+ \rfloor + 1 & \text{if } \Delta\phi_f \leq \Delta\phi_b \\ \lfloor E_\tau^\phi / \Delta\phi_{g,\tau}^- \rfloor + 1 & \text{if } \Delta\phi_f \geq \Delta\phi_b \end{cases}, \tag{6.28}$$

where $\lfloor \cdot \rfloor$ denotes the floor function.

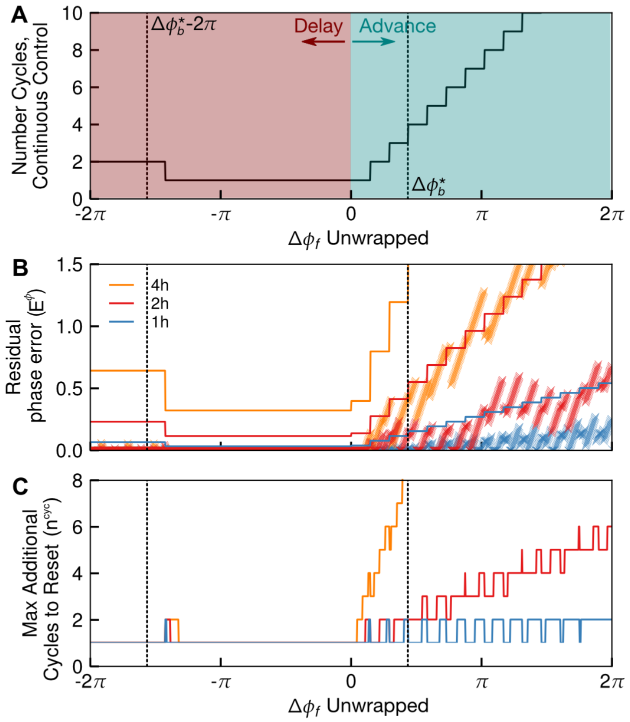

Figure 6.6: Sampling time τ affects circadian phase resetting for optimal control with evenly-spaced switching times, a common feature of feedback control and MPC. (**A**) Plot of number of cycles required to achieve each phase advance or delay under continuous-time optimal control. Errors due to switching timing occurs where the ipPRC crosses 0, and thus is residual phase error is a function of the number of cycles required for continuous-time optimal control. (**B**) A bound on E^{ϕ}_{τ}, the distance to the final phase that will remain at $t = t_f^{\text{opt}}$ under optimal control with a constant sampling time is derived from the continuous optimal control trajectory. Here, the derived bound is shown as a line, and the numerically calculated optimal control solutions are shown as x markers for each τ. The residual phase error in each case indeed obeys the theoretical bounds. (**C**) A bound on $n^{\text{add}}_{\text{cyc}}$ is also derived. For this example, 1 h and 2 h shifts yield similar residual phase error and allow a complete reset in at most two additional cycles, under $\Delta\phi^b = \Delta\phi^\star$. Thus, either is a reasonable choice for sampling time, though a 2 h sampling time will reduce the cost of sampling by half. Alternately, if this drug were used only to achieve phase delays, a 4 h sampling rate would be similarly suitable.

Proof. Let $\Delta\phi^{+}_{g,\tau}$ denote the phase advance that are guaranteed to be achievable in a single cycle. This is more simply thought of as the maximum total phase advance or delay achievable in a cycle minus the worst-case zero-cross error. For advances, the maximum phase advance achieved in a cycle is achieved by the continuous time optimal control policy for advances:

$$\Delta\phi^{+}_{\text{cyc}} = \int_{0}^{T^{+}} B(\varphi(t')) \cdot u^{\star}_{-}(t')dt'. \tag{6.29}$$

The phase shift that is guaranteed to be achievable for each cycle for a step size of τ is therefore

$$\Delta\phi^{+}_{g,\tau} = \Delta\phi^{+}_{\text{cyc}} - E^{0,+}_{\tau} - E^{0,-}_{\tau}, \tag{6.30}$$

and an equivalent method can be used to calculate $\Delta\phi^{-}_{g,\tau}$.

The bound may be calculated by dividing the remaining error E^{ϕ}_{τ} by the advance or delay that is guaranteed to be achieved each cycle for a sampling time of τ. This implies (6.28). ■

This bound is plotted for the use of KL001 and $\tau = 1, 2, 4$ h in Fig. 6.6C. For sampling times of 1 or 2 h, the residual phase error may corrected in 1-2 cycles, with the vast majority of cases needing only an additional cycle. Furthermore, because this method assumes the worst possible alignment of the control switching times for every cycle, it is unlikely that the full two additional cycles will be needed. Alternately, the 4 h sampling time potentially results in many additional cycles needed to achieve a complete reset. This is because, as shown in Fig. 6.4, a 4 h step could be aligned such that nearly the entire phase advance region of the ipPRC is lost. Correspondingly, $\Delta\phi^{+}_{g,\tau}$ is small in value. Thus, we may conclude that a sampling time of 2 h is approximately as effective as 1 h, and provides a 50% reduction in computational and sampling costs over 1 h sampling times, given our assumptions. Our controller designed in Section 6.4 therefore uses $\tau = 2$ h. However, if a controller was designed to only produce phase delays, a 4 h sampling time is sufficiently near to the optimal control. This metric is therefore useful in designing controllers for a given problem and potential pharmaceutical given its ipPRC.

For these plots, dashed lines bound the phase shifts that are performed by the continuous-time optimal control to achieve complete coverage of phase shifts from 0 to 2π. This implicitly assumes that the direction of optimal phase shifting is known for our choice of τ, and is identical to the continuous time optimal control bound $\Delta\phi^{\star}$. The following subsection addresses the choice of resetting direction (given $\Delta\phi^{\star}$ for the continuous optimal case).

While numerical calculation of the infinite-horizon optimal control may seem advantageous, the optimizations involved are costly, as the selection of each step affects the region of the ipPRC available in the ensuing steps. Rather, we propose to formulate the MPC problem using the bounds derived from the optimal control as guidelines, and perform phase shifts by repeatedly solving the finite-horizon optimal control. It must be emphasized that because the bound we have derived is for the maximum residual phase error incurred at each zero-cross, a controller need not solve the infinite-time optimal sampling time control to be governed by the bound. Solving a finite-horizon optimal control problem is sufficient for these bounds on accumulated error to apply.

On MPC formulation and the selection of a prediction and control horizon

MPC involves repeatedly solving a finite horizon optimal control problem. For the continuous-time optimal control (in Section 6.2) the direction of phase shifting was determined by calculation of the equal-time phase shift boundary $\Delta\phi^{\star}$. For MPC, whether the oscillator should advance or delay is implicitly solved in the finite horizon optimization. This subsection demonstrates via simulations that the finite-horizon optimal control in MPC is dependent on the number of steps. Ultimately, we propose a multi-staged optimization for solving the finite-horizon optimal control.

The MPC problem is formulated in a similar fashion as [270], where the prediction and control horizons are set to be identical. The prediction horizon consists of N_p steps with sampling time τ. For an oscillator at $t = t_k$ this yields:

$$U \triangleq \begin{bmatrix} u(t_k+\tau) & \cdots & u\left(t_k+N_p\tau\right) \end{bmatrix}^{\top} \tag{6.31}$$

as the knots of the control trajectory defined at each of the N_p steps. Eqn. (6.10) is used as the MPC predictor, which estimates the oscillator phase at the end of each of $\ell \in [1, \cdots, N_p]$ steps.

The predictor formulation of (6.10) is

$$\hat{\varphi}(t_i + \ell\tau) = \varphi(t_i) + \omega\tau - \sum_{k=1}^{\ell} \int_{t_i+(k-1)\tau}^{t_i+k\tau} B(\varphi) \cdot u_k \, dt. \tag{6.32}$$

Here, i is the index of the applied control steps, and k is the index of the predictor. The predicted phase error $\hat{\chi}(t)$ is defined as the magnitude of the phase difference between the predicted phase $\hat{\varphi}$ and the environmental phase:

$$\hat{\chi}(t) \triangleq \hat{\varphi}(t) - \varphi_r(t) \mod 2\pi. \tag{6.33}$$

Driving phase error to precisely zero is numerically unstable, so we ignore phase error below a constant δ_ϕ:

$$g_\phi(t) \triangleq \begin{cases} 0 & \text{if } |\hat{\chi}(t)| < \delta_\phi \\ \hat{\chi}(t) & \text{otherwise} \end{cases} \tag{6.34}$$

so that numerical imprecisions do not result in controller action. Thus, the finite-horizon optimal control problem at each time t_i may be solved for the optimal trajectory $u^\star_{\text{MPC}}$:

$$\begin{aligned} u^\star_{\text{MPC}} &= \arg\min_U \textstyle\sum_{\ell=1}^{N_p} w^\phi g_\phi^2(t_i + \ell\tau) + w^u u_\ell^2 \\ &\qquad \text{subject to:} \\ &\qquad \text{Eqn. (6.33)} \\ &\qquad u_{\min} \le u_\ell \le u_{\max}, \end{aligned} \tag{6.35}$$

for all $\ell = 1, \cdots, N_p$, where w^ϕ and w^u are positive weighting scalars evaluated at the end of the time step and start of the time step, respectively, as phase error is calculated after the control is applied for that step. After identifying the optimal piecewise control trajectory $u^\star$, the initial step $u_1^\star$ is applied to the system (in this case the full 8-state ODE model) for $t \in (t_i, t_i + \tau]$ as is standard in model predictive control.

For the ensuing simulations, a sampling time of $\tau = 2$ h was used, as described in the prior section. Additionally, weights $w^\phi = 10$ and $w^u = 1$, so that no control is delivered for marginal gains in phase shifting, and $\delta_\phi = 0.1$ as in [271].

Simulations demonstrate that the optimization step in the MPC is susceptible to errors induced by choosing the slower direction to achieve a phase reset. The example in Fig. 6.7 shows how the finite horizon optimal control $u^{\star}_{\text{MPC}}$ calculated for $\Delta\phi_f = \pi$, $\phi_0 = 0$ varies with N_p. For short prediction horizons, the controller applies a phase advance, because more of the positive ipPRC lobe is immediately visible to the predictor, suggesting that this will achieve most rapid reset. By extending the prediction horizon to $N_p = 10$ (20 h), more of the negative lobe of the ipPRC is available, and so the controller waits for this region before applying input, consistent with the infinite-time optimal control for $\tau = 2$ h. In some cases, performing the optimization in this manner could result in an "indecisive" controller that changes directions during the phase shifting, causing excessive lags to reset.

One solution to the problem of inconsistent finite-horizon optimal control policies is to extend the prediction horizon such that it always observes the entirety of the reset, to guarantee that the finite-horizon optimal control calculated during MPC is equal to the infinite-horizon optimal control, that is: $u^{\star}_{\text{MPC}} = u^{\star}_{\o}$. However, this leads to excessive computational costs, especially for small sampling times. Furthermore, the optimization formulation itself poses challenges. Minimizing the time to complete the reset is challenging, as there is no gradient along which to move unless the reset is completed during the prediction horizon, leading to cases with an infinite cost. Minimizing phase error at each step may be suboptimal as well: the fastest reset achievable may involve temporarily increasing $\chi(t)$ for cases where $\Delta\phi_f < \pi$ and $\Delta\phi_f > \Delta\phi^{\star}_{\tau}$.

An alternate approach, which is employed in the following section, is to use a two-stage optimization, where the direction of the reset (advance or delay) is chosen first using bound $\Delta\phi^b$. Furthermore, we propose using $\Delta\phi^b = \Delta\phi^{\star}$, as this will ensure that the bounds on residual phase error and additional cycles to reset hold, as derived in the prior section, and thus provide guarantees on controller performance in the absence of plant-model mismatch or noise. One further important consideration is that a controller with $N_p = 1$ will be unable to avoid accumulating error at the zero-crosses, whereas a controller with a larger N_p provides flexibility to adjust the control inputs preceding a zero-cross to minimize the accumulated error. For this reason, the design parameters were set to $N_p = 5$ and $\Delta\phi^b = \Delta\phi^{\star}$ for our controller. We note, however, that the derived bounds hold even for $N_p = 1$.

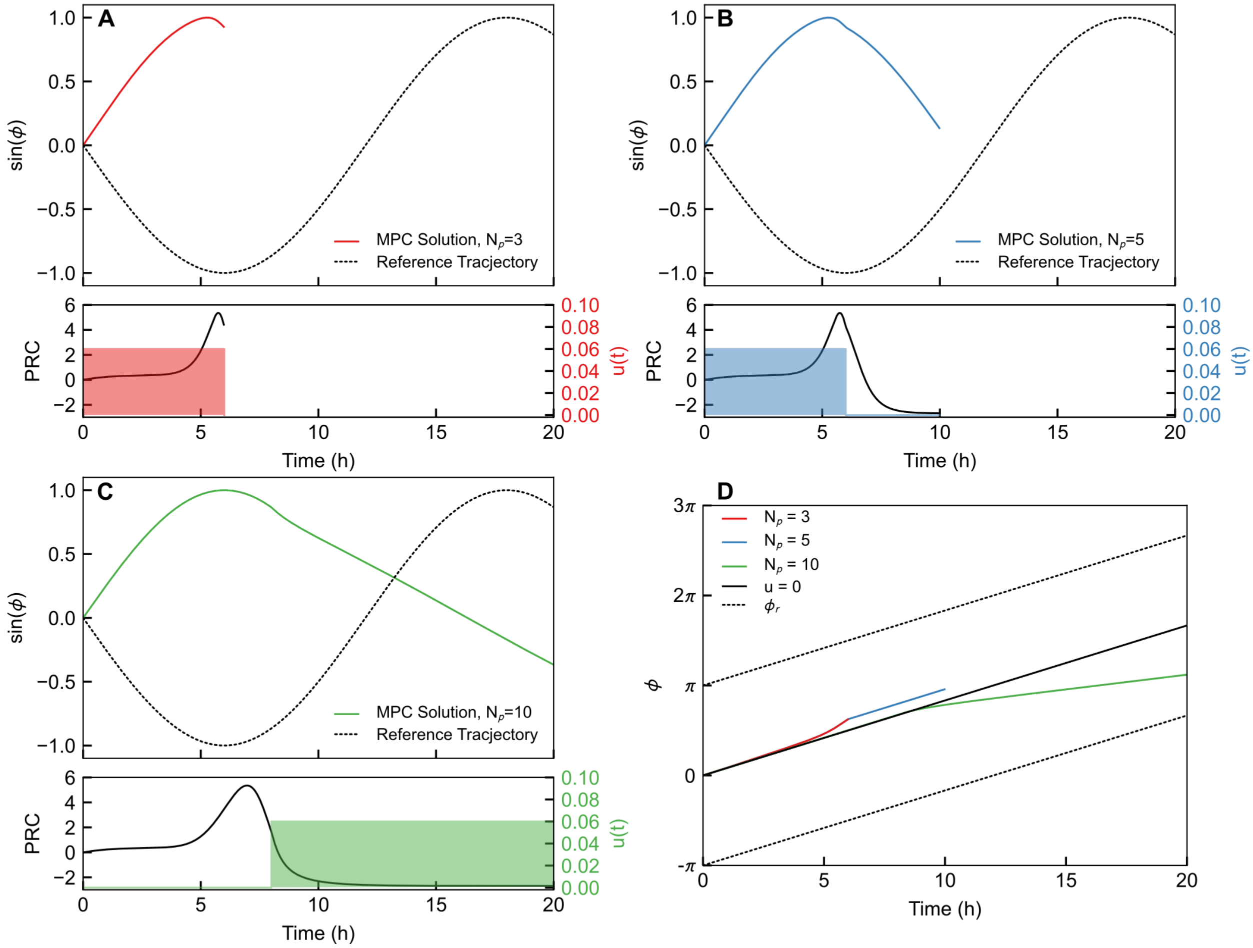

Figure 6.7: Changes in the prediction horizon affect the finite-horizon optimal control trajectory based on the observable PRC. This is demonstrated by computing the first finite-horizon optimal control trajectory and varying that horizon. (**A-C**) Finite-horizon optimal control trajectories for $N_p = 3$, 4, and 5, respectively. In all cases, $\tau = 2$h, $\Delta\phi_f = \pi$, and $\phi_0 = 0$. Note that not only do the finite horizon optimal controls computed by the MPC differ, they seek to achieve the same shift by either advances (A,B) or delays (C). The infinite-horizon optimal control is achieved via delays ($\Delta\phi_f > \Delta\phi^\star$), and so A or B would lead to excessively-long resetting by either selecting advances to achieve the shift, or first selecting advances then later choosing delays. (**D**) This result is visualized by plotting the phase progression for each MPC case and for the 0-input case. Phase advances evidently yield slower progress toward the reference phase, and thus short prediction horizons choose ineffectively. This complication in MPC problem formulation may be circumvented by providing the controller with the optimal resetting direction *a priori*.

6.4 In silico application of designed MPC controller for phase resetting

To demonstrate the efficacy of this control approach, this section presents two control scenarios in our *in silico* circadian simulator (shown schematically in Fig. 6.8). The controller used has $\tau = 2$h, $N_p = 5$, and $\Delta\phi^b = \Delta\phi^\star$, as prescribed by the design considerations in the prior sections.

The first scenario (Fig. 6.9) is an example of extreme jet lag, in which the environment undergoes a 5 h phase advance, followed three days later by a phase delay of 11 h. This is the equivalent of a flight from Boston to London, then London to Honolulu. Here, the controller first waits for a positive region of the PRC rather than immediately attempting a delay, as $\Delta\phi_f < \Delta\phi^b$. Thus, it completes this phase advance in approximately 30 h. The 11 h delay occurs during a region where $B(\varphi) < 0$, and thus control input is provided immediately. This shift is completed in a total of two continuous doses, in approximately 36 h. Without a control approach, light input alone achieves a shift of 2-3h per day at most, thus, this represents a significant speed up in phase resetting. If light is delivered under optimal control, these shifts are predicted to take several days [28], thus demonstrating the potential for improvement by a pharmaceutical input.

The second scenario (Fig. 6.10) involves the delivery of KL001 to align an individual working on a rotating shift pattern, from [277]. Here, the time on the x-axis is local time, and the phase of the oscillator is initialized for an individual entrained to a normal light-dark cycle. In this protocol the individual works two days of morning shift, followed by two days of evening shift, followed by two days of night shift (work shifts denoted by gray boxes. This perpetually phase-delaying schedule is easily tracked by KL001 input, as KL001 more easily achieves phase delays. Notably, by taking one large dose after the conclusion of each pair of shifts, the individual rapidly shifts to the new work phase. Each shift worked in this protocol occurs while the individual is exactly phase-aligned with their work environment. This scenario exclusively involves phase delays, and so under the analysis of Section 6.3 a larger sampling time of $\tau = 4$ h (or possibly even larger) would be similarly effective.

Importantly, the possibly competing effects of light was neglected in these scenarios. This could be achieved simply by restricting light input during the phase-shifting steps, or treating light as a complementary control input, using an approach such as [266]. This is a possible topic for future study.

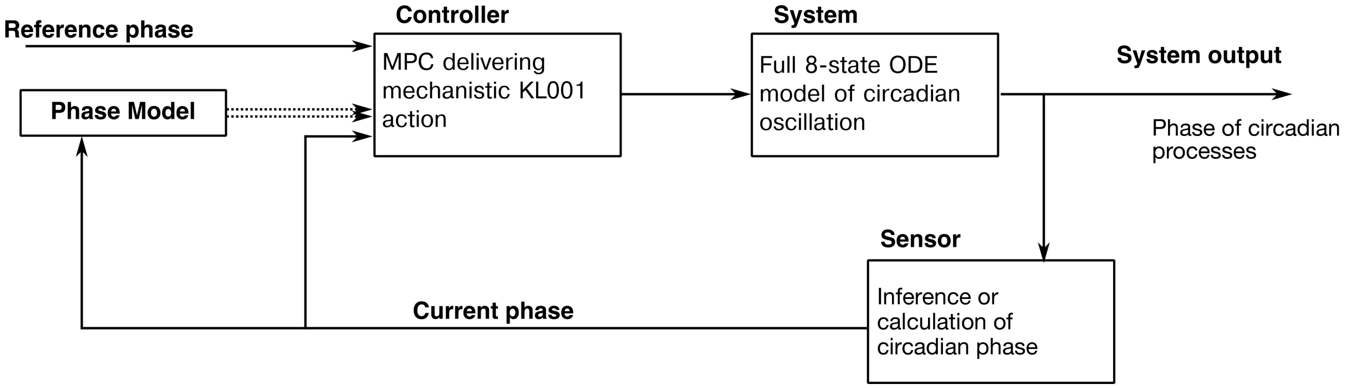

Figure 6.8: *In-silico* scheme for MPC of circadian rhythms. In experimental or clinical application, the human, organism, or cell culture would replace the 8-state ODE model (Table 6.1) as the system under control.

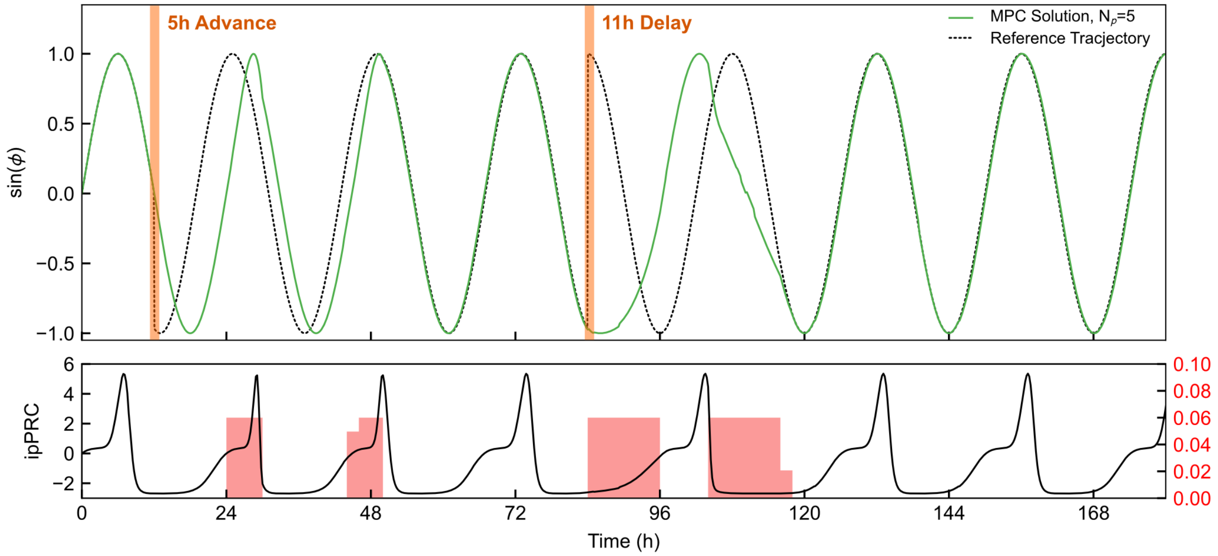

Figure 6.9: Demonstration of MPC for phase resetting in response to jet lag. This scenario involves a 5h (0.417π rad) phase advance followed by a 11h (0.917π rad) phase delay, the equivalent of flying from Boston to London, then London to Honolulu three days later. (**A**) Phase of oscillator under MPC compared to reference phase (local time) for the jet lag problem. For this problem, $\tau = 2$h and $N_p = 5$. (**B**) Timing of control inputs and PRC throughout the simulation. In both cases, the reset is completely achieved in less than 48h, a drastic speedup in comparison to the untreated case or the light-input case [269]. For simplicity, no light input to the clock was assumed in this case, though it may be incorporated as an additional disturbance input to the phase model, or applied as part of multi-input control.

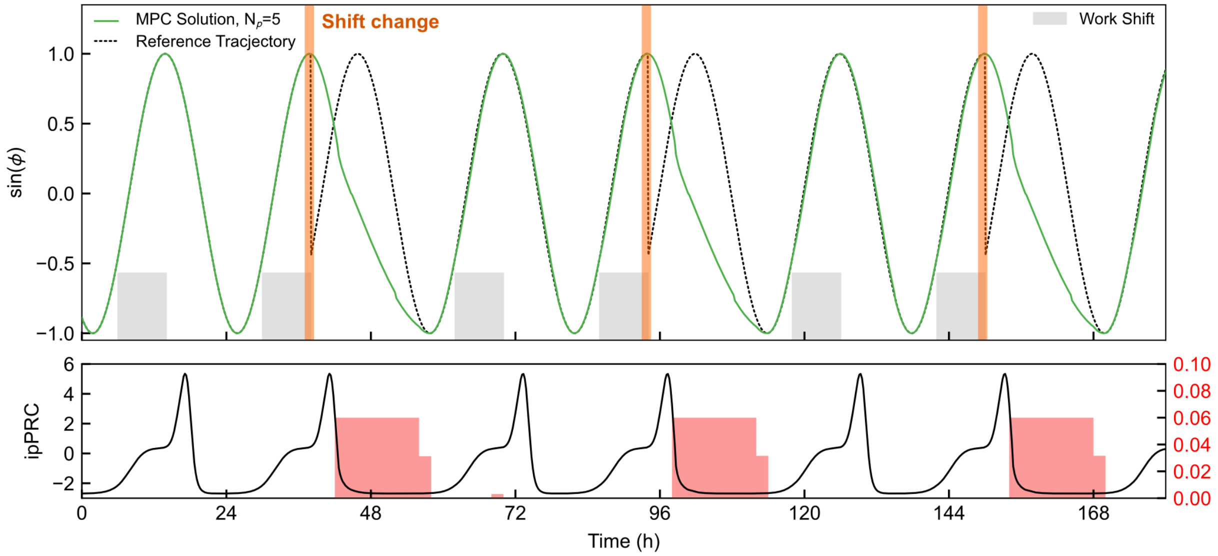

Figure 6.10: Demonstration of MPC for phase resetting in response to a weeklong rotating shift work schedule, described in [277]. This scenario involves 8h phase delays every two days when rotating from morning (06:00-14:00), to evening (14:00-22:00) to night (22:00-06:00) shifts, followed by days off. (**A**) Phase of oscillator under MPC compared to reference phase for the shift work problem. In this example, time corresponds to clock time, such that *Per* expression in an individual entrained for morning work will occur near dusk. The reference phase was adjusted to the next rotating shift following the last work cycle of the prior rotating shift. For this problem, $\tau = 2\text{h}$ and $N_p = 5$. (**B**) Timing of control inputs and PRC throughout the simulation. Because all shifts are achieved by delays, a slower sampling rate (longer duration between dosage changes) would have a similar efficacy. For simplicity, no light input to the clock was assumed in this case, though it may be incorporated as an additional disturbance input to the phase model, or applied as part of multi-input control.

6.5 Summary

This chapter presents tools for designing feedback control of circadian rhythms with explicit consideration for pharmaceutical inputs. Importantly, this chapter provides a bound on the errors incurred by sampling time control of circadian oscillation, and may be applied to compare against the efficacy of a light-based approach; see, for example, [269]. Furthermore, it demonstrates the advantages provided by pharmacological actuation, as any phase reset is predicted to be achievable in under 60 h. Uniquely, this work proposes a formulation of the nonlinear MPC based on the bounds derived from the optimal control problem.

Since drug discovery for the manipulation of circadian rhythms is ongoing, this chapter presents a perspective on which pharmaceuticals will enable control. Specifically, an ideal circadian pharmaceutical will have (i) large-magnitude positive and negative ipPRC lobes, to enable bidirectional phase resetting, and (ii) rapid pharmacokinetics, to enable precise timing of its effect and minimal losses during ipPRC zero-crosses. This is in contrast to traditional pharmaceutical approaches that select for a long drug half-life to ensure its effect is sustained. Future studies should explicitly incorporate simple pharmacokinetic profiles, rather than piecewise-constant control. However, achieving closed-form solutions or error bounds for these problems is challenging.

A remaining link in achieving closed-loop circadian control is the development of a noninvasive circadian phase sensor. While phase may be assessed relatively simply from cellular bioluminescent reporters, noninvasive *in vivo* phase inference in mammals is an open challenge. Recent work in assessing phase from ambulatory monitoring has shown promise and reasonably accurate predictions [278], however, the propagation of measurement errors through such a control algorithm also remains an open question. An ideal phase sensor would rely on simple data such as solely actigraphy, rather than additional biophysical sensors (e.g. skin temperature, salivary melatonin), and remains in development. The abilities of phase inference methods and controller robustness will be of consequence for the implementation of any form of circadian feedback control mentioned herein.

Finally, this chapter has assumed the system under control to be a single oscillator and thus neglected the contributions of intercellular synchrony to circadian function. A more detailed approach would involve controlling the multi-oscillator system with a multi-oscillator model, using formalisms developed in Chapter 1. This problem could be approached through optimal control as in [279]. Specifically, this would involve formulating the optimal control problem as a population of phase-only oscillators with identical PRCs but heterogeneous initial conditions, and possibly heterogeneous intrinsic frequencies. Then, the minimum-power or time-optimal control problem can be solved with computational approaches, as analytic methods are intractable for large oscillator ensembles. Alternately, this problem could be approached by simple augmentations to the MPC algorithm from this chapter. In the following chapter, I demonstrate that the single-oscillator approach performs poorly under certain conditions where the oscillator is susceptible to desynchronization, and I present a simple approach to modify the nonlinear MPC of this chapter to correct for this issue.

Chapter 7

Model predictive control for synchronous phase shifting of circadian oscillator populations

7.1 Introduction

High amplitude circadian oscillations are associated with good metabolic health [280], commensurate with the broad integration of circadian regulation with metabolic function [49, 87]. High amplitude oscillation within peripheral (i.e. non-neural) tissues of the body is achieved by high oscillatory amplitudes from the individual oscillators comprising the tissue, as well as a high degree of synchrony among the oscillator population [100, 101, 281]. Since disruption to the circadian oscillator can take the form of either misaligned phase (as in the prior chapter) there is a need to develop therapies to mitigate the effects of disruption to the circadian clock, to rapidly re-align circadian phase with the environment following jet lag or shift work to avoid cognitive difficulty, and to promote high-amplitude circadian oscillation. Since circadian rhythms are complex phenomena, phase, synchrony, and amplitude control of the clock may be better approached by control theory rather than an ad hoc approach to the delivery of drugs or light [26, 28, 29].

As mentioned in the previous chapter, control strategies devised for manipulation of mammalian circadian rhythms may analogously be applied to other oscillatory biological systems, provided they are well-described by limit-cycle oscillators. Circadian oscillators in other species

---

Major portions of this chapter appear as J.H. Abel, A. Chakrabarty, and F.J. Doyle III, "Controlling time: nonlinear model predictive control for populations of circadian oscillators," in *Emerging Applications of Control and System Theory*, R. Tempo, S. Yurkovich, P. Misra Eds. New York, NY: Springer Publishing, 2018. ISBN: 978-3-319-67068-3. All theoretical and computational results were by J.H. Abel. Research approach was conceived in collaboration with and under the mentorship of F.J. Doyle III and A. Chakrabarty, with additional inspiration from the work of P.C. St. John.

such as the KaiABC system in the cyanobacterium *Synechococcus* [5], or the *Period-Timeless* oscillator in *Drosophila* [282] have been modeled as limit-cycle oscillators for more than a decade. More generally, genetic or phosphorylation-driven oscillators are a ubiquitous biological motif involved in the metabolic processes of numerous organisms from prokaryotes to mammals [71, 283], and the development of strategies for manipulating both phase and synchrony of these systems is broadly desirable. To-date, control of circadian rhythms has been A more detailed approach to control of circadian dynamics would integrate tissue or population-scale effects, pharmacokinetics and pharmacodynamics, and interactions between different oscillator populations.

Herein, we begin to approach this detailed formulation by presenting a MPC framework for manipulating phase and synchrony within populations of uncoupled biological oscillators using a pharmaceutical agent, and demonstrate the efficacy of such an approach by *in silico* simulations of phase shifting in the mammalian clock. We do so by describing the population of oscillators as a phase probability density function, as in [101], and using the parametric infinitesimal phase response curve (PRC) to calculate how the phase PDF evolves in response to control input. By using a predictor that accounts explicitly for the variability in phase within a synchronized population, we are able to maintain synchrony of oscillators while performing a phase shift, unlike the single-oscillator case.

In this chapter, we present a framework for the control of a population of biological oscillators, motivated by the example of the mammalian circadian clock. First, we use our previously-derived simplification of oscillator dynamics using the parametric phase response to a control input to reduce the dynamical model to a phase-only representation [270]: this is advantageous in reducing the dimensionality of the MPC problem, thereby curbing computational effort. We then present a controller for the case for a single oscillator, designed using the principles of the previous chapter, and demonstrate its function *in silico*. Next we demonstrate that although this formulation may successfully control a single oscillator, applying this controller to manipulate mean phase of a population of oscillators may effect a desynchronization detrimental to biological function. We then modify the MPC problem using a probability density function of population phase in conjunction with the simplified dynamics to exert simultaneous control over phase and synchrony within an oscillator population. We demonstrate the *in silico* efficacy of this approach in maintaining synchrony throughout a phase realignment. Finally, we discuss limitations of this approach, and challenges to its implementation *in vivo* and *in vitro*.

7.2 Control of a single circadian oscillator

A standard approximation in the control of the circadian oscillator is describing the targeted circadian system (i.e., the population of cells comprising clocks in brain or peripheral tissues such as the liver) as a single limit-cycle oscillator [26, 28, 29, 127, 267, 268, 270, 271]. We begin our treatment of applying control to phase-shift the circadian oscillator by exploiting this approximation, as in our previous work [270, 271] as well as the prior chapter, to illustrate where it fails to capture population-scale phenomena.

Modeling the circadian oscillator

As described in detail in Chapter 1, the mammalian circadian oscillator within an individual cell is comprised of interlocked transcriptional-translational feedback loops. The core negative feedback loop involves isoforms of the genes *Period* (*Per*) and *Cryptochrome* (*Cry*), which form PER-CRY heterodimers and enter the nucleus to bind to BMAL1-CLOCK E-box activators to repress their own transcription. As these repressors are degraded, BMAL1-CLOCK dimers activate transcription of *Per*s and *Cry*s, resulting in a self-sustained oscillation. Downstream of the circadian feedback loops, clock components regulate transcriptional architecture through D-box, E-box, and ROR-binding elements. For an excellent review of the genetic components of the mammalian oscillator, see [41].

Numerous dynamical models of the circadian oscillator have been proposed. In this work, as in the previous chapter, we selected the model from [19, 133], as it was created to identify the effect of the small-molecule KL001 on the mammalian oscillator. This model consists of 8 nonlinear coupled ODEs and 21 kinetic parameters, fully described in the supplement to [133] and reproduced in Table 6.1. Because KL001 was found to stabilize nuclear PER-CRY transcription factors, control is implemented in the model by modifying the ODEs describing the degradation of PER-CRY dimers as follows:

$$\frac{d\mathrm{C1P}}{dt} = v_{\mathrm{a,CP}}\mathrm{P}\cdot\mathrm{C1} - v_{\mathrm{d,CP}}\mathrm{C1P} - \frac{(v_{\mathrm{dCn\text{-}u(t)}})\mathrm{C1P}}{k_{\mathrm{deg,Cn}} + \mathrm{C1P} + \mathrm{C2P}} \tag{7.1a}$$

$$\frac{d\mathrm{C2P}}{dt} = v_{\mathrm{a,CP}}\mathrm{P}\cdot\mathrm{C2} - v_{\mathrm{d,CP}}\mathrm{C2P} - \frac{(v_{\mathrm{dCn}} - u(t))m_{\mathrm{C2N}}\mathrm{C2P}}{k_{\mathrm{deg,Cn}} + \mathrm{C2P} + \mathrm{C1P}}, \tag{7.1b}$$

where $u(t) \in [0, \bar{u}]$ is control input at time t, which reduces degradation rate v_{dCn}. Generally $\bar{u}$ should not be greater than v_{dCn}, as a degradation reaction cannot be reversed so far as to synthesize new PER-CRY. Throughout, we set this value to 0.08. The states present in this model, and the effect of KL001, is shown in the schematic in Fig. 7.1A.

Model reduction and the phase control problem

Control of the circadian clock is primarily focused on shifting the phase of the circadian oscillator. A unique phase $\phi \in [0, 2\pi)$ may be assigned to each unique point on the limit cycle and as in the prior chapter, points in state-space that are not on the limit cycle may be assigned the phase of the point on the limit cycle to which they converge asymptotically in time. The 8-ODE oscillator may be reduced to a single ODE describing asymptotic phase (φ):

$$\frac{d\varphi}{dt} = \omega + u(t)\cdot B(\varphi), \tag{7.2}$$

where ω is the radial frequency ($2\pi/T$, where T is period of oscillation), $u(t)$ is the control input, and $B(\varphi)$ is the infinitesimal parametric infinitesimal phase response curve (ipPRC) with respect to changing parameter v_{dCn}, as defined in the prior chapter and under the same assumptions. This function may be calculated numerically in advance from the 8-ODE model by previously-defined methods [270, 284]. The PRC is plotted in Fig. 7.1B. One may consider the control input to be either "speeding up" or "slowing down" the oscillation depending on the sign of the PRC. We opted to set the reference $\phi = 0$ where the concentration of *Per* mRNA is at a maximum.

As in the prior chapter, we are aiming to align the phase of the circadian oscillator (φ) with an external tracking phase (denoted φ_r), for example, the phase of the environment before and after a plane flight through multiple time zones or before and after beginning a shift work cycle.

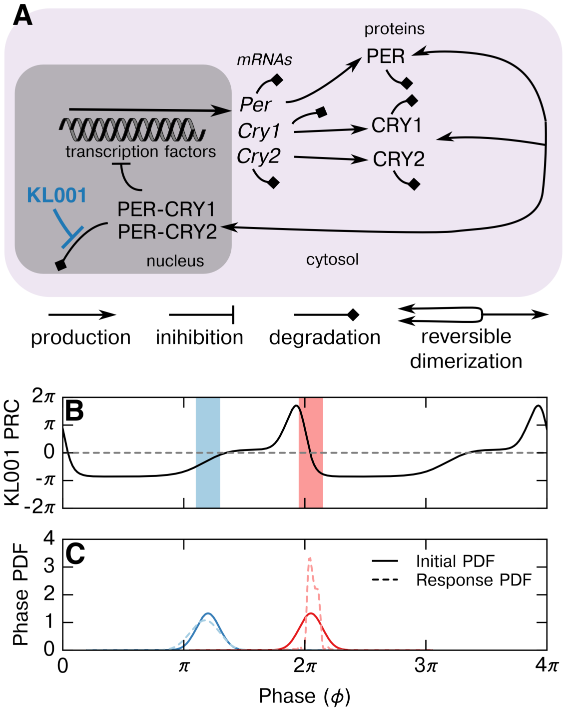

Figure 7.1: Schematic of mammalian circadian oscillator and effect of KL001. (**A**) Diagram of the core negative feedback loop driving mammalian circadian rhythms. This schematic is adapted from Figure 6.2 for easy reference. All states and reactions shown are included explicitly in the model (from [133]) as shown in Table 6.1. (**B**) Parametric infinitesimal PRC describing response to KL001 (reduction in parameter v_{dCn}). Note that this is double plotted to allow visualization. (**C**) Synchrony of a population is affected by timing of KL001 application. Two example probability density functions (PDFs) of phase are plotted before (solid) and after (dashed) application of KL001 at the phases shown. In regions of positive slope (blue), the phase PDF is dispersed, whereas in regions of negative slope (red), the PDF is condensed, even though the mean phase is unchanged.

This externally-imposed phase may be captured by a single ODE as well:

$$\frac{d\varphi_r}{dt} = \omega + \Delta\phi\,\delta(t_{shift}), \tag{7.3}$$

where $\Delta\phi \in [-\pi, \pi)$ is the phase shift of the environment that occurs at time t_{shift}, for example, when disembarking from the flight or starting a period of shift work. We are searching for a control trajectory that will drive the oscillator φ to external phase φ_r and maintain it at φ_r for all subsequent time. That is:

$$\lim_{t\to\infty} \|\varphi(t,u) - \varphi_r(t)\| \quad = \quad 0.$$

Control of single oscillator phase

While light may be applied or removed instantaneously, pharmaceutical perturbation of the clock is constrained by pharmacokinetics. To alleviate numerical complications arising due to unidentified (and likely nonlinear) pharmacokinetics, we selected a piecewise-constant parameterization of the control:

$$u(t) = u(t_k)\;\forall\; t_k \leq t < t_{k+1}, \tag{7.4}$$

and denote the sampling time $t_{k+1} - t_k$ as τ. For a predictive horizon of N_p steps of duration τ, we define

$$U \quad \triangleq \quad \begin{bmatrix} u(t_k) & u(t_k+\tau) & \cdots & u\left(t_k + (N_p-1)\tau\right) \end{bmatrix}^\top \tag{7.5}$$

as the knots of the control trajectory defined at each of the N_p steps. To estimate the phase at the end of each step the phase dynamics in (7.2) may be integrated over each of the $\ell \in \begin{bmatrix} 1 & \cdots & N_p \end{bmatrix}$ steps to yield:

$$\hat{\varphi}(t_i + \ell\tau) = \varphi(t_i) + \frac{2\pi\ell\tau}{T} - \sum_{k=0}^{\ell-1} \int_{t_{k+i}}^{t_{k+1+i}} u(t_k) B(\varphi)\, dt, \tag{7.6}$$

where $\hat{\varphi}$ is the predicted phase, t_i is the current time, $\varphi(t_i)$ is measured, and the PRC is a function of $\hat{\varphi}$. We define the phase error to be the magnitude of the phase difference between the predicted phase and the environmental phase:

$$e_\phi(\cdot) \triangleq |\angle(\exp(\mathrm{i}\hat{\varphi}(\cdot) - \mathrm{i}\varphi_r(\cdot)))|, \tag{7.7a}$$

where $\mathrm{i} = \sqrt{-1}$. Computationally, driving phase error to 0 is numerically unstable, so we relax the terminal constraint by ignoring phase error below a constant δ_ϕ:

$$g_\phi(\cdot) \triangleq \begin{cases} 0 & \text{if } e_\phi(\cdot) < \delta_\phi \\ e_\phi(\cdot) & \text{otherwise} \end{cases} \tag{7.7b}$$

so that numerical imprecisions do not result in controller action. Thus, the finite-horizon optimal control problem at each time t_j may be solved for the optimal trajectory $u^\star$:

$$\begin{aligned} u^\star &= \arg\min_U \sum_{\ell=1}^{N_p} w_\ell^\phi g_\phi^2(t_i + \ell\tau) + w_{\ell-1}^u u^2(t_i + (\ell-1)\tau) \\ &\text{subject to:} \\ \hat{\varphi}(t_i + \ell\tau) &= \varphi(t_i) + \frac{2\pi\ell\tau}{T} - \sum_{k=0}^{\ell-1} \int_{t_{k+i}}^{t_{k+1+i}} u(t_k) B(\varphi)\, dt, \\ 0 &\leq u_{\ell-1} \leq \bar{u}, \end{aligned} \tag{7.8}$$

for all $\ell = 1, \cdots, N_p$, where w_ℓ^ϕ and $w_{\ell-1}^u$ are positive weighting scalars evaluated at the end of the time step and start of the time step, respectively, as phase error is calculated after the control is applied for that step. After identifying the optimal piecewise control trajectory $u^\star$, we applied $u^\star(t_i)$ to the full 8-state ODE model for $t \in (t_i, t_i + \tau]$ as is standard in model predictive control.

For this MPC formulation, w^ϕ, w^u, N_p, and τ are design parameters which may vary. We have selected:

$$w_\ell^\phi = \ell,$$

$$w_{\ell-1}^u = 1,$$

for $\ell = 1, \cdots, N_p$. We have elsewhere investigated optimal selection of design variables N_p and τ for this exact formulation of MPC [271]. Based on these findings, we set $N_p = 3$ (and $N_u = N_p$

where N_u is the number of length of the control horizon) and $\tau = 2$h, and instead studied the how phase control of a single oscillator differs from an oscillator population.

Case study #1: nonlinear MPC for a single oscillator

To demonstrate the behavior of this controller, we applied it for the phase shifting control problem where a phase delay of 6h occurs at 12h (a phase delay of $\pi/4$ at a phase of π). The environmental phase for this example was given by 7.3, where $\Delta\phi = -\pi/2$, and $t_{shift} = 12$h. We used the Python language to solve the MPC problem, specifically, we used CasADi [285] and SciPy for formulation, and PySwarm to solve the nonlinear programming optimization problem. Here, the numerical error in calculating phase was $\mathcal{O}(10^{-2})$ and so design variable $\delta_\phi = 0.1$.

The results of this simulation are shown in Fig. 7.2. Briefly, the controller began its action at $t = 12$h to achieve a phase delay. The full 6h phase delay could not be achieved within the initial negative region, and so the remainder of the shift was accomplished when the PRC returned to a negative value near 30h. A decrease in amplitude occurred near $t = 30$h due to transient deviation from the limit cycle, and the full amplitude returned for the following peak.

7.3 Control of population phase and synchrony

The circadian oscillator is cell-autonomous, and each tissue is comprised of many thousands of individual oscillators. While the SCN master pacemaker maintains its synchrony through intercellular communication, other tissues such as the liver lack paracrine signaling and are kept synchronized through a variety of identified and as-yet unidentified means, as guided by the SCN [9]. The application of a pharmaceutical to any of these populations will affect this synchrony, and thus the amplitude of oscillation [100, 101].

While transient deviations from the limit-cycle eventually return to the limit-cycle amplitude, reduction in amplitude due to desynchrony will persist in the absence of signaling, making populations with weak coupling susceptible to long-term desynchrony from mistimed control. The change in synchrony in response to perturbation may be calculated from the PRC [101]. In Fig. 7.1C we show how this may be intuitively understood based on the slope of the PRC: oscillator populations that lie on regions of positive slope result in the cells which are ahead in phase advancing further (or being delayed less) than oscillators which lag to begin with, broadening the probability density function (PDF) of phase. Inversely, populations lying on a region of negative slope are condensed in phase by a similar argument.

Here, we first apply the previously-described controller to a population of uncoupled oscillators to demonstrate the deleterious effect of a population-agnostic nonlinear MPC on synchrony. We then modify the MPC controller to explicitly penalize population desynchronization and demonstrate the ability to simultaneously control phase and synchrony of a population.

Case study #2: limitation of single-oscillator assumption

We first applied the single-oscillator controller to a population of oscillators, with slight modification for tracking the mean phase of the population. We modified the predictor in (7.6) to use the mean phase of the population $\bar{\varphi}$ rather than the phase of an individual oscillator:

$$\hat{\varphi}(t_i + \ell\tau) = \bar{\varphi}(t_i) + \frac{2\pi\ell\tau}{\tau} - \sum_{k=0}^{\ell-1} \int_{t_{k+i}}^{t_{k+1+i}} u(t_k) B(\varphi)\, dt. \tag{7.9}$$

Here, we calculated $\bar{\varphi}(t_i)$ from the phases of each oscillator φ_n in the population by the parameter $z \in \mathbb{C}$ describing the population:

$$z = \rho \exp(\mathrm{i}\bar{\varphi}) = \frac{1}{N} \sum_{n=1}^{N} \exp(\mathrm{i}\varphi_n), \tag{7.10}$$

where ρ is the Kuramoto order parameter, or colloquially, the synchrony index. We emphasize that the controller did not observe any information about the population aside from its mean phase, and as such, the predictor (7.6) used in the finite horizon optimal control problem was imprecise due to slight differences between single-cell and population-mean phase response [101]. The controller was otherwise parameterized identically to that in the prior section.

Fig. 7.3 shows the result of applying this controller to a population of 200 identical uncoupled oscillators with initial phases sampled from the PDF:

$$p(\varphi) = f_{WN}(\varphi; \phi_0, \sigma), \tag{7.11}$$

where f_{WN} indicates a wrapped normal distribution with mean ϕ_0 (set to 0, to match the mean with the single oscillator case), and standard deviation σ (set to $\pi/12$, approximately capturing the distribution of phases observed) [101]. As in the single-cell case, control was applied immediately starting at $t = 12$h to begin correcting for the 6h phase delay. In the population case, this corresponds to a region of positive slope of the PRC, and intuitively resulted in a desynchronization of phase as evidenced by the decline in synchrony index for the duration of the KL001 pulse. Despite the amplitudes of the individual oscillators (gray) returning after a transient to their pre-pulse levels, the population mean [PER] amplitude was reduced by approximately one-third due to desynchronization of the population. Because there was no intercellular or external communication driving synchrony, the amplitude of the mean remained diminished for the duration of the simulation.

Population MPC algorithm for phase coherence

A more sophisticated approach to control of an oscillator population involves predicting the evolution of the PDF itself rather than only mean phase. Methods have been developed previously to compute the change in PDF directly in response to stimulation [101]. A change in variables allows the numerical computation of the new phase PDF:

$$\hat{p}(\varphi, t)dh(\varphi) = p(\varphi, t)d\varphi, \tag{7.12}$$

where $\hat{p}(\varphi, t)$ is the predicted PDF at time t for phases φ, and $h(\varphi) = \varphi + \Delta\phi$, called the phase transition curve (PTC), is the total response to perturbation. We may therefore revise the prediction model to explicitly involve calculation of the phase PDF at each step of the predictive horizon. The PTC for each step within the predictive horizon may be calculated in a similar fashion to the predictor for the single-oscillator case:

$$h_k(\varphi) = \varphi + \frac{2\pi\tau}{T} - u(t_k) \int_{t_k}^{t_{k+1}} B(\varphi)\, dt, \tag{7.13}$$

where u is piecewise-constant and the integrand is a function of φ which may be calculated numerically in advance as previously defined. This function may be calculated numerically for

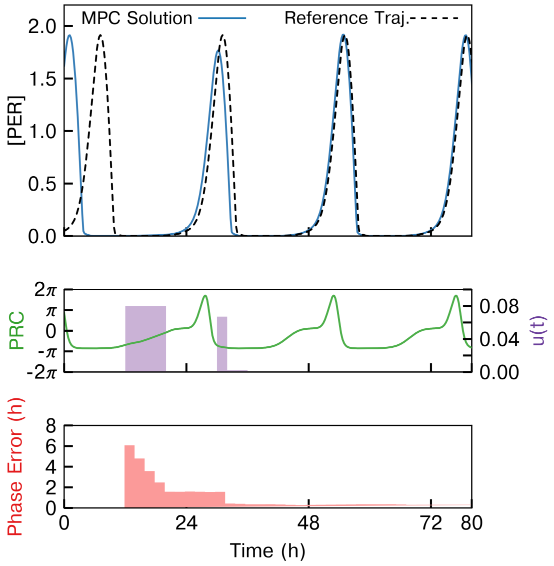

Figure 7.2: Application of the single-oscillator controller for a single oscillator achieving a phase delay of 6h ($\Delta\phi = -\pi/2$) with $t_{shift} = 12$h. The controller acts immediately beginning at $t = 12$h, and completes the phase delay to align with the desired reference trajectory after the PRC returns to a negative value. Note that the initial negative region of the PRC is elongated due to control slowing the advance of phase and maintaining the oscillator in a phase with a negative PRC for longer.

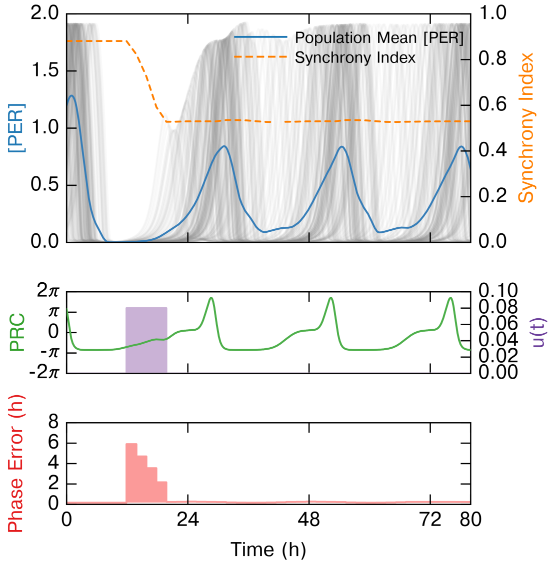

Figure 7.3: Application of the single-oscillator controller for a phase delay of 6 h ($\Delta\phi = -\pi/2$) with $t_{shift} = 12$ h, for shifting mean phase of a population of 200 circadian oscillators (individual trajectories plotted in gray). While control is applied in nearly the same regions as Fig. 7.1 and a −6 h shift was attained, this resulted in a dispersion of phase, a decrease in synchrony index, and a reduction in mean oscillatory amplitude.

each step, and used to calculate the evolution of the PDF:

$$\hat{p}(\varphi, t_{k+1}) dh_k(\varphi) = \hat{p}(\varphi, t_k) d\varphi. \tag{7.14}$$

To calculate the first step, $\hat{p}(\varphi, t) = p(\varphi, t)$ is measured from the population under control. The population predicted mean phase $\hat{\varphi}$ and synchrony index $\hat{\rho}$ may then be calculated from the predicted PDF:

$$\hat{\rho}(t_k) \exp(\mathrm{i}\hat{\varphi}(t_k)) = \int_0^{2\pi} \hat{p}(\theta, t_k) \exp(\mathrm{i}\theta) d\theta, \tag{7.15}$$

where θ is a dummy variable of phase. The phase error term g_ϕ may remain as defined in (7.7), and we define a similar error term penalizing desynchrony

$$g_\rho(\cdot) \triangleq \begin{cases} 0 & \text{if } \rho > \delta_\rho \\ (1 - \rho(\cdot)) & \text{otherwise} \end{cases} \tag{7.16}$$

which reduces to 0 for a satisfactorily synchronized population.

Thus, the population control problem is:

$$\begin{aligned} u^\star &= \arg\min_U \ \mathcal{J} \\ \text{subject to:} & \\ \mathcal{J} &= \sum_{\ell=1}^{N_p} w_\ell^\phi g_\phi^2(t_i + \ell\tau) + w_\ell^\rho g_\rho^2(t_i + \ell\tau) + w_{\ell-1}^u u^2(t_i + (\ell - 1)\tau), \\ h_k(\varphi) &= \frac{2\pi\tau}{T} - u(t_k) \int_{t_k}^{t_{k+1}} B(\varphi)\, dt, \\ \hat{p}(\varphi, t_{k+1}) dh_k(\varphi) &= \hat{p}(\varphi, t_k) d\varphi \\ \hat{\rho}(t_k) \exp(\mathrm{i}\hat{\varphi}(t_k)) &= \int_0^{2\pi} \hat{p}(\theta, t_k) \exp(\mathrm{i}\theta) d\theta \\ 0 &\leq u_{\ell-1} \leq \bar{u}, \end{aligned} \tag{7.17}$$

where phase error and synchrony are calculated at the end of each step within the predictive horizon.

Case study #3: implementation of population nonlinear MPC controller

As before, w^{ϕ}, w^{u}, w^{ρ}, N_p and τ are design parameters. These parameters were set as before, with the exception of the new weighting of synchrony:

$$w^{\rho} = 10(\ell + 1),$$

which was set such that the synchrony term is of the same order of magnitude as the phase term, and increases to allow flexibility of synchrony early in the horizon. Tuning this parameter will adjust the sensitivity of the controller to temporary desynchrony. As $w^{\rho} \to \infty$, the controller will take no action unless it results in no loss of synchrony, i.e., the population lies completely on a region of negative slope of the PRC. For lower but nonzero w^{ρ}, as in the case here, some flexibility is permitted, in that the controller may apply action that desynchronizes the population if it results in a large reduction in phase error. Correspondingly, the controller will later resynchronize the population to account for this early desynchrony. For $w^{\rho} = 0$, the controller will behave as the popualtion-agnostic case. After calculating the finite horizon optimal control $u^{\star}$, we apply the first step $u^{\star}(t_j)$ to all oscillators within the population for $t \in [t_j, t_j + \tau)$, and repeat this process.

We applied the controller described in Sec. 7.3 to the same phase shifting problem as the previous controllers: $t_{shift} = 12\text{h}$, $\Delta\phi = -6\text{h}$. The initial phase of the 200 uncoupled oscillators comprising the population was sampled from the PDF:

$$p(\varphi) = f_{WN}(\varphi; \phi_0, \sigma), \tag{7.18}$$

where f_{WN} indicates a wrapped normal distribution with mean $\phi_0 = 0$ and standard deviation $\sigma = \pi/12$.

Results from this simulation are shown in Fig. 7.4. The controller first applied input briefly in a slight desynchronizing region of the PRC, then paused for the remainder of the first negative PRC region due to the likelihood of further desynchronizing the population. Once the population PDF returned to a region of negative PRC and a negative first derivative of the PRC the controller resumed input driving the population to its 6h phase delay and restoring full synchrony. Strikingly, changing the time of input resulted in a slight increase in the synchrony of the population in comparison to its original state, evidenced by an increase in the synchrony index. Visually, this is evident from the clear alignment of individual oscillators within the population (plotted in gray) in comparison to the dispersion in phase evident in Fig. 7.3 where synchrony was ignored.

7.4 Summary

We have presented a modification of nonlinear MPC for phase manipulation of circadian oscillator populations, in which a PDF of phase is used in solving the finite horizon optimal control problem, allowing mean phase and population synchrony to be regulated simultaneously. For many PRCs that have been calculated, there exists a region where the PRC or first derivative of the PRC is zero [44], it is therefore possible to manipulate phase and synchrony independently for a population of circadian oscillators through a single control input. In reality, the ability to target these regions is limited by precision of the measurements of the PRC and population phase PDF.

One significant challenge in implementing this control algorithm *in vitro* or *in vivo* is the construction of an observer with sufficient accuracy to accurately reconstruct the phase PDF. Current methods of assessing the phase of circadian oscillators relies on either noisy single-cell bioluminescent markers *in vitro* or system level metrics *in vivo* such as melatonin, activity, or body temperature. However, even a simplistic assumption such as a wrapped normal PDF with an arbitrary estimate of standard deviation of phase could help avoid delivering control inputs where the slope of the PRC is expected to be positive, and thus help avoid desynchrony. In this case, a long predictive horizon would quickly become inaccurate, however, necessitating careful selection of design variables τ and N_p.

Another challenge toward implementing such an algorithm is incorporating the as-yet uncharacterized pharmacokinetics and pharmacodynamics (PK/PD) for a small-molecule such as KL001. This could potentially be achieved by including these terms directly in the prediction step of the MPC. Uncertainty and individual variability in PK/PD measurements may reduce the accuracy of such an approach, however, further study is necessary to determine the extent of this variability, and how these inaccuracies affect controller performance.

It is our hope that these and similar control theoretic methods will inform the discovery of circadian therapies, and enable novel experimental design toward better understanding the dynamics of cellular populations and communication.

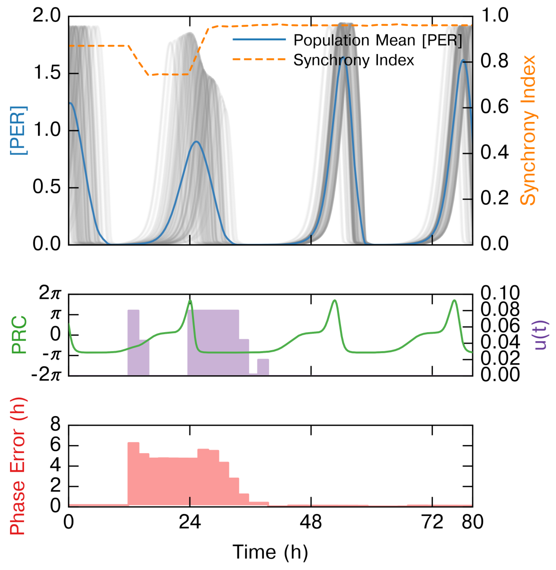

Figure 7.4: Application of the phase PDF controller to achieve a phase delay of 6 h ($\Delta\phi = -\pi/2$) at $t_{shift} = 12$ h for a population of 200 oscillators (individual trajectories plotted in gray). This controller explicitly accounted for synchrony of the population. After a brief input to begin the shift, the controller delayed the majority of its input to find a region where population synchrony would be maintained. Indeed, synchrony is slightly improved by the control action, and a phase delay of $6h$ was achieved.

Chapter 8

Summary and future directions: preliminary and proposed studies of circadian control

The prior two chapters have presented preliminary theoretical studies of circadian control. The first result, a comparison of optimal with model predictive control, presents an important benchmark for the performance of any applied control scheme, and uses this to identify how MPC design parameters affect control optimality. The second result proposes a method for controlling populations of oscillators without adversely affecting population synchrony. While these propose a path toward translational closed-loop circadian control, there are remaining challenges before either may be implemented.

Herein, I briefly discuss future research directions toward the control of circadian rhythms. The first of these is the development of a real-time sensor of circadian phase, an essential development for circadian control in ambulatory conditions. The second proposed direction involves improving control abilities by relaxing the assumption that the oscillator stays near its limit cycle. By relaxing this assumption, we may shift the oscillator closer to its fixed point, where phases are more condensed in state space, and therefore may be shifted between more easily.

8.1 Closing the loop: development of a circadian phase sensor

Although we have made significant progress in developing control algorithms for circadian oscillation, there remains significant barriers to achieving closed-loop control in clinical settings. Most prominently, there is little current capability for real-time sensing of circadian phase, and even less ability when invasive or expensive methods are excluded. Open loop control does not require sensing of phase, and therefore it has been used exclusively to-date in publicly available phase resetting protocols [131]. The ability of feedback control to overcome imprecise modeling and poor model assumptions arises directly from the incorporation of feedback, and so sensing phase is an essential component of more advanced control systems. In clinical settings, circadian phase is generally assessed by salivary or blood melatonin levels, core body temperature (as recorded from a rectal thermometer), or, rarely, cortisol levels [129, 286, 287]. While these techniques allow precise phase calculations in clinic, they are insufficient for ambulatory settings and prohibitively invasive for widespread adoption.

There has been a recent push to use machine learning techniques to sense circadian phase from ambulatory data; for example, recent studies have combined skin temperature sensors and actigraphy recordings to estimate phase [130, 278]. Machine learning methods have shown promise and improved performance in comparison simple multiple regression models, with the majority of phase estimates within ±0.3 radians (approximately 1 h). In these cases, the actigraphy recordings provided little utility in comparison to the skin temperature sensors [278]. However, actigraphy data is the most readily available to the average individual through motion sensing in smartphones or smartwatches. An improved approach might include sampling the individual's ambient light environment in addition to activity. Data of this sort have already been collected by the Klerman lab at Harvard Medical School/Brigham and Women's Hospital from a cohort of approximately 150 college undergraduates. A logical next step would be using machine learning to estimate continuous phase from this dataset, and compare with clinical phase measurements.

A potentially helpful approach in linking the sensor to the control algorithm would be the use of a confidence index, a scalar metric describing the historical accuracy of phase prediction given the input data [288]. In this case, the confidence index could indicate a high degree of certainty in the estimated phase, or if the confidence in phase estimation is low, a high degree of certainty regarding the predicted response (i.e. if all likely phases result in the same phase shift). This metric would then be used to tune the aggressiveness of the controller or the sampling rate. A simple confidence index would, for example, stop control action when in the vicinity of ipPRC zero crosses, to prevent accidentally shifting the phase in the non-optimal direction. Approaches such as those in Chapter 6 could be used to similarly find bounds on the error incurred due to imprecision in the phase estimation, and these calculations would dictate how the confidence index would be incorporated into the controller.

When combined with the MPC approaches from the prior two chapters, the development of a phase sensor will enable the first closed-loop control of circadian phase. Though there are no current plans to perform closed-loop human circadian control experiments, I anticipate that closed-loop circadian control will be feasible in a clinical setting within the next five years. Aside from circadian control, the ability to sense circadian phase has potential benefits in other aspects of precision medicine. For example, the majority of common pharmaceuticals target clock products, and circadian phase affects the pharmacokinetic and pharmacodynamic properties of nearly any therapeutic, since RNA abundance of about 40% of protein-coding genes are thought to cycle with a circadian rhythm [289]. Thus, the ability to accurately and noninvasively assess circadian phase is critical for the development of next-generation dynamic drug delivery strategies.

8.2 Critical-resetting MPC: leveraging the limit-cycle fixed point

Introduction

When developing controls methods for manipulating circadian phase, we made the decision to reduce the limit-cycle oscillator model to a phase-only formulation. In doing so, we reduced the dimensionality of state space from n dimensions to a single dimension. This allowed simple use of the phase response curve to identify when the oscillator would be phase-delayed or phase-advanced by the stimulus. We applied control based off the ipPRC we calculated, and referred to such a PRC as “type 1.” For large perturbations, or in some cases repeated perturbations [11], a “type 0” PRC has also been observed [290]. A type 0 PRC (called so because the mean slope of the phase transition curve, or PTC, is 0) contains a discontinuity resulting from the large magnitude phase shifts it describes. This discontinuity mathematically arises from the oscillator being shifted far from the limit cycle in state space, and as a result, only having access to a subset of all possible final phases.

Type 0 resetting that results from the oscillator being pushed close to the critical point (from here, called “critical resetting”) has an additional feature: a sustained reduction in the amplitude of circadian processes such as melatonin or core body temperature rhythms, which reverts to the pre-stimulus amplitude very slowly [11, 291]. The critical point is without phase, and correspondingly, individuals that have been shifted sufficiently near this point may be easily phase shifted into any desirable final phase. Thus, it is feasible to design a "critical MPC" protocol for achieving large phase shifts by first forcing the individual to the critical point, then aligning them with the desired final phase. However, this violates the phase-only assumption of the prior chapters.

A further to-date unexplained curiosity from these early studies of human circadian phase and amplitude resetting is that only a fraction ($\approx 25\%$) of individuals respond to an identical series of stimuli with a critical resetting. The preliminary work in this section sought to first explain this result, and in doing so, determine if critical resetting may be more widely achieved and used in circadian control.

Modeling light input to the human circadian oscillator

The most widely-used model of the circadian clock was developed by Kronauer and his collaborators nearly two decades ago [11, 292]. This model incorporates two processes.

Process P is a limit cycle oscillator, modified from the van der Pol oscillator, intended to capture endogenous circadian oscillation. The two states of process P are given by:

$$\frac{dX}{dt} = \left(\frac{\pi}{12}\right)\left(X_c + \mu\left(\frac{1}{3}X + \frac{4}{3}X^3 - \frac{256}{105}X^7\right) + B(t)\right) \tag{8.1}$$

$$\frac{dX_c}{dt} = \left(\frac{\pi}{12}\right)\left(qB(t)\left(\frac{24}{0.99729\tau}\right)^2 X_c X + kB(t)X\right) \tag{8.2}$$

where X represents core body temperature, and X_c is a non-biological co-state that drives oscillation. Parameter τ, here, is the period of oscillation, which may be selected *a priori* and is typically set to 24.2 h, to correspond with the human circadian period [275]. The kinetic parameters μ, q, and k do not have biological significance beyond parameterizing the shape of the limit cycle and are given in [11]. Term $B(t)$ is the photic drive, which is determined by process L.

Process L describes the dynamic effect of light input into the oscillator. Experiments where light pulses were applied for varying durations and with varying spacing have shown that light response is pseudosaturating. That is, the initial response to the pulse evokes a large-magnitude shift. Continuing the light stimulus for a longer duration yields diminishing returns, until a constant, low level of drive is reached. This response can be captured by modeling the dynamics of a population of light receptors, where $n(t)$ are the fraction of the population that is inactive, and $1 - n(t)$ are active. The conversion between active and inactive states is given by

$$\frac{dn}{dt} = 60(\alpha(t)(1-n) - \beta n) \tag{8.3}$$

where α and β are the kinetic rates of inactivation and activation, respectively. Thus, after a constant, sustained pulse, the fraction of the population that is active is given by $n_\infty = \alpha/(\alpha+\beta)$, yielding the pseudosaturation. The kinetic term α is a function of light intensity, given by

$$\alpha(t) = \alpha_0 \left(\frac{I}{I_0}\right)^p. \tag{8.4}$$

The light drive from the receptors, $\hat{B}(t)$, is then a function of light intensity and the fraction of active states:

$$\hat{B}(t) = G\alpha(t)(1-n(t)). \tag{8.5}$$

Because the clock is more sensitive to light at certain phases, $\hat{B}$ is rescaled by the photic sensitivity state of the oscillator, to yield the effective light drive term $B(t)$:

$$B(t) = (1-0.4X)(1-0.4X_c)\hat{B}(t), \tag{8.6}$$

which is incorporated in process P. The techniques used for fitting this model are explained in detail in [11].

Importantly, this model was fit to exhibit critical resetting in response to three five-hour pulses centered at the core body temperature (X) minimum (corresponding to approximately 5AM local time).

Inter-individual period variability explains critical resetting prevalence

Core body temperature minimum corresponds to the positive zero-cross of the type 1 PRC for this model (see Figure 11 in [11]). The critical resetting protocol (three 5-h pulses of 9500 lux 19 h

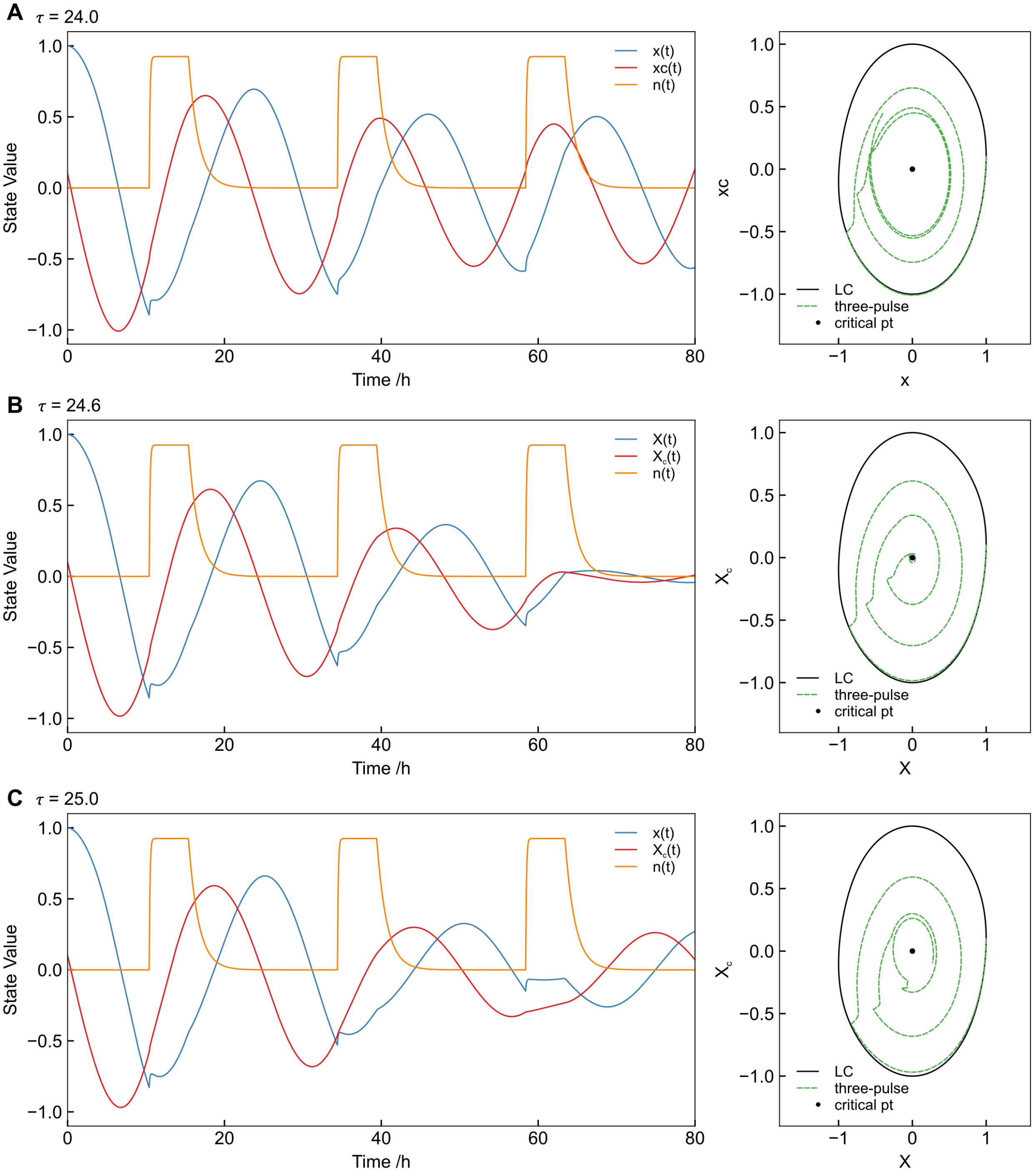

Figure 8.1: Simulation of the three pulse experiment from [11] demonstrates effect of period on critical resetting. Periods that are short (**A**) or long (**C**) do not reach the critical point, whereas an intermediate value (**B**) yields a trajectory that very nearly approaches the critical point.

apart, centered at core body temperature minimum on the first day) is therefore highly sensitive to period variability. If the oscillatory period is too short, the 5 h pulse will occur primarily after the minimum, in the phase advance region. This would result in the ensuing core body temperature minimum occurring even earlier due to the phase advance, and the ensuing pulse falling further into the phase advance region each time, and missing the timing that results in a critical resetting. Likewise, if the period is too long, the pulse will be applied primarily before the minimum, incurring phase delays. The minimum will occur later each each day, and the pulse will not be delayed, resulting in also missing the core body temperature minimum.

Three simulation examples of the three-pulse experiment are shown in Figure 8.1, demonstrating the effect of short period (8.1A), "just right" period (8.1B), and long period (8.1C) responses to the protocol. Human period is near 24.2 h, but varies between individuals (24.18 ± 0.13 mean ± standard deviation [275]), and so this may explain why only some individuals achieve a critical reset.

To test this further, I performed this simulation for a range of τ values and plotted the distance to the critical point following the third pulse (Figure 8.2). The results show that slight changes in the period drastically alter the timing of each pulse, and thus the final distance to the critical point. Importantly, the "perfect" predicted period for achieving a critical resetting ($\approx$ 24.6 h) is dependent on the whole model parameterization in addition to τ, and therefore may not exactly correspond to that observed in humans. However, I predict that the general trend will be the same: the damping of amplitudes indicative of a critical resetting will be a function of individual period, with both long and short periods unable to reach the critical point.

A simple feedback control scheme to achieve critical resetting

Achieving a critical reset is desirable for the ability to return to the limit cycle at any phase following the resetting. The prior result suggests that simply applying the three light pulses under feedback control would allow targeting of the core body temperature minimum, even if it were to shift following a light pulse. This would enable critical resetting even in individuals that could not achieve it under open loop (i.e. no feedback) application of light. Here, I tested that prediction.

To do so, I first identified the phase at which the light pulse begins for the optimal individual

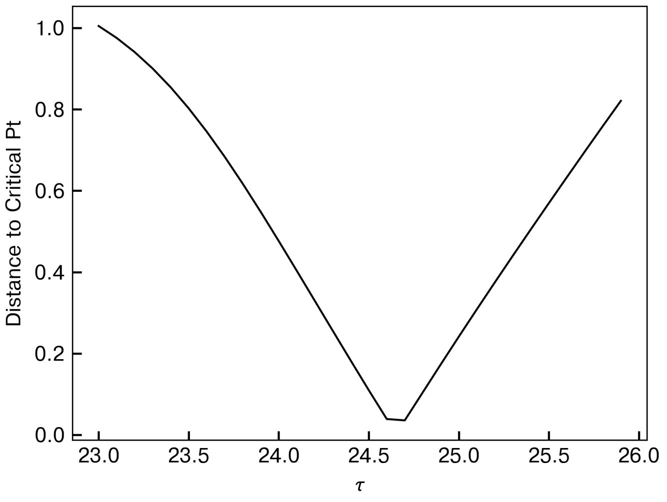

Figure 8.2: Simulation of the three pulse experiment from [11] yields a plot of distance from the critical point for a range of individual periods (τ).

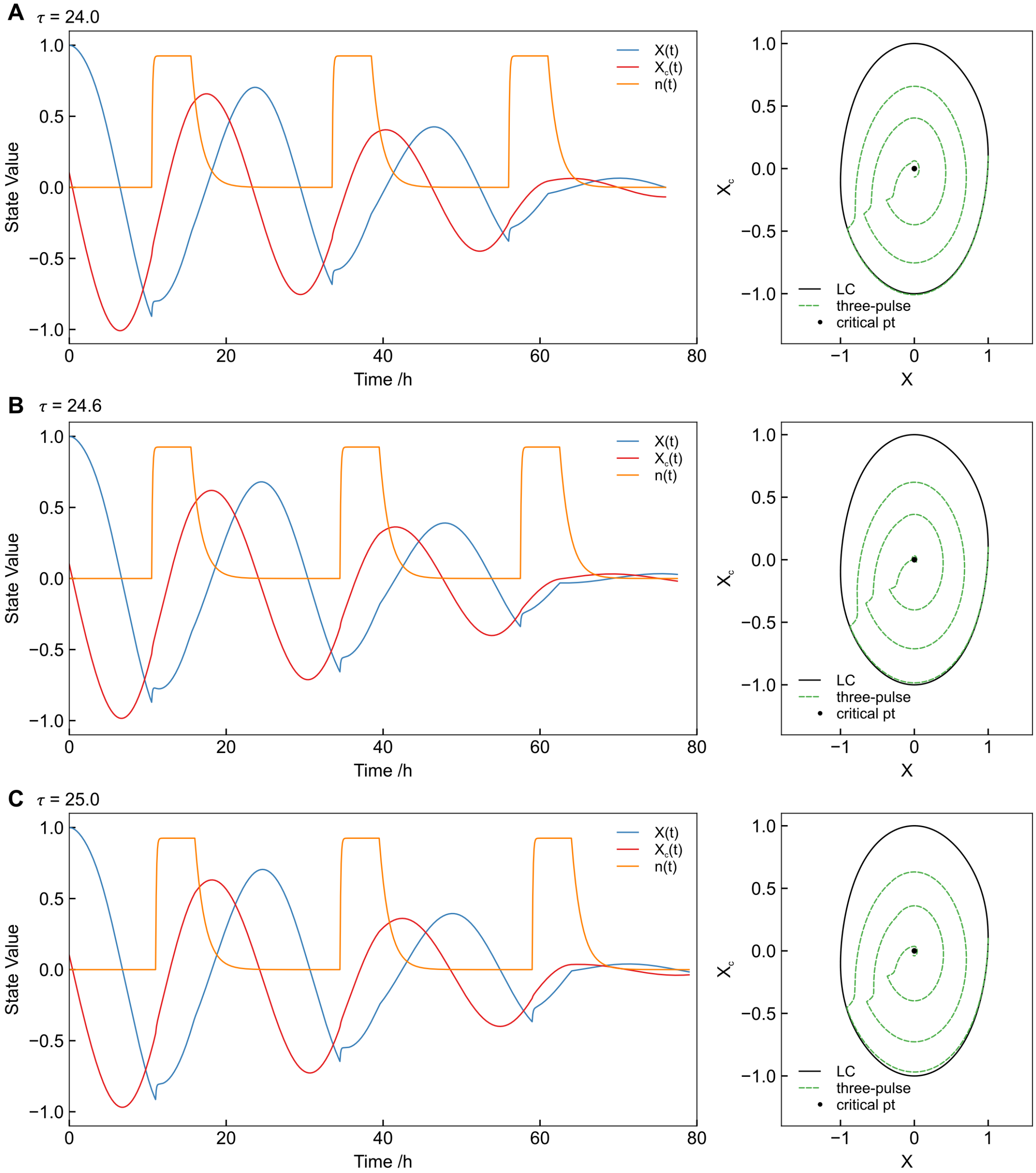

Figure 8.3: Simulation of the three pulse experiment from [11] under closed-loop control. Oscillators with periods that are short (**A**) or long (**C**) are now able to reach the critical point comparably to that with the “ideal” period length of 24.6 h (**B**).

period ($\tau = 24.6$ h). This phase was found to be approximately 2.66 radians, and denoted ϕ_{start}. I then performed feedback control simulations where the phase was calculated every 30 minutes. When the measured phase first exceeded ϕ_{start}, the 5 h pulse was applied. Phase tracking resumed following the pulse.

Figures 8.3 and 8.4 demonstrate the results of the three pulse experiment now under feedback control. Because the application of light is now performed in closed-loop, a critical resetting is achieved irrespective of long or short oscillatory periods (Figure 8.3A,C). Furthermore, any oscillator with a period within physiological range is predicted to approach the critical point under closed-loop control (Figure 8.4).

These very encouraging results warrant further examination, and work is currently underway to (i) design a feedback control protocol based on amplitude response curves rather than phase comparison, and (ii) determine if it is feasible to implement such a strategy in a clinical or ambulatory setting. Toward aim (i), the infinitesimal parametric amplitude response curve can be calculated for this model for the light input (term $B(t)$). This might allow us to better guide the delivery of light based on properties of the oscillator, rather than simply relying on repeating a clinical protocol. In approaching aim (ii), the essential element for implementing this protocol is the ability to sense phase sufficiently accurately for achieving a critical reset. A first step, then, would be examining exactly how sensitive critical resetting is to mistimed application of the light pulse due to imprecisions in on-line phase sensing. The controller, as currently formulated, applies feedback within a half hour of the desired phase. This is sufficient to achieve critical resetting, as errors do not compound from cycle-to-cycle, unlike the open loop case.

8.3 Conclusion

In sum, closed-loop circadian control is a relatively unexplored problem at the interface of control theory and systems biology. Whether by incurring incremental shifts via a pharmaceutical stimulus, or by exploiting the oscillatory critical point, circadian control has the potential to improve quality of life for shift workers or any individual attempting to maximize cognitive or physical performance. Though significant challenges remain in implementing closed-loop circadian control, the technology to do so exists. It is my hope that the research contained in this dissertation is an incremental step in the direction of understanding and control over the circadian rhythms that affect nearly every living organism.

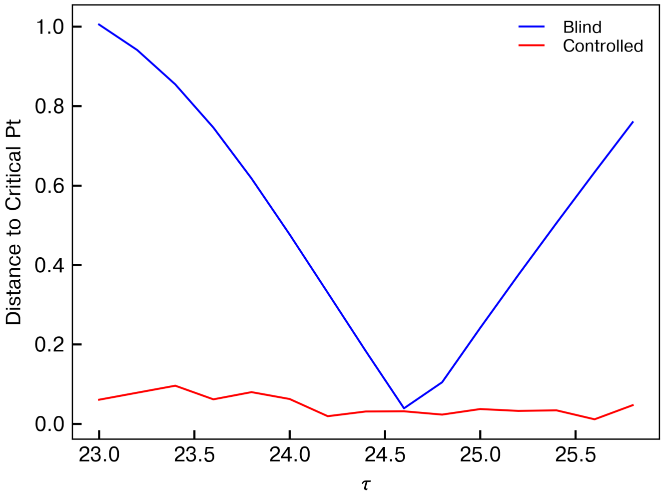

Figure 8.4: Simulation of the three pulse experiment from [11] either shooting blind (open-loop) or under closed-loop control yields a plot of distance from the critical point for a range of individual periods (τ). Notably, the distance to the critical point is reduced in all cases.

Bibliography

[1] S. M. Reppert and D. R. Weaver, "Coordination of circadian timing in mammals," *Nature*, vol. 418, no. 6901, pp. 935–941, 2002.

[2] P. E. Hardin, "The circadian timekeeping system of Drosophila," *Curr. Biol.*, vol. 15, no. 17, pp. R714–R722, 2005.

[3] S. L. Harmer, J. B. Hogenesch, M. Straume, H. S. Chang, B. Han, T. Zhu, X. Wang, J. A. Kreps, and S. A. Kay, "Orchestrated transcription of key pathways in Arabidopsis by the circadian clock," *Science*, vol. 290, no. 5499, pp. 2110–2113, 2000.

[4] J. C. Dunlap, "The Neurospora Circadian System," *J. Biol. Rhythms*, vol. 19, no. 5, pp. 414–424, 2004.

[5] M. Ishiura, S. Kutsuna, S. Aoki, H. Iwasaki, C. R. Andersson, A. Tanabe, S. S. Golden, C. H. Johnson, and T. Kondo, "Expression of a gene cluster kaiABC as a circadian feedback process in cyanobacteria," *Science*, vol. 281, no. 5382, pp. 1519–1523, 1998.

[6] M. Nakajima, K. Imai, H. Ito, T. Nishiwaki, Y. Murayama, H. Iwasaki, T. Oyama, and T. Kondo, "Reconstitution of circadian oscillation of cyanobacterial KaiC phosphorylation in vitro," *Science*, vol. 308, no. 5720, pp. 414–415, 2005.

[7] J. C. Dunlap, "Molecular Bases for Circadian Clocks," *Cell*, vol. 96, no. 2, pp. 271–290, 1999.

[8] J. S. O'Neill, G. van Ooijen, L. E. Dixon, C. Troein, F. Corellou, F.-Y. Bouget, A. B. Reddy, and A. J. Millar, "Circadian rhythms persist without transcription in a eukaryote," *Nature*, vol. 469, no. 7331, pp. 554–558, 2011.

[9] D. K. Welsh, J. S. Takahashi, and S. A. Kay, "Suprachiasmatic nucleus: cell autonomy and network properties," *Annu. Rev. Physiol.*, vol. 72, pp. 551–577, 2010.

[10] F. J. Doyle III, R. Gunawan, N. Bagheri, H. Mirsky, and T. L. To, "Circadian rhythm: A natural, robust, multi-scale control system," *Comput. Chem. Eng.*, vol. 30, no. 10-12, pp. 1700–1711, 2006.

[11] R. E. Kronauer, D. B. Forger, and M. E. Jewett, "Quantifying human circadian pacemaker response to brief, extended, and repeated light stimuli over the phototopic range," *J. Biol. Rhythms*, vol. 14, no. 6, pp. 500–515, 1999.

[12] M. E. Jewett, D. B. Forger, and R. E. Kronauer, "Revised Limit Cycle Oscillator Model of Human Circadian Pacemaker," *J. Biol. Rhythms*, vol. 14, no. 6, pp. 493–500, 1999.

[13] J.-C. Leloup and A. Goldbeter, "Toward a detailed computational model for the mammalian circadian clock," *Proc. Natl. Acad. Sci. U. S. A.*, vol. 100, pp. 7051–7056, 2003.

[14] D. Gonze, J. Halloy, J.-C. Leloup, and A. Goldbeter, “Stochastic models for circadian rhythms: effect of molecular noise on periodic and chaotic behaviour,” *C. R. Biol.*, vol. 326, no. 2, pp. 189–203, 2003.

[15] D. B. Forger and C. S. Peskin, “Stochastic simulation of the mammalian circadian clock,” *Proc. Natl. Acad. Sci. U. S. A.*, vol. 102, no. 2, pp. 321–324, 2005.

[16] T.-L. To, M. A. Henson, E. D. Herzog, and F. J. Doyle III, “A molecular model for intercellular synchronization in the mammalian circadian clock,” *Biophys. J.*, vol. 92, no. 11, pp. 3792–3803, 2007.

[17] H. P. Mirsky, A. C. Liu, D. K. Welsh, S. A. Kay, and F. J. Doyle III, “A model of the cell-autonomous mammalian circadian clock,” *Proc. Natl. Acad. Sci. U. S. A.*, vol. 106, no. 27, pp. 11 107–11 112, 2009.

[18] C. H. Ko, Y. R. Yamada, D. K. Welsh, E. D. Buhr, A. C. Liu, E. E. Zhang, M. R. Ralph, S. A. Kay, D. B. Forger, and J. S. Takahashi, “Emergence of noise-induced oscillations in the central circadian pacemaker,” *PLoS Biol.*, vol. 8, no. 10, p. e1000513, 2010.

[19] T. Hirota, J. W. Lee, P. C. St. John, M. Sawa, K. Iwaisako, T. Noguchi, P. Y. Pongsawakul, T. Sonntag, D. K. Welsh, D. A. Brenner, F. J. Doyle III, P. G. Schultz, and S. A. Kay, “Identification of small molecule activators of cryptochrome,” *Science*, vol. 337, no. 6098, pp. 1094–1097, 2012.

[20] D. Gonze and A. Goldbeter, “Circadian rhythms and molecular noise,” *Chaos*, vol. 16, no. 2, p. 026110, 2006.

[21] J. Rougemont and F. Naef, “Dynamical signatures of cellular fluctuations and oscillator stability in peripheral circadian clocks,” *Mol. Syst. Biol.*, vol. 3, p. 93, 2007.

[22] S. R. Taylor, R. Gunawan, L. R. Petzold, and F. J. Doyle III, “Sensitivity Measures for Oscillating Systems: Application to Mammalian Circadian Gene Network,” *IEEE Trans. Automat. Contr.*, vol. 53, pp. 177–188, 2008.

[23] A. Wilkins, B. Tidor, J. White, and P. Barton, “Sensitivity analysis for oscillating dynamical systems,” *SIAM J. Sci. Comput.*, vol. 31, no. 4, pp. 2706–2732, 2009.

[24] P. C. St John and F. J. Doyle III, “Estimating confidence intervals in predicted responses for oscillatory biological models,” *BMC Syst. Biol.*, vol. 7, no. 71, 2013.

[25] S. R. Taylor, A. Cheever, and S. M. Harmon, “Velocity response curves demonstrate the complexity of modeling entrainable clocks,” *J. Theor. Biol.*, vol. 363, pp. 307–317, 2014.

[26] N. Bagheri, S. R. Taylor, K. Meeker, L. R. Petzold, and F. J. Doyle III, “Synchrony and entrainment properties of robust circadian oscillators,” *J. R. Soc. Interface*, vol. 5, pp. S17–S28, 2008.

[27] N. Bagheri, J. Stelling, and F. J. Doyle III, “Circadian Phase Resetting via Single and Multiple Control Targets,” *PLoS Comput. Biol.*, vol. 4, no. 7, p. e1000104, 2008.

[28] K. Serkh and D. B. Forger, “Optimal Schedules of Light Exposure for Rapidly Correcting Circadian Misalignment,” *PLoS Comput. Biol.*, vol. 10, no. 4, p. e1003523, 2014.

[29] J. Zhang, W. Qiao, J. T. Wen, and A. Julius, "Light-based circadian rhythm control: Entrainment and optimization," *Automatica*, vol. 68, pp. 44–55, 2016.

[30] C. R. McClung, "Plant Circadian Rhythms," *Plant Cell*, vol. 18, no. 4, pp. 792–803, 2006.

[31] J. de Mairan, "Observation botanique," *Hist. Acad. Roy. Sci*, vol. 35, p. 36, 1729.

[32] A. Kiesel, "Untersuchungen zur physiologie des facettierten auges," *Akad. Wiss. Wien*, 1894.

[33] C. P. Richter, "A behavioristic study of the activity of the rat," *Comp. Psychol. Monogr.*, 1922.

[34] R. J. Konopka and S. Benzer, "Clock mutants of Drosophila melanogaster," *Proc. Natl. Acad. Sci. U. S. A.*, vol. 68, no. 9, pp. 2112–2116, 1971.

[35] P. E. Hardin, J. C. Hall, and M. Rosbash, "Feedback of the Drosophila period gene product on circadian cycling of its messenger RNA levels," *Nature*, vol. 343, no. 6258, pp. 536–540, 1990.

[36] L. Vosshall, J. Price, A. Sehgal, L. Saez, and M. Young, "Block in nuclear localization of period protein by a second clock mutation, timeless," *Science*, vol. 263, no. 5153, pp. 1606–1609, 1994.

[37] M. H. Vitaterna, C. P. Selby, T. Todo, H. Niwa, C. Thompson, E. M. Fruechte, K. Hitomi, R. J. Thresher, T. Ishikawa, J. Miyazaki, J. S. Takahashi, and A. Sancar, "Differential regulation of mammalian Period genes and circadian rhythmicity by cryptochromes 1 and 2," *Proc. Natl. Acad. Sci. U. S. A.*, vol. 96, no. 21, pp. 12 114–12 119, 1999.

[38] M. H. Vitaterna, D. P. King, A. M. Chang, J. M. Kornhauser, P. L. Lowrey, J. D. McDonald, W. F. Dove, L. H. Pinto, F. W. Turek, and J. S. Takahashi, "Mutagenesis and mapping of a mouse gene, Clock, essential for circadian behavior," *Science*, vol. 264, no. 5159, pp. 719–725, 1994.

[39] T. Darlington, K. Wager-Smith, M. Ceriani, D. Staknis, N. Gekakis, T. Steeves, C. Weitz, J. Takahashi, and S. Kay, "Closing the Circadian Loop: CLOCK-Induced Transcription of Its Own Inhibitors per and tim," *Science*, vol. 280, no. 5369, pp. 1599–1603, 1998.

[40] E. E. Zhang, A. C. Liu, T. Hirota, L. J. Miraglia, G. Welch, P. Y. Pongsawakul, X. Liu, A. Atwood, J. W. Huss, J. Janes, A. I. Su, J. B. Hogenesch, and S. A. Kay, "A genome-wide RNAi screen for modifiers of the circadian clock in human cells," *Cell*, vol. 139, no. 1, pp. 199–210, 2009.

[41] J. S. Takahashi, "Transcriptional architecture of the mammalian circadian clock," *Nat. Rev. Genet.*, vol. 18, no. 3, pp. 164–179, 2017.

[42] P. L. Lowrey and J. S. Takahashi, "Mammalian circadian biology: elucidating genome-wide levels of temporal organization," *Annu. Rev. Genomics Hum. Genet.*, vol. 5, no. 47, pp. 407–441, 2004.

[43] R. S. Edgar, E. W. Green, Y. Zhao, G. van Ooijen, M. Olmedo, X. Qin, Y. Xu, M. Pan, U. K. Valekunja, K. A. Feeney, E. S. Maywood, M. H. Hastings, N. S. Baliga, M. Merrow, A. J. Millar, C. H. Johnson, C. P. Kyriacou, J. S. O'Neill, and A. B. Reddy, "Peroxiredoxins are conserved markers of circadian rhythms," *Nature*, vol. 489, no. 7417, pp. 590–590, 2012.

[44] J. C. Dunlap, J. J. Loros, and P. J. DeCoursey, *Chronobiology*. Sinauer Associates, Inc., 2004.

[45] E. D. Herzog and R. M. Huckfeldt, “Circadian Entrainment to Temperature, But Not Light, in the Isolated Suprachiasmatic Nucleus,” *J. Neurophysiol.*, vol. 90, no. 2, pp. 763–770, 2003.

[46] C. H. Ko and J. S. Takahashi, “Molecular components of the mammalian circadian clock,” *Hum. Mol. Genet.*, vol. 15, no. 2, pp. 271–277, 2006.

[47] J. A. Mohawk, C. B. Green, and J. S. Takahashi, “Central and Peripheral Circadian Clocks in Mammals,” *Annu. Rev. Neurosci.*, vol. 35, no. 1, pp. 445–462, 2012.

[48] K. A. Lamia, K.-F. Storch, and C. J. Weitz, “Physiological significance of a peripheral tissue circadian clock,” *Proc. Natl. Acad. Sci. U. S. A.*, vol. 105, no. 39, pp. 15 172–15 177, 2008.

[49] S. Panda, M. P. Antoch, B. H. Miller, A. I. Su, A. B. Schook, M. Straume, P. G. Schultz, S. A. Kay, J. S. Takahashi, and J. B. Hogenesch, “Coordinated transcription of key pathways in the mouse by the circadian clock,” *Cell*, vol. 109, no. 3, pp. 307–320, 2002.

[50] H. R. Ueda, W. Chen, A. Adachi, H. Wakamatsu, S. Hayashi, T. Takasugi, M. Nagano, K.-i. Nakahama, Y. Suzuki, S. Sugano, M. Iino, Y. Shigeyoshi, and S. Hashimoto, “A transcription factor response element for gene expression during circadian night,” *Nature*, vol. 418, no. 6897, pp. 534–539, 2002.

[51] K.-A. Stokkan, “Entrainment of the Circadian Clock in the Liver by Feeding,” *Science*, vol. 291, no. 5503, pp. 490–493, 2001.

[52] C. B. Green, J. S. Takahashi, and J. Bass, “The Meter of Metabolism,” *Cell*, vol. 134, no. 5, pp. 728–742, 2008.

[53] B. Marcheva, K. M. Ramsey, E. D. Buhr, Y. Kobayashi, H. Su, C. H. Ko, G. Ivanova, C. Omura, S. Mo, M. H. Vitaterna, J. P. Lopez, L. H. Philipson, C. A. Bradfield, S. D. Crosby, L. JeBailey, X. Wang, J. S. Takahashi, and J. Bass, “Disruption of the clock components CLOCK and BMAL1 leads to hypoinsulinaemia and diabetes,” *Nature*, vol. 466, no. 7306, pp. 627–631, 2010.

[54] M. Hatori, C. Vollmers, A. Zarrinpar, L. DiTacchio, E. A. Bushong, S. Gill, M. Leblanc, A. Chaix, M. Joens, J. A. Fitzpatrick, M. H. Ellisman, and S. Panda, “Time-Restricted Feeding without Reducing Caloric Intake Prevents Metabolic Diseases in Mice Fed a High-Fat Diet,” *Cell Metab.*, vol. 15, no. 6, pp. 848–860, 2012.

[55] H. C. Chang and L. Guarente, “XSIRT1 mediates central circadian control in the SCN by a mechanism that decays with aging,” *Cell*, vol. 153, no. 7, pp. 1448–1460, 2013.

[56] A. Pan, E. S. Schernhammer, Q. Sun, and F. B. Hu, “Rotating night shift work and risk of type 2 diabetes: Two prospective cohort studies in women,” *PLoS Med.*, vol. 8, no. 12, 2011.

[57] A. Mukherji, A. Kobiita, M. Damara, N. Misra, H. Meziane, M.-F. Champy, and P. Chambon, “Shifting eating to the circadian rest phase misaligns the peripheral clocks with the master SCN clock and leads to a metabolic syndrome,” *Proc. Natl. Acad. Sci. U. S. A.*, vol. 112, no. 48, pp. E6691–E6698, 2015.

[58] K. Wulff, S. Gatti, J. G. Wettstein, and R. G. Foster, “Sleep and circadian rhythm disruption in psychiatric and neurodegenerative disease,” *Nat. Rev. Neurosci.*, vol. 11, no. 8, pp. 589–599, 2010.

[59] R. Yehuda, M. H. Teicher, R. L. Trestman, R. A. Levengood, and L. J. Siever, “Cortisol regulation in posttraumatic stress disorder and major depression: A chronobiological analysis,” *Biol. Psychiatry*, vol. 40, no. 2, pp. 79–88, 1996.

[60] A. M. Rosenwasser, “Circadian clock genes: Non-circadian roles in sleep, addiction, and psychiatric disorders?” *Neurosci. Biobehav. Rev.*, vol. 34, no. 8, pp. 1249–1255, 2010.

[61] B. Lemmer, “Circadian rhythms and drug delivery,” *J. Control. Release*, vol. 16, no. 1-2, pp. 63–74, 1991.

[62] F. Lévi, A. Okyar, S. Dulong, P. F. Innominato, and J. Clairambault, “Circadian Timing in Cancer Treatments,” *Annu. Rev. Pharmacol. Toxicol.*, vol. 50, no. 1, pp. 377–421, 2010.

[63] J. S. O’Neill and A. B. Reddy, “Circadian clocks in human red blood cells,” *Nature*, vol. 469, no. 7331, pp. 498–503, 2011.

[64] R. Ye, C. P. Selby, N. Ozturk, Y. Annayev, and A. Sancar, “Biochemical Analysis of the Canonical Model for the Mammalian Circadian Clock,” *J. Biol. Chem.*, vol. 286, no. 29, pp. 25 891–25 902, 2011.

[65] P. Emery and S. M. Reppert, “A Rhythmic Ror,” *Neuron*, vol. 43, no. 4, pp. 443–446, 2004.

[66] J. C. Dunlap and J. J. Loros, “Just-So Stories and Origin Myths: Phosphorylation and Structural Disorder in Circadian Clock Proteins,” *Mol. Cell*, no. 2017, pp. 1–4, 2017.

[67] Y. Fan, A. Hida, D. a. Anderson, M. Izumo, and C. H. Johnson, “Cycling of CRYPTOCHROME Proteins Is Not Necessary for Circadian-Clock Function in Mammalian Fibroblasts,” *Curr. Biol.*, vol. 17, pp. 1091–1100, 2007.

[68] K. L. Ode and H. R. Ueda, “Design Principles of Phosphorylation-Dependent Timekeeping in Eukaryotic Circadian Clocks,” *Cold Spring Harb. Perspect. Biol.*, p. a028357, 2017.

[69] K. L. Ode, H. Ukai, E. A. Susaki, R. Narumi, K. Matsumoto, J. Hara, N. Koide, T. Abe, M. T. Kanemaki, H. Kiyonari, and H. R. Ueda, “Knockout-Rescue Embryonic Stem Cell-Derived Mouse Reveals Circadian-Period Control by Quality and Quantity of CRY1,” *Mol. Cell*, vol. 65, no. 1, pp. 176–190, 2017.

[70] H. R. Ueda, S. Hayashi, W. Chen, M. Sano, M. Machida, Y. Shigeyoshi, M. Iino, and S. Hashimoto, “System-level identification of transcriptional circuits underlying mammalian circadian clocks,” *Nat. Genet.*, vol. 37, no. 2, pp. 187–192, 2005.

[71] B. C. Goodwin, “Oscillatory behavior in enzymatic control processes,” *Adv. Enzyme Regul.*, vol. 3, pp. 425–437, 1965.

[72] M. B. Elowitz, A. J. Levine, E. D. Siggia, and P. S. Swain, “Stochastic gene expression in a single cell,” *Sci. Signal.*, vol. 297, no. 5584, p. 1183, 2002.

[73] E. D. Herzog, S. J. Aton, R. Numano, Y. Sakaki, and H. Tei, “Temporal Precision in the Mammalian Circadian System: A Reliable Clock from Less Reliable Neurons,” *J. Biol. Rhythms*, vol. 19, no. 1, pp. 35–46, 2004.

[74] D. K. Welsh, S.-H. Yoo, A. C. Liu, J. S. Takahashi, and S. A. Kay, “Bioluminescence Imaging of Individual Fibroblasts Reveals Persistent, Independently Phased Circadian Rhythms of Clock Gene Expression,” *Curr. Biol.*, vol. 14, no. 24, pp. 2289–2295, 2004.

[75] N. Barkai and S. Leibler, "Circadian clocks limited by noise," *Nature*, vol. 403, no. 6767, pp. 267–268, 2000.

[76] J. H. Abel, L. A. Widmer, P. C. St. John, J. Stelling, and F. J. Doyle III, "A Coupled Stochastic Model Explains Differences in Cry Knockout Behavior," *IEEE Life Sci. Lett.*, vol. 1, no. 1, pp. 3–6, 2015.

[77] P. C. St. John and F. J. Doyle III, "Quantifying Stochastic Noise in Cultured Circadian Reporter Cells," *PLOS Comput. Biol.*, vol. 11, no. 11, p. e1004451, 2015.

[78] S.-H. Yoo, S. Yamazaki, P. L. Lowrey, K. Shimomura, C. H. Ko, E. D. Buhr, S. M. Siepka, H.-K. Hong, W. J. Oh, O. J. Yoo, M. Menaker, and J. S. Takahashi, "PERIOD2::LUCIFERASE real-time reporting of circadian dynamics reveals persistent circadian oscillations in mouse peripheral tissues," *Proc. Natl. Acad. Sci. U. S. A.*, vol. 101, no. 15, pp. 5339–5346, 2004.

[79] S. J. Aton, C. S. Colwell, A. J. Harmar, J. Waschek, and E. D. Herzog, "Vasoactive intestinal polypeptide mediates circadian rhythmicity and synchrony in mammalian clock neurons," *Nat. Neurosci.*, vol. 8, no. 4, pp. 476–483, 2005.

[80] S. J. Aton, J. E. Huettner, M. Straume, and E. D. Herzog, "GABA and Gi/o differentially control circadian rhythms and synchrony in clock neurons," *Proc. Natl. Acad. Sci. U. S. A.*, vol. 103, no. 50, pp. 19 188–19 193, 2006.

[81] J. A. Evans, T. L. Leise, O. Castanon-Cervantes, and A. J. Davidson, "Dynamic Interactions Mediated by Nonredundant Signaling Mechanisms Couple Circadian Clock Neurons," *Neuron*, vol. 80, no. 4, pp. 973–983, 2013.

[82] J. Myung, S. Hong, D. DeWoskin, E. De Schutter, D. B. Forger, and T. Takumi, "GABA-mediated repulsive coupling between circadian clock neurons in the SCN encodes seasonal time," *Proc. Natl. Acad. Sci. U. S. A.*, vol. 112, no. 29, pp. E3920–E3929, 2015.

[83] H. Albus, M. J. Vansteensel, S. Michel, G. D. Block, and J. H. Meijer, "A GABAergic mechanism is necessary for coupling dissociable ventral and dorsal regional oscillators within the circadian clock," *Curr. Biol.*, vol. 15, no. 10, pp. 886–893, 2005.

[84] D. DeWoskin, J. Myung, M. D. C. Belle, H. D. Piggins, T. Takumi, and D. B. Forger, "Distinct roles for GABA across multiple timescales in mammalian circadian timekeeping," *Proc. Natl. Acad. Sci. U. S. A.*, vol. 112, no. 29, pp. E3911–E3919, 2015.

[85] J. H. Abel, K. Meeker, D. Granados-Fuentes, P. C. St. John, T. J. Wang, B. B. Bales, F. J. Doyle III, E. D. Herzog, and L. R. Petzold, "Functional network inference of the suprachiasmatic nucleus," *Proc. Natl. Acad. Sci. U. S. A.*, vol. 113, no. 16, pp. 4512–4517, 2016.

[86] J. A. Evans, T.-C. Suen, B. L. Callif, A. S. Mitchell, O. Castanon-Cervantes, K. M. Baker, I. Kloehn, K. Baba, B. J. Teubner, J. C. Ehlen, K. N. Paul, T. J. Bartness, G. Tosini, T. Leise, and A. J. Davidson, "Shell neurons of the master circadian clock coordinate the phase of tissue clocks throughout the brain and body," *BMC Biol.*, vol. 13, no. 1, p. 43, 2015.

[87] J. Bass and J. S. Takahashi, "Circadian integration of metabolism and energetics," *Science*, vol. 330, no. 6009, pp. 1349–1354, 2010.

[88] F. Damiola, “Restricted feeding uncouples circadian oscillators in peripheral tissues from the central pacemaker in the suprachiasmatic nucleus,” *Genes Dev.*, vol. 14, no. 23, pp. 2950–2961, 2000.

[89] J. K. Kim and D. B. Forger, “A mechanism for robust circadian timekeeping via stoichiometric balance,” *Mol. Syst. Biol.*, vol. 8, no. 1, p. 630, 2012.

[90] P. O. Westermark, D. K. Welsh, H. Okamura, and H. Herzel, “Quantification of circadian rhythms in single cells,” *PLoS Comput. Biol.*, vol. 5, no. 11, p. e1000580, 2009.

[91] H. Koeppl, M. Hafner, A. Ganguly, and A. Mehrotra, “Deterministic characterization of phase noise in biomolecular oscillators,” *Phys. Biol.*, vol. 8, no. 5, p. 055008, 2011.

[92] R. J. Field, “Oscillations in chemical systems. IV. Limit cycle behavior in a model of a real chemical reaction,” *J. Chem. Phys.*, vol. 60, no. 5, p. 1877, 1974.

[93] B. van der Pol, “On “relaxation-oscillations”,” *London, Edinburgh, Dublin Philos. Mag. J. Sci.*, vol. 2, no. 11, pp. 978–992, 1926.

[94] J. Huang and D. L. Turcotte, “Are earthquakes an example of deterministic chaos?” *Geophys. Res. Lett.*, vol. 17, no. 3, pp. 223–226, 1990.

[95] C. S. Pittendrigh and S. Daan, “A functional analysis of circadian pacemakers in noctural rodents: I. The stability and lability of circadian frequency,” *J. Comp. Physiol. A*, vol. 106, pp. 223–252, 1976.

[96] M. H. Vitaterna, C. H. Ko, A.-M. Chang, E. D. Buhr, E. M. Fruechte, A. Schook, M. P. Antoch, F. W. Turek, and J. S. Takahashi, “The mouse Clock mutation reduces circadian pacemaker amplitude and enhances efficacy of resetting stimuli and phase-response curve amplitude,” *Proc. Natl. Acad. Sci. U. S. A.*, vol. 103, no. 24, pp. 9327–9332, 2006.

[97] M. Comas, D. G. M. Beersma, K. Spoelstra, and S. Daan, “Phase and period responses of the circadian system of mice (Mus musculus) to light stimuli of different duration,” *J. Biol. Rhythms*, vol. 21, no. 5, pp. 362–372, 2006.

[98] R. Gunawan, Y. Cao, L. Petzold, and F. J. Doyle III, “Sensitivity analysis of discrete stochastic systems,” *Biophys. J.*, vol. 88, no. 4, pp. 2530–2540, 2005.

[99] S. R. Pulivarthy, N. Tanaka, D. K. Welsh, L. De Haro, I. M. Verma, and S. Panda, “Reciprocity between phase shifts and amplitude changes in the mammalian circadian clock,” *Proc. Natl. Acad. Sci. U. S. A.*, vol. 104, no. 51, pp. 20 356–20 361, 2007.

[100] H. Ukai, T. J. Kobayashi, M. Nagano, K.-H. Masumoto, M. Sujino, T. Kondo, K. Yagita, Y. Shigeyoshi, and H. R. Ueda, “Melanopsin-dependent photo-perturbation reveals desynchronization underlying the singularity of mammalian circadian clocks singularity behaviour in circadian clocks,” *Nat. Cell Biol.*, vol. 9, no. 11, pp. 1327–1334, 2007.

[101] P. C. St. John, S. R. Taylor, J. H. Abel, and F. J. Doyle III, “Amplitude Metrics for Cellular Circadian Bioluminescence Reporters,” *Biophys. J.*, vol. 107, no. 11, pp. 2712–2722, 2014.

[102] H. Rabitz, M. Kramer, and D. Dacol, “Sensitivity Analysis in Chemical Kinetics,” *Annu. Rev. Phys. Chem.*, vol. 34, no. 1, pp. 419–461, 1983.

[103] M. A. Kramer, H. Rabitz, and J. M. Calo, “Sensitivity analysis of osciallatory systems,” *Appl. Math. Model.*, vol. 8, pp. 328–340, 1984.

[104] B. Novák and J. J. Tyson, “Design principles of biochemical oscillators,” *Nat. Rev. Mol. Cell Biol.*, vol. 9, no. 12, pp. 981–991, 2008.

[105] Y. Kuramoto, *Chemical oscillations, waves, and turbulence*. Springer-Verlag, 2004.

[106] D. Gonze, J. Halloy, and A. Goldbeter, “Robustness of circadian rhythms with respect to molecular noise,” *Proc. Natl. Acad. Sci. U. S. A.*, vol. 99, no. 2, pp. 673–678, 2002.

[107] J. N. Teramae and D. Tanaka, “Robustness of the noise-induced phase synchronization in a general class of limit cycle oscillators,” *Phys. Rev. Lett.*, vol. 93, no. 20, pp. 1–4, 2004.

[108] D. A. Lauffenburger, “Cell signaling pathways as control modules: Complexity for simplicity?” *Proc. Natl. Acad. Sci. U. S. A.*, vol. 97, no. 10, pp. 5031–5033, 2000.

[109] J. Bailey and W. Haddad, “Drug dosing control in clinical pharmacology,” *IEEE Control Syst. Mag.*, vol. 25, no. 2, pp. 35–51, 2005.

[110] A. A. Julius, Á. Halasz, M. S. Sakar, H. Rubin, V. Kumar, and G. J. Pappas, “Stochastic Modeling and Control of Biological Systems: The Lactose Regulation System of Escherichia Coli,” *IEEE Trans. Automat. Contr.*, vol. 53, pp. 51–65, 2008.

[111] J. P. Perley, J. Mikolajczak, M. L. Harrison, G. T. Buzzard, and A. E. Rundell, “Multiple Model-Informed Open-Loop Control of Uncertain Intracellular Signaling Dynamics,” *PLoS Comput. Biol.*, vol. 10, no. 4, 2014.

[112] G. Yan, P. E. Vértes, E. K. Towlson, Y. L. Chew, D. S. Walker, W. R. Schafer, and A.-L. Barabási, “Network control principles predict neuron function in the Caenorhabditis elegans connectome,” *Nature*, vol. 550, no. 7677, pp. 519–523, 2017.

[113] H. El-Samad, H. Kurata, J. C. Doyle, C. A. Gross, and M. Khammash, “Surviving heat shock: Control strategies for robustness and performance,” *Proc. Natl. Acad. Sci. U. S. A.*, vol. 102, no. 8, pp. 2736–2741, 2005.

[114] R. Gondhalekar, E. Dassau, and F. J. Doyle III, “Periodic zone-MPC with asymmetric costs for outpatient-ready safety of an artificial pancreas to treat type 1 diabetes,” *Automatica*, vol. 71, pp. 237–246, 2016.

[115] S. Chen, P. Harrigan, B. Heineike, J. Stewart-Ornstein, and H. El-Samad, “Building robust functionality in synthetic circuits using engineered feedback regulation,” *Curr. Opin. Biotechnol.*, vol. 24, no. 4, pp. 790–796, 2013.

[116] D. Del Vecchio, H. Abdallah, Y. Qian, and J. J. Collins, “A Blueprint for a Synthetic Genetic Feedback Controller to Reprogram Cell Fate,” *Cell Syst.*, vol. 4, no. 1, pp. 109–120, 2017.

[117] S. Craven, J. Whelan, and B. Glennon, “Glucose concentration control of a fed-batch mammalian cell bioprocess using a nonlinear model predictive controller,” *J. Process Control*, vol. 24, no. 4, pp. 344–357, 2014.

[118] N. Giordano, F. Mairet, J. L. Gouzé, J. Geiselmann, and H. de Jong, “Dynamical Allocation of Cellular Resources as an Optimal Control Problem: Novel Insights into Microbial Growth Strategies,” *PLoS Comput. Biol.*, vol. 12, no. 3, pp. 1–28, 2016.

[119] W. M. Haddad, T. Hayakawa, and J. M. Bailey, “Adaptive control for non-negative and compartmental dynamical systems with applications to general anesthesia,” *Int. J. Adapt. Control Signal Process.*, vol. 17, no. 3, pp. 209–235, 2003.

[120] C. Luni and F. J. Doyle III, “Robust multi-drug therapy design and application to insulin resistance in type 2 diabetes,” *Int. J. Robust Nonlinear Control*, vol. 21, no. 15, pp. 1730–1741, 2011.

[121] J. Yu, Y. Zhang, J. Yan, A. R. Kahkoska, and Z. Gu, “Advances in bioresponsive closed-loop drug delivery systems,” *Int. J. Pharm.*, p. (online), 2017.

[122] X. Jin, C.-S. Kim, G. A. Dumont, J. M. Ansermino, and J.-O. Hahn, “A semi-adaptive control approach to closed-loop medication infusion,” *Int. J. Adapt. Control Signal Process.*, vol. 31, no. 2, pp. 240–254, 2017.

[123] S. Amendola, R. Lodato, S. Manzari, C. Occhiuzzi, and G. Marrocco, “RFID technology for IoT-based personal healthcare in smart spaces,” *IEEE Internet Things J.*, vol. 1, no. 2, pp. 144–152, 2014.

[124] S. Zavitsanou, A. Chakrabarty, E. Dassau, and F. Doyle III, “Embedded Control in Wearable Medical Devices: Application to the Artificial Pancreas,” *Processes*, vol. 4, no. 4, p. 35, 2016.

[125] Y. Qiu, S. Tong, L. Zhang, Y. Sakurai, D. R. Myers, L. Hong, W. A. Lam, and G. Bao, “Magnetic forces enable controlled drug delivery by disrupting endothelial cell-cell junctions,” *Nat. Commun.*, vol. 8, p. 15594, 2017.

[126] N. A. Bakh, A. B. Cortinas, M. A. Weiss, R. S. Langer, D. G. Anderson, Z. Gu, S. Dutta, and M. S. Strano, “Glucose-responsive insulin by molecular and physical design,” *Nat. Chem.*, vol. 9, no. 10, pp. 937–943, 2017.

[127] N. Bagheri, J. Stelling, and F. J. Doyle III, “Circadian phase entrainment via nonlinear model predictive control,” *Int. J. Robust Nonlinear Control*, vol. 17, pp. 1555–1571, 2007.

[128] D. Efimov, P. Sacre, and R. Sepulchre, “Controlling the phase of an oscillator: A phase response curve approach,” in *IEEE Conf. Decis. Control 2009*, pp. 7692–7697.

[129] E. B. Klerman, H. B. Gershengorn, J. F. Duffy, and R. E. Kronauer, “Comparisons of the Variability of Three Markers of the Human Circadian Pacemaker,” *J. Biol. Rhythms*, vol. 17, no. 2, pp. 181–193, 2002.

[130] V. Kolodyazhniy, J. Späti, S. Frey, T. Götz, A. Wirz-Justice, K. Kräuchi, C. Cajochen, and F. H. Wilhelm, “Estimation of human circadian phase via a multi-channel ambulatory monitoring system and a multiple regression model,” *J. Biol. Rhythms*, vol. 26, no. 1, pp. 55–67, 2011.

[131] O. J. Walch, A. Cochran, and D. B. Forger, “A global quantification of "normal" sleep schedules using smartphone data,” *Sci. Adv.*, vol. 2, no. 5, p. e1501705, 2016.

[132] T. Hirota, J. W. Lee, W. G. Lewis, E. E. Zhang, G. Breton, X. Liu, M. Garcia, E. C. Peters, J.-P. Etchegaray, D. Traver, P. G. Schultz, and S. A. Kay, “High-Throughput Chemical Screen Identifies a Novel Potent Modulator of Cellular Circadian Rhythms and Reveals CKIα as a Clock Regulatory Kinase,” *PLoS Biol.*, vol. 8, no. 12, p. e1000559, 2010.

[133] P. C. St. John, T. Hirota, S. A. Kay, and F. J. Doyle III, "Spatiotemporal separation of PER and CRY posttranslational regulation in the mammalian circadian clock," *Proc. Natl. Acad. Sci. U. S. A.*, vol. 111, no. 5, pp. 2040–2045, 2014.

[134] S. An, R. Harang, K. Meeker, D. Granados-Fuentes, C. A. Tsai, C. Mazuski, J. Kim, F. J. Doyle III, L. R. Petzold, and E. D. Herzog, "A neuropeptide speeds circadian entrainment by reducing intercellular synchrony," *Proc. Natl. Acad. Sci. U. S. A.*, vol. 110, no. 46, pp. E4355–E4361, 2013.

[135] N. J. Kingsbury, S. R. Taylor, and M. A. Henson, "Inhibitory and excitatory networks balance cell coupling in the suprachiasmatic nucleus: A modeling approach," *J. Theor. Biol.*, vol. 397, pp. 135–144, 2016.

[136] C. Vasalou, E. Herzog, and M. Henson, "Small-world network models of intercellular coupling predict enhanced synchronization in the suprachiasmatic nucleus," *J. Biol. Rhythms*, vol. 24, no. 3, pp. 1–19, 2009.

[137] S. Bernard, D. Gonze, B. Cajavec, H. Herzel, and A. Kramer, "Synchronization-induced rhythmicity of circadian oscillators in the suprachiasmatic nucleus," *PLoS Comput. Biol.*, vol. 3, no. 4, p. e68, 2007.

[138] D. DeWoskin, W. Geng, A. R. Stinchcombe, and D. B. Forger, "It is not the parts, but how they interact that determines the behaviour of circadian rhythms across scales and organisms," *Interface Focus*, vol. 4, no. 3, p. 20130076, 2014.

[139] J. H. Meijer, S. Michel, H. T. VanderLeest, and J. H. T. Rohling, "Daily and seasonal adaptation of the circadian clock requires plasticity of the SCN neuronal network," *Eur. J. Neurosci.*, vol. 32, no. 12, pp. 2143–2151, 2010.

[140] G. M. Freeman, R. M. Krock, S. J. Aton, P. Thaben, and E. D. Herzog, "GABA networks destabilize genetic oscillations in the circadian pacemaker," *Neuron*, vol. 78, no. 5, pp. 799–806, 2013.

[141] S. Yamaguchi, H. Isejima, T. Matsuo, R. Okura, K. Yagita, M. Kobayashi, and H. Okamura, "Synchronization of cellular clocks in the suprachiasmatic nucleus," *Science*, vol. 302, no. 5649, pp. 1408–1412, 2003.

[142] W. J. Schwartz, R. A. Gross, and M. T. Morton, "The suprachiasmatic nuclei contain a tetrodotoxin-resistant circadian pacemaker," *Proc. Natl. Acad. Sci. U. S. A.*, vol. 84, no. 6, pp. 1694–1698, 1987.

[143] D. N. Reshef, Y. A. Reshef, H. K. Finucane, S. R. Grossman, G. McVean, P. J. Turnbaugh, E. S. Lander, M. Mitzenmacher, and P. C. Sabeti, "Detecting novel associations in large data sets," *Science*, vol. 334, no. 6062, pp. 1518–1524, 2011.

[144] V. M. Eguíluz, D. R. Chialvo, G. a. Cecchi, M. Baliki, and A. V. Apkarian, "Scale-Free Brain Functional Networks," *Phys. Rev. Lett.*, vol. 94, no. 1, p. 018102, 2005.

[145] E. D. Herzog, S. J. Aton, R. Numano, Y. Sakaki, and H. Tei, "Temporal Precision in the Mammalian Circadian System: A Reliable Clock from Less Reliable Neurons," *J. Biol. Rhythms*, vol. 19, no. 1, pp. 35–46, 2004.

[146] S. Schroder, E. D. Herzog, and I. Z. Kiss, "Transcription-based oscillator model for light-induced splitting as antiphase circadian gene expression in the suprachiasmatic nuclei," *J. Biol. Rhythms*, vol. 27, no. 1, pp. 79–90, 2012.

[147] A. B. Webb, N. Angelo, J. E. Huettner, and E. D. Herzog, "Intrinsic, nondeterministic circadian rhythm generation in identified mammalian neurons," *Proc. Natl. Acad. Sci. U. S. A.*, vol. 106, no. 38, pp. 16 493–16 498, 2009.

[148] C. A. Schneider, W. S. Rasband, and K. W. Eliceiri, "NIH Image to ImageJ: 25 years of image analysis," *Nat. Methods*, vol. 9, no. 7, pp. 671–675, 2012.

[149] D. Albanese, M. Filosi, R. Visintainer, S. Riccadonna, G. Jurman, and C. Furlanello, "Minerva and minepy: a C engine for the MINE suite and its R, Python and MATLAB wrappers," *Bioinformatics*, vol. 29, no. 3, pp. 407–408, 2013.

[150] A. A. Hagberg, "Exploring Network Structure, Dynamics, and Function using NetworkX," *Proc. 7th Python Sci. Conf.*, pp. 11–15, 2008.

[151] J. Alstott, E. Bullmore, and D. Plenz, "powerlaw: A Python Package for Analysis of Heavy-Tailed Distributions," *PLoS One*, vol. 9, no. 1, p. e85777, 2014.

[152] A. Clauset, C. R. Shalizi, and M. E. J. Newman, "Power-Law Distributions in Empirical Data," *SIAM Rev.*, vol. 51, no. 4, p. 661, 2009.

[153] K. R. Sanft, S. Wu, M. Roh, J. Fu, R. K. Lim, and L. R. Petzold, "StochKit2: software for discrete stochastic simulation of biochemical systems with events," *Bioinformatics*, vol. 27, no. 17, pp. 2457–2458, 2011.

[154] J. H. Abel, B. Drawert, A. Hellander, and L. R. Petzold, "GillesPy: A Python Package for Stochastic Model Building and Simulation," *IEEE Life Sci. Lett.*, vol. 2, no. 3, pp. 35–38, 2017.

[155] E. D. Buhr, S.-H. Yoo, and J. S. Takahashi, "Temperature as a Universal Resetting Cue for Mammalian Circadian Oscillators," *Science*, vol. 330, no. 6002, pp. 379–385, 2010.

[156] M. Garofalo, T. Nieus, P. Massobrio, and S. Martinoia, "Evaluation of the performance of information theory-based methods and cross-correlation to estimate the functional connectivity in cortical networks," *PLoS One*, vol. 4, no. 8, p. e6482, 2009.

[157] L. Bettencourt, G. Stephens, M. Ham, and G. Gross, "Functional structure of cortical neuronal networks grown in vitro," *Phys. Rev. E*, vol. 75, no. 2, p. 021915, 2007.

[158] M. Kaminski, M. Ding, W. A. Truccolo, and S. L. Bressler, "Evaluating causal relations in neural systems: Granger causality, directed transfer function and statistical assessment of significance," *Biol. Cybern.*, vol. 85, no. 2, pp. 145–157, 2001.

[159] A. Pourzanjani, E. D. Herzog, and L. R. Petzold, "On the Inference of Functional Circadian Networks Using Granger Causality," *PLoS One*, vol. 10, no. 9, p. e0137540, 2015.

[160] K. A. Fujita, Y. Toyoshima, S. Uda, Y.-i. Ozaki, H. Kubota, and S. Kuroda, "Decoupling of receptor and downstream signals in the Akt pathway by its low-pass filter characteristics," *Sci. Signal.*, vol. 3, no. 132, p. ra56, 2010.

[161] D. J. Watts and S. H. Strogatz, “Collective dynamics of ’small-world’ networks,” *Nature*, vol. 393, no. 6684, pp. 440–442, 1998.

[162] M. E. Newman, C. Moore, and D. J. Watts, “Mean-field solution of the small-world network model,” *Phys. Rev. Lett.*, vol. 84, no. 14, pp. 3201–3204, 2000.

[163] L. Yan, N. C. Foley, J. M. Bobula, L. J. Kriegsfeld, and R. Silver, “Two antiphase oscillations occur in each suprachiasmatic nucleus of behaviorally split hamsters,” *J. Neurosci.*, vol. 25, no. 39, pp. 9017–9026, 2005.

[164] J. A. Evans, J. A. Elliott, and M. R. Gorman, “Dim nighttime illumination interacts with parametric effects of bright light to increase the stability of circadian rhythm bifurcation in hamsters,” *Chronobiol. Int.*, vol. 28, no. 6, pp. 488–496, 2011.

[165] T. Watanabe, E. Naito, N. Nakao, H. Tei, T. Yoshimura, and S. Ebihara, “Bimodal Clock Gene Expression in Mouse,” *J. Biol. Rhythms*, vol. 22, no. 1, pp. 58–68, 2007.

[166] H. O. de la Iglesia, J. Meyer, A. Carpino, and W. J. Schwartz, “Antiphase oscillation of the left and right suprachiasmatic nuclei,” *Science*, vol. 290, no. 5492, pp. 799–801, 2000.

[167] H. Ohta, S. Yamazaki, and D. G. McMahon, “Constant light desynchronizes mammalian clock neurons,” *Nat. Neurosci.*, vol. 8, no. 3, pp. 267–269, 2005.

[168] S. Michel, R. Marek, H. T. VanderLeest, M. J. VanSteensel, W. J. Schwartz, C. S. Colwell, and J. H. Meijer, “Mechanism of bilateral communication in the suprachiasmatic nucleus,” *Eur. J. Neurosci.*, vol. 37, no. 6, pp. 964–971, 2013.

[169] F. Ebling, “The role of glutamate in the photic regulation of the suprachiasmatic nucleus,” *Prog. Neurobiol.*, vol. 50, no. 2-3, pp. 109–132, 1996.

[170] P. Indic, W. J. Schwartz, and D. Paydarfar, “Design principles for phase-splitting behaviour of coupled cellular oscillators: clues from hamsters with ’split’ circadian rhythms,” *J. R. Soc. Interface*, vol. 5, no. 25, pp. 873–883, 2008.

[171] R. Albert and A.-L. Barabási, “Statistical mechanics of complex networks,” *Rev. Mod. Phys.*, vol. 74, no. 1, pp. 47–97, 2002.

[172] M. Hafner, H. Koeppl, and D. Gonze, “Effect of network architecture on synchronization and entrainment properties of the circadian oscillations in the suprachiasmatic nucleus,” *PLoS Comput. Biol.*, vol. 8, no. 3, 2012.

[173] J. Ozik, B. R. Hunt, and E. Ott, “Growing networks with geographical attachment preference: Emergence of small worlds,” *Phys. Rev. E*, vol. 69, no. 1, pp. 1–5, 2004.

[174] A. Zitin, A. Gorowara, S. Squires, M. Herrera, T. M. Antonsen, M. Girvan, and E. Ott, “Spatially embedded growing small-world networks,” *Sci. Rep.*, vol. 4, p. 7047, 2014.

[175] M. Shimada and T. Nakamura, “Time of neuron origin in mouse hypothalamic nuclei,” *Exp. Neurol.*, vol. 41, no. 1, pp. 163–173, 1973.

[176] C. S. Kabrita and F. C. Davis, “Development of the mouse suprachiasmatic nucleus: Determination of time of cell origin and spatial arrangements within the nucleus,” *Brain Res.*, vol. 1195, pp. 20–27, 2008.

[177] T. Shimogori, D. A. Lee, A. Miranda-Angulo, Y. Yang, H. Wang, L. Jiang, A. C. Yoshida, A. Kataoka, H. Mashiko, M. Avetisyan, L. Qi, J. Qian, and S. Blackshaw, "A genomic atlas of mouse hypothalamic development," *Nat. Neurosci.*, vol. 13, no. 6, pp. 767–775, 2010.

[178] C. VanDunk, L. A. Hunter, and P. A. Gray, "Development, Maturation, and Necessity of Transcription Factors in the Mouse Suprachiasmatic Nucleus," *J. Neurosci.*, vol. 31, no. 17, pp. 6457–6467, 2011.

[179] D. D. Clark, M. R. Gorman, M. Hatori, J. D. Meadows, S. Panda, and P. L. Mellon, "Aberrant Development of the Suprachiasmatic Nucleus and Circadian Rhythms in Mice Lacking the Homeodomain Protein Six6," *J. Biol. Rhythms*, vol. 28, no. 1, pp. 15–25, 2013.

[180] J. L. Bedont, T. A. LeGates, E. A. Slat, M. S. Byerly, H. Wang, J. Hu, A. C. Rupp, J. Qian, G. W. Wong, E. D. Herzog, S. Hattar, and S. Blackshaw, "Lhx1 Controls Terminal Differentiation and Circadian Function of the Suprachiasmatic Nucleus," *Cell Rep.*, vol. 7, no. 3, pp. 609–622, 2014.

[181] Y. J. Moore and E. Bernstein, "Synaptogenesis in the Rat Suprachiasmatic Nucleus Demonstrated by Electron Microscopy and Synapsin I Immunoreactivity," *J. Neurosci.*, vol. 9, no. 6, pp. 2151–2162, 1989.

[182] S. M. Reppert and W. J. Schwartz, "Maternal coordination of the fetal biological clock in utero," *Science*, vol. 220, no. 4600, pp. 969–971, 1983.

[183] S. Reppert and W. Schwartz, "The suprachiasmatic nuclei of the fetal rat: characterization of a functional circadian clock using 14C-labeled deoxyglucose," *J. Neurosci.*, vol. 4, no. 7, pp. 1677–1682, 1984.

[184] S. Shibata and R. Y. Moore, "Development of neuronal activity in the rat suprachiasmatic nucleus," *Brain Res.*, vol. 431, no. 2, pp. 311–315, 1987.

[185] M. Sladek, A. Sumova, Z. Kovacikova, Z. Bendova, K. Laurinova, and H. Illnerova, "Insight into molecular core clock mechanism of embryonic and early postnatal rat suprachiasmatic nucleus," *Proc. Natl. Acad. Sci. U. S. A.*, vol. 101, no. 16, pp. 6231–6236, 2004.

[186] Z. Kováčiková, M. Sládek, Z. Bendová, H. Illnerová, and A. Sumová, "Expression of Clock and Clock-Driven Genes in the Rat Suprachiasmatic Nucleus during Late Fetal and Early Postnatal Development," *J. Biol. Rhythms*, vol. 21, no. 2, pp. 140–148, 2006.

[187] P. Houdek and A. Sumová, "In Vivo Initiation of Clock Gene Expression Rhythmicity in Fetal Rat Suprachiasmatic Nuclei," *PLoS One*, vol. 9, no. 9, p. e107360, 2014.

[188] K. Shimomura, "Genome-Wide Epistatic Interaction Analysis Reveals Complex Genetic Determinants of Circadian Behavior in Mice," *Genome Res.*, vol. 11, no. 6, pp. 959–980, 2001.

[189] N. Ansari, M. Agathagelidis, C. Lee, H.-W. Korf, and C. von Gall, "Differential maturation of circadian rhythms in clock gene proteins in the suprachiasmatic nucleus and the pars tuberalis during mouse ontogeny," *Eur. J. Neurosci.*, vol. 29, no. 3, pp. 477–489, 2009.

[190] D. Landgraf, C. Achten, F. Dallmann, and H. Oster, "Embryonic development and maternal regulation of murine circadian clock function," *Chronobiol. Int.*, vol. 32, no. 3, pp. 416–427, 2015.

[191] D. Wreschnig, H. Dolatshad, and F. C. Davis, “Embryonic Development of Circadian Oscillations in the Mouse Hypothalamus,” *J. Biol. Rhythms*, vol. 29, no. 4, pp. 299–310, 2014.

[192] J. A. Mohawk and J. S. Takahashi, “Cell autonomy and synchrony of suprachiasmatic nucleus circadian oscillators,” *Trends Neurosci.*, vol. 34, no. 7, pp. 349–358, 2011.

[193] E. D. Herzog, I. Z. Kiss, and C. Mazuski, “Measuring synchrony in the mammalian central circadian circuit,” *Methods Enzymol.*, vol. 552, pp. 3–22, 2015.

[194] J. Evans and M. Gorman, “In synch but not in step: Circadian clock circuits regulating plasticity in daily rhythms,” *Neuroscience*, vol. 320, pp. 259–280, 2016.

[195] A. J. Harmar, H. M. Marston, S. Shen, C. Spratt, K. M. West, W. Sheward, C. F. Morrison, J. R. Dorin, H. D. Piggins, J.-C. Reubi, J. S. Kelly, E. S. Maywood, and M. H. Hastings, “The VPAC2 Receptor Is Essential for Circadian Function in the Mouse Suprachiasmatic Nuclei,” *Cell*, vol. 109, no. 4, pp. 497–508, 2002.

[196] C. S. Colwell, S. Michel, J. Itri, W. Rodriguez, J. Tam, V. Lelievre, Z. Hu, X. Liu, J. A. Waschek, and S. Christopher, “Disrupted circadian rhythms in VIP- and PHI-deficient mice,” *Am. J. Physiol. Regul. Integr. Comp. Physiol.*, vol. 285, no. 5, pp. R939–R949, 2003.

[197] E. S. Maywood, A. B. Reddy, G. K. Y. Wong, J. S. O’Neill, J. A. O’Brien, D. G. McMahon, A. J. Harmar, H. Okamura, and M. H. Hastings, “Synchronization and maintenance of timekeeping in suprachiasmatic circadian clock cells by neuropeptidergic signaling,” *Curr. Biol.*, vol. 16, no. 6, pp. 599–605, 2006.

[198] C. M. Ciarleglio, K. L. Gamble, J. C. Axley, B. R. Strauss, J. Y. Cohen, C. S. Colwell, and D. G. McMahon, “Population Encoding by Circadian Clock Neurons Organizes Circadian Behavior,” *J. Neurosci.*, vol. 29, no. 6, pp. 1670–1676, 2009.

[199] M. H. Wang, N. Chen, and J. H. Wang, “The coupling features of electrical synapses modulate neuronal synchrony in hypothalamic superachiasmatic nucleus,” *Brain Res.*, vol. 1550, pp. 9–17, 2014.

[200] D. Ono, S. Honma, and K.-i. Honma, “Differential roles of AVP and VIP signaling in the postnatal changes of neural networks for coherent circadian rhythms in the SCN,” *Sci. Adv.*, vol. 2, no. 9, pp. e1 600 960–e1 600 960, 2016.

[201] G. L. Fain, *Molecular and cellular physiology of neurons*. Harvard University Press, 1999.

[202] T. Ruf, “The Lomb-Scargle periodogram in biological rhythm research: Analysis of incomplete and unequally spaced time-series,” *Biol. Rhythm Res.*, vol. 30, no. 2, pp. 178–201, 1999.

[203] T. L. Leise and M. E. Harrington, “Wavelet-based time series analysis of circadian rhythms,” *J. Biol. Rhythms*, vol. 26, no. 5, pp. 454–463, 2011.

[204] E. Jones, T. Oliphant, and P. Peterson, “SciPy: open source scientific tools for Python,” 2014.

[205] S. Seabold and J. Perktold, “Statsmodels: econometric and statistical modeling with Python,” *Proc. 9th Python Sci. Conf.*, pp. 57–61, 2010.

[206] J. D. Hunter, “Matplotlib: A 2D graphics environment,” *Comput. Sci. Eng.*, vol. 9, no. 3, pp. 99–104, 2007.

[207] F. Pérez and B. E. Granger, "IPython: A system for interactive scientific computing," *Comput. Sci. Eng.*, vol. 9, no. 3, pp. 21–29, 2007.

[208] D. J. Cutler, M. Haraura, H. E. Reed, S. Shen, W. J. Sheward, C. F. Morrison, H. M. Marston, A. J. Harmar, and H. D. Piggins, "The mouse VPAC2 receptor confers suprachiasmatic nuclei cellular rhythmicity and responsiveness to vasoactive intestinal polypeptide in vitro," *Eur. J. Neurosci.*, vol. 17, no. 2, pp. 197–204, 2003.

[209] L. Yan and H. Okamura, "Gradients in the circadian expression of Per1 and Per2 genes in the rat suprachiasmatic nucleus," *Eur. J. Neurosci.*, vol. 15, no. 7, pp. 1153–1162, 2002.

[210] J. E. Quintero, S. J. Kuhlman, and D. G. McMahon, "The biological clock nucleus: a multiphasic oscillator network regulated by light," *J. Neurosci.*, vol. 23, no. 22, pp. 8070–8076, 2003.

[211] T. K. Sato, S. Panda, L. J. Miraglia, T. M. Reyes, R. D. Rudic, P. McNamara, K. A. Naik, G. A. Fitzgerald, S. A. Kay, and J. B. Hogenesch, "A functional genomics strategy reveals rora as a component of the mammalian circadian clock," *Neuron*, vol. 43, no. 4, pp. 527–537, 2004.

[212] M. H. Hastings, M. Brancaccio, and E. S. Maywood, "Circadian Pacemaking in Cells and Circuits of the Suprachiasmatic Nucleus," *J. Neuroendocrinol.*, vol. 26, no. 1, pp. 2–10, 2014.

[213] K. Yagita, K. Horie, S. Koinuma, W. Nakamura, I. Yamanaka, A. Urasaki, Y. Shigeyoshi, K. Kawakami, S. Shimada, J. Takeda, and Y. Uchiyama, "Development of the circadian oscillator during differentiation of mouse embryonic stem cells in vitro," *Proc. Natl. Acad. Sci. U. S. A.*, vol. 107, no. 8, pp. 3846–3851, 2010.

[214] Y. Inada, H. Uchida, Y. Umemura, W. Nakamura, T. Sakai, N. Koike, and K. Yagita, "Cell and tissue-autonomous development of the circadian clock in mouse embryos," *FEBS Lett.*, vol. 588, no. 3, pp. 459–465, 2014.

[215] J. A. Evans, T. L. Leise, O. Castanon-Cervantes, and A. J. Davidson, "Intrinsic Regulation of Spatiotemporal Organization within the Suprachiasmatic Nucleus," *PLoS One*, vol. 6, no. 1, p. e15869, 2011.

[216] B. Jeong, J. H. Hong, H. Kim, H. K. Choe, K. Kim, and K. J. Lee, "Multi-stability of circadian phase wave within early postnatal suprachiasmatic nucleus," *Sci. Rep.*, vol. 6, no. 1, p. 21463, 2016.

[217] J. L. Bedont and S. Blackshaw, "Constructing the suprachiasmatic nucleus: a watchmaker's perspective on the central clockworks," *Front. Syst. Neurosci.*, vol. 9, pp. 1–21, 2015.

[218] M. R. Buijink, A. Almog, C. B. Wit, O. Roethler, A. H. O. Olde Engberink, J. H. Meijer, D. Garlaschelli, J. H. T. Rohling, and S. Michel, "Evidence for Weakened Intercellular Coupling in the Mammalian Circadian Clock under Long Photoperiod," *PLoS One*, vol. 11, no. 12, p. e0168954, 2016.

[219] S. Honma, W. Nakamura, T. Shirakawa, and K. I. Honma, "Diversity in the circadian periods of single neurons of the rat suprachiasmatic nucleus depends on nuclear structure and intrinsic period," *Neurosci. Lett.*, vol. 358, no. 3, pp. 173–176, 2004.

[220] Y. Ban, Y. Shigeyoshi, and H. Okamura, "Development of vasoactive intestinal peptide mRNA rhythm in the rat suprachiasmatic nucleus," *J. Neurosci.*, vol. 17, no. 10, pp. 3920–3931, 1997.

[221] E. D. Herzog, M. S. Grace, C. Harrer, J. Williamson, K. Shinohara, and G. D. Block, "The role of Clock in the developmental expression of neuropeptides in the suprachiasmatic nucleus," *J. Comp. Neurol.*, vol. 424, no. 1, pp. 86–98, 2000.

[222] T. M. Brown, "Gastrin-Releasing Peptide Promotes Suprachiasmatic Nuclei Cellular Rhythmicity in the Absence of Vasoactive Intestinal Polypeptide-VPAC2 Receptor Signaling," *J. Neurosci.*, vol. 25, no. 48, pp. 11 155–11 164, 2005.

[223] E. S. Maywood, J. E. Chesham, Q.-J. Meng, P. M. Nolan, A. S. I. Loudon, and M. H. Hastings, "Tuning the Period of the Mammalian Circadian Clock: Additive and Independent Effects of CK1 Tau and Fbxl3Afh Mutations on Mouse Circadian Behavior and Molecular Pacemaking," *J. Neurosci.*, vol. 31, no. 4, pp. 1539–1544, 2011.

[224] R. P. Rubin, "Role of calcium in the release substances of neurotransmitter and hormones," *Pharmacol. Rev.*, vol. 22, no. 144, pp. 389–428, 1970.

[225] O.-H. Shin, J.-S. Rhee, J. Tang, S. Sugita, C. Rosenmund, and T. C. Südhof, "Sr2+ Binding to the Ca2+ Binding Site of the Synaptotagmin 1 C2B Domain Triggers Fast Exocytosis without Stimulating SNARE Interactions," *Neuron*, vol. 37, no. 1, pp. 99–108, 2003.

[226] R. M. Buijs, J. Wortel, and Y.-X. Hou, "Colocalization of gamma-aminobutyric acid with vasopressin, vasoactive intestinal peptide, and somatostatin in the rat suprachiasmatic nucleus," *J. Comp. Neurol.*, vol. 358, no. 3, pp. 343–352, 1995.

[227] C. Salio, L. Lossi, F. Ferrini, and A. Merighi, "Neuropeptides as synaptic transmitters," *Cell Tissue Res.*, vol. 326, no. 2, pp. 583–598, 2006.

[228] C. I. Eastman, R. E. Mistlberger, and A. Rechtschaffen, "Suprachiasmatic nuclei lesions eliminate circadian temperature and sleep rhythms in the rat," *Physiol. Behav.*, vol. 32, no. 3, pp. 357–368, 1984.

[229] J. M. Ding, L. E. Faiman, W. J. Hurst, L. R. Kuriashkina, and M. U. Gillette, "Resetting the biological clock: mediation of nocturnal CREB phosphorylation via light, glutamate, and nitric oxide," *J. Neurosci.*, vol. 17, no. 2, pp. 667–675, 1997.

[230] M. E. Harrington, S. Hoque, A. Hall, D. Golombek, and S. Biello, "Pituitary adenylate cyclase activating peptide phase shifts circadian rhythms in a manner similar to light," *J. Neurosci.*, vol. 19, no. 15, pp. 6637–6642, 1999.

[231] J. Hannibal, M. Møller, O. P. Ottersen, and J. Fahrenkrug, "PACAP and glutamate are co-stored in the retinohypothalamic tract," *J. Comp. Neurol.*, vol. 418, no. 2, pp. 147–155, 2000.

[232] M. Mieda, D. Ono, E. Hasegawa, H. Okamoto, K.-I. Honma, S. Honma, and T. Sakurai, "Cellular clocks in AVP neurons of the SCN are critical for interneuronal coupling regulating circadian behavior rhythm," *Neuron*, vol. 85, no. 5, pp. 1103–1116, 2015.

[233] E. D. Herzog, T. Hermanstyne, N. J. Smyllie, and M. H. Hastings, "Regulating the suprachiasmatic nucleus (SCN) circadian clockwork: Interplay between cell- autonomous and circuit-level mechanisms," *Cold Spring Harb. Perspect. Biol.*, vol. 9, no. 1, 2017.

[234] J. R. Jones, M. C. Tackenberg, and D. G. McMahon, "Manipulating circadian clock neuron firing rate resets molecular circadian rhythms and behavior," *Nat. Neurosci.*, vol. 18, no. 3, pp. 373–375, 2015.

[235] T. M. Brown, C. S. Colwell, J. A. Waschek, and H. D. Piggins, "Disrupted neuronal activity rhythms in the suprachiasmatic nuclei of vasoactive intestinal polypeptide-deficient mice," *J. Neurophysiol.*, vol. 97, no. 3, pp. 2553–2558, 2007.

[236] S. An, C. Tsai, J. Ronecker, A. Bayly, and E. D. Herzog, "Spatiotemporal distribution of vasoactive intestinal polypeptide receptor 2 in mouse suprachiasmatic nucleus," *J. Comp. Neurol.*, vol. 520, no. 12, pp. 2730–2741, 2012.

[237] Z. Travnickova-Bendova, N. Cermakian, S. M. Reppert, and P. Sassone-Corsi, "Bimodal regulation of mPeriod promoters by CREB-dependent signaling and CLOCK/BMAL1 activity," *Proc. Natl. Acad. Sci. U. S. A.*, vol. 99, no. 11, pp. 7728–7733, 2002.

[238] A. C. Liu, W. G. Lewis, and S. A. Kay, "Mammalian circadian signaling networks and therapeutic targets," *Nat. Chem. Biol.*, vol. 3, no. 10, pp. 630–639, 2007.

[239] E. S. Maywood, J. S. O'Neill, A. B. Reddy, J. E. Chesham, H. M. Prosser, C. P. Kyriacou, S. I. H. Godinho, P. M. Nolan, and M. H. Hastings, "Genetic and Molecular Analysis of the Central and Peripheral Circadian Clockwork of Mice," *Cold Spring Harb. Symp. Quant. Biol.*, vol. 72, no. 1, pp. 85–94, 2007.

[240] M. Verhage, H. T. McMahon, W. E. J. M. Ghijsen, F. Boomsma, G. Scholten, V. M. Wiegant, and D. G. Nicholls, "Differential release of amino acids, neuropeptides, and catecholamines from isolated nerve terminals," *Neuron*, vol. 6, no. 4, pp. 517–524, 1991.

[241] E. D. Herzog, J. S. Takahashi, and G. D. Block, "Clock controls circadian period in isolated suprachiasmatic nucleus neurons," *Nat. Neurosci.*, vol. 1, no. 8, pp. 708–713, 1998.

[242] A. B. Webb, S. R. Taylor, K. A. Thoroughman, F. J. Doyle III, and E. D. Herzog, "Weakly Circadian Cells Improve Resynchrony," *PLoS Comput. Biol.*, vol. 8, no. 11, p. e1002787, 2012.

[243] T. O. Hermanstyne, C. L. Simms, Y. Carrasquillo, E. D. Herzog, and J. M. Nerbonne, "Distinct Firing Properties of Vasoactive Intestinal Peptide-Expressing Neurons in the Suprachiasmatic Nucleus," *J. Biol. Rhythms*, vol. 31, no. 1, pp. 57–67, 2016.

[244] F. Pedregosa, G. Varoquaux, A. Gramfort, V. Michel, B. Thirion, O. Grisel, M. Blondel, P. Prettenhofer, R. Weiss, V. Dubourg, J. Vanderplas, A. Passos, D. Cournapeau, M. Brucher, M. Perrot, and É. Duchesnay, "Scikit-learn: Machine Learning in Python," *J. Mach. Learn. Res.*, vol. 12, pp. 2825–2830, 2012.

[245] G. Wu, R. C. Anafi, M. E. Hughes, K. Kornacker, and J. B. Hogenesch, "MetaCycle: an integrated R package to evaluate periodicity in large scale data," *Bioinformatics*, vol. 32, no. 21, pp. 3351–3353, 2016.

[246] S. Salvador and P. Chan, "Toward accurate dynamic time warping in linear time and space," *Intell. Data Anal.*, vol. 11, no. 5, pp. 561–580, 2007.

[247] S. J. Aton, G. D. Block, H. Tei, S. Yamazaki, and E. D. Herzog, "Plasticity of Circadian Behavior and the Suprachiasmatic Nucleus Following Exposure to Non-24-Hour Light Cycles," *J. Biol. Rhythms*, vol. 19, no. 3, pp. 198–207, 2004.

[248] T. L. Leise, "Wavelet analysis of circadian and ultradian behavioral rhythms," *J. Circadian Rhythms*, vol. 11, no. 1, p. 5, 2013.

[249] J. Fan, H. Zeng, D. P. Olson, K. M. Huber, J. R. Gibson, and J. S. Takahashi, "Vasoactive Intestinal Polypeptide (VIP)-Expressing Neurons in the Suprachiasmatic Nucleus Provide Sparse GABAergic Outputs to Local Neurons with Circadian Regulation Occurring Distal to the Opening of Postsynaptic GABAA Ionotropic Receptors," *J. Neurosci.*, vol. 35, no. 5, pp. 1905–1920, 2015.

[250] M. V. Tsodyks and H. Markram, "The neural code between neocortical pyramidal neurons depends on neurotransmitter release probability," *Proc. Natl. Acad. Sci. U. S. A.*, vol. 94, no. 2, pp. 719–723, 1997.

[251] E. Neher and T. Sakaba, "Multiple roles of calcium ions in the regulation of neurotransmitter release," *Neuron*, vol. 59, no. 6, pp. 861–872, 2008.

[252] C. M. Pennartz, M. T. De Jeu, A. M. Geurtsen, A. A. Sluiter, and M. L. Hermes, "Electrophysiological and morphological heterogeneity of neurons in slices of rat suprachiasmatic nucleus," *J. Physiol.*, vol. 506 (Pt 3, no. 3, pp. 775–793, 1998.

[253] S. An, R. P. Irwin, C. N. Allen, C. Tsai, and E. D. Herzog, "Vasoactive intestinal polypeptide requires parallel changes in adenylate cyclase and phospholipase C to entrain circadian rhythms to a predictable phase," *J. Neurophysiol.*, vol. 105, no. 5, pp. 2289–2296, 2011.

[254] J. Bieler, R. Cannavo, K. Gustafson, C. Gobet, D. Gatfield, and F. Naef, "Robust synchronization of coupled circadian and cell cycle oscillators in single mammalian cells," *Mol. Syst. Biol.*, vol. 10, no. 7, p. 739, 2014.

[255] F. van Oosterhout, E. A. Lucassen, T. Houben, H. T. VanderLeest, M. C. Antle, and J. H. Meijer, "Amplitude of the SCN clock enhanced by the behavioral activity rhythm," *PLoS One*, vol. 7, no. 6, 2012.

[256] J. S. Marvin, B. G. Borghuis, L. Tian, J. Cichon, M. T. Harnett, J. Akerboom, A. Gordus, S. L. Renninger, T. W. Chen, C. I. Bargmann, M. B. Orger, E. R. Schreiter, J. B. Demb, W. B. Gan, S. A. Hires, and L. L. Looger, "An optimized fluorescent probe for visualizing glutamate neurotransmission," *Nat. Methods*, vol. 10, no. 2, pp. 162–170, 2013.

[257] M. Brancaccio, E. S. Maywood, J. E. Chesham, A. S. I. Loudon, and M. H. Hastings, "A Gq-Ca2+Axis controls circuit-level encoding of circadian time in the suprachiasmatic nucleus," *Neuron*, vol. 78, no. 4, pp. 714–728, 2013.

[258] E. G. Govorunova, O. A. Sineshchekov, R. Janz, X. Liu, and J. L. Spudich, "Natural light-gated anion channels: A family of microbial rhodopsins for advanced optogenetics," *Science*, vol. 349, no. 6248, pp. 647–650, 2015.

[259] T. Noguchi, T. L. Leise, N. Kingsbury, T. Diemer, L. L. Wang, M. A. Henson, and D. K. Welsh, "Calcium Circadian Rhythmicity in the Suprachiasmatic Nucleus: Cell Autonomy and Network Modulation," *Eneuro*, vol. 4, 2017.

[260] E. J. Hancock, J. Ang, A. Papachristodoulou, and G.-B. Stan, "The Interplay between Feedback and Buffering in Cellular Homeostasis," *Cell Syst.*, vol. 5, no. 5, pp. 498–508, 2017.

[261] L. Potvin-Trottier, N. D. Lord, G. Vinnicombe, and J. Paulsson, "Synchronous long-term oscillations in a synthetic gene circuit," *Nature*, vol. 538, no. 7626, pp. 514–517, 2016.

[262] T. W. Chen, T. J. Wardill, Y. Sun, S. R. Pulver, S. L. Renninger, A. Baohan, E. R. Schreiter, R. A. Kerr, M. B. Orger, V. Jayaraman, L. L. Looger, K. Svoboda, and D. S. Kim, "Ultrasensitive fluorescent proteins for imaging neuronal activity," *Nature*, vol. 499, no. 7458, pp. 295–300, 2013.

[263] T. Klabunde and G. Hessler, "Drug design strategies for targeting G-protein-coupled receptors," *Chem Biochem*, vol. 3, no. 10, pp. 928–944, 2002.

[264] Y. Okuno, A. Tamon, H. Yabuuchi, S. Niijima, Y. Minowa, K. Tonomura, R. Kunimoto, and C. Feng, "GLIDA: GPCR - Ligand database for chemical genomics drug discovery - Database and tools update," *Nucleic Acids Res.*, vol. 36, pp. 907–912, 2008.

[265] J.-C. Marquié, P. Tucker, S. Folkard, C. Gentil, and D. Ansiau, "Chronic effects of shift work on cognition: findings from the VISAT longitudinal study," *Occup. Environ. Med.*, vol. 72, no. 4, pp. 258–264, 2015.

[266] A. Julius, J. Yin, and J. T. Wen, "Time-Optimal Control for Circadian Entrainment for a Model with Circadian and Sleep Dynamics," in *IEEE Conf. Decis. Control 2017*, pp. 4709–4714.

[267] O. Slaby, S. Sager, O. S. Shaik, U. Kummer, and D. Lebiedz, "Optimal control of self-organized dynamics in cellular signal transduction," *Math. Comput. Model. Dyn. Syst.*, vol. 13, no. 5, pp. 487–502, 2007.

[268] O. Shaik, S. Sager, O. Slaby, and D. Lebiedz, "Phase tracking and restoration of circadian rhythms by model-based optimal control," *IET Syst. Biol.*, vol. 2, no. 1, pp. 16–23, 2008.

[269] W. Qiao, J. T. Wen, and A. Julius, "Entrainment Control of Phase Dynamics," *IEEE Trans. Automat. Contr.*, vol. 62, no. 1, pp. 445–450, 2017.

[270] J. H. Abel and F. J. Doyle III, "A systems theoretic approach to analysis and control of mammalian circadian dynamics," *Chem. Eng. Res. Des.*, vol. 116, pp. 48–60, 2016.

[271] J. H. Abel, A. Chakrabarty, and F. J. Doyle III, "Nonlinear Model Predictive Control For Circadian Entrainment Using Small-Molecule Pharmaceuticals," *IFAC-PapersOnLine*, vol. 50, no. 1, pp. 9864–9870, 2017.

[272] J. K. Kim, D. B. Forger, M. Marconi, D. Wood, A. Doran, T. Wager, C. Chang, and K. M. Walton, "Modeling and Validating Chronic Pharmacological Manipulation of Circadian Rhythms," *CPT Pharmacometrics Syst. Pharmacol.*, vol. 2, no. 7, p. e57, 2013.

[273] C. H. Johnson, "Forty years of PRCs–what have we learned?" *Chronobiol. Int.*, vol. 16, no. 6, pp. 711–743, 1999.

[274] A. T. Winfree, *The geometry of biological time*. Springer-Verlag, 2001.

[275] C. A. Czeisler, J. F. Duffy, T. L. Shanahan, E. N. Brown, F. Jude, D. W. Rimmer, J. M. Ronda, E. J. Silva, J. S. Allan, S. Jonathan, D.-j. J. Dijk, and R. E. Kronauer, "Stability, precision, and near-24-hour period of the human circadian pacemaker," *Science*, vol. 284, no. 5423, pp. 2177–2181, 1999.

[276] D. E. Kirk, *Optimal Control Theory: An Introduction*. Dover Publications, 2012.

[277] C. Vetter, D. Fischer, J. L. Matera, and T. Roenneberg, "Aligning work and circadian time in shift workers improves sleep and reduces circadian disruption," *Curr. Biol.*, vol. 25, no. 7, pp. 907–911, 2015.

[278] V. Kolodyazhniy, J. Späti, S. Frey, T. Götz, A. Wirz-Justice, K. Kräuchi, C. Cajochen, and F. H. Wilhelm, "An improved method for estimating human circadian phase derived from multichannel ambulatory monitoring and artificial neural networks," *Chronobiol. Int.*, vol. 29, no. 8, pp. 1078–1097, 2012.

[279] J.-S. Li, I. Dasanayake, and J. Ruths, "Control and Synchronization of Neuron Ensembles," *IEEE Trans. Automat. Contr.*, vol. 58, no. 8, pp. 1919–1930, 2013.

[280] A. Ramkisoensing and J. H. Meijer, "Synchronization of Biological Clock Neurons by Light and Peripheral Feedback Systems Promotes Circadian Rhythms and Health," *Front. Neurol.*, vol. 6, no. 128, 2015.

[281] S. Gan and E. K. O'Shea, "An Unstable Singularity Underlies Stochastic Phasing of the Circadian Clock in Individual Cyanobacterial Cells," *Mol. Cell*, pp. 1–14, 2017.

[282] N. R. Glossop, L. C. Lyons, and P. E. Hardin, "Interlocked feedback loops within the Drosophila circadian oscillator," *Science*, vol. 286, no. 5440, pp. 766–768, 1999.

[283] K. C. Huang, Y. Meir, and N. S. Wingreen, "Dynamic structures in Escherichia coli: Spontaneous formation of MinE rings and MinD polar zones," *Proc. Natl. Acad. Sci. U. S. A.*, vol. 100, no. 22, pp. 12 724–12 728, 2003.

[284] S. R. Taylor, F. J. Doyle III, and L. R. Petzold, "Oscillator model reduction preserving the phase response: application to the circadian clock," *Biophys. J.*, vol. 95, no. 4, pp. 1658–1673, 2008.

[285] J. Andersson, J. Akesson, and M. Diehl, *Recent Advances in Algorithmic Differentiation*. Springer-Verlag, 2012, vol. 87.

[286] A.-M. Chang, N. Santhi, M. St Hilaire, C. Gronfier, D. S. Bradstreet, J. F. Duffy, S. W. Lockley, R. E. Kronauer, and C. A. Czeisler, "Human responses to bright light of different durations," *J. Physiol.*, vol. 590, no. 13, pp. 3103–3112, 2012.

[287] M. A. St Hilaire, J. J. Gooley, S. B. S. Khalsa, R. E. Kronauer, C. A. Czeisler, and S. W. Lockley, "Human phase response curve to a 1 h pulse of bright white light," *J. Physiol.*, vol. 590, no. 13, pp. 3035–3045, 2012.

[288] A. J. Laguna Sanz, F. J. Doyle III, and E. Dassau, "An Enhanced Model Predictive Control for the Artificial Pancreas Using a Confidence Index Based on Residual Analysis of Past Predictions," *J. Diabetes Sci. Technol.*, vol. 11, no. 3, pp. 537–544, 2017.

[289] R. Zhang, N. F. Lahens, H. I. Ballance, M. E. Hughes, and J. B. Hogenesch, "A circadian gene expression atlas in mammals: Implications for biology and medicine," *Proc. Natl. Acad. Sci. U. S. A.*, vol. 111, no. 45, pp. 16 219–16 224, 2014.

[290] C. A. Czeisler, R. E. Kronauer, J. S. Allan, J. F. Duffy, M. E. Jewett, E. N. Brown, and J. M. Ronda, "Bright Light Induction of Strong (Type-0) Resetting of the Human Circadian Pacemaker," *Science*, vol. 244, no. 4910, pp. 1328–1333, 1989.

[291] M. E. Jewett, R. E. Kronauer, and C. A. Czeisler, “Phase-Amplitude Resetting of the Human Circadian Pacemaker via Bright Light: A Further Analysis,” *J. Biol. Rhythms*, vol. 9, no. 3-4, pp. 295–314, 1994.

[292] M. E. Jewett and R. E. Kronauer, “Refinement of a limit cycle oscillator model of the effects of light on the human circadian pacemaker,” *J. Theor. Biol.*, vol. 192, no. 4, pp. 455–465, 1998.